

**Momentum Distributions from  
Bichromatic Ionization of Atoms and Molecules**

Von der Fakultät für Mathematik und Physik  
der Gottfried Wilhelm Leibniz Universität Hannover  
zur Erlangung des Grades

Doktor der Naturwissenschaften  
Dr. rer. nat.

genehmigte Dissertation von

M.Sc. Nicolas Thomas Eicke

2020

Referent: Prof. Dr. Manfred Lein  
Leibniz Universität Hannover

Korreferent: Prof. Dr. Ulf Saalman  
MIPPKS Dresden

Korreferent: Prof. Dr. Dieter Bauer  
Universität Rostock

Tag der Promotion: 02.09.2020

# Abstract

When a sufficiently strong laser field acts on an atom or a molecule, ionization can occur. Electrons released in this process are accelerated by the laser field and the distribution of their final momenta can be measured. As opposed to using linear or circular polarization to drive the ionization process, tailored fields provide additional degrees of freedom to create field shapes with special properties. The present thesis investigates the interaction of atoms and molecules with such fields through numerical calculation of photoelectron momentum distributions, and their application towards a time-resolved picture of strong-field ionization.

For a two-color scheme where a weak orthogonal second harmonic is used to probe the ionization process in a strong linearly polarized laser field by observing the modulation of the signal as a function of the delay between the two colors, we solve the time-dependent Schrödinger equation in three dimensions and find the time of ionization resolved by final photoelectron momentum. We demonstrate that the delay scan is sensitive to Coulomb focusing and reveals signatures of photoelectron holography.

While two-color schemes can be used to measure ionization times in linear polarization, the attoclock is used in circular polarization. There, the ionization time is inferred from the detection angle of the photoelectron. Because of Coulomb effects, a theoretical model is always required to determine the precise mapping. Contrary to models that are typically used, we obtain this mapping without relying on the notion of an electron trajectory. This is achieved by considering the stationary points of the Dyson integral representation of the time-dependent Schrödinger equation. We find these stationary points using numerical wave function propagation in complex time and confirm that the maximum of the momentum distributions corresponds well to the time of peak field strength.

Using a counter-rotating bicircular laser field, the concept of the attoclock can be transferred to other types of polarization. For suitable field strength ratio, the electric field is approximately linearly polarized around the time of peak field strength while the shape of the vector potential is similar to the attoclock. First, we apply the trajectory-free theory to this field to find the most probable time of ionization. Second, we combine the bicircular field with the two-color scheme. This allows us to compare the ionization time measured in the two-color scheme with the one measured in the attoclock. We find that the orthogonal two-color scheme measures ionization time as if the Coulomb potential were not present. However, switching to parallel polarization, we obtain meaningful ionization times in accordance with the attoclock principle that ionization takes place most likely at the peak of the pulse. Applying the bicircular field to a polar molecule, we find that the momentum distribution shows a dependence on the orientation, but this does not imply an orientation dependence of the ionization time.

**Keywords:** strong-field ionization, time-dependent Schrödinger equation, two-color fields



# Acknowledgments

This thesis is the result of my research as a member of the Theoretical Quantum Dynamics Group of the Institute for Theoretical Physics at Leibniz Universität Hannover. During my time at the university, I have met, worked with, and been supported by many wonderful people.

Above all, I would like to thank my supervisor Manfred Lein for his continuous support. He gave me the chance to work on interesting projects and provided a perfect mix of coming up with ideas while encouraging me to develop my own. I have enjoyed the time we have spent together in discussions for which he always had time.

I would also like to thank my current and former colleagues from Hanover for valuable discussions and cheerful conversations – especially Simon Brennecke with whom I had a great time sharing an office. My lunch-break companions and long-term friends Simon Brandhorst, Natascha Lange, Inken Siemon, Jakob Schweer, Erik Schwanke, Pavel Sterin, and Lars Dammeier contributed a lot to me enjoying my time at the institute.

I express my gratitude to my parents Ilona and Günther Eicke and my brother Daniel Eicke. They allowed me the freedom to pursue my interests and would always support me when I needed it. Finally, a big thank you goes to my wife Yiting Wang for being there for me during all these years.



# Contents

<b>Abstract</b>	<b>iii</b>
<b>Acknowledgments</b>	<b>v</b>
<b>Contents</b>	<b>vii</b>
<b>List of abbreviations</b>	<b>ix</b>
<b>1 Introduction</b>	<b>1</b>
1.1 Outline of the thesis . . . . .	4
<b>2 Concepts and methods</b>	<b>7</b>
2.1 Regimes of laser-induced ionization . . . . .	7
2.2 The simple man's model . . . . .	8
2.3 Time-dependent Schrödinger equation . . . . .	10
2.3.1 Simple solutions of the TDSE . . . . .	11
2.4 Strong-field approximation . . . . .	12
2.4.1 Saddle-point approximation . . . . .	13
2.5 Analytical R-matrix theory . . . . .	14
2.6 Semiclassical two-step model . . . . .	16
<b>3 Streaking with orthogonal two-color laser fields</b>	<b>19</b>
3.1 Introduction . . . . .	19
3.2 Computational details . . . . .	21
3.3 Linear polarization . . . . .	22
3.4 Two-color delay scan . . . . .	22
3.5 Lateral dependence of the two-color scan . . . . .	27
3.6 Two-color scan in a molecule . . . . .	28
3.7 Conclusion . . . . .	31
<b>4 Trajectory-free ionization times</b>	<b>35</b>
4.1 Introduction . . . . .	35
4.2 Strong-field approximation with full integrand . . . . .	38
4.3 The attoclock . . . . .	42
4.4 Computational details . . . . .	45
4.5 TDSE in the complex plane . . . . .	46
4.6 Geometrical factors and origin of the angle ambiguity . . . . .	49
4.7 Intensity scan . . . . .	52
4.8 Conclusion . . . . .	54

<b>5</b>	<b>Attoclock with bicircular fields</b>	<b>55</b>
5.1	Introduction	55
5.2	Strong-field ionization in bicircular laser fields	57
5.3	The quasilinear field	58
5.4	Attoclock analysis	62
5.5	Saddle-point approximation in the Dyson integral	66
5.6	Classical backpropagation	72
5.7	Analytical R-matrix theory	77
5.8	Eikonal approximation in the Dyson integral	82
5.9	Conclusion	84
5.10	Outlook	85
<b>6</b>	<b>Streaking with tailored fields</b>	<b>87</b>
6.1	Introduction	87
6.2	The parallel two-color scheme	88
6.3	Computational details	90
6.4	Results	90
6.5	Experimentally realistic parameters	95
6.6	Orientation dependence in molecules	98
6.7	Conclusion	100
<b>7</b>	<b>Summary and conclusion</b>	<b>103</b>
<b>A</b>	<b>Methods</b>	<b>105</b>
A.1	Time-dependent Schrödinger equation	105
A.1.1	Calculating the momentum distribution	105
A.1.2	Obtaining the bound state	107
A.1.3	Choice of the potential	107
A.1.4	Choice of the absorbing potential	111
A.2	Strong-field approximation	112
A.2.1	Adiabatic expansion of the saddle-point equation	112
A.2.2	Adiabatic limit of the action	113
A.2.3	Angular momentum states	114
A.2.4	Explicit solution of the saddle-point equation	115
A.3	Stationary points of the full Dyson integrand	115
A.4	Analytical R-matrix theory	116
A.4.1	Correction after the end of the laser pulse	116
A.4.2	Boundary matching for soft-core potentials	116
A.4.3	Momentum shift in the attoclock	117
A.4.4	Semiclassical action	117
A.5	Static ionization rates	118
	<b>Bibliography</b>	<b>123</b>
	<b>Curriculum vitae</b>	<b>145</b>
	<b>List of publications</b>	<b>147</b>



# List of abbreviations

ADK	Ammosov-Delone-Krainov
ARM	Analytical R-matrix (theory)
ATI	Above-threshold ionization
CCSFA	Coulomb-corrected strong-field approximation
CEP	Carrier-envelope phase
COLTRIMS	Cold-target recoil-ion-momentum spectroscopy
CQSFA	Coulomb quantum-orbit strong-field approximation
CW	Continuous wave
DCS	Differential cross section
HATI	High-order above-threshold ionization
HHG	High-harmonic generation
KFR	Keldysh-Faisal-Reiss
LIED	Laser-induced electron diffraction
NSDI	Non-sequential double ionization
OTC	Orthogonal two color
PMD	Photoelectron momentum distribution
PPT	Perelomov-Popov-Terent'ev
PTC	Parallel two color
QOM	Quantum-orbit model
QTMC	Quantum-trajectory Monte Carlo
RABBIT	Reconstruction of attosecond beating by interference of two-photon transitions
SCTS	Semiclassical two-step (model)
SFA	Strong-field approximation
SMM	Simple man's model
SPA	Saddle-point approximation
TDDFT	Time-dependent density-functional theory
TDSE	Time-dependent Schrödinger equation
TIPIS	Tunnel ionization in parabolic coordinates with induced dipole and Stark shift
VMI	Velocity-map imaging
XUV	Extreme ultra violet



# Chapter 1

## Introduction

The study of light matter interaction is one of the cornerstones of modern physics. Black-body radiation and the photoelectric effect lead to the development of quantum mechanics. The discrete level structure of the hydrogen atom was first inferred from its spectral lines and much of the knowledge we have today about the structure of matter was obtained by observing its interaction with radiation.

Strong-field physics studies the interaction of matter with strong electromagnetic fields, typically provided by an infrared laser that in its focus reaches field strengths comparable to the static electric field strength acting on a bound electron in an atom. The presence of the strong field leads to photoionization, but instead of absorbing a single photon upon ionization, the photoelectron can absorb many more photons than required to overcome the ionization threshold [1, 2]. This process is called above-threshold ionization (ATI). The physical mechanism of the strong-field ionization process extends from multiphoton absorption to tunnel ionization or even barrier suppression in the case of very strong fields.

Studying the interaction of atoms and molecules with strong fields gives us access to their electronic or molecular structure on the angstrom spatial scale and their dynamics on the attosecond time scale – the natural time scale of electron dynamics in atoms and molecules. This is remarkable because the driving laser field has a wavelength much larger (several hundred nanometers) and varies on a time scale much longer (femtoseconds).

Three mechanisms are primarily responsible for this. First, in the tunneling regime, the ionization probability depends exponentially on the field strength and is extremely sensitive to small fluctuations [3–5]. Observable features in the photoelectron momentum distribution (PMD) can be traced back to the time of ionization with attosecond precision. This is the main idea behind attosecond angular streaking, or the “attoclock,” where a circularly polarized laser pulse is used to both ionize an atom and map the ionization time of the photoelectron to its detection angle [6, 7].

Second, the electron can be driven back to the parent ion after ionization which leads to laser-induced electron diffraction or rescattering [8–10], high-harmonic generation (HHG) [11, 12], and non-sequential double ionization (NSDI) [13, 14]. Typically, the returning electron has a high energy and a small de-Broglie wavelength such that the atomic or molecular structure is imprinted onto the momentum distribution or the harmonic signal with high resolution. For example, the high-energy backscattering signal in the momentum distribution directly reflects the scattering cross section of the target [15–17]. The diffraction pattern reveals the molecular structure [18–20]. The harmonic signal reflects the electronic structure of the

target [21] and allows for full tomographic reconstruction of molecular orbitals [22–24]. The harmonic emission frequency depends on the return time (attochirp) which can be used to track molecular dynamics on the attosecond time scale [25, 26].

The third mechanism is related to the second in that high-harmonic generation can be used as a tabletop source of coherent extreme ultraviolet (XUV) radiation in subsequent experiments. Using long linearly polarized pulses to drive the process, the harmonics come in the shape of attosecond pulse trains [27]. With few-cycle drivers [28–30] or techniques such as polarization gating [31–33], single isolated attosecond pulses can be generated with the current record for the shortest pulse being less than 50 as [34]. Isolated pulses can be used together with the infrared driver in pump-probe schemes such as attosecond transient absorption spectroscopy to achieve attosecond resolution on induced electron dynamics [35–37]. Another achievement is the measurement of a time delay between single-photon ionization from different subshells of rare-gas atoms [38, 39].

Strong-field ionization allows us to study some of the most fundamental manifestations of quantum mechanics such as the tunneling of an electron through a (time-dependent) potential barrier. Several variations of the double-slit experiment are realized on the microscopic level as interference between different pathways of the ionization or harmonic-generation process [40–42]. Practical applications include the generation of spin-polarized electrons [43, 44] and the discrimination of enantiomers of chiral molecules via photoelectron circular dichroism [45, 46]. Strong-field physics is also beginning to move into other fields of research. In particular, there is currently a large interest in high-harmonic generation from solids [47–56] or photoemission from nanotips [57–62].

The photoelectron momentum distribution and the harmonic signal are the main observables in a strong-field experiment, whereby in this thesis we focus mostly on the momentum distribution. Much of the experimental success of strong-field physics stems from developing techniques to measure this quantity accurately. Experimentally, velocity-map imaging and reaction microscopes give access to the full three-dimensional momentum distribution. In velocity-map imaging, a static electric field is used to focus all photoelectrons with a given momentum to one point on a detector, independently of where in the interaction region the electron originated [63]. This provides directly a two-dimensional projection of the momentum distribution. The full three-dimensional PMD can be reconstructed using tomography or inversion techniques [64–67]. In a reaction microscope, ions and photoelectrons are deflected by electric and magnetic fields to detector plates. From the position of the fragments on the detectors and their time of flight, the full three-dimensional momentum vector can be calculated directly for every event [68, 69]. Attosecond bursts from high-harmonic generation can be fully reconstructed in the time domain using the attosecond streak camera [70] in case of isolated attosecond pulses or using interference of two-photon transitions (RABBIT) [27] in case of attosecond pulse trains.

On the theory side, strong-field physics is located in a physical regime between classical and quantum mechanics. A common trait of most strong-field phenomena is that they are inherently nonperturbative. In particular, tunnel ionization, rescattering and harmonic-generation are highly nonlinear processes. Instead, many effects can be understood in terms of classical trajectories. The most striking examples are the simple man’s model (SMM) of above-threshold ionization [71] and the three-step model of high-harmonic generation which describes the generation process as tunnel ionization, followed by free propagation in the laser

field, and recombination under emission of high-order harmonics [72, 73]. Assuming classical motion in the excursion step, the model predicts a maximal return energy of  $3.17 U_p$  and harmonic cutoff of  $I_p + 3.17 U_p$ . Here,  $U_p$  is the ponderomotive potential, i.e. the average kinetic energy of an electron in the laser field, and  $I_p$  is the ionization potential. Applying the model to high-order above-threshold ionization (HATI), a maximum photoelectron energy of  $10.01 U_p$  is found [74].

Complementary to the simple intuitive picture of classical trajectories lies the solution of the time-dependent Schrödinger equation which is generally required to achieve quantitative agreement with experimental results. The Schrödinger equation is usually solved in single-active-electron approximation where the photoelectron is described by a three-dimensional wave function and the influence of the nucleus and all other electrons is modeled by a static effective potential [75]. Although this works remarkably well in most cases [76], the search for multielectron effects is a constant companion in both theory and experiment [77–80]. A well-known example of the breakdown of the single-active electron approximation is the non-sequential double ionization of the helium atom [13, 14]. As of now, time-dependent calculations in full dimensionality are available for strong-field ionization of helium, but the exponential growth of the associated Hilbert space makes calculations with more degrees of freedom infeasible [81]. Therefore, there is a strong interest to develop new methods (or adapt established methods to the strong-field ionization problem) in order to find an efficient description of the relevant degrees of freedom and reduce the computational effort, such as time-dependent density-functional theory (TDDFT), or modified quantum-chemistry methods [82–86].

Although a solution of the time-dependent Schrödinger equation can be used to reproduce experimental results and predict new phenomena, it gives limited understanding of the physical mechanism involved. A very successful approach that lies between the full numerical solution and the simple man’s model is the strong-field approximation (SFA) in which the ionization amplitude or the harmonic signal is written as an integral over ionization time [87–90]. Applying the saddle-point approximation to the SFA integral leads to the quantum orbit model (QOM) in which the ionization amplitude is written as a coherent sum of “quantum orbits” – classical trajectories moving in complex time [91, 92]. The quantum-orbit model allows us to interpret strong-field phenomena in terms of trajectories while, to some degree, pertaining comparability with experimental results. Agreement with experimental results or the numerical solution of the time-dependent Schrödinger equation is improved by related techniques such as analytical R-matrix theory (ARM) [93, 94] as well as semi-classical models such as the semi-classical two-step model (SCTS) [95], the Coulomb-corrected strong-field approximation (CCSFA) [96–100] or the Coulomb quantum-orbit strong-field approximation (CQSFA) [101].

Trajectory-based models of strong-field ionization have an inherent notion of ionization time which is frequently used to interpret strong-field phenomena in a time-resolved way. This is most visible in the attoclock where a theoretical model is always required to associate an ionization time with the observed photoelectron momentum. The first main topic of this thesis is to investigate a way to retrieve momentum-resolved ionization times in strong-field ionization without the notion of an electron trajectory and apply the method to the attoclock setup. There, we also compare our results with those obtained by previously used models such as analytical R-matrix theory [78] or classical backpropagation [102–104].

Going beyond pure linear or circular polarization to drive the ionization process, new insight and applications have been found by using tailored fields such as parallel, orthogonal,

or bicircular two-color fields. It is common to use the second (or third) harmonic of the fundamental (infrared) field because it is easily accessible experimentally by frequency doubling. In the few-photon regime, the interference between one and two-photon transitions in a  $\omega$ - $2\omega$  field can be used to induce an asymmetry in the emission direction of photoelectrons [105, 106]. Interference between one and three-photon transitions in a  $\omega$ - $3\omega$  field can be used to control the product yields in photodissociation of molecules [107]. In the strong-field regime, the use of two-color fields relies on the interpretation of results in terms of trajectories and a bichromatic field can be used to both control and extract information about them. For example, in both above-threshold ionization and high-harmonic generation, there are typically at least two relevant trajectories that contribute to one final momentum or harmonic order. A weak second-harmonic field can be used to disentangle their contributions [108–110] and to find the ionization times or the return times of the dominant trajectory branch [111–115]. In other cases, the second-harmonic field is nonperturbative. Instead, it is used to create completely new field shapes where especially the counter-rotating bicircular field [116–119] has drawn much attention recently because it allows for rescattering and the generation of circular harmonics [120, 121].

The second main topic of this thesis is to demonstrate the use of tailored fields to investigate the ionization dynamics in strong-field ionization on the attosecond time scale. First, we consider an orthogonal streaking scheme with strong infrared and weak second-harmonic field as in [114] where we assess the role of Coulomb-focusing [122–124] and photoelectron holography [125, 126]. Then we demonstrate that with a suitable choice of field-strength ratio, bicircular fields can be used in an attoclock setup to probe the ionization process in approximately linear polarization. We use the bicircular field to investigate orientation-dependent properties of strong-field ionization of an asymmetric molecule. Going one step further, combining two-color streaking with the bicircular field allows us to compare the two concepts of ionization time – two-color streaking and angular streaking.

## 1.1 Outline of the thesis

This thesis comprises seven chapters. After the introduction presented here, Chapter 2 introduces basic concepts and methods used to describe the strong-field ionization of atoms and molecules. The mechanism of the laser-induced ionization process in various physical regimes is discussed. The simple man’s model and the three-step model are presented to provide basic intuition along with the time-dependent Schrödinger equation and derived methods such as the strong-field approximation, analytical R-matrix theory as well as semiclassical methods.

The following chapters investigate the concept of ionization time in strong-field physics. Chapter 3 extends work by Henkel and Lein [114] where a two-color streaking scheme was used to extract trajectory information and ionization times for photoelectrons in linear polarization. In particular, the role of Coulomb focusing and photoelectron holography on the relative weights between different types of trajectories is assessed. The same technique is then applied to an asymmetric molecule to probe orientation-dependent properties of the ionization process. In Chapter 4, a different approach is pursued. There, ionization time is defined via an integral-representation of the time-dependent Schrödinger equation. The formalism is applied to the attoclock to investigate the long-standing question of whether there is a de-

lay between the time of peak field strength and the time of most probable electron emission. Chapter 5 introduces the “bicircular attoclock,” which transfers the idea of the attoclock to linear polarization. We analyze photoelectron momentum distributions in regard to the temporal structure of the ionization process using the trajectory-free method presented in Chapter 4, but also using different established methods such as classical backpropagation or analytical R-matrix theory. In Chapter 6, the idea of the attoclock is combined with streaking such that the two different notions of ionization time can be unified. The thesis concludes in Chapter 7 with a summary and an outlook. Additional content that is not required for reading the thesis but to reproduce the presented results is provided in Appendix A.

In parts, the thesis contains results from the following works that are published in peer-reviewed scientific journals. A full list of the author’s publications can be found at the end of the thesis.

- [N. Eicke](#) and M. Lein,  
“Extracting trajectory information from two-color strong-field ionization,”  
[Journal of Modern Optics](#) 64, 981 (2017).
- [N. Eicke](#) and M. Lein,  
“Trajectory-free ionization times in strong-field ionization,”  
[Physical Review A](#) 97, 031402(R) (2018).
- [N. Eicke](#) and M. Lein,  
“Attoclock with counter-rotating bicircular laser fields,”  
[Physical Review A](#) 99, 031402(R) (2019).
- [N. Eicke](#), S. Brennecke, and M. Lein,  
“Attosecond-Scale Streaking Methods for Strong-Field Ionization by Tailored Fields,”  
[Physical Review Letters](#) 124, 043202 (2020).





## Chapter 2

# Concepts and methods

This chapter provides the basic physical mechanisms of strong-field ionization as well as the theoretical methods used in this thesis to describe the interaction of strong laser fields with atoms and molecules. All of these methods are derived from the nonrelativistic time-dependent Schrödinger equation in single-active electron approximation.

Atomic units are used throughout the thesis unless stated otherwise. In this system of units, length is measured in units of the Bohr radius, mass in units of the electron mass, charge in units of the elementary charge and the unit of time is defined such that the numerical value of the speed of light becomes the inverse of the fine structure constant. This implies that the unit of energy is twice the Rydberg energy and the reduced Planck constant is equal to unity. The unit of the electric field strength is the force acting on an electron in the Coulomb potential at a distance of one atomic unit, divided by its charge.

### 2.1 Regimes of laser-induced ionization

The system that is under consideration mostly throughout this thesis consists of an atom or a molecule in an external electric field. The atom is characterized by its ionization potential  $I_p$  which is the energy difference between the ground-state energy of the singly charged ion and the ground-state energy of the neutral.<sup>1</sup> The electric field at time  $t$ , in the simplest case linearly polarized, can be written as

$$\mathbf{E}(t) = E_0 \cos(\omega t) \mathbf{e}_z \quad (2.1)$$

and is characterized by its field strength  $E_0$  and frequency  $\omega$ . Out of the three relevant parameters  $I_p$ ,  $\omega$  and  $E_0$  one can form two dimensionless parameters usually chosen as

$$\gamma = \frac{\sqrt{2I_p} \omega}{E_0} \text{ (Keldysh parameter), } K = \frac{I_p}{\omega} \text{ (Multiphoton parameter).} \quad (2.2)$$

The multiphoton parameter separates the field-induced ionization process into two regimes depending on whether absorption of a single photon is sufficient to overcome the ionization threshold ( $K < 1$ ) or whether multiple photons are required ( $K > 1$ ). When more photons are absorbed than required to overcome the ionization threshold, the process is called above-threshold ionization (ATI) [1]. The single-photon case is usually reached with photon energies

---

<sup>1</sup>For a molecule, this is the definition of the *adiabatic* ionization potential while the *vertical* ionization potential is defined as the energy required to ionize at fixed molecular geometry.

in the XUV or X-ray while the case of large  $K$  is reached with visible or near-infrared laser fields. In this regime, the Keldysh parameter describes the degree of adiabaticity of the ionization process [87]. For small Keldysh parameter ( $\gamma \ll 1$ ) the combined potential of the atom and the laser field forms a static barrier through which ionization can occur via tunneling (unless the field strength becomes too large and the barrier is suppressed).

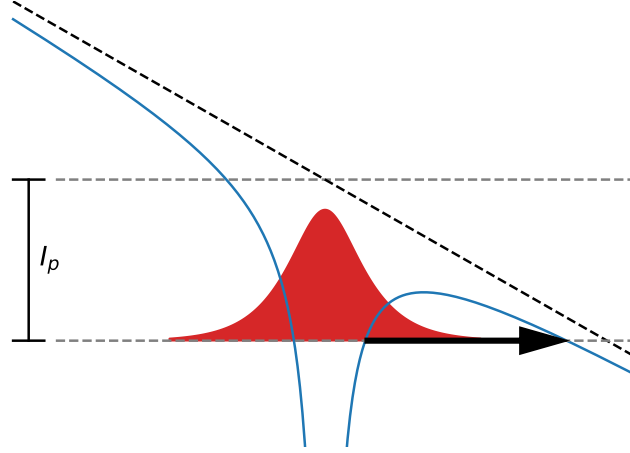


Figure 2.1: Schematic depiction of the strong-field-induced tunneling process. The laser potential (black dashed line) bends the atomic potential (blue curve) such that the bound-state wave function (red area) can tunnel through the barrier.

This is illustrated in Fig. 2.1. On the contrary, large values of the Keldysh parameter  $\gamma \gg 1$  lead to the multiphoton regime. The difference in the physical mechanism of the ionization process is reflected in the ionization rates associated with the two cases. In the multiphoton regime, the rate scales like an  $n$ -photon process  $\Gamma \propto I^n$  where  $I = \epsilon_0 c / 2 E_0^2$  is the intensity (in SI units) and  $n$  is the number of photons absorbed [127, 128]. In the tunneling regime, on the other hand, the ionization probability depends exponentially on the field strength<sup>2</sup> and it can be approximated by the PPT (or ADK) rate [3–5]

$$\Gamma_{\text{PPT}} \propto \exp\left(-\frac{2\kappa^3}{3E_0}\right). \quad (2.3)$$

Here,  $\kappa = \sqrt{2I_p}$  is the momentum associated with the ionization potential. The intermediate regime  $\gamma \lesssim 1$  is described as nonadiabatic tunnel ionization. It is the regime that is most frequently visited in present-day strong-field experiments and also the case that is considered primarily in this thesis.

## 2.2 The simple man's model

The ionization process in the tunneling or nonadiabatic tunneling regime is usually depicted as a two or three-step process [71–73]. After the electron passes the barrier in the tunnel-ionization process (ionization step) it appears in the continuum where it is accelerated by the electric field (propagation step). There, it can be described approximately as a classical point

<sup>2</sup>In this context, the “ $\propto$ ” symbol indicates proportionality in “exponential accuracy.” The prefactor typically depends on the field strength as well, but not exponentially.

particle. Assuming the electron appears in the continuum at some time  $t_0$  with vanishing velocity, we can write Newton's equation of motion

$$\ddot{\mathbf{r}}(t) = -\mathbf{E}(t), \quad \mathbf{r}(t_0) = 0, \quad \dot{\mathbf{r}}(t_0) = 0. \quad (2.4)$$

It can be integrated once to give the velocity  $\mathbf{v}(t) = \dot{\mathbf{r}}(t)$  as

$$\mathbf{v}(t) = \mathbf{A}(t) - \mathbf{A}(t_0), \quad \mathbf{A}(t) = - \int_{-\infty}^t dt' \mathbf{E}(t') \quad (2.5)$$

where we have introduced the vector potential  $\mathbf{A}(t)$ . Since for a realistic laser pulse we impose the conditions

$$\lim_{t \rightarrow \pm\infty} \mathbf{E}(t) = 0, \quad \lim_{t \rightarrow \pm\infty} \mathbf{A}(t) = 0, \quad (2.6)$$

$\mathbf{A}(t)$  will eventually vanish and the final photoelectron momentum after the end of the pulse is simply  $\mathbf{p} = -\mathbf{A}(t_0)$ , giving a relation between the observed photoelectron momentum and the time of ionization. For the linearly polarized pulse (2.1), the vector potential is given by

$$\mathbf{A}(t) = - \underbrace{E_0/\omega}_{\Lambda_0} \sin(\omega t) \mathbf{e}_z. \quad (2.7)$$

Therefore, there is a maximal observable photoelectron momentum  $p_{\max}^{\text{ATI}} = E_0/\omega$  and a maximal observable photoelectron energy  $(p_{\max}^{\text{ATI}})^2/2 = 2U_p$  where

$$U_p = \frac{E_0^2}{4\omega^2} \quad (2.8)$$

is called the ponderomotive potential.

Integrating (2.5) again, we find the position of the photoelectron

$$z(t) = E_0/\omega \sin(\omega t_0)(t - t_0) + E_0/\omega^2(\cos(\omega t) - \cos(\omega t_0)). \quad (2.9)$$

Here, the first term describes the drift of the photoelectron with its final momentum and the second term describes its quiver motion in the time-dependent electric field with amplitude  $E_0/\omega^2$ .

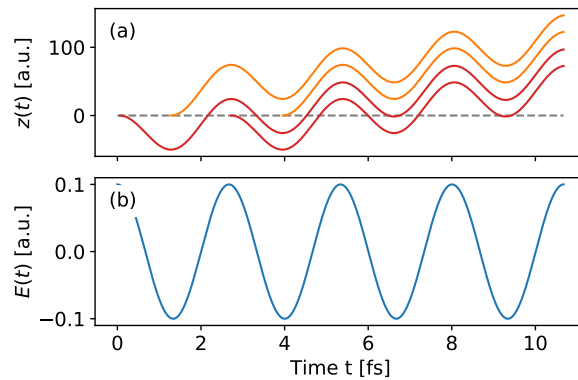


Figure 2.2: (a) All trajectories in the simple man's model that start in the first two cycles of the depicted laser field (panel (b),  $E_0 = 0.1$  a.u., 800 nm wavelength) and lead to the final photoelectron momentum  $p_z = 0.22$  a.u. Red curves show trajectories starting in a descending quarter cycle of the electric field and orange curves those starting in an ascending quarter cycle.

A few of these electron trajectories are shown in Fig. 2.2. For a given photoelectron momentum  $|p_z| < E_0/\omega$ , there are two trajectories per cycle of the laser field that lead to that momentum. The short ATI trajectory starts in an ascending quarter cycle and does not revisit the parent ion. The long ATI trajectory starts in a descending quarter cycle and revisits the parent ion. This can lead to rescattering [8], high-harmonic generation [11, 12] or non-sequential double ionization [13, 14] (recollision or recombination step). In case of backscattering by  $180^\circ$ , the final electron momentum is

$$\mathbf{p} = -\mathbf{A}(t_1) - \mathbf{v}(t_1) = -2\mathbf{A}(t_1) + \mathbf{A}(t_0) \quad (2.10)$$

where the rescattering time  $t_1$  is a solution of (2.9) such that  $z(t_1) = 0$ . Optimizing (2.10) numerically gives  $p_{\max}^{\text{HATI}} \approx 2.24 E_0/\omega$  which corresponds to a maximum observable photoelectron energy of approximately  $\mathcal{E}_{\max}^{\text{HATI}} \approx 10.01 U_p$  [74]. For high-harmonic generation, on the other hand, the return energy has to be optimized and a harmonic cutoff at  $\mathcal{E}_{\max}^{\text{HHG}} \approx 3.17 U_p + I_p$  is found [72, 73]. Except for the case where the maximum return energy is actually obtained, every harmonic order can be reached by two trajectories called the short and long (HHG) trajectory.

For a continuous wave (cw) field, the ATI process is repeated in every cycle of the driving field. Intercycle interference between contributions from different cycles lead to the occurrence of ATI peaks in the photoelectron momentum distribution. These peaks correspond to an integer number of absorbed photons [1]. The HHG process, on the other hand, is repeated in every half-cycle of the driving field. For inversion-symmetric potentials, this leads to peaks in the harmonic spectrum at odd integer multiples of the frequency of the driving field while even harmonics are missing [12].

## 2.3 Time-dependent Schrödinger equation

The interaction of an atom or molecule with a laser field can be described by the nonrelativistic time-dependent Schrödinger equation

$$i \frac{\partial}{\partial t} |\psi(t)\rangle = H(t) |\psi(t)\rangle \quad (2.11)$$

where  $\psi$  is the wave function containing the electronic and nuclear degrees of freedom and  $H(t)$  describes the interaction of the constituents with each other as well as the time-dependent interaction with the electromagnetic field. To describe the strong-field ionization process, we employ the following approximations. Since the nuclei are much heavier than the electrons, their motion is neglected and they are considered at fixed position. Then, for a single-ionization process, only one of the electrons is described fully quantum-mechanically. This is called the *single-active-electron approximation*. The spin is also not taken into account. The interaction with the electromagnetic field is described within *dipole approximation*, i.e. effects of the magnetic field as well as the spatial dependence of the electric field are neglected.<sup>3</sup>

<sup>3</sup>Although working in these approximations is adequate for the effects considered in this thesis, there is a large interest in strong-field physics to go beyond them. For example, to incorporate multielectron effects, a very simple way is to reduce dimensionality. Instead of considering one electron in two spatial dimensions, one can equally well consider two electrons in one dimension [14, 129, 130]. Similarly, to describe nuclear dynamics for a diatomic molecule, one electron in one dimension and one degree of freedom in the internuclear distance can be simulated [131, 132]. An efficient technique to incorporate nondipole effects to first order in  $1/c$  was introduced in [133, 134].

For a wave function  $\psi(\mathbf{r}, t)$  in one spatial coordinate  $\mathbf{r}$ , the Hamiltonian can be written as

$$H(t) = \frac{1}{2} \mathbf{p}^2 + V(\mathbf{r}) + \mathbf{E}(t) \cdot \mathbf{r} \quad (2.12)$$

with some effective potential  $V(\mathbf{r})$  that describes the interaction of the active electron with the nuclei but also contains an effective interaction of the active electron with the other electrons. Above form of the Hamiltonian is called the *length-gauge* Hamiltonian. With the vector-potential (2.5) and the gauge transformation

$$\psi(\mathbf{r}, t) \rightarrow e^{i\mathbf{A}(t) \cdot \mathbf{r}} \psi(\mathbf{r}, t), \quad (2.13)$$

the Hamiltonian becomes

$$H(t) = \frac{1}{2} (\mathbf{p} + \mathbf{A}(t))^2 + V(\mathbf{r}). \quad (2.14)$$

This is called the *velocity gauge* form.

Our main observable is the photoelectron momentum distribution  $|\mathcal{M}(\mathbf{p})|^2$ , i.e. the distribution of final asymptotic momenta after the end of the laser pulse. For a vector potential  $\mathbf{A}(t)$  that is zero outside of an interval  $[0, T]$ , it can be expressed via the ionization amplitude

$$\mathcal{M}(\mathbf{p}) = \langle \psi_{\mathbf{p}}^{(-)} | \mathcal{U}(T, 0) | \psi_0 \rangle. \quad (2.15)$$

Here,  $\mathcal{U}(T, 0)$  is the time-evolution operator that propagates the initial state  $|\psi_0\rangle$  to time  $T$  in the presence of the laser field and  $|\psi_{\mathbf{p}}^{(-)}\rangle$  is the incoming scattering state of momentum  $\mathbf{p}$ .<sup>4</sup>

### 2.3.1 Simple solutions of the TDSE

It proves useful to split the full Hamiltonian  $H$  in different ways. We define the field-free Hamiltonian as  $H_0 = \mathbf{p}^2/2 + V$  and

$$H_I(t) = H(t) - H_0 = \begin{cases} \mathbf{E}(t) \cdot \mathbf{r}, & \text{length gauge} \\ \mathbf{A}(t) \cdot \mathbf{p} + \frac{1}{2} \mathbf{A}(t)^2, & \text{velocity gauge} \end{cases} \quad (2.16)$$

as the interaction Hamiltonian. If the system is initially in an eigenstate of  $H_0$  with energy  $\varepsilon_0$ , the field-free time evolution is given by

$$\mathcal{U}_0(t, t') |\psi_0\rangle = e^{-i\varepsilon_0(t-t')} |\psi_0\rangle \quad (2.17)$$

where  $\mathcal{U}_0$  denotes the field-free time-evolution operator. For an atom in single-active-electron approximation, usually the energy of the initial state reflects the ionization potential,  $\varepsilon_0 = -I_p$ . On the other hand, neglecting the potential  $V$  instead of the time-dependent interaction leads to the Volkov Hamiltonian

$$H_V(t) = \mathbf{p}^2/2 + H_I(t) = \begin{cases} \frac{1}{2} \mathbf{p}^2 + \mathbf{E}(t) \cdot \mathbf{r}, & \text{length gauge} \\ \frac{1}{2} (\mathbf{p} + \mathbf{A}(t))^2, & \text{velocity gauge} \end{cases} \quad (2.18)$$

---

<sup>4</sup>In a short-range potential: for any state  $|\psi_{\text{out}}\rangle$  that under free time evolution approaches a state  $|\psi\rangle$  under full time evolution, the incoming scattering state provides the momentum-space representation of the free state according to  $\langle \mathbf{p} | \psi_{\text{out}} \rangle = \langle \psi_{\mathbf{p}}^{(-)} | \psi \rangle$  [135]. Asymptotically, it corresponds to a plane wave of momentum  $\mathbf{p}$  plus an incoming spherical wave.

where the time-evolution has explicit solutions in terms of Volkov states [136]

$$U_V(t, t')|\mathbf{p}\rangle = \exp\left(-\frac{i}{2}\int_{t'}^t dt'' (\mathbf{p} + \mathbf{A}(t''))^2\right) \times \begin{cases} |\mathbf{p} + \mathbf{A}(t)\rangle, & \text{length gauge} \\ |\mathbf{p}\rangle, & \text{velocity gauge} \end{cases}. \quad (2.19)$$

Thus, in velocity gauge, the momentum  $\mathbf{p}$  used as label of the Volkov state is conserved and it is also called the *canonical momentum* or *drift momentum* while the *kinematic momentum*  $\mathbf{v}(t) = \mathbf{p} + \mathbf{A}(t)$  is time dependent.<sup>5</sup>

## 2.4 Strong-field approximation

The strong-field approximation provides an approximate way to evaluate photoelectron momentum distributions [92, 137]. It relies on the Dyson representation [138] of the time-evolution operator

$$U(t, 0) = U_0(t, 0) - i \int_0^t dt' U(t, t') H_I(t') U_0(t', 0). \quad (2.20)$$

Using the orthogonality of bound states with scattering states, the ionization amplitude (2.15) becomes

$$\mathcal{M}(\mathbf{p}) = -i \int_0^T dt \langle \psi_{\mathbf{p}}^{(-)} | U(T, t) H_I(t) U_0(t, 0) | \psi_0 \rangle. \quad (2.21)$$

The strong-field approximation consists of (i) neglecting the potential  $V$  in the time evolution after the interaction Hamiltonian  $H_I(t)$  has acted at time  $t$ , i.e. replacing  $U(T, t)$  by  $U_V(T, t)$ ; (ii) replacing the scattering state  $\langle \psi_{\mathbf{p}}^{(-)} |$  by a plane wave  $\langle \mathbf{p} |$ . Using these approximations, the KFR amplitude [87–89]

$$\mathcal{M}_1(\mathbf{p}) = -i \int_0^T dt \langle \mathbf{p} | U_V(T, t) H_I(t) U_0(t, 0) | \psi_0 \rangle \quad (2.22)$$

is obtained. With the Volkov states (2.19), this can be written as

$$\mathcal{M}_1(\mathbf{p}) = -i \int_0^T dt M(\mathbf{p}, t) e^{-iS(\mathbf{p}, t)} \quad (2.23)$$

with the action

$$S(\mathbf{p}, t) = -I_p t + \frac{1}{2} \int_t^T dt (\mathbf{p} + \mathbf{A}(t))^2 \quad (2.24)$$

and the transition matrix element

$$M(\mathbf{p}, t) = \begin{cases} \langle \mathbf{p} + \mathbf{A}(t) | \mathbf{E}(t) \cdot \mathbf{r} | \psi_0 \rangle, & \text{length gauge} \\ \langle \mathbf{p} | \mathbf{A}(t) \cdot \mathbf{p} + \mathbf{A}(t)^2/2 | \psi_0 \rangle, & \text{velocity gauge} \end{cases}. \quad (2.25)$$

The length-gauge expression has a clear physical interpretation in terms of ground-state evolution up to time  $t$ , followed by ionization via interaction with the laser field at time  $t$  and propagation to the detector afterwards. The integral over  $t$  can be understood as an integral

<sup>5</sup>In atomic units it is numerically equal to the velocity, hence the notation. Denoting  $\mathbf{p}$  the canonical momentum is common terminology in strong-field physics. In the terminology of Hamiltonian mechanics,  $\mathbf{p}$  would be the canonical momentum only in velocity gauge, while in length gauge both the canonical and the kinematic momentum equal  $\mathbf{p} + \mathbf{A}(t)$ .

over ionization time. In the velocity-gauge expression, this interpretation is problematic. This is because in velocity gauge the initial state  $|\psi_0\rangle$  is not a good approximation of the ground state of the system in the presence of the laser field. In fact, it is well known that the KFR amplitude is not gauge invariant and length and velocity forms give different results. The length gauge form is usually favored because it can accurately reproduce PMDs for short range potentials while the velocity gauge form cannot [138]. For long-range potentials, however, both gauges give wrong results [137].

Eq. (2.22) is also called the *direct* SFA amplitude because it only describes direct ionization without rescattering. One scattering event can be included in the SFA by approximating the time evolution after ionization more accurately according to

$$U(T, t) \approx U_V(T, t) - i \int_t^T dt' U_V(T, t') V U_V(t', t). \quad (2.26)$$

This leads to the improved SFA amplitude [139]

$$\mathcal{M}_2(\mathbf{p}) = - \int_0^T dt \int_t^T dt' \langle \mathbf{p} | U_V(T, t') V U_V(t', t) H_I(t) U_0(t, 0) | \psi_0 \rangle \quad (2.27)$$

where now there are two integrals over ionization time  $t$  and rescattering time  $t'$ . The total SFA amplitude is  $\mathcal{M}_{\text{SFA}}(\mathbf{p}) = \mathcal{M}_1(\mathbf{p}) + \mathcal{M}_2(\mathbf{p})$ . The second-order (and even higher-order) contributions can be calculated conveniently by reformulating the SFA integral expression as an evolution equation [140]. However, including higher-order terms does not prove fruitful as the perturbation series generally does not converge [141].

### 2.4.1 Saddle-point approximation

When the electric field is not too strong,  $E_0 \ll (2I_p)^{3/2}$ , and the multiphoton parameter is large,  $I_p/\omega \gg 1$ , the action is a quickly oscillating function of time and the KFR amplitude can be evaluated in saddle-point approximation (SPA) [91, 92, 142]. There, the full amplitude (2.23) is replaced by a sum over stationary points  $t_s = t_r + i t_i$  of the action (2.24), defined by

$$\left. \frac{\partial}{\partial t} S(\mathbf{p}, t) \right|_{t=t_s} = 0 \quad (2.28)$$

and given by

$$\frac{1}{2}(\mathbf{p} + \mathbf{A}(t_s))^2 + I_p = 0. \quad (2.29)$$

The solutions are generally complex where relevant solutions have  $\text{Im}(t_s) > 0$  [143]. When the matrix element  $M(\mathbf{p}, t)$  is well behaved at  $t_s$ , the amplitude can be expressed as<sup>6</sup>

$$\mathcal{M}_1(\mathbf{p}) \approx \sum_{t_s} \sqrt{\frac{-2\pi i}{\dot{S}(\mathbf{p}, t_s)}} M(\mathbf{p}, t_s) e^{-iS(\mathbf{p}, t_s)}. \quad (2.30)$$

The integral in the action (2.24) evaluated in complex time is independent of the specific integration path, assuming the components of  $\mathbf{A}(t)$  are holomorphic functions. However, the choice of the standard path first down to the real axis and then along the real axis to the final time  $T$  as depicted in Fig. 2.3 gives the two legs an interpretation of under-the-barrier motion and propagation after ionization.

<sup>6</sup>For a function that depends on multiple variables, we use a prime to denote the full derivative with respect to all variables. A dot always refers to the derivative with respect to time. For functions that depend only on time, both notations are used.

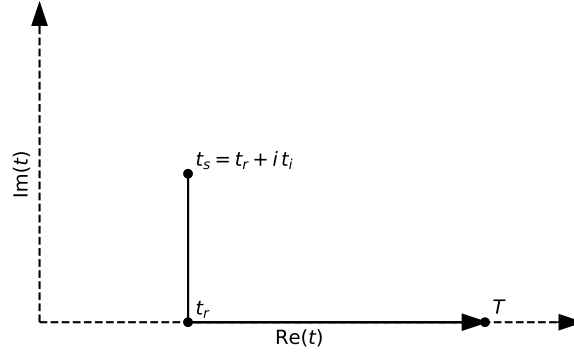


Figure 2.3: Standard integration path in the complex plane to evaluate the action (2.24).

At each time on the integration path, the associated *quantum orbit* has a velocity  $\mathbf{v}(t) = \mathbf{p} + \mathbf{A}(t)$  that enters the kinetic part of the action. Since the action is real on the real axis, the ionization probability associated with a given stationary point is determined as soon as the under-the-barrier motion is completed. Integrating the velocity again with respect to time, a position  $\mathbf{r}(t)$  is formally obtained. However, the action (2.24) does not depend on position so the saddle-point equation does not provide the integration constant.<sup>7</sup> Setting the position to zero at the saddle-point time  $t_s$ , the real part of the position becomes nonzero already during the first leg of the integration contour. This is because both the line element as well as the velocity are (mostly) imaginary. In this case, the position  $\text{Re } \mathbf{r}(t_r)$  is frequently interpreted as the tunnel-exit position of the photoelectron. In the adiabatic limit  $\gamma \rightarrow 0$ , it is equal to  $-I_p/E(t_r)^2 \mathbf{E}(t_r)$  which is exactly the point where the potential in a triangular tunneling barrier matches the (negative) ionization potential of the system.

For the length-gauge amplitude, Eq. (2.30) cannot be used because typically the transition matrix element has a pole at  $t_s$ . For a pole of order  $\mu$ , a reduced matrix element can be defined,

$$\widetilde{M}(\mathbf{p}, t_s) = \lim_{t \rightarrow t_s} (t - t_s)^\mu M(\mathbf{p}, t). \quad (2.31)$$

In this case, the ionization amplitude becomes [143, 144]

$$\mathcal{M}_1(\mathbf{p}) \approx \sum_{t_s} i^\mu \frac{\Gamma(\mu/2)}{2\Gamma(\mu)} \sqrt{\frac{-2\pi i}{\dot{S}(\mathbf{p}, t_s)}} [2i\dot{S}(\mathbf{p}, t_s)]^{\mu/2} \widetilde{M}(\mathbf{p}, t_s) e^{-iS(\mathbf{p}, t_s)}. \quad (2.32)$$

## 2.5 Analytical R-matrix theory

Analytical R-matrix theory provides an approximate way to evaluate photoelectron momentum distributions including Coulomb effects. It relies on a splitting of position space into two parts at a sphere of radius  $a$  such that different approximations can be applied in the two regions. The boundary radius is chosen rather close to the atom within the tunneling barrier ( $1/\kappa \ll a \ll I_p/E_0$ ). Introducing (for arbitrary  $b$ ) the Bloch operator

$$L(a) = \delta(r - a) \left( \frac{\partial}{\partial r} + \frac{1-b}{r} \right), \quad (2.33)$$

<sup>7</sup>This is different in analytical R-matrix theory or when applying the eikonal approximation to the Dyson integral. See Sections 2.5, 5.7, and 5.8.



a Hamiltonian  $H_{\text{out}}(t) = H(t) - L(\mathbf{a})$  is defined for the outer region where the wave function satisfies the inhomogeneous Schrödinger equation

$$i \frac{\partial}{\partial t} \psi(\mathbf{r}, t) = H_{\text{out}}(t) \psi(\mathbf{r}, t) + L(\mathbf{a}) \psi(\mathbf{r}, t). \quad (2.34)$$

The ionization amplitude can be written as a surface integral [93, 94] which reads<sup>8</sup>

$$\mathcal{M}(\mathbf{p}) = -i \int_0^T dt \int d^3r \langle \mathbf{p} | \mathbf{U}_{\text{out}}(T, t) | \mathbf{r} \rangle L(\mathbf{a}) \psi(\mathbf{r}, t). \quad (2.35)$$

Here,  $\mathbf{U}_{\text{out}}$  is the time-evolution operator for the homogeneous Schrödinger equation  $i \partial_t \psi(\mathbf{r}, t) = H_{\text{out}} \psi(\mathbf{r}, t)$ . The analytical R-matrix approach consists of certain approximations in both the inner and the outer region. In the inner region, the electric field is neglected and  $\psi(\mathbf{r}, t)$  is taken as the field-free time-evolved bound state  $e^{iI_p t} \psi_0(\mathbf{r})$ . In a potential  $V(r) \simeq -Z/r$ , the bound state is described by its (large  $r$ ) asymptotic expression  $\psi_0(\mathbf{r}) \simeq B (\kappa r)^{Z/\kappa-1} e^{-\kappa r}$ . (Here,  $B$  is a constant and we neglect a possible angular momentum of the bound state). This defines the source term in (2.35). In the outer region, the propagator is approximated using eikonal-Volkov states [145, 146]

$$\langle \mathbf{p} | \mathbf{U}_{\text{out}}(T, t) | \mathbf{r} \rangle \approx \frac{1}{(2\pi)^{3/2}} e^{-i(\mathbf{p} + \mathbf{A}(t)) \cdot \mathbf{r}} e^{-\frac{i}{2} \int_t^T dt' (\mathbf{p} + \mathbf{A}(t'))^2} e^{-i \int_t^T dt' V(\mathbf{r} + \mathbf{r}_L(t'; \mathbf{p}, t))} \quad (2.36)$$

which include the effect of the atomic potential  $V$  to first order in the exponent. Here,

$$\mathbf{r}_L(t'; \mathbf{p}, t) = \int_t^{t'} dt'' (\mathbf{p} + \mathbf{A}(t'')) \quad (2.37)$$

is the (potential-free) trajectory of the electron in the laser field. Choosing  $\mathbf{b} = Z/\kappa$  in the Bloch operator, these approximations lead to

$$\mathcal{M}(\mathbf{p}) \approx \frac{i\kappa}{(2\pi)^{3/2}} \int_0^T dt \int d^3r \delta(r - a) e^{-iS(\mathbf{p}, T; \mathbf{r}, t)} \left( B (\kappa r)^{Z/\kappa-1} e^{-\kappa r} \right) \quad (2.38)$$

with the action

$$S(\mathbf{p}, T; \mathbf{r}, t) = -I_p t + (\mathbf{p} + \mathbf{A}(t)) \cdot \mathbf{r} + \frac{1}{2} \int_t^T dt' (\mathbf{p} + \mathbf{A}(t'))^2 + \int_t^T dt' V(\mathbf{r} + \mathbf{r}_L(t'; \mathbf{p}, t)). \quad (2.39)$$

The expression for the ionization amplitude (2.38) can be evaluated in saddle-point approximation. When aiming for consistency to first order in the potential, the Coulomb correction to the saddle-point time can be neglected. However, the saddle point  $t_a$  still depends on the choice of the boundary radius  $a$ . Generally, the smaller  $a$  becomes, the larger the imaginary part of  $t_a$  becomes; this reflects the increased distance the electron has to travel in imaginary time from the boundary to the tunnel-exit position. To first order in the potential, the ionization amplitude is approximately independent of the boundary radius because the boundary dependence of the asymptotic expression for the bound state is compensated by the boundary dependence due to the action.

In the next step, the result is made explicitly independent of  $a$ . To this end, the boundary-dependent saddle point  $t_a$  is expressed via the standard SFA saddle point  $t_s$  from (2.29). In

<sup>8</sup>We assume that  $T$  is large enough so the scattering state can be replaced by a plane wave.

the potential-independent part of the action, the remaining  $\alpha$ -dependent terms then lead to cancellation of the exponential part of the asymptotic expression for the bound state. In the electron trajectory, the remaining  $\alpha$ -dependent term cancels the initial position at the boundary so the trajectory starts at the origin at  $t_s$  and moves through the boundary at  $t_a$ . With this trajectory, the Coulomb term produces the corresponding term  $(\kappa\alpha)^{Z/\kappa}$  from the asymptotic expression of the bound state automatically when the lower limit of the integral is moved to a time  $t_\kappa$  such that the boundary-matching condition<sup>9</sup>

$$(\kappa\alpha)^{Z/\kappa} = \exp\left(-i \int_{t_\kappa}^{t_a} dt' V(\mathbf{r}_L(t'; \mathbf{p}, t_s))\right) \approx \exp\left(-\frac{1}{\kappa} \int_{a_0}^{\alpha} dz V(z)\right) \quad (2.40)$$

is fulfilled. For the Coulomb potential,  $a_0 = 1/\kappa$  or  $t_\kappa = t_s - i\kappa^{-2}$ . Finally, the expression for the ionization amplitude [78, 147, 148] becomes

$$\mathcal{M}_{\text{ARM}}(\mathbf{p}) = R(\mathbf{p}, t_s) e^{-iS_{\text{ARM}}(\mathbf{p}, t_s)} \quad (2.41)$$

with an atomic shape factor  $R(\mathbf{p}, t_s)$  and the action

$$S_{\text{ARM}}(\mathbf{p}, t_s) = S_{\text{SFA}}(\mathbf{p}, t_s) + S_{\text{C}}(\mathbf{p}, t_s). \quad (2.42)$$

Here, the Coulomb correction to the action is given by

$$S_{\text{C}}(\mathbf{p}, t_s) = \int_{t_s - i\kappa^{-2}}^T dt' V(\mathbf{r}_L(t'; \mathbf{p}, t_s)). \quad (2.43)$$

To determine PMDs accurately in long-range potentials,  $T$  should be moved to infinity (see Appendix A.4.1).

## 2.6 Semiclassical two-step model

The semiclassical two-step model [95] is based on splitting the ionization process into an ionization and a propagation step. The ionization step is described by launching classical trajectories at various times  $t$  and velocities  $v$  perpendicular to the instantaneous electric field  $\mathbf{E}(t)$  according to the (velocity-resolved) PPT (or ADK) rate [3–5]

$$\Gamma_{\text{PPT}}(t, v) \propto \exp\left(-\frac{2\kappa^3}{3E(t)}\right) \exp\left(-\frac{\kappa v^2}{E(t)}\right). \quad (2.44)$$

Here,  $E(t) = |\mathbf{E}(t)|$ . The initial position is derived from the TIPIS model [77, 149]. There, the time-independent Schrödinger equation for a potential behaving asymptotically as  $V(r) \simeq -Z/r$  as  $r \rightarrow \infty$  is solved<sup>10</sup> in the presence of a (weak) static electric field  $E$ . Assuming the field points along the  $z$  axis, the problem can be approximately separated in parabolic coordinates  $(\xi, \eta, \phi)$  defined by

$$x = \sqrt{\xi\eta} \cos(\phi), \quad y = \sqrt{\xi\eta} \sin(\phi), \quad z = (\xi - \eta)/2. \quad (2.45)$$

<sup>9</sup>Close to the standard SFA saddle point  $t_s$ , the electron velocity is approximately  $i\kappa$  and  $t_a$  can be expressed in terms of  $t_s$  as  $t_a \approx t_s - i\alpha/\kappa$ . Similarly,  $t_\kappa \approx t_s - i\alpha_0/\kappa$  and  $\alpha_0$  plays the role of the effective radius at which the contribution due to the potential is accumulated. Its value is calculated for soft-core potentials in Appendix A.4.2.

<sup>10</sup>The TIPIS model (tunnel ionization in parabolic coordinates with induced dipole and Stark shift) as presented originally includes the possibility to introduce a multielectron polarizability via an additional potential  $-\alpha/r^3 E \cdot z$  that we neglect here. We also neglect a possible angular momentum around the polarization axis and set  $m = 0$ .

This procedure leads to effective potentials in the  $\xi$  and  $\eta$  coordinates where the electron remains bound in the former and a tunneling barrier is formed in the latter. The tunnel-exit position is found as the point where the effective potential in the  $\eta$  coordinate matches the energy of the bound state. It is given by

$$z_0 \approx -\frac{I_p(E) + \sqrt{I_p(E)^2 - 4\beta(E)E}}{2E}, \quad \beta(E) = Z - \frac{\sqrt{2I_p(E)}}{2}. \quad (2.46)$$

Here,  $I_p(E)$  is the Stark-shifted ionization potential and the separation constant  $\beta(E)$  can be interpreted as the remaining nuclear charge in the tunneling coordinate.

After the ionization step, Newtonian motion in the combined laser and Coulomb potential is assumed in the propagation step. With every trajectory, there is a phase associated that is based on the semiclassical propagator [150]

$$G_{SC}(\mathbf{p}, T; \mathbf{r}, t) = \frac{1}{(2\pi i)^{3/2}} \left( \det \left( \frac{\partial^2 S_{SC}(\mathbf{p}, T; \mathbf{r}, t)}{\partial \mathbf{r} \partial \mathbf{p}} \right) \right)^{1/2} e^{-iS_{SC}(\mathbf{p}, T; \mathbf{r}, t)} \quad (2.47)$$

and given by<sup>11</sup>

$$S_{SC}(\mathbf{p}, T; \mathbf{r}, t) = \dot{\mathbf{r}}_N(t) \cdot \mathbf{r} + \int_t^T dt' \left\{ \frac{1}{2} \dot{\mathbf{r}}_N(t')^2 + V(\mathbf{r}_N(t')) - \mathbf{r}_N(t') \cdot \nabla V(\mathbf{r}_N(t')) \right\} \quad (2.48)$$

evaluated along the Newtonian trajectory

$$\ddot{\mathbf{r}}_N(t') = -\nabla V(\mathbf{r}_N(t')) - \mathbf{E}(t'), \quad \mathbf{r}_N(t) = \mathbf{r}, \quad \dot{\mathbf{r}}_N(T) = \mathbf{p}. \quad (2.49)$$

The final expression for the ionization amplitude is

$$\mathcal{M}_{SC}(\mathbf{p}) = \sum_{t, \nu} \sqrt{\frac{\Gamma_{PPT}(t, \nu)}{|\det \mathbf{D}'(t, \nu)|}} e^{-i(S_{SC}(\mathbf{p}, T; \mathbf{r}, t) - I_p t)} \quad (2.50)$$

where the deflection function  $\mathbf{D}(t, \nu)$  [152] maps the initial conditions to the final momentum and the sum is taken over all pairs of initial conditions where  $\mathbf{D}(t, \nu) = \mathbf{p}$ .

It should be noted that the frequently employed way of evaluating the expression (2.50) using importance sampling in the (square root of the) PPT rate and subsequent binning in the space of final momenta leads to a wrong power ( $-1$  instead of  $-1/2$ ) of the Jacobian  $|\det \mathbf{D}'(t, \nu)|$  in the final result. This can be corrected either by taking the Jacobian into account already in the sampling procedure or by adding a weight corresponding to the missing power in the binning procedure. Another approach is the use of clustering algorithms [153].

The SCTS model neglects nonadiabatic effects at the ionization step while including Coulomb effects through use of the TIPIS model. Complementary, the similar CCSFA [96–100] includes nonadiabatic effects by taking initial conditions from saddle-point SFA but neglects Coulomb effects on the tunnel-exit position at the ionization step.

<sup>11</sup>The expression adds a term depending on the gradient of the potential that was missing in the otherwise similar QTMC (quantum-trajectory Monte Carlo) model [151].



## Chapter 3

# Streaking with orthogonal two-color laser fields

In this chapter, a two-color streaking scheme is implemented to extract information about electron trajectories in above-threshold ionization of atoms and molecules in linearly polarized laser fields. In the photoelectron momentum distribution, the two-color delay scan shows signatures of Coulomb focusing and photoelectron holography. Applying the scheme to an asymmetric molecule, we find a strong orientation dependence in the relative weights of short and long ATI trajectories. Most of the results from this chapter are published in [154].

### 3.1 Introduction

Irradiation of atoms and molecules by strong linearly-polarized infrared laser fields produces rich structures in the photoelectron momentum distribution such as intracycle interference patterns [40–42], holographic fringes [125, 126], the high-energy backscattering plateau [8], and the recently discovered low-energy structures [152, 155–158], very low-energy structures [159], and zero-energy structures [160, 161]. When adding a second or third harmonic to the linearly polarized field, the signal is modified depending on the relative phase between the two colors [162–166]. In a few-cycle pulse, the observed structures depend on the carrier-envelope phase (CEP) [167–169]. Bichromatic fields with control of the relative phase and few-cycle pulses with control of the CEP are the most basic examples of a tailored field.

Most of the structures appearing in the momentum distribution can be understood as a coherent sum of a finite number of trajectories or quantum orbits which are characterized by their relative amplitude and phase as well as their departure or return time. The tunable parameter provided by the tailored field can be used both to control these trajectories, as well as extract information about them by observing the modulation of the signal depending on the relative phase or CEP. For example, in high-harmonic generation – where a given harmonic order can generally be reached by two trajectories (the short and the long HHG trajectory) – a weak second-harmonic  $2\omega$  field polarized orthogonal to the driving field of frequency  $\omega$  can be used to disentangle the two contributions [110]. The presence of the  $2\omega$  field induces a lateral motion of the photoelectron during excursion and with suitable choice of the relative phase between the  $\omega$  and the  $2\omega$  field only one of the two possible trajectories can recombine. It was later shown experimentally by Shafir et al. [112] and verified theoretically by Zhao and

Lein [113] that the same setup can be used to retrieve both the ionization and the recombination time resolved by harmonic order. Depending on the relative phase between the two colors, only trajectories launched at a certain ionization time can recombine. This leads to a modulation of the harmonic intensity. In addition to the lateral displacement, the  $2\omega$  field induces a nonzero lateral velocity component at recombination time which leads to symmetry breaking between adjacent half-cycles of the fundamental field and the observation of even harmonics. Observing the harmonic yield as well as the asymmetry between even and odd harmonics, both the ionization and the return time can be retrieved; they were found to be in excellent agreement with the quantum-orbit model.

The orthogonal two-color (OTC) scheme can also be applied to photoelectrons. The counterpart of trajectory-selection in harmonic generation is the streaking double-slit experiment in above-threshold ionization. With a  $2\omega$  field perpendicular to the fundamental  $\omega$  field, the short and long ATI trajectory that usually lead to the same final momentum can be separated to switch their interference structure off or they can be focused in the same direction to enhance it [108, 109]. This is similar to the “attosecond double slit” where control over the intracycle interference pattern is achieved via the CEP of a few-cycle pulse [40, 41].

Henkel and Lein showed via numerical solution of the TDSE that an ionization time retrieval similar to the one in HHG can also be performed in ATI [114]. There, the presence of the  $2\omega$  field leads to a deflection of the electron trajectories away from the polarization axis. By observing the modulation of the signal in the direction of the fundamental  $\omega$  field as a function of the two-color phase, it is possible to retrieve momentum-resolved ionization times for the long ATI trajectory as well as the relative weight between the long and the short ATI trajectory. Again, excellent agreement with the quantum-orbit model was found.

The OTC schemes as described above can be termed kinematical schemes because they rely on modifying the electron trajectory after ionization. Control and analysis of electron trajectories is also possible with parallel two-color (PTC) schemes which are based on modifying the ionization process directly by modulating the electric field strength at ionization time. By adding a weak second-harmonic field parallel to the strong fundamental field, Porat et al. were able to retrieve ionization times of trajectories involved in photoelectron holography [115]. This is closely related to phase-of-the-phase spectroscopy – a systematic approach to interpret a set of momentum distributions from two-color irradiation with control of the relative phase [170–175]. Since the two-color field is periodic in the relative phase, the momentum distribution can be written as a Fourier series. Often, the variation of the signal at a given momentum is captured accurately by the lowest-frequency component of the series. In that case, the argument of the complex coefficient (the “phase of the phase”) is related to the relative phase that maximizes the signal at that momentum.

Other non-kinematical schemes rely on modulating the phase the electron picks up along its trajectory due to the  $2\omega$  field. In HHG, recombination times, ionization probabilities, and initial velocities can be measured by using a PTC scheme to modify the phase in the two arms of the interferometer made up by otherwise equivalent trajectories from adjacent half cycles that lead to the same harmonic order [111, 176]. This symmetry breaking is again observable in the production of even harmonics [177]. In ATI, it was shown that ionization times can also be retrieved using an OTC scheme to modify the phases of the direct and rescattered trajectory in photoelectron holography and observing the changes in the interference pattern [178, 179]. Similarly, the initial momentum of the photoelectron at the tunnel exit can be resolved [180].

A completely different approach is taken by two-color schemes where the  $\omega$  component is weak compared to the  $2\omega$  such as the transfer of the attosecond streak camera and the RABBIT technique to the strong-field regime [181, 182]. At comparable intensities of the two fields, completely new field shapes are produced with many applications such as controlling the recolliding wave packet [183, 184], controlling the direction emission of photoelectrons in rescattering [185, 186], probing Coulomb effects [187, 188], measuring the time evolution of the phase of a bound state [189, 190], controlling electron-electron correlation in non-sequential double ionization [191], separating intracycle and intercycle interference patterns [192, 193], and measuring the sub-barrier phase upon tunnel ionization [194]. In molecules, two-color fields can be used to control the asymmetry in photoionization or dissociation [195–200].

In this chapter, we consider the OTC scheme proposed and implemented by Henkel and Lein [114]. There, a numerical solution of the TDSE in two spatial dimensions was used to find the relative weight of the long and the short ATI trajectory as well as the ionization time of the long ATI trajectory for a model helium atom in a linearly polarized laser field resolved by final momentum. We present results obtained from the 3D TDSE for the same setting. After providing the computational details in Section 3.2, we discuss the PMD for the linearly polarized field in Section 3.3 and for the tailored bichromatic field in Section 3.4 where we perform the ionization-time retrieval for long trajectories. Section 3.5 repeats the analysis in the lateral direction which was inaccessible in the previous 2D study. In Section 3.6, the scheme is applied to the asymmetric helium hydride molecular ion  $\text{HeH}^+$ . Section 3.7 concludes the chapter.

## 3.2 Computational details

We solve the 3D TDSE on a Cartesian grid of size  $246 \times 246 \times 246$  a.u. and 768 points in each dimension using the split-operator method [201] with step size 0.03 a.u. over a propagation time of 1500 a.u.. The electric field is chosen as in [114], i.e.

$$\mathbf{E}(t) = E_0 f(t) (\cos(\omega t) \mathbf{e}_x + \epsilon \cos(2\omega t + \phi) \mathbf{e}_y). \quad (3.1)$$

Here,  $\omega = 0.05695$  a.u. corresponds to 800 nm wavelength and the envelope  $f(t)$  describes a 10-cycle trapezoidal pulse of 2 ascending, 6 constant, and 2 descending cycles. We choose  $E_0 = 0.107$  a.u. corresponding to an intensity of  $4 \times 10^{14}$  W/cm<sup>2</sup>. The potential is

$$V(r) = -\frac{1 + e^{-r/r_0}}{\sqrt{r^2 + \alpha}} \quad (3.2)$$

where  $\alpha = 0.1$  a.u. and  $r_0 \approx 1.613$  a.u. is optimized to reproduce the ionization potential  $I_p \approx 0.904$  a.u. of the helium atom. The relative phase  $\phi$  is varied from 0 to  $2\pi$  in 32 steps.<sup>1</sup> The photoelectron momentum distribution is obtained by projecting outgoing parts of the wave function onto Volkov states using an absorber that starts at a distance of 100 a.u. from the origin. In addition to the solution of the 3D TDSE, we obtain momentum distributions in the  $p_x p_y$  and  $p_x p_z$  planes with high resolution using a two-dimensional Cartesian grid of size  $1312 \times 1312$  a.u. and 4096 points in each dimension. The details of numerical time propagation are described in Appendix A.1.1.

<sup>1</sup>Actually, only calculations for the first 16 steps have to be carried out. This is because  $\phi \rightarrow \phi + \pi$  leads to a sign change in the  $2\omega$  field and a flip of the PMD in  $p_y$  direction.

### 3.3 Linear polarization

A slice ( $p_z = 0$ ) through the photoelectron momentum distribution for the case of purely linear polarization ( $\epsilon = 0$ ) is shown in Fig. 3.1. At low energies, the signal is dominated by

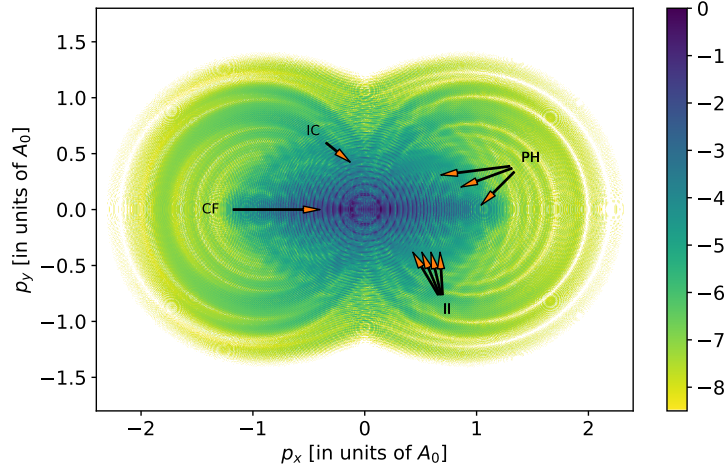


Figure 3.1: Slice ( $p_z = 0$ ) through the photoelectron momentum distribution for the linearly polarized pulse ( $\epsilon = 0$ , log-10 scale). The distribution is normalized to maximum signal 1. Certain structures of the PMD are highlighted: (CF) Coulomb focusing; (PH) photoelectron holography; (II) intracycle interference; (IC) interference carpet. Adapted from Fig. 1 in [154].

direct electrons whereas high energies can only be reached by rescattered electrons [8]. These contributions form two rescattering spheres that extend up to the  $10 U_p$  cutoff. For the direct electrons, the long trajectory exhibits Coulomb focusing when passing the parent ion, leading to a concentration of the signal on the  $p_x$  axis [122–124]. Interference of the dominant long trajectory with the short trajectory generates intracycle interference [40–42] which is visible as a modulation of the signal when traversing the  $p_x$  direction. Interference of long scattered and long non-scattered trajectories leads to photoelectron holography. This is observable as a modulation of the signal perpendicular to the  $p_x$  direction, forming a finger-like structure [125, 126]. In the symmetry plane  $p_y = 0$ , the strong-field ionization process is repeated not in every cycle but in every half cycle of the driving field. This leads to destructive interference at every second ATI peak and a structure in the momentum distribution that was called an “interference carpet” in [202].

### 3.4 Two-color delay scan

Momentum distributions in the presence of the  $2\omega$  field ( $\epsilon = 0.1$ ) for relative phase  $\phi = 0$  and  $\phi = \pi/2$  are shown in Fig. 3.2.  $\phi = 0$  leads to a separation of short and long trajectories such that the intracycle interference becomes less pronounced.  $\phi = \pi/2$  leads to both long and short trajectories being deflected in the same direction such that the intracycle interference becomes more pronounced, as was observed experimentally in the streaking double-slit [108, 109]. The direct-ionization part of the spectrum follows roughly the bent shape of the negative vector potential with the effect being less relevant at small energies [109].

In the following, we focus on the signal on the (positive)  $p_x$  axis ( $p_y = 0, p_x > 0$ ), i.e. vanishing photoelectron momentum in the direction of the  $2\omega$  field. While in the absence



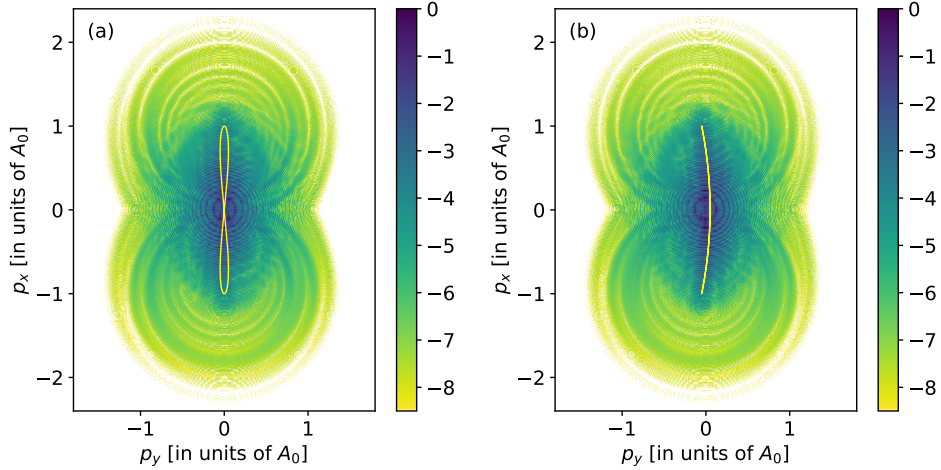


Figure 3.2: Slices through momentum distributions in the presence of the  $2\omega$  field (log-10 scale) for  $\epsilon = 0.1$  and relative phases  $\phi = \pi$  (a) and  $\phi = \pi/2$  (b). The yellow lines show the shape of the negative vector potential  $-\mathbf{A}(t)$ . Both distributions are normalized to maximum signal 1. Adapted from Fig. 1 in [154].

of the  $2\omega$  field this is the preferred direction of photoelectron emission, the presence of the  $2\omega$  field leads to a deflection of the photoelectrons and thus a modulation of the signal as a function of the relative phase. Since the  $2\omega$ -field just changes sign when  $\phi \rightarrow \phi + \pi$ , the on-axis signal is  $\pi$ -periodic.

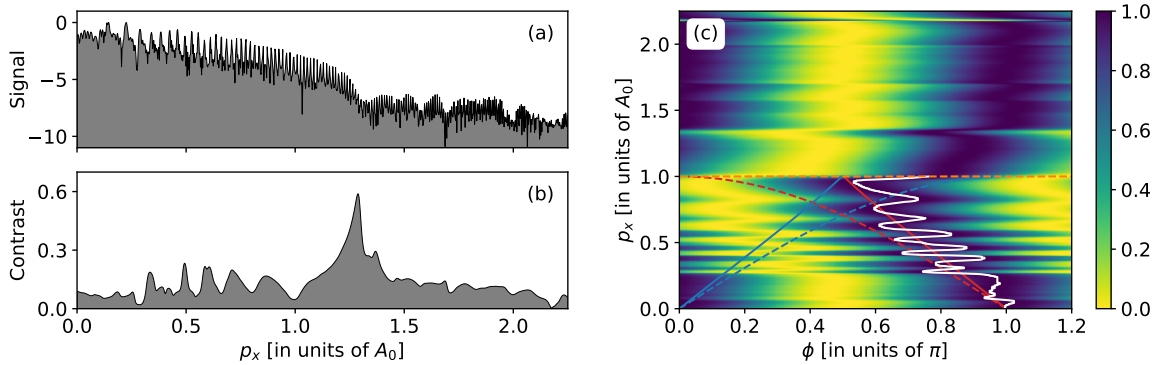


Figure 3.3: (a) On-axis signal for the 800 nm field (log-10 scale). (b) Michelson contrast for the modulation of the on-axis signal due to the 400 nm field. (c) Variation of the on-axis signal as a function of the relative phase, normalized for each  $p_x$  separately to vary between 0 and 1. The white curve shows the position of the maximum for each momentum  $p_x$ . The solid lines show the predictions for maximum signal made by the quantum-orbit model (3.15) and the dashed lines show the predictions made by the simple man's model (3.7). The red lines show the solution for the long ATI trajectory and the blue lines show the one for the short ATI trajectory. In (b) and (c), a Gaussian filter (width  $0.04 A_0$ ) has been applied in the  $p_x$  direction to remove oscillations in the signal that are due to low signal between the ATI peaks which are clearly visible in (a). We have also interpolated the values along  $\phi$  from 32 to 256 points in the  $[0, 2\pi]$  interval using Fourier transformation. Adapted from Fig. 2 in [154].

Fig. 3.3(a) shows the on-axis signal for ionization in the 800 nm field and Fig. 3.3(c) shows the variation of the on-axis signal as a function of the relative phase in the presence of the 400 nm field. Here, the signal has been normalized for each momentum  $p_x$  separately to vary between 0 and 1. For every  $p_x$  we find the optimal phase  $\phi_0$  that maximizes the on-axis signal (white line) and compare it to the predictions for maximum signal made by the simple man's (Section 2.2) and the quantum-orbit model (Section 2.4.1) for both the short and the long ATI

trajectory, see also the derivation in [203].

In the simple man's model, it can be assumed that a maximum is obtained when no deflection in the direction of the  $2\omega$  field occurs, i.e. the ionization takes place at a zero of the  $2\omega$  vector potential. At constant envelope,

$$A_y(t_0) = -\epsilon A_0/2 \sin(2\omega t_0 + \phi_0) = 0 \quad \Leftrightarrow \quad \phi_0 = -2\omega t_0 \pmod{\pi}, \quad (3.3)$$

providing a direct relation between the observed optimal phase  $\phi_0$  and the time of ionization  $t_0$ . When  $t = 0$  denotes a maximum of the fundamental electric field and we consider ionization in the following cycle, we find

$$\phi_a = 2\pi - 2\omega t_a \text{ (short trajectory)}, \quad \phi_b = \pi - 2\omega t_b \text{ (long trajectory)}. \quad (3.4)$$

Here, the multiples of  $\pi$  have been chosen such that  $\phi \in [0, \pi]$ , noting that the long trajectories originate in the first quarter cycle and the short trajectories in the second quarter cycle. In the simple man's model,

$$p_x = -A_x(t_0) = A_0 \sin(\omega t_0), \quad (3.5)$$

so the ionization time is given by

$$\omega t_a = \pi - \arcsin\left(\frac{p_x}{A_0}\right), \quad \omega t_b = \arcsin\left(\frac{p_x}{A_0}\right). \quad (3.6)$$

Thus, the optimal phase derived from the simple man's model is

$$\phi_a = 2 \arcsin\left(\frac{p_x}{A_0}\right), \quad \phi_b = \pi - 2 \arcsin\left(\frac{p_x}{A_0}\right). \quad (3.7)$$

For the quantum-orbit model, since the second-harmonic field is weak compared to the fundamental, we can make a first-order expansion of the SFA exponent (2.24). Because the action is evaluated at its stationary point  $t_s$ , a first-order correction to  $t_s$  can change the action only in second order. Therefore, we can evaluate the perturbation at the unperturbed saddle-point.<sup>2</sup> Neglecting preexponential factors, the signal (2.30) at  $p_y = 0$  can be written as

$$\mathcal{M}(p_x, \phi) = e^{-iS(p_x, t_s(p_x), \phi)} \quad (3.8)$$

where

$$S(p_x, t, \phi) = -I_p t + \frac{1}{2} \int_t^T dt \left\{ (p_x + A_x(t))^2 + A_y(t, \phi)^2 \right\} \quad (3.9)$$

and  $t_s(p_x)$  is the obtained as either one of the two solutions of the perturbation-free saddle-point equation (2.29)

$$\frac{1}{2} (p_x + A_x(t_s))^2 + I_p = 0 \quad (3.10)$$

that correspond to the short or the long ATI trajectory,

$$\omega t_a = \pi - \arcsin\left(\frac{p_x - i\sqrt{2I_p}}{A_0}\right), \quad \omega t_b = \arcsin\left(\frac{p_x + i\sqrt{2I_p}}{A_0}\right). \quad (3.11)$$

We define  $a(p_x, \phi)$  as the amplitude according to (3.8) using the solution of (3.10) for the short trajectory  $t_a$  and  $b(p_x, \phi)$  as the one for the long trajectory  $t_b$ .

---

<sup>2</sup>Note that at  $p_y = 0$  the linear term in the action vanishes and the correction  $\frac{1}{2} \int_t^T dt A_y(t, \phi)^2$  is actually proportional to  $\epsilon^2$ . This is also the case in the saddle-point equation. Using the same reasoning as above, this second-order correction to  $t_s$  can change the action only in fourth order.

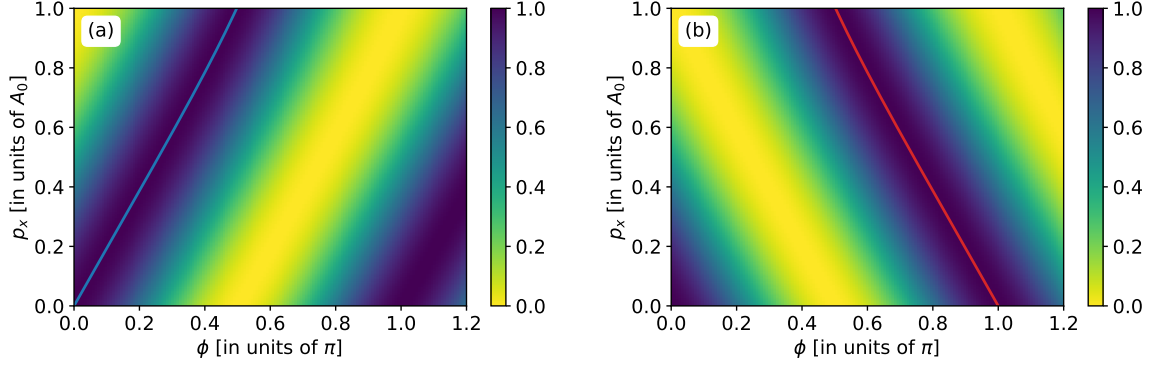


Figure 3.4: Two-color scan in the quantum-orbit model. (a) Signal  $|a(p_x, \phi)|^2$  for the short trajectories only. (b) Signal  $|b(p_x, \phi)|^2$  for the long trajectories only. As above, the signal is normalized row wise to vary between 0 and 1. In both panels, the colored line shows for every  $p_x$  the optimal phase  $\phi_0$  where the on-axis signal has a maximum. Adapted from Fig. 3 in [154].

The signals  $|a(p_x, \phi)|^2$  and  $|b(p_x, \phi)|^2$  corresponding to the two amplitudes alone are shown in Fig. 3.4. To obtain the optimal phase, we evaluate the condition for maximum signal

$$0 \stackrel{!}{=} \frac{\partial}{\partial \phi} 2 \operatorname{Im} S(p_x, t_s, \phi) = \frac{\partial}{\partial \phi} \operatorname{Im} \int_{t_s}^T dt A_y(t, \phi)^2. \quad (3.12)$$

Assuming more generally that the phase  $\phi$  induces a time shift of the perturbing field, i.e.  $A_y(t, \phi) = A_y(\Omega t + \phi)$  for suitable  $\Omega$ , and using that  $A_y(t, \phi)$  is real for real  $t$ , we can further simplify

$$\frac{\partial}{\partial \phi} \operatorname{Im} \int_{t_s}^T dt A_y(t, \phi)^2 = \frac{1}{\Omega} \operatorname{Im} \int_{t_s}^T dt \frac{\partial}{\partial t} A_y(t, \phi)^2 = -\frac{1}{\Omega} \operatorname{Im} A_y(t_s, \phi)^2. \quad (3.13)$$

Thus, the final condition is  $\operatorname{Re} A_y(t_s, \phi_0) = 0$  or  $\operatorname{Im} A_y(t_s, \phi_0) = 0$ . The former can be understood in that the signal is maximized if the “tunnel-entrance velocity” in the direction of the streaking field vanishes.<sup>3</sup> The latter usually gives the condition for a minimum and is not relevant here. In the present case, the streaking field is chosen as in (3.3), so the condition for the maximum becomes

$$\phi_0 = -2\omega \operatorname{Re} t_s \pmod{\pi}. \quad (3.14)$$

This relation gives us direct access to the real part of the complex ionization time  $t_s$ . Assuming a real ionization time, the condition is exactly equivalent to the simple man’s expression (3.3). Inserting the stationary points (3.11), we get

$$\phi_a = 2 \operatorname{Re} \arcsin \left( \frac{p_x - i\sqrt{2I_p}}{A_0} \right), \quad \phi_b = \pi - 2 \operatorname{Re} \arcsin \left( \frac{p_x + i\sqrt{2I_p}}{A_0} \right), \quad (3.15)$$

from which the simple man’s expression (3.7) is retrieved in the limit  $\gamma \rightarrow 0$ .

These relations provide the predictions shown in Fig. 3.3(c). There, it can be seen that in the range of direct ATI electrons ( $p_x < A_0$ ), the TDSE result agrees well with the maxima from the quantum-orbit model for the long trajectories. However, there are oscillations around the position of maximum signal predicted by the quantum-orbit model. These oscillations were

<sup>3</sup>This condition was assumed in [114, 203] but it was not derived there.

previously interpreted as intracycle interference of the dominant long trajectory with the weak short trajectory [114]. In 3D, the oscillations are weaker as compared to the previous 2D study (see Fig. 2 in the reference). To model the complete signal, we write (up to a  $p_x$ -dependent normalization)

$$|\mathcal{M}(p_x, \phi)|^2 = |\alpha(p_x, \phi) + \beta b(p_x, \phi)|^2 \quad (3.16)$$

and optimize the fitting parameter  $\beta$  to make the  $p_x$ -dependent maxima of the model signal fit to the curve of maxima from the TDSE delay scan (Fig. 3.3(c)) in the intermediate momentum range ( $0.4 < p_x/A_0 < 0.6$ ). Here,  $\beta$  is complex to allow for an additional phase shift between short and long trajectories which is expected due to sub-barrier Coulomb effects [99, 188, 190]. The fit returns  $|\beta| \approx 2.80$ ,  $\arg(\beta)/\pi \approx 1.20$ . This can be compared with the 2D value  $\beta \approx 2.3$  from [114], supporting our argument that Coulomb focusing leads to an increased weight of the long-trajectory branch.<sup>4</sup>

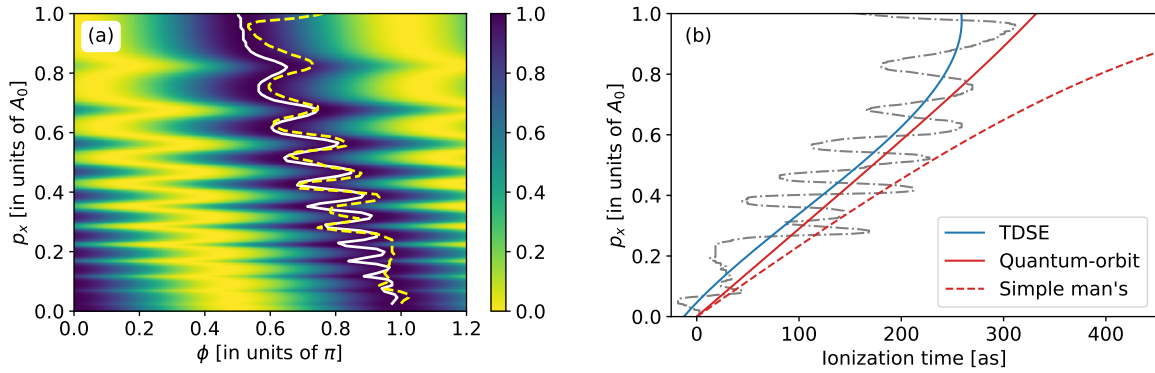


Figure 3.5: (a) Model signal (normalized row wise) according to Eq. (3.16) with  $\beta$  optimized to fit the TDSE result. The white curve shows the maxima from the model signal and the yellow-dashed curve the maxima from the TDSE delay scan (Fig. 3.3(c)). (b) Momentum-resolved ionization time (relative to the time of peak field strength) for the long ATI trajectory (blue curve) in comparison with the simple man's (red dashed curve) and the quantum-orbit model (red solid curve). The gray curve corresponds to the points of maximum signal in Fig. 3.3(c) with phase converted to time according to Eq. (3.14). Adapted from Figs. 3 and 5 in [154].

The model signal with optimized  $\beta$  is shown in Fig. 3.5(a). The agreement of the model signal with the TDSE persists to much higher momenta compared to the previous 2D study [114]. Two reasons can be given for this. On the one hand, the increased weight of long trajectories due to Coulomb focusing makes the signal more robust to perturbations by other types of trajectories. On the other hand, the 2D calculation overestimates the importance of rescattered trajectories in this momentum range due to the increased recollision probability.

Finally, we retrieve the ionization time from the two-color scan. The ability to do this relies on the relations (3.3) and (3.14) that connect the ionization time to the observed optimal phase. To isolate the signal due to the long ATI trajectory, we remove the oscillations due to the short trajectories from the delay scan by fitting a third-order polynomial in  $p_x$  to the curve of maxima (white curve in Fig. 3.3(c)) and convert the optimal phase to time. The result is shown in Fig. 3.5(b). As in the 2D case, the retrieved ionization time is in good agreement with the quantum-orbit model for the long trajectory branch and shows significant disagreement with the simple

<sup>4</sup>In the previous work [114],  $\beta$  was real. Instead, a weakly  $p_x$ -dependent phase between the short and the long trajectory branch was introduced to fix the position of the maxima and minima in the delay scan. We find that this is not necessary here and the model signal can be fitted well using only a single (complex) parameter.

man's model. This disagreement is due to the fact that for nonadiabatic tunnel ionization in linear polarization, the quantum orbit models predicts that the tunnel-exit velocity of the photoelectron in field direction is nonzero – contrary to a central assumption in the simple man's model (see for example [95, 98, 204] or Appendix A.2). For a given ionization time, the initial velocity is given by the momentum difference between the two red curves in Fig. 3.5(b).

### 3.5 Lateral dependence of the two-color scan

While in the previous section we investigated the signal along the direction of the fundamental 800 nm field, this section extends the retrieval scheme to nonzero lateral momentum. We consider  $p_z \neq 0$  instead of  $p_y \neq 0$  such that the  $\pi$  periodicity of the delay scan remains intact and the retrieval scheme can be used almost unchanged.

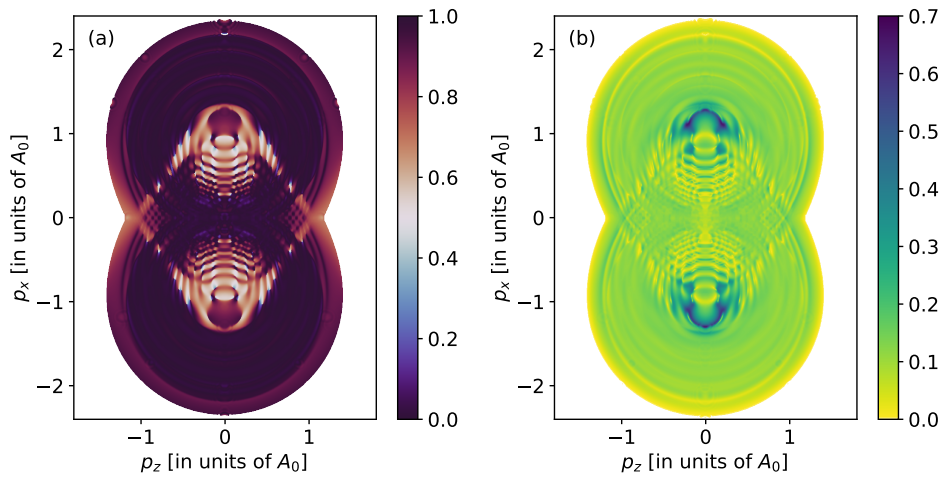


Figure 3.6: (a) Optimal phase (in units of  $\pi$ ) for photoelectron momenta in the  $p_x p_z$  plane. (b) Michelson contrast in the same plane. In both panels, a two-dimensional Gaussian filter (width  $0.04 A_0$ ) has been applied before determining the optimal phase to remove oscillations due to a small signal between the ATI rings.

Fig. 3.6(a) shows the optimal phase  $\phi_0$  at which maximum signal occurs for every momentum in the  $p_x p_z$  plane<sup>5</sup>. While the signal in the rescattering region is mostly optimized by phases around  $\phi_0 = 0$ , the direct ionization signal shows the same kind of oscillations found on axis for a wide range of lateral momenta. In Saddle-point SFA, when the prefactor is neglected, the effect of the lateral momentum  $p_z$  can be included simply by replacing  $I_p \rightarrow I_p + p_z^2/2$  in the action (3.9) and in the saddle-point equation (3.10). We can fit the maxima of the delay scan to the modified model signal, resulting in a  $p_z$ -dependent fitting parameter  $\beta(p_z)$  which is shown in Fig. 3.7.

While the argument of  $\beta$  does not change significantly, the absolute value shows strong oscillations.  $\beta$  drops to about  $|\beta| \approx 1$  at  $p_z \approx 0.12 A_0$ , indicating equal strength of the short and long trajectory branch. At  $p_z \approx 0.19 A_0$  there is a revival to  $|\beta| \approx 2.2$ . Such oscillations are expected due to holography [125, 126]. While in the quantum-orbit model there is only

<sup>5</sup>This is similar to the phase-of-the-phase method where every momentum is associated with the phase of the first Fourier component with respect to  $\phi$  [170]. In this case, however, the first Fourier component is zero because in the  $p_x p_z$  plane the PMD is periodic in  $\phi$  with periodicity  $\pi$ . Thus, the phase of the second Fourier component must be considered instead (see also [172]).

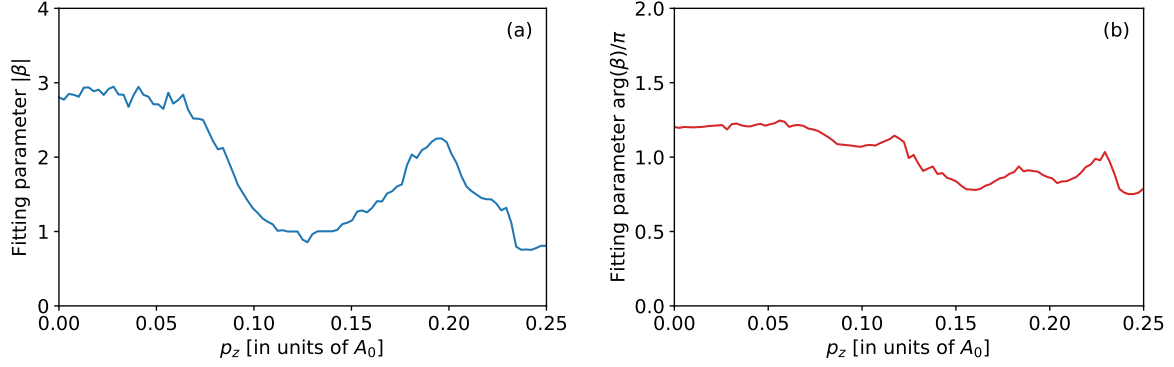


Figure 3.7: Argument (a) and phase (b) of the fitting parameter  $\beta$  as a function of lateral momentum  $p_z$ , obtained by repeating the retrieval scheme from Section 3.4 for  $p_y = 0$  and in the momentum range ( $0.4 < p_x/A_0 < 0.6$ ) as above. Adapted from Fig. 4 in [154].

one kind of long ATI trajectory, in the presence of the Coulomb potential a scattered and non-scattered long trajectory must be distinguished. These two kinds of long trajectories interfere to produce holographic structures in the photoelectron momentum distribution. In this case,  $\beta$  can be thought of as the combined amplitude of two types of long trajectories relative to the short trajectory. A minimum in the fitting parameter then indicates destructive interference between the reference and the scattered long trajectory. Indeed, the position of the minima and maxima of the fitting parameter agree well with the interference minima and maxima in the holographic structure that can be seen in the unstreaked photoelectron momentum distribution, Fig. 3.1.

### 3.6 Two-color scan in a molecule

The short and the long ATI trajectories interfere to produce the oscillations in the delay scan (Fig. 3.3(c)) from which their relative amplitude is retrieved. They start in neighboring quarter-cycles of the fundamental 800 nm field where it points in opposite directions. For the atom, there is no preferred direction for electron emission so the retrieved weight  $|\beta|$  depends mostly on the propagation after ionization. In an asymmetric molecule on the other hand, the relative weight is expected to depend also on the ionization step and we can use the orthogonal two-color scheme to probe orientation-dependent properties of the strong-field ionization process. One of the simplest example of an asymmetric system is the helium hydride molecular ion  $\text{HeH}^+$ . It is the first molecule that formed after the big bang [205] and was very recently discovered in terahertz radiation from a planetary nebula [206].

We solve the TDSE in two dimensions on a Cartesian grid of size  $512 \times 512$  a.u. and 2048 points in each dimension with the split-operator method and time step 0.01 a.u. until the final time  $T = 2500$  a.u. We choose a model potential [207]

$$V(\mathbf{r}) = \frac{-1}{\sqrt{(\mathbf{r} - \mathbf{r}_1)^2 + \alpha_1}} + \frac{-(1 + e^{-(\mathbf{r} - \mathbf{r}_2)^2/r_0^2})}{\sqrt{(\mathbf{r} - \mathbf{r}_2)^2 + \alpha_2}} \quad (3.17)$$

where the distance between the two centers is  $|\mathbf{r}_1 - \mathbf{r}_2| = 1.4$  a.u., which is approximately the equilibrium distance of  $\text{HeH}^+$ . We assume alignment on the  $x$  axis and probe both possible orientations. The soft-core parameters are chosen as  $\alpha_1 = \alpha_2 = 0.5$  a.u. Then,  $r_0 \approx 0.970$  a.u.

is tuned such that the ground-state energy of the system reproduces the ionization potential  $I_p \approx 1.66$  a.u. of  $\text{HeH}^+$  at said internuclear distance.

The dominant ionization channel of  $\text{HeH}^+$  typically includes nuclear dynamics [132]. At small intensities, the ion reaches a vibrationally excited state first before it is ionized. At larger intensities ( $I > 2 \times 10^{15}$  W/cm<sup>2</sup>), ionization can take place directly from the vibrational ground state, but the measured kinetic-energy release after subsequent dissociation reflects a larger internuclear distance than the equilibrium distance because ionization at large distances is preferred due to the decrease of the ionization potential.

In our calculation, we define the electric field as

$$\mathbf{E}(t) = E_0 f(t) (\cos(\omega t - \pi/2) \mathbf{e}_x + \epsilon \cos(2\omega t + \phi) \mathbf{e}_y). \quad (3.18)$$

Here,  $\epsilon = 0.04$ ,  $E_0 = 0.24$  a.u. ( $2 \times 10^{15}$  W/cm<sup>2</sup>) and  $\omega = 0.05695$  a.u. (800 nm) as above.  $f(t)$  describes a three-cycle trapezoidal envelope consisting of one ascending, one constant, and one descending cycle.

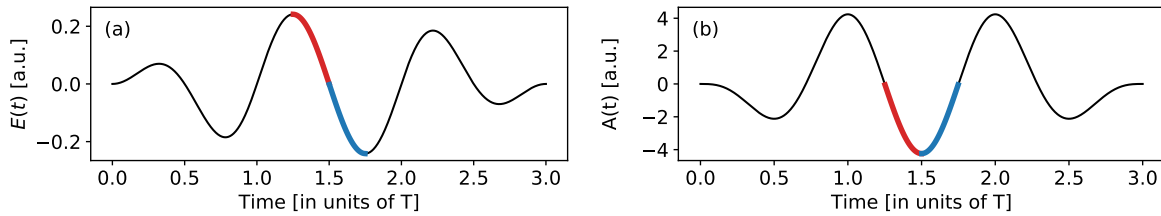


Figure 3.8: (a) Electric field at intensity  $2 \times 10^{15}$  W/cm<sup>2</sup> and CEP  $-\pi/2$ . (b) Corresponding vector potential. The red thick lines mark the ionization times of the dominant branch of long ATI trajectories on the positive  $p_x$  axis. The blue thick lines mark the corresponding ionization times of short ATI trajectories.

The electric field of the fundamental and its vector potential are shown in Fig. 3.8. The choice of pulse length and CEP ensures that for the direct photoelectrons on the positive  $p_x$  axis there are dominant contributions only from two neighboring quarter-cycles of the fundamental electric field, one branch of long and one branch of short ATI trajectories, and no ATI peaks occur. We distinguish two cases corresponding to the two possible orientations of the molecular ion. In case (a), the helium atom is located on the negative  $x$  axis and the proton is located on the positive  $x$  axis. Here, the long trajectory originates from the helium side and the short trajectory from the hydrogen side. Case (b) describes the opposite orientation where the proton is located on the negative  $x$  axis and the helium atom on the positive  $x$  axis. Here, the short trajectory originates from the helium side and the long trajectory from the hydrogen side. The two cases are shown schematically in Fig. 3.9.

The photoelectron momentum distributions for both possible orientations (in absence of the  $2\omega$  field) are shown in Fig. 3.10. In both cases, there are two large scattering rings due to recollision in the central cycle of the applied field. Additionally, there is one smaller inner ring that is due to recollision in the trailing flank of the envelope; it does not extend up to the  $10 U_p$  cutoff because of the reduced value of the vector potential at the recollision time [208]. Focusing on the direct-ionization spectrum on the positive  $p_x$  axis, we observe significant differences. In case (b), there are clear holographic fringes and only weak intracycle interference structures which suggests a dominance of long trajectories. In case (a), the holographic structures originating from long trajectories are strongly modified by intracycle interference, see

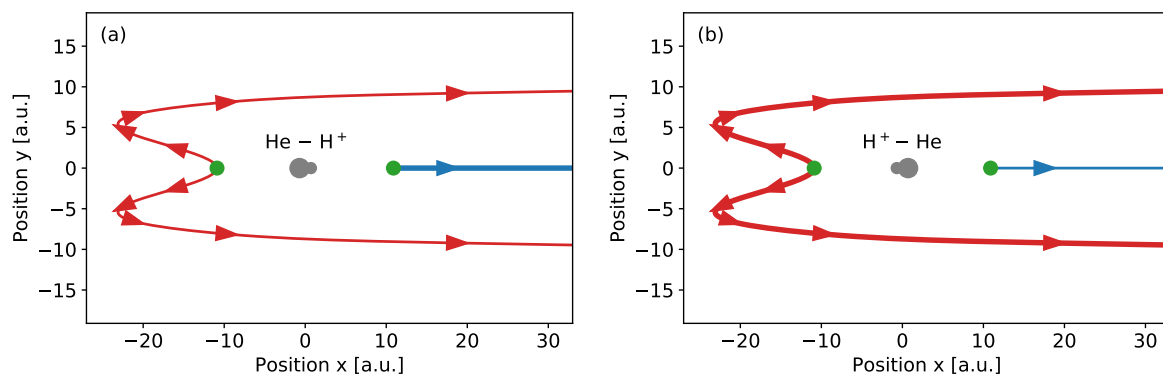


Figure 3.9: Orientation-dependent ionization of  $\text{HeH}^+$ . (a) Helium atom on the negative  $x$  axis and proton on the positive  $x$  axis. (b) Helium atom on the positive  $x$  axis and proton on the negative  $x$  axis. Classical trajectories are launched at the tunnel exit (chosen for simplicity as  $-I_p/E_x(t_0) \mathbf{e}_x$ ); they are subsequently accelerated by the laser field and move in a  $-2/r$  potential. The long trajectories (red curves) start at a time of 12 a.u. before a zero of the electric field with lateral velocity  $\pm 0.25$  a.u.. The short trajectory (blue curve) starts 12 a.u. after a zero of the electric field.

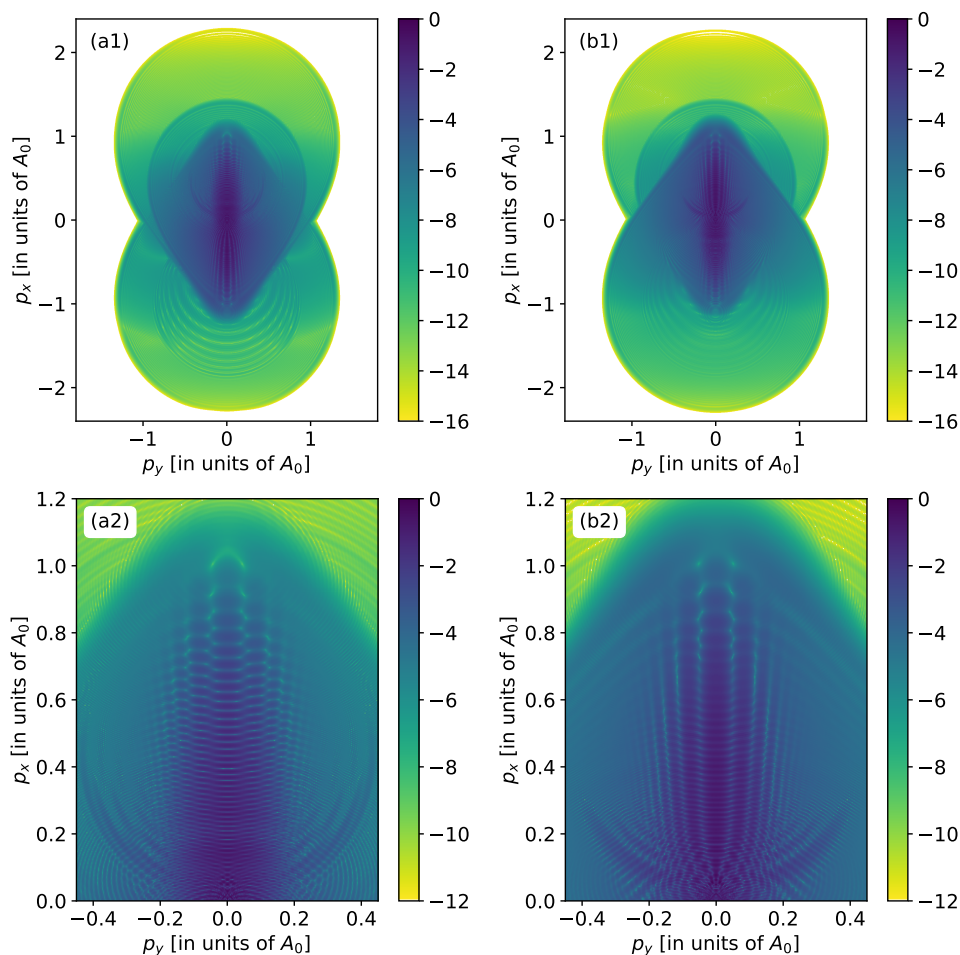


Figure 3.10: Momentum distributions in the absence of the  $2\omega$  field (log-10 scale). (a)  $\text{HeH}^+$  oriented such that the helium atom is located on the negative  $x$  axis and the proton on the positive  $x$  axis. (b). Other orientation with the helium atom on the positive  $x$  axis and the proton on the negative  $x$  axis. Both distributions are normalized independently to maximum signal 1.



also the modulation of the PMD on the  $p_x$  axis shown in Fig. 3.11(a1) and the large contrast in that region when the 400 nm field is switched on in 3.11(a2). This points to comparable strength of the short compared to the long ATI trajectory.

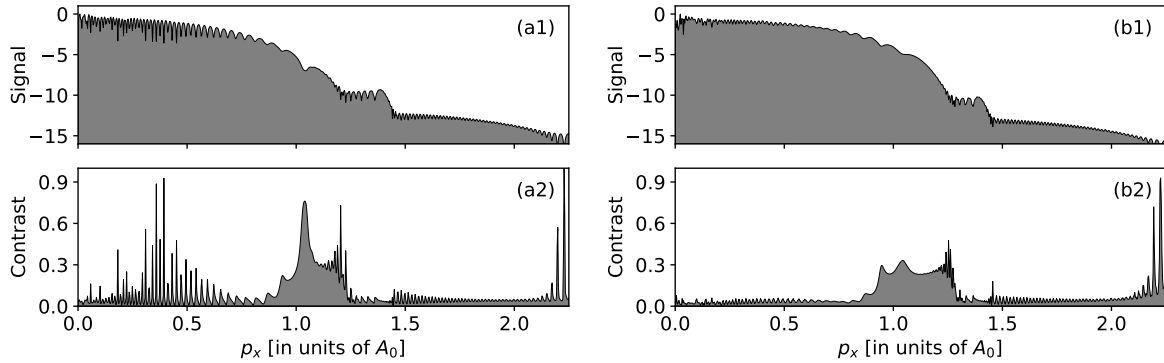


Figure 3.11: (a1, b1) On-axis signal for the 800 nm field (log-10 scale normalized to maximum signal 1) and the two possible orientations. (a2, b2) Michelson contrast for the modulation of the on-axis signal due to the 400 nm field.

Both observations can be explained by assuming a higher yield when ionization occurs via the hydrogen side compared to the helium side [209]. That is, at the ionization step, the short trajectory is favored in case (a) and the long trajectory in case (b). Since Coulomb focusing increases the weight of the long trajectory on axis after the ionization step, the dominance of the short trajectory in case (a) is mitigated such that on axis the weights are comparable while in case (b) the dominance of the long trajectory on axis becomes even stronger.

These findings are confirmed by the two-color delay scan, shown in Fig. 3.12 for both orientations. Here, results from both the TDSE (upper panels) and the SFA (lower panels) using the model signal (3.16) are shown. In case (b), a clear dominance of the long-trajectory branch is observed with only small oscillations due to short trajectories. Fitting the TDSE result to the model signal (in the region  $0.4 < p_x/A_0 < 0.6$ ), the dominance of the long trajectory is reflected in a large value of the fitting parameter  $|\beta| \approx 4.12$ . On the other hand, very strong oscillations are observed in case (a), confirming approximately equal strength of both types of trajectories. The oscillations follow the signal of short trajectories at small momenta  $p_x \lesssim 0.5 A_0$  and the signal of long trajectories at high momenta  $p_x \gtrsim 0.5 A_0$ . This is in agreement with Fig. 3.10(a) where the holographic interference does become slightly more pronounced when going to higher  $p_x$  while it is almost completely invisible at small  $p_x$ . Fitting the model signal to the TDSE in the upper region ( $0.55 < p_x/A_0 < 0.75$ ), we find  $|\beta| \approx 1.24$  which indicates only a slightly larger weight of long trajectories in that region. In the lower region ( $0.25 < p_x/A_0 < 0.35$ ), we find  $|\beta| \approx 0.81$  which confirms a slightly larger weight of short trajectories.

### 3.7 Conclusion

In this chapter, strong field ionization in a linearly polarized laser field was analyzed by adding a weak orthogonal second-harmonic probe field. Observing changes in the photoelectron momentum distribution depending on the relative phase between the two colors, information about the electron trajectories that constitute the momentum distribution can be extracted. By

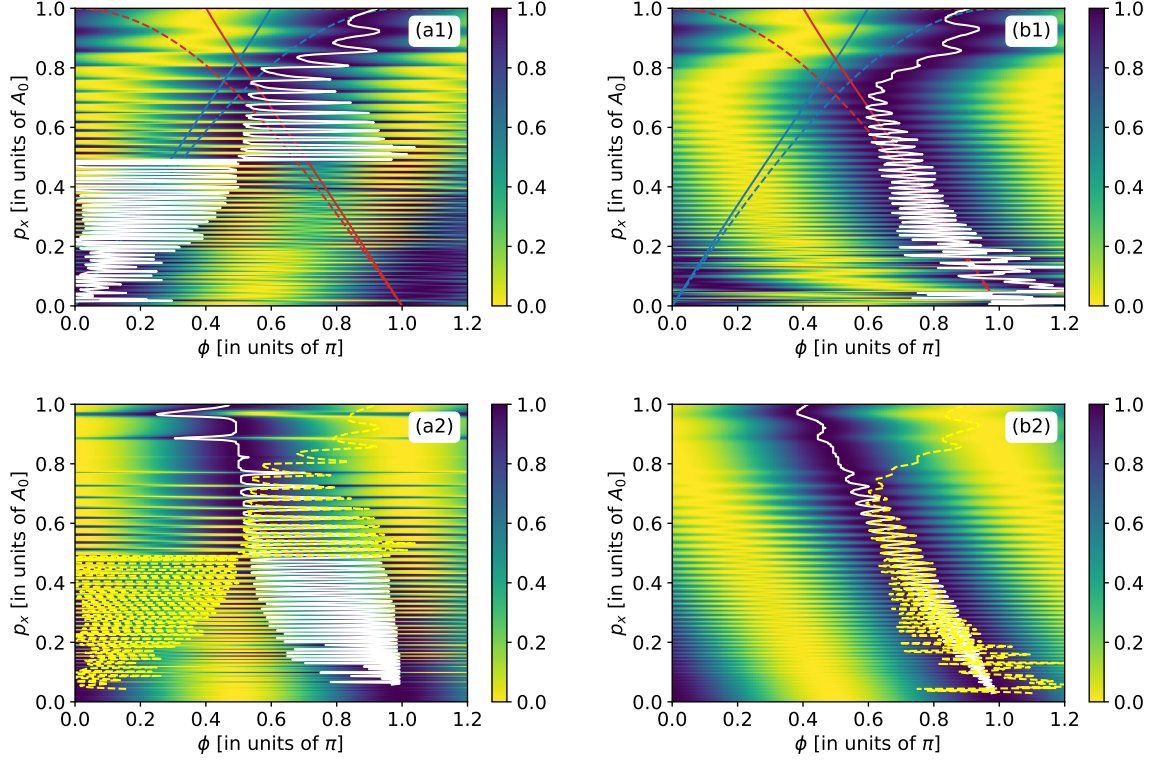


Figure 3.12: Variation of the on-axis signal as a function of the relative phase, normalized for each  $p_x$  independently to vary between 0 and 1. The upper panels (a1) and (b1) show the TDSE result. Here, the white line shows for every  $p_x$  the two-color phase  $\phi_0$  at which maximum signal is obtained. (a2) and (b2) show the model signal (3.16). Here the free parameter  $\beta$  in the model signal has been optimized to fit the maxima of the model signal (white line) to the curve of maxima from the TDSE (yellow dashed line) in the momentum range  $0.55 < p_x/A_0 < 0.75$  in case (a) and in the range  $0.4 < p_x/A_0 < 0.6$  in case (b).

fitting the observed signal to a model signal obtained from the quantum-orbit model, it is possible to retrieve the amplitude of the long trajectory relative to the amplitude of the short trajectory as well as the ionization time of the long trajectory resolved by final momentum. Compared to a previous study in 2D, we found that in 3D the weight of the long trajectory is increased due to Coulomb focusing. Together with the fact that rescattering is less pronounced in 3D compared to 2D, this enabled us to isolate the long trajectory accurately and retrieve its ionization time in a comparably large momentum range. We confirmed that this ionization time is in good agreement with the quantum-orbit model and shows significant disagreement with the simple man's model. This effect can be seen as a signature of a nonzero initial velocity of the photoelectron due to nonadiabatic effects. Extending the OTC scheme to nonzero lateral momentum reveals a modulation of the relative amplitude between long and short trajectories due to photoelectron holography.

In a diatomic molecule, the scheme can be used to probe orientation-dependent properties of the ionization process and disentangle the contributions arising from different ionization pathways. While for an atom only the ionization time of the dominant long trajectory can be accessed, probing asymmetric molecules allowed us observe the short trajectory, at least in a region of momentum space. Unfortunately, the dominance of the short trajectory is only weakly pronounced, leading to large oscillations in the delay scan. This makes it hard to actually retrieve its ionization time.

It would be interesting to test the sensitivity of the two-color scheme on the initial state. For example, when ionizing from a p state instead of from an s state, an additional  $\pi$  shift between short and long trajectories should be detectable in the phase of the fitting parameter. Also, the effect of the Coulomb potential on the ionization time could be investigated. However, this is not straightforward because the oscillations due to short trajectories are much larger compared to the expected effect. For the molecule, it would be interesting to extend the two-color scan to 3D. There, the Coulomb-focused branch of long trajectories is expected to be even stronger which could lead to a very clear signal with only small oscillations and an accurate ionization time retrieval, maybe accurate enough to estimate the importance of Coulomb effects on the ionization time. Coulomb focusing could even lead to the long trajectory being dominant when ionizing via the helium side. In that case, the two orientations could be compared to investigate the orientation-dependence of the ionization time.

We will come back to this point in Chapter 6 where the linear driver is replaced by a bi-circular field. This will allow us to observe the contributions from short and long trajectories completely independently of each other and to estimate the importance of Coulomb effects on the ionization time retrieval.



## Chapter 4

# Trajectory-free ionization times

While in the previous chapter an experimentally feasible scheme to measure ionization time in linear polarization was explored, this chapter focuses on a purely theoretical definition of momentum-resolved ionization time based on the Dyson representation of the time-evolution operator. Applied to the attoclock where strong-field ionization in a nearly circularly polarized field maps time to the detection angle of the photoelectron, we investigate the question of a possible time delay between the time of most probable electron emission and the time of peak field strength. Many results contained in this chapter are published in [210].

### 4.1 Introduction

With access to subfemtosecond or attosecond time scales provided by strong laser fields, the question about the exact timing of the ionization process arises. A central achievement of attosecond physics was the observation of time delays in single-photon ionization from different subshells of rare-gas atoms measured with the RABBIT technique and the attosecond streak camera [38, 39]. In single-photon ionization, this ionization time delay has a clear physical interpretation in terms of a Wigner time [211].

In the strong-field regime, on the other hand, the concept of ionization time arises naturally due to the trajectory picture which connects a given final momentum of the photoelectron with a time of ionization. It is closely related to the question of tunneling time, i.e. the time spent by a particle under a tunneling barrier [212], but is more involved because the barrier formed by the atomic potential and the laser field is time dependent. Tunneling time has been a controversial topic in quantum mechanics ever since Pauli's remark about the difficulties in defining a time operator as a self-adjoint operator conjugate to the Hamiltonian [213]. In case of tunneling through a time-independent potential barrier, several expressions have therefore been suggested for the tunneling time, many of which can be written in terms of the derivative of the absolute value or phase of the transmission amplitude through the barrier with respect to the barrier height or the energy of the incident particle [214]. This includes for example the Büttiker-Landauer time [215, 216] which is similar to the Keldysh time, i.e. the imaginary time needed by a particle with imaginary momentum to cross a tunneling barrier in real space, and the Larmor time which uses spin precession as a stopwatch to track the time spent under the barrier [217].

Within strong-field physics, attempts have been made to define or measure both the ion-

ization time as well as the tunneling time. While in linear polarization the ionization time can be probed using streaking schemes such as the OTC scheme presented in Chapter 3, ionization time measurements in circular polarization rely on the attoclock. First implemented by Eckle et al. [6], the attoclock makes use of the fact that in the simple man's model the ionization time of an electron (in strong-field ionization of an atom in a circularly polarized laser pulse) is mapped to its detection angle [71]. In a perfectly circularly polarized laser pulse, there is no preferred direction so the photoelectron momentum distribution has rotational symmetry. This symmetry can be broken either by using a slightly elliptically polarized field or a short pulse envelope. In both cases, the PMD exhibits a clear maximum which in the simple man's model is aligned with the negative value of the vector potential at the time of peak field strength.

In a real experiment, or when solving the time-dependent Schrödinger equation, one finds that this is not exactly the case. Instead, the maximum is rotated, usually forward with respect to the handedness of the electric field [218]. This offset angle is the main observable in an attoclock experiment from which the ionization time is inferred. For this purpose, however, a theoretical model is required. In the trajectory picture, the momentum distribution can be thought of being composed of trajectories that are characterized by a set of initial conditions (ionization time, position, and velocity), and a mapping that connects the initial conditions with the final momentum. In this picture, the origin of the shift could be due to an ionization time delay with respect to the time of peak field strength, but also due to the Coulomb force of the parent ion on the outgoing electron as well as due to an initial velocity of the photoelectron in field direction. Making assumptions about some of the initial conditions as well as the mapping, the ionization time that corresponds to the maximum of the momentum distribution can be retrieved and is usually thought of as the most probable time the electron leaves the tunneling barrier [219].

Assuming classical motion after tunnel ionization, Eckle et al. obtained an upper limit of 34 as on the ionization time delay with respect to the time of peak field strength in strong-field ionization of helium [7]. Using a more advanced classical model that starts trajectories with vanishing initial velocity at the tunnel exit position given by a separation of the Schrödinger equation in parabolic coordinates including the Stark shift (TIPIS), Pfeiffer et al. found vanishing ionization time delay within experimental accuracy in argon and helium [77]. Later, Landsman et al. found a small positive ionization time delay using the same method and interpreted this delay as tunneling time [220, 221]. Indeed, it was confirmed shortly after that in helium the offset angle in experimental [222] or theoretical [223] momentum distributions cannot be explained by the TIPIS model when assuming that ionization is most likely at the peak of the pulse. Camus et al. measured the difference in the attoclock offset angle between argon and krypton by considering a mixture of two gases, derived initial conditions for classical trajectories using Wigner trajectories that predict a nonzero initial velocity of the photoelectron in field direction and interpreted their result as a nonzero tunneling time [224, 225]. On the contrary, in a purely theoretical work, zero ionization time delay was found when applying analytical R-matrix theory to the attoclock problem to find the ionization time that corresponds to the peak of the momentum distribution obtained from the TDSE in strong-field ionization of the hydrogen atom [78]. Theoretical offset angles from strong-field ionization of atomic hydrogen were eventually verified experimentally [226, 227].

Instead of interpreting the attoclock by observing the momentum distribution, it is possible to define the ionization time directly from the time-dependent wave function. Teeny et

al. measured the probability flow through the tunnel exit of a time-dependent tunneling barrier and found both large positive delay times as well as an initial velocity offset at the tunnel exit position [228, 229]. Yuan et al. defined an instantaneous ionization rate by observing the overlap of the time-dependent state with the bound states of the system and found that it peaks later than the field maximum [230]. Douguet et al. employed Bohmian trajectories and also found a large positive mean ionization time [231]. Another approach that can be used to interpret attoclock experiments as well as obtain the instantaneous ionization rate directly is classical backpropagation [102–104]. There, the outgoing electron wave packet from a solution of the TDSE is represented as phase-space distribution of classical trajectories which are propagated backwards in time until a suitable tunnel-exit condition is met. Using the zeros of the electron velocity in the direction of the instantaneous electric field for this purpose, vanishing ionization time delay was found.

In all of the above works where the observable was the photoelectron momentum distribution, some kind of an electron trajectory was used to relate the observed photoelectron momentum at the peak of the momentum distribution to the time of ionization. In this chapter, we use a method that does not require the notion of an electron trajectory to define a momentum-resolved ionization time. Similar to the derivation of the KFR amplitude (2.22) presented in Section 2.4, we start from the Dyson expression (2.21) for the ionization amplitude

$$\mathcal{M}(\mathbf{p}) = -i \int_0^T dt \mathcal{D}(\mathbf{p}, t) \quad (4.1)$$

where the integrand is given by

$$\mathcal{D}(\mathbf{p}, t) = \langle \psi_{\mathbf{p}}^{(-)} | U(T, t) H_I(t) U_0(t, 0) | \psi_0 \rangle. \quad (4.2)$$

In the SFA as described in Section 2.4, the full time-evolution operator is replaced by the Volkov time-evolution operator and the scattering state by a plane wave. Ionization time is then defined as a stationary point of the action. Here, we do not employ the above approximations and we consider the full integrand of the Dyson representation. Since it is not clear how to split the integrand into transition matrix element and action when the strong-field approximation is not employed, we instead use the stationary points of the entire integrand and define the ionization time for given momentum  $\mathbf{p}$  via

$$\left. \frac{\partial}{\partial t} \log \mathcal{D}(\mathbf{p}, t) \right|_{t=t_s} = 0. \quad (4.3)$$

The solution of this equation provides a mapping from photoelectron momentum  $\mathbf{p}$  to the complex ionization time  $t_s$ . We evaluate this mapping and apply it to the attoclock setup to find the most probable ionization time.<sup>1</sup>

The chapter is organized as follows. In Section 4.2, we demonstrate the validity of the saddle-point approximation using the full integrand when the atomic potential after ionization is neglected as in standard SFA. Afterwards, we apply the definition to the attoclock setup where we proceed with a full numerical solution of (4.3). Section 4.3 gives a formal introduction to the attoclock and derives the conditions that must be imposed on target and pulse in an attoclock setup. Section 4.4 gives the computational details. In Section 4.5, we explain the

<sup>1</sup>The idea is based on previous work by M. Hartmann [232] who investigated imaginary-time displacements of the integration path in the Dyson integral (4.1).

details of solving the TDSE in the complex plane and present first results. In Section 4.6, we give details on how to properly define the offset angle. In Section 4.7, we obtain the ionization time in the attoclock setup for a wide range of intensities and investigate the question of a possible ionization time delay. Section 4.8 concludes the chapter.

## 4.2 Strong-field approximation with full integrand

Even when the strong-field approximation is applied to the integrand (4.2), the stationary points (4.3) do not necessarily resemble the ones found in standard SFA (as described in Section 2.4) because only the action is considered there.

Thus, before proceeding with a full numerical evaluation of (4.3), we explore how the stationary points of the full integrand behave when the potential after interaction with the field is neglected. That is, we consider the simplified integrand

$$\mathcal{D}(\mathbf{p}, t) = M(\mathbf{p}, t) e^{-iS_{\text{SFA}}(\mathbf{p}, t)} \quad (4.4)$$

with  $S_{\text{SFA}}(\mathbf{p}, t)$  and  $M(\mathbf{p}, t)$  given by (2.24) and (2.25). To evaluate this expression, we have to make some assumption on the matrix element. We adopt the form given by Gribakin and Kuchiev [143] who state the asymptotic form of a bound  $s$ -state wave function in a potential  $V(\mathbf{r}) \simeq -Z/r$  at  $r \rightarrow \infty$  as

$$\psi_0(r) \simeq A r^{\nu-1} e^{-\kappa r}, \quad \nu = Z/\kappa \quad (4.5)$$

and its Fourier transform in the vicinity of the ‘‘standard’’ SFA saddle point as<sup>2</sup>

$$\tilde{\psi}_0(\mathbf{q}) = \frac{1}{(2\pi)^{3/2}} \int d^3r e^{-i\mathbf{q}\cdot\mathbf{r}} \psi_0(r) \simeq \frac{A}{\sqrt{\pi/2}} \frac{(2\kappa)^\nu \Gamma(\nu+1)}{(q^2 + \kappa^2)^{\nu+1}}. \quad (4.6)$$

In length gauge, the transition matrix element (2.25) becomes

$$\begin{aligned} \langle \mathbf{p} + \mathbf{A}(t) | \mathbf{E}(t) \cdot \mathbf{r} | \psi_0 \rangle &= \mathbf{E}(t) \cdot i \nabla_{\mathbf{k}} \tilde{\psi}_0(\mathbf{k})|_{\mathbf{k}=\mathbf{p}+\mathbf{A}(t)} \\ &\propto \frac{(\mathbf{p} + \mathbf{A}(t)) \cdot \mathbf{E}(t)}{((\mathbf{p} + \mathbf{A}(t))^2 + \kappa^2)^{\nu+2}} \propto \frac{\check{S}_{\text{SFA}}(\mathbf{p}, t)}{(\dot{S}_{\text{SFA}}(\mathbf{p}, t))^{\nu+2}} \end{aligned} \quad (4.7)$$

where in the last line we have omitted  $\mathbf{p}$ -independent prefactors. As a result, the (simplified) Dyson integrand (4.4) becomes

$$\mathcal{D}(\mathbf{p}, t) \propto \frac{\check{S}_{\text{SFA}}(\mathbf{p}, t)}{(\dot{S}_{\text{SFA}}(\mathbf{p}, t))^{\nu+2}} e^{-iS_{\text{SFA}}(\mathbf{p}, t)}. \quad (4.8)$$

In the following, we consider strong-field ionization of atomic hydrogen ( $I_p = 0.5$  a.u.,  $\nu = 1$ ) in a circularly polarized laser field

$$\begin{aligned} A_x(t) &= -E_0/\omega \cos(\omega t), \\ A_y(t) &= -E_0/\omega \sin(\omega t). \end{aligned} \quad (4.9)$$

Here,  $\omega = 0.05695$  a.u. corresponds to a wavelength of 800 nm.

The logarithmic derivative and the absolute value of the Dyson integrand (4.4) in the complex plane at the classically expected momentum  $\mathbf{p} = E_0/\omega$  are shown in Fig. 4.1. For the

<sup>2</sup>The full expression is slightly different as the stationary point (4.3) does not necessarily have to be close to the SFA saddle point. For the hydrogen atom and a (zero-range)  $\delta$  potential, however, (4.6) is exact.



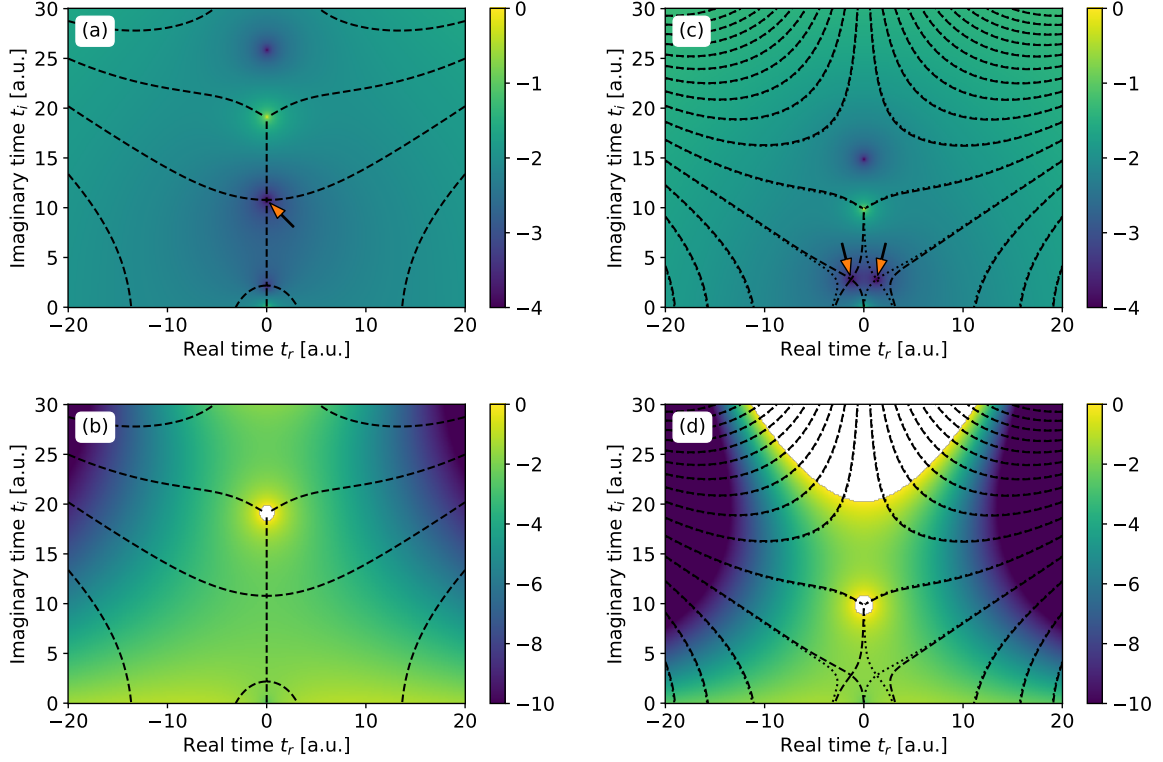


Figure 4.1: (a) Logarithmic derivative (4.3) of the Dyson integrand in strong-field approximation (4.4) at  $E_0 = 0.05$  (log-10 scale, arb. units). The contour lines show times of constant argument and indicate the path of steepest descent from the relevant stationary point (marked by an arrow). (b) Absolute value of the Dyson integrand at the same field strength (log-10 scale, arb. units). (c,d) Same as (a,b) but for higher field strength  $E_0 = 0.10$ . Here, two relevant stationary points are found and the integrand has a slightly different argument at each of them. Therefore, there are two slightly different types of contours (dashed and dotted), each going through one of the two points. The contours meet on the real axis in a zero of the integrand where its argument changes from one to the other.

small field strength, there are two saddle points below the standard SFA saddle point (which shows up as a pole here because the logarithmic derivative (4.3) includes a term with  $\dot{S}_{\text{SFA}}$  in the denominator), the upper of which ( $t_i \approx 10.8$  a.u.) is the relevant one. Going to higher field strengths, the two saddle points approach each other, merge and split horizontally in the complex plane. In this case, they both become relevant.

The critical field strength at which the second stationary points becomes relevant can be estimated. We write the saddle-point equation (4.3) for the full integrand as

$$\dot{S}_{\text{SFA}} \ddot{S}_{\text{SFA}} - (\nu + 2)(\dot{S}_{\text{SFA}})^2 - i(\dot{S}_{\text{SFA}})^2 \ddot{S}_{\text{SFA}} = 0, \quad (4.10)$$

where for simplicity we have omitted the arguments  $(\mathbf{p}, t)$ . To simplify the equation, we go to the adiabatic regime and expand the vector  $\mathbf{A}(t)$  at some real time  $t_r$  to first order in imaginary time  $t_i$ ,

$$\mathbf{A}(t) = \mathbf{A}(t_r) - it_i \mathbf{E}(t_r) + \mathcal{O}(t_i^2). \quad (4.11)$$

Here, higher orders correspond to derivatives of the electric field which can be neglected when

the field is varying slowly. In this approximation we get

$$\begin{aligned}\dot{S}_{\text{SFA}} &\approx -\frac{1}{2}(\mathbf{v}_0 - i\mathbf{E}(t_r)t_i)^2 - I_p, \\ \ddot{S}_{\text{SFA}} &\approx (\mathbf{v}_0 - i\mathbf{E}(t_r)t_i) \cdot \mathbf{E}(t_r), \\ \dddot{S}_{\text{SFA}} &\approx -\mathbf{E}(t_r)^2.\end{aligned}\quad (4.12)$$

Here,  $\mathbf{v}_0 = \mathbf{p} + \mathbf{A}(t_r)$  is the initial velocity of the photoelectron. Inserting this into the saddle-point equation (4.10), we find that the equation for the imaginary part can be satisfied with  $\mathbf{v}_0 \cdot \mathbf{E}(t_r) = 0$ , while for the real part one obtains

$$f(t_i) = \left( I_p^{\text{eff}} - \frac{E_0^2 t_i^2}{2} \right) - t_i \left( I_p^{\text{eff}} - \frac{E_0^2 t_i^2}{2} \right)^2 + E_0^2 t_i^2 (\nu + 2) = 0. \quad (4.13)$$

Here,  $E_0 = E(t_r)$  and the effective ionization potential is given by  $I_p^{\text{eff}} = I_p + \mathbf{v}_0^2/2$ .

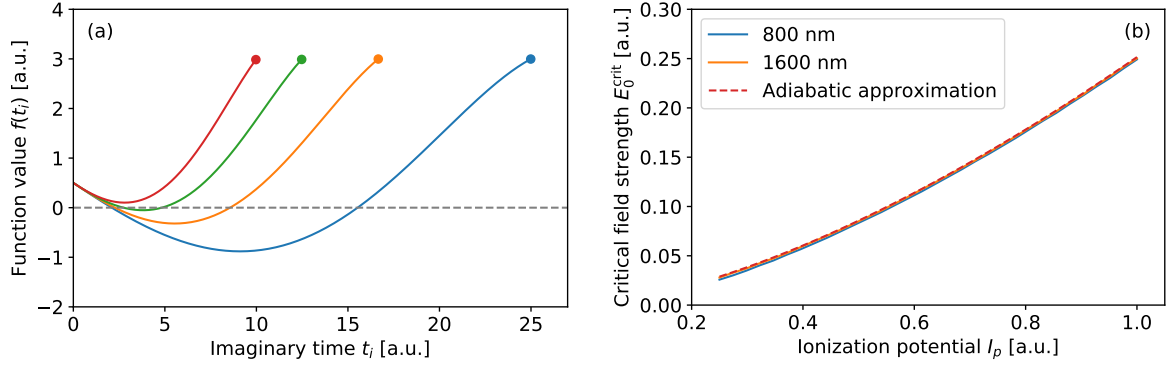


Figure 4.2: (a) Saddle-point condition (4.13) evaluated at  $I_p^{\text{eff}} = 0.5$  a.u.,  $\nu = 1$  (hydrogen) and various field strengths 0.04 a.u. (blue), 0.06 a.u. (orange), 0.08 a.u. (green) and 0.10 a.u. (red). The dots at the end of the curves mark the Keldysh time at which the standard SFA saddle-point (2.29) is expected in the adiabatic limit. (b) Critical field strengths at  $Z = 1$  for various values of the ionization potential evaluated numerically (solid lines) and in adiabatic approximation (4.15) (dashed line).

This fifth-order polynomial is plotted in Fig. 4.2(a). In general, the equation is fulfilled twice between the real axis and the Keldysh time  $t_K = \sqrt{2I_p^{\text{eff}}/E_0}$ , while for high intensities there is no solution. This shows that at a given  $t_r$ , the imaginary time  $t_i$  must “become imaginary” itself to correct the real time. In this case, which corresponds to the horizontal splitting in Fig. 4.1(c,d), there are two solutions at different real part with identical imaginary part.

The emergence of two solutions is necessary. Inserting the Keldysh time into (4.13), we find  $f(t_K) = 2I_p^{\text{eff}}(\nu + 2) > 0$  while also  $f(0) = I_p^{\text{eff}} > 0$ . Thus, solutions in  $t_i \in (0, t_K)$  always come in pairs. In the weak field limit, the two solutions can be approximated by

$$t_i^{(0)} = \frac{1}{I_p^{\text{eff}}} + \mathcal{O}(E_0^2), \quad t_i^{(1)} = \frac{\sqrt{2I_p^{\text{eff}}}}{E_0} - \frac{\sqrt{\nu + 2}}{(2I_p^{\text{eff}})^{1/4} \sqrt{E_0}} - \frac{1}{4I_p^{\text{eff}}} + \mathcal{O}(E_0^{1/2}). \quad (4.14)$$

When the field strength increases, the two solutions approach each other until they merge. To find the critical field strength, we solve the conditions  $f(t_i) = 0$  and  $f'(t_i) = 0$  exactly. The result can be written as

$$E_0^{\text{crit}} = g(\nu) (2I_p^{\text{eff}})^{3/2}, \quad t_i^{\text{crit}} = h(\nu) \sqrt{2I_p^{\text{eff}}/E_0^{\text{crit}}} \quad (4.15)$$

Species	$\nu$	$g(\nu)$	$h(\nu)$
Short range	0.000	0.099	0.333
Helium	0.744	0.089	0.305
Hydrogen	1.000	0.086	0.297

Table 4.1: Some values of the functions  $g(\nu)$  and  $h(\nu)$  that give the dependence of the critical field strength on the wave function asymptotics for different species.

with functions  $g$  and  $h$  that depend only weakly on  $\nu$ . Some values of both functions are listed in Table 4.1.<sup>3</sup>

Fig. 4.2(b) shows the numerically obtained critical field strength in circular polarization for different  $I_p$  in comparison with our estimate. Even at 800 nm, there is good agreement which can be attributed to the fact that since the critical field strength is comparably large one automatically moves into the adiabatic regime where the approximation is valid.

In the next step, we proceed with evaluating the momentum distribution in saddle-point approximation using the full stationary points of the Dyson integrand. To this end, we write

$$\mathcal{M}(\mathbf{p}) = -i \int_0^T dt \mathcal{D}(\mathbf{p}, t) = -i \int_0^T dt e^{-iS(\mathbf{p}, t)} \quad (4.16)$$

with  $S(\mathbf{p}, t) = i \log \mathcal{D}(\mathbf{p}, t)$  and  $\mathcal{D}(\mathbf{p}, t)$  given by (4.4). The simplest case is just to consider the upper saddle point. Since this saddle point avoids the pole of the matrix element at the conventional SFA saddle point, we can simply use (2.30), giving

$$\mathcal{M}(\mathbf{p}) \approx \sqrt{\frac{-2\pi i}{\ddot{S}(\mathbf{p}, t_s)}} e^{-iS(\mathbf{p}, t_s)} = \sqrt{\frac{-2\pi}{\ddot{D}(\mathbf{p}, t_s)}} (\mathcal{D}(\mathbf{p}, t_s))^{3/2}. \quad (4.17)$$

More accurately, we can use the uniform approximation [233]. There, both saddle points (before and after the merger) can be taken into account by expanding the action to third order at a point between the two and evaluating the resulting integrals analytically. Both approximations can be compared with a full numerical evaluation of the KFR amplitude (2.23) as well as with the saddle-point approximation at the conventional SFA saddle point including the pole according to (2.32).

The result is shown in Fig. 4.3 for the same parameters as above. For the lower field strength, the saddle points stay separated and the saddle-point approximation using only the upper one gives decent result, especially in the regions of momentum space where the separation between the saddle points is large. For the higher field strength, in the vicinity of the maximum of the photoelectron momentum distribution the separation is lost and the saddle-point approximation for one saddle point diverges. The uniform approximation, on the other hand, agrees very well with the full numerical result and is superior to the conventional saddle-point approximation at the pole.

The good agreement with the full numerical solution in SFA suggests that the stationary points of the full integrand can be interpreted as ionization time in a meaningful way. In the following, we obtain these stationary points in the TDSE to generate a time-to-momentum mapping as is required to interpret attoclock momentum distributions.

<sup>3</sup>The results (4.14) and (4.15) are derived in Appendix A.3. There, approximate forms for  $g$  and  $h$  are provided as well.

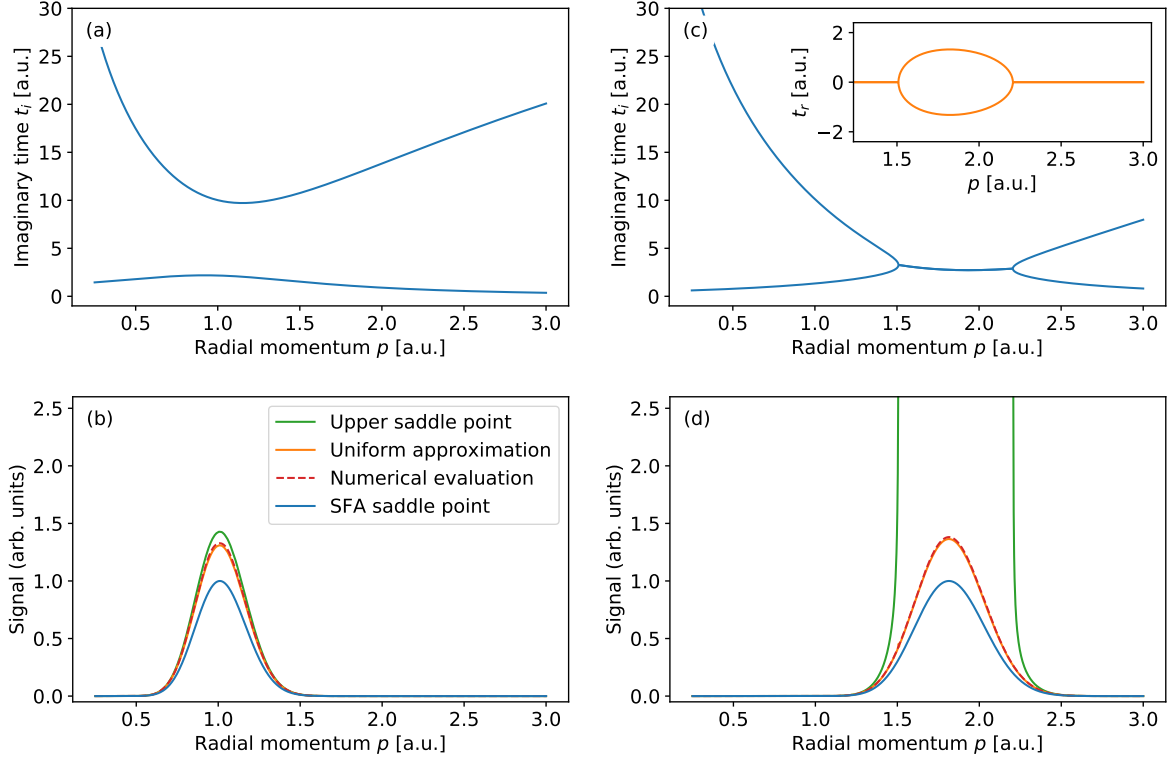


Figure 4.3: (a) Imaginary part of the saddle-point time as a function of radial momentum for field strength  $E_0 = 0.05$  a.u. (b) Radial slice through the photoelectron momentum distribution in various approximations. (c,d) Same as (a,b) for higher field strength  $E_0 = 0.10$  a.u. The inset in panel (c) shows the real part of the saddle-point time.

### 4.3 The attoclock

Attosecond angular streaking, or the “attoclock,” makes use of the fact that in a circularly polarized laser pulse

$$\begin{aligned} A_x(t) &= -A_0 \cos(\omega t) \\ A_y(t) &= -A_0 \sin(\omega t) \end{aligned} \quad (4.18)$$

the ionization time  $t_0$  is mapped to the detection angle of the photoelectron. In the simple man’s model, where the final photoelectron momentum is given by the negative vector potential at ionization time,  $\mathbf{p} = -\mathbf{A}(t_0)$ , the photoelectron is detected at

$$\begin{aligned} p_x &= A_0 \cos(\omega t_0) \\ p_y &= A_0 \sin(\omega t_0) \end{aligned} \quad (4.19)$$

such that the detection angle is simply  $\phi = \angle(\mathbf{p}_x, \mathbf{p}_y) = \omega t_0$ . In reality, this mapping must be modified, mainly because the force due to the Coulomb potential of the parent ion on the outgoing electron shifts the angle forward with respect to the handedness of the electric field. This is sketched in Fig. 4.4 for a classical trajectory that propagates in the laser field in the presence of the Coulomb potential.

A simple expression for the classical offset angle due to the Coulomb force can be given in limiting cases. In the long-wavelength limit, the electron essentially moves out of the Coulomb potential in straight line. When the field is sufficiently weak, the tunnel-exit position is far

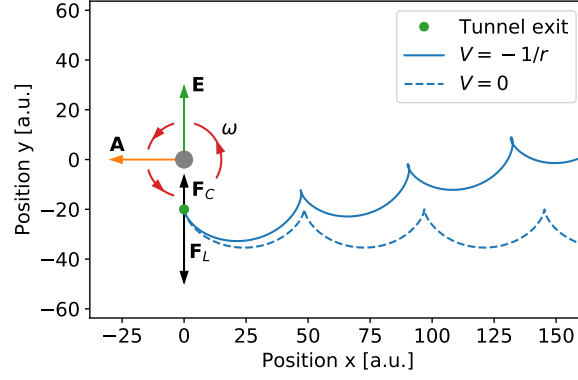


Figure 4.4: Atto-clock principle. At the time of ionization, the electric field  $\mathbf{E}$  points in the  $+y$  direction. The photoelectron appears at the tunnel exit in  $-y$  direction and is accelerated by the force  $\mathbf{F}_L$  due to the laser field. In the absence of a potential, the electron follows the blue dashed trajectory with asymptotic momentum opposite to the instantaneous vector potential  $\mathbf{A}$ . When the potential is taken into account (blue solid curve), the Coulomb force  $\mathbf{F}_C$  changes the angle at which the electron is emitted with respect to the Coulomb-free case. The image shows the strong-field ionization of hydrogen ( $I_p = 0.5$  a.u.) at  $E_0 = 0.025$  a.u. and 800 nm wavelength. The electron starts at the tunnel exit chosen for simplicity as  $-I_p/E_0 \mathbf{e}_y$  and it subsequently moves according to Newton's equations of motion in the combined potential of Coulomb attraction and laser field.

enough away to justify a perturbative treatment of the Coulomb force which acts as a braking force on the outgoing electron [234, 235]. This leads to<sup>4</sup>

$$\phi = \frac{\omega\pi}{(2I_p)^{3/2}}. \quad (4.20)$$

In another approach, the attoclock offset is interpreted as a Rutherford (half) scattering event [236]. There, the impact parameter is approximated by the tunnel-exit position  $I_p/E_0$  and the final momentum is chosen as the classically expected value  $E_0/\omega$ . This approach results in

$$\phi = \frac{\omega^2}{E_0 I_p}. \quad (4.21)$$

When a cw field as in (4.18) is used, the photoelectron momentum distribution is cylindrically symmetric and the attoclock offset cannot be observed. Thus, a slightly elliptically polarized pulse or an ultrashort pulse envelope is used to break the symmetry.<sup>5</sup> In that case, the PMD exhibits a maximum from which the offset angle is inferred. The basic requirement we have on a meaningful attoclock setup (consisting of a target and a pulse) is that in the absence of the atomic potential the maximum is attributed to an ionization time that corresponds to the peak of the electric field strength and is aligned with the negative vector potential at that time. This is not always the case.<sup>6</sup> In the following, we derive conditions under which this statement holds in SFA. Consider a pulse in the  $xy$  plane symmetric around  $t = 0$  given by

$$\begin{aligned} A_x(-t) &= A_x(t), \\ A_y(-t) &= -A_y(t). \end{aligned} \quad (4.22)$$

<sup>4</sup>See also Appendix A.4.3 or [94] where (almost) the same expression is derived from ARM theory.

<sup>5</sup>Instead of using elliptically polarized fields where the exact location of the polarization ellipse might be unknown, a circularly polarized field can be used together with a second-harmonic linearly polarized field to break the symmetry [237].

<sup>6</sup>See [238]. Using an orthogonal two-color field with comparable field strengths of the two colors, it is possible to devise a field shape where the maximum of the PMD does not correspond to the time of peak field strength, already in SFA.

The symmetry condition implies that  $\mathbf{A}$  points in the  $\pm x$  direction at  $t = 0$  and all odd derivatives of  $A_x$  and all even derivatives of  $A_y$  vanish, so  $\mathbf{A}(0) \cdot \mathbf{E}(0) = 0$  and  $\mathbf{E}(0) \cdot \dot{\mathbf{E}}(0) = 0$ . In particular, the electric field  $\mathbf{E}(t)$  has an extremum at  $t = 0$ ,

$$\left. \frac{d}{dt} \mathbf{E}(t) \right|_{t=0} = \frac{\mathbf{E}(0) \cdot \dot{\mathbf{E}}(0)}{E(0)} = 0. \quad (4.23)$$

Evaluating the vector potential in the complex plane at zero real part of the ionization time,  $t_s = i t_i$ , we find that  $A_x(t_s)$  is purely real and  $A_y(t_s)$  purely imaginary, as can be quickly verified by writing their Taylor expansions and using the symmetry properties (4.22) on the derivatives. This means that the saddle-point equation (2.29),

$$\frac{1}{2}(p_x + A_x(t_s))^2 + \frac{1}{2}(p_y + A_y(t_s))^2 + \frac{1}{2}p_z^2 + I_p = 0, \quad (4.24)$$

can be split into real and imaginary parts as

$$\begin{aligned} (\text{Im } A_y(t_s))^2 &= (p_x + \text{Re } A_x(t_s))^2 + 2I_p + p_y^2 + p_z^2, \\ 0 &= p_y \text{Im } A_y(t_s). \end{aligned} \quad (4.25)$$

The equation for the real part implies  $\text{Im } A_y(t_s) \neq 0$ , so from the imaginary part we find  $p_y = 0$ . Thus, the saddle-point condition assigns time zero to the  $p_x p_z$  plane.

We show that the momentum distribution also has an extremum there. The momentum distribution (2.23) in length-gauge SFA (up to a  $\mathbf{p}$ -dependent phase) can be written as

$$\mathcal{M}_1(\mathbf{p}) = -i \int_{-T/2}^{T/2} dt M(\mathbf{p}, t) e^{-iS(\mathbf{p}, t)} \quad (4.26)$$

with the action

$$S(p_x, p_y, p_z, t) = - \int_0^t dt' \left\{ \frac{1}{2}(p_x + A_x(t'))^2 + \frac{1}{2}(p_y + A_y(t'))^2 + \frac{1}{2}p_z^2 + I_p \right\} \quad (4.27)$$

and matrix element

$$M(p_x, p_y, p_z, t) = \langle p_x + A_x(t), p_y + A_y(t), p_z | E_x(t) x + E_y(t) y | \psi_0 \rangle. \quad (4.28)$$

Replacing  $p_y \rightarrow -p_y$  and  $t \rightarrow -t$  in (4.27) and using the conditions on the field (4.22), we find that the action simply changes its sign,  $S(p_x, -p_y, p_z, -t) = -S(p_x, p_y, p_z, t)$ . For the matrix element we obtain

$$M(p_x, -p_y, p_z, -t) = \overline{\langle p_x + A_x(t), p_y + A_y(t), p_z | (E_x(t) x + E_y(t) y) C | \psi_0^{xz} \rangle}, \quad (4.29)$$

where  $\psi_0^{xz}(x, y, z) = \psi_0(-x, y, -z)$  and we have introduced the antihermitian conjugation operator  $\langle \mathbf{r} | C | \psi \rangle = \overline{\langle \mathbf{r} | \psi \rangle}$ . Assuming a condition on the initial state,

$$C | \psi_0^{xz} \rangle = e^{i\varphi} | \psi_0 \rangle, \quad (4.30)$$

this implies  $M(p_x, -p_y, p_z, -t) = e^{-i\varphi} \overline{M(p_x, p_y, p_z, t)}$ . Putting everything together, we find that the KFR amplitude satisfies

$$\mathcal{M}_1(p_x, -p_y, p_z) = -e^{-i\varphi} \overline{\mathcal{M}_1(p_x, p_y, p_z)} \quad \Rightarrow \quad |\mathcal{M}_1(p_x, -p_y, p_z)|^2 = |\mathcal{M}_1(p_x, p_y, p_z)|^2. \quad (4.31)$$

That is, if the pulse has forward-backward symmetry and the initial state is compatible with that symmetry, this symmetry will carry over to the photoelectron momentum distribution which must have extrema in the  $p_x p_z$  plane when traversing the  $p_y$  direction. Condition (4.30) is obviously fulfilled for atomic s states. For atomic p states states co- or counter-rotating with  $m = \pm 1$  it can also be fulfilled, but for molecules it generally cannot (unless the molecule is aligned with a symmetry axis).

## 4.4 Computational details

We now go beyond the SFA and solve the 2D TDSE (2.11) on a Cartesian grid of size  $400 \times 400$  a.u. and 2048 bins in each dimension using the split-operator method with step size 0.01 a.u. up to the final time  $T = 880$  a.u. The photoelectron momentum distribution is obtained by projecting outgoing parts of the wave function onto Volkov states via an absorber that starts at a distance of 150 a.u. from the origin. The vector potential describes a two-cycle circularly polarized laser pulse,

$$\begin{aligned} A_x(t) &= -A_0 \cos(\omega t/4)^4 \cos(\omega t), \\ A_y(t) &= -A_0 \cos(\omega t/4)^4 \sin(\omega t). \end{aligned} \quad (4.32)$$

Here,  $\omega = 0.05695$  a.u. corresponds to 800 nm wavelength. The atomic potential is defined as

$$V(r) = \frac{-1}{\sqrt{r^2 + \alpha}}, \quad (4.33)$$

where  $\alpha = 0.64$  a.u. is chosen to approximately reproduce the ionization potential  $I_p = 0.5$  a.u. of the hydrogen atom. Pulse and ground state clearly satisfy the symmetry conditions (4.22) and (4.30).

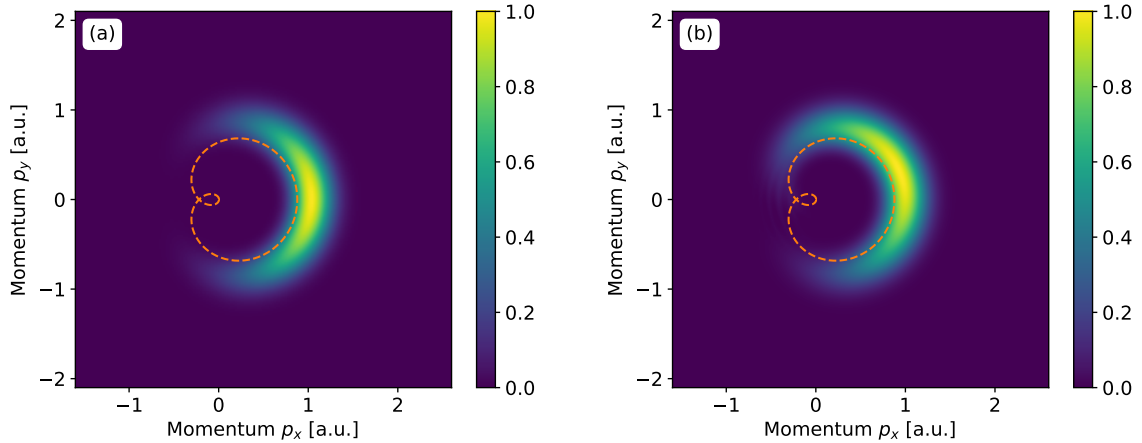


Figure 4.5: 2D Momentum distributions for strong-field ionization of an hydrogen atom in a circularly polarized field at field strength  $E_0 = 0.05$  a.u. ( $1.75 \times 10^{14}$  W/cm<sup>2</sup>). (a) Strong-field approximation. (b) Time-dependent Schrödinger equation. In both panels, the orange dashed line gives the values of the negative vector potential (4.32). Panel (b) is adapted from Fig. 1 in [210].

The momentum distribution for field strength  $E_0 = 0.05$  a.u. is shown in Fig. 4.5. The SFA momentum distribution in panel (a), calculated by numerical evaluation of the KFR integral

(2.23), is clearly symmetric with a maximum on the positive  $p_x$  axis. In the TDSE, this symmetry is broken and the distribution is rotated forward with respect to the handedness of the electric field. While from the previous section it is clear that the quantum-orbit model assigns  $t = 0$  to the maximum of the SFA distribution, our goal is to assign an ionization time to the maximum of the distribution calculated by solving the TDSE. Several mappings have been suggested for this purpose that typically rely on the trajectory picture of strong-field ionization. Here, we employ the trajectory-free definition of ionization time provided by the Dyson representation (4.1).

## 4.5 TDSE in the complex plane

In order to evaluate the saddle-point condition (4.3), we must calculate the Dyson integrand

$$\mathcal{D}(\mathbf{p}, t) = \langle \psi_{\mathbf{p}}^{(-)} | \mathcal{U}(T, t) H_I(t) \mathcal{U}_0(t, 0) | \psi_0 \rangle \quad (4.34)$$

given by (4.2) for complex time  $t$ . To this end, we propagate the state  $H_I(t) \mathcal{U}_0(t, 0) | \psi_0 \rangle$  in complex time along the standard integration path (Fig. 2.3) first down to the real axis and then along the real axis to the final time  $T$  using the split operator method with real or imaginary time step and a complex absorbing potential to determine the momentum amplitude as usual.

For time propagation, we always use the velocity gauge. In order to evaluate the length-gauge form of the Dyson integrand, the interaction operator  $H_I(t) = \mathbf{E}(t) \cdot \mathbf{r}$  is applied at initial time  $t$  and the resulting state is transformed to velocity gauge using (2.13). This makes the computation much more stable compared to propagation in length gauge because it avoids calculating terms that include complex  $\mathbf{E}$  and large  $\mathbf{r}$ . When calculating the initial state  $|\psi_0\rangle$ , the kinetic-energy operator is defined using a five-point finite-difference scheme instead of using the fast Fourier transformation. This is necessary because the noise in the initial state introduced by the FFT would be amplified by the length-gauge interaction. The saddle-point condition is then evaluated using two or three evaluations of the Dyson integrand and a finite-difference scheme in the imaginary time direction (which we find to be more stable compared to a real time step).<sup>7</sup>

This procedure provides the values of the logarithmic derivative (4.3) at all  $\mathbf{p}$  simultaneously. While generally some kind of root finding and several calculations are required to find the saddle-point time  $t_s$  for a given  $\mathbf{p}$ , the saddle-point momentum for a *given* ionization time can be found directly. Since in the attoclock setup we are interested in how the rotation angle of the distribution compares to the time of peak field strength,  $t = 0$ , we evaluate the saddle-point condition at  $\text{Re}(t) = 0$  and various imaginary parts. This is shown in Fig. 4.6 for both length and velocity gauge.

In both cases, for sufficiently large imaginary part  $\text{Im}(t)$  two saddle points (denoted by  $S_1$  and  $S_2$ ) emerge that show a rotation similar to the maximum of the PMD in Fig. 4.5(b). Scanning through the imaginary part systematically, we find the mapping shown in Fig. 4.7.

In (a), it is evident that the imaginary time at which saddle points emerge in length gauge is much smaller compared to velocity gauge which is closer to standard SFA (2.29) that considers only the action. Fig. 4.7(b) compares the rotation angle of time-zero saddle points. They

<sup>7</sup>The Dyson integrand (4.2) in complex time was also considered in [232]. There, propagation was always performed in length gauge where the split-operator FFT scheme does not work. Instead, finite differences were used to discretize the Laplace operator and a Runge-Kutta scheme was used for time propagation.



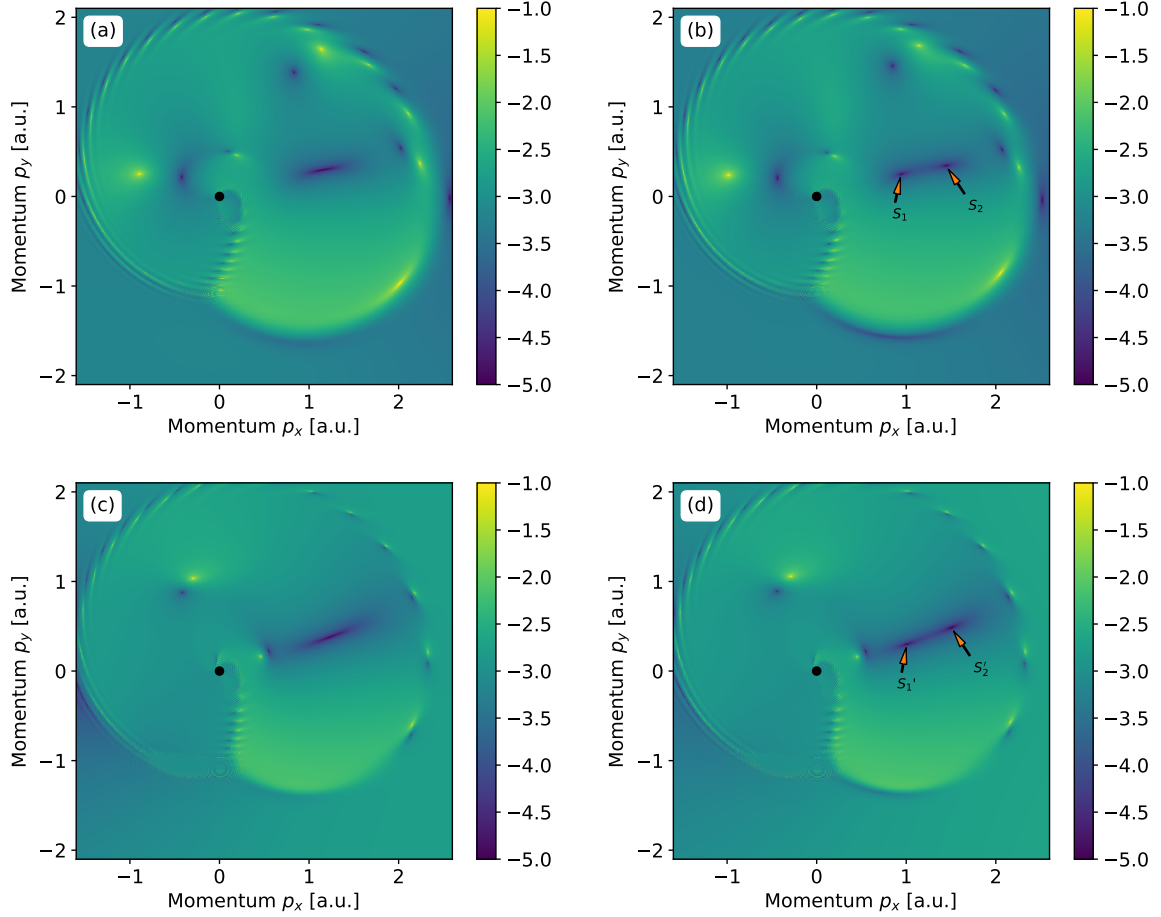


Figure 4.6: Logarithmic derivative (4.3) at field strength  $E_0 = 0.05$  a.u. and  $\text{Re}(t) = 0$  (arbitrary normalization, log-10 scale). (a, b) Length gauge. (a)  $\text{Im}(t) = 8.2$  a.u. (b)  $\text{Im}(t) = 8.8$  a.u. (c, d) Velocity gauge. (c)  $\text{Im}(t) = 15.0$  a.u., (d)  $\text{Im}(t) = 15.4$  a.u. Panels (a) and (b) are adapted from Fig. 1 in [210].

are found to be approximately constant in the vicinity of the bulk of the PMD ( $p \approx 1$  a.u.) but also different in both gauges. This difference is not surprising. While the momentum distribution as an observable quantity must be independent of the choice of gauge, the integrand in the Dyson representation does not have to be gauge independent so the imaginary times and rotation angles of the saddle points do not have to be gauge independent, either. To interpret the stationary points as ionization time, we argue that the length-gauge form should be used. This is because the interpretation of the Dyson integral as field-free evolution, followed by ionization and subsequent propagation to the detector only holds in length gauge [138]. In velocity gauge, the initial state  $U_0(t, 0)|\psi_0\rangle$  appearing in the Dyson integral is not a good approximation of the field-free time-evolved ground state which would carry an additional spatially-dependent phase due to the gauge transformation (2.13).

To investigate whether the ionization is most probable at the peak of the electric field strength, the rotation angle corresponding to time zero must be compared with the rotation angle of the PMD maximum. Measuring this angle accurately is a nontrivial task. This is because the PMD is extremely flat along the angular direction in vicinity of the maximum and a small amount of noise in the PMD already changes its position. Additionally, it must be checked that the angle is converged with respect to the simulation volume that effectively cuts

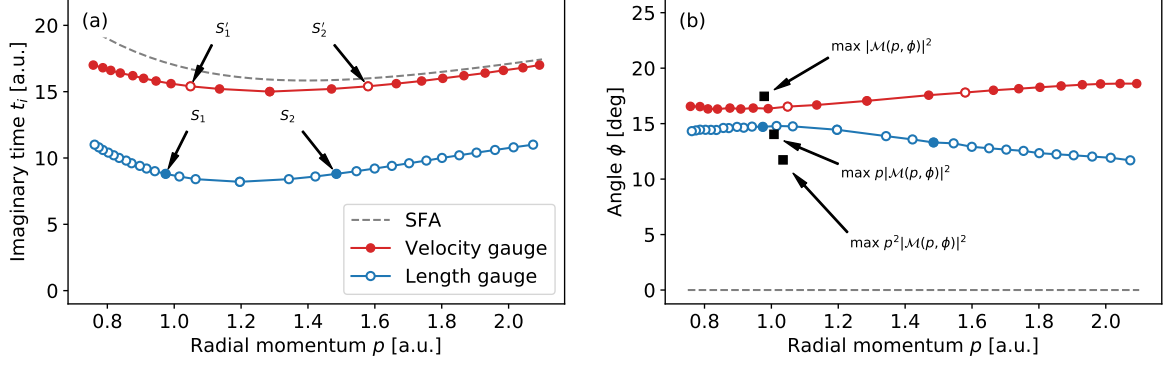


Figure 4.7: Imaginary part (a) and rotation angles (b) of saddle-point time at time zero and  $E_0 = 0.05$  a.u. In both panels, red curves correspond to velocity gauge and blue curves to length gauge. The dashed lines are calculated using standard SFA, Eq. (2.29). The points marked  $S_1$ ,  $S_2$ ,  $S'_1$  and  $S'_2$  correspond to the points at the same imaginary time in Fig. 4.6(b,d). Adapted from Fig. 1 in [210].

Method	Bins	Size [a.u.]	Angle [deg]
Linear fit	2048	400	17.46
Power method	2048	400	17.44
Linear fit	4096	800	17.40
Eikonal	4096	800	17.55

Table 4.2: Maximum angle of the PMD at  $E_0 = 0.05$  a.u. calculated with the methods described in the text.

off the long-range Coulomb potential at a radius of about 150 a.u. and that it is independent of the absorber used to measure the PMD.

In Table 4.2, we compare two methods to find angle  $\phi = \angle(p_x, p_y)$  at which the maximum of the PMD  $|\mathcal{M}(p_x, p_y)|^2$  is found, as well as two different grid sizes. The first two rows show results for the present calculation using the grid parameters as above and an absorbing boundary to measure the PMD (which results in a discretized momentum-space wave function). Here, *linear fit* uses the zero of a linear fit to the (three-point finite difference) gradient of the PMD in the vicinity of the array maximum and is our preferred method. *Power method* is an ad-hoc method based on the expectation value of the probability distribution  $\propto |\mathcal{M}|^{2/\epsilon}$  with  $\epsilon = 0.01$ . (For  $\epsilon = 1$  this would correspond to the mean value and for  $\epsilon \rightarrow 0$  to the array maximum). Both methods give results very close to each other.

The lower two rows show results for a calculation with a larger simulation volume. There, *linear fit* uses absorbing boundaries as above, but with a larger (and softer) absorber that covers a distance of 100 a.u. The good agreement with the above values indicates only a small change due to the use of the absorber and its position. This is confirmed by the *eikonal* method. There, the wave function is propagated only over a time span of 250 a.u. such that it stays confined to the simulation volume. Defining  $|\psi\rangle$  as the final state and  $|\psi_0\rangle$  as the ground state, the contribution of the latter is removed via

$$|\tilde{\psi}\rangle = (\mathbb{I} - |\psi_0\rangle\langle\psi_0|) |\psi\rangle. \quad (4.35)$$

Afterwards, a region around the origin is removed using a mask function

$$f(\mathbf{r}) = \frac{1}{1 + e^{-(\mathbf{r}-\mathbf{r}_0)/\Delta\mathbf{r}}} \quad (4.36)$$

Prescription	Angle [deg]	Difference [deg]	Time difference [as]
Differential, prefactor 1	17.46	3.42	25.38
Differential, prefactor p	14.04	0.00	0.00
Differential, prefactor p <sup>2</sup>	11.73	-2.30	-17.08
Integrated	13.77	-0.27	-1.96
Differential, envelope corrected	14.85	0.81	6.03
Integrated, envelope corrected	13.98	-0.05	-0.40

Table 4.3: Rotation angle of the PMD at  $E_0 = 0.05$  a.u. according to different prescriptions. “Differential” denotes the angle of the PMD maximum. “Integrated” denotes the maximum of the radially integrated distribution (4.38). The third column gives the difference of the observed angle with respect to the cylindrical one and the fourth column the resulting time delay as above. The envelope correction is explained in the next section.

with  $r_0 = 40$  a.u. and  $\Delta r = 5$  a.u. The remaining part of the final state is projected onto eikonal states, Eq (2.36) with  $\mathbf{A} = 0$  evaluated using (A.53), leading to

$$\mathcal{M}(\mathbf{p}) \approx \frac{1}{(2\pi)^{3/2}} \int d^3r e^{-i\mathbf{p}\cdot\mathbf{r}} e^{-i/p \log(r\cdot\mathbf{p}+r\mathbf{p})} f(\mathbf{r}) \tilde{\psi}(\mathbf{r}). \quad (4.37)$$

Here, the integral is evaluated using Romberg integration [239]. Using eikonal states does not require an absorber and incorporates the force on the outgoing photoelectron due to the Coulomb potential perturbatively, but does so up to  $r \rightarrow \infty$ .

In addition to the practical question of measuring the rotation angle of the PMD, we find that there is a more fundamental ambiguity in defining that angle. The angle at which the Cartesian distribution  $|\mathcal{M}(p, \phi)|^2$  (probability per  $dp_x dp_y$ ) peaks is different from the angle at which the distribution  $p|\mathcal{M}(p, \phi)|^2$  in cylindrical coordinates (probability per angle element  $d\phi$  per radial-momentum element  $dp$ ) peaks.<sup>8</sup> This dependence is quite significant. Between the Cartesian and the cylindrical maximum, the difference is  $\Delta\phi = 3.42^\circ$  which corresponds to a time difference of  $\Delta\phi/\omega = 25.4$  as. Different prescriptions have been used throughout the literature. In the recent 3D study using ARM theory [78] the volume element  $p^2$  in spherical coordinates was included whereas many experiments use the integrated distribution, in 2D given by

$$w(\phi) = \int_0^\infty dp p |\mathcal{M}(p, \phi)|^2, \quad (4.38)$$

i.e. the angular distribution. We find the maximum from this prescription to be very close to the maximum of the cylindrical distribution. The angles  $\phi$ , their differences  $\Delta\phi$  and the time differences  $\Delta t = \Delta\phi/\omega$  implied by them are printed in Table 4.3.

## 4.6 Geometrical factors and origin of the angle ambiguity

In order to understand this ambiguity, we consider a function

$$F(\mathbf{p}, \alpha) = |\mathcal{M}(\mathbf{p})|^2 (1 + \alpha(G(\mathbf{p}) - 1)) \quad (4.39)$$

where  $\alpha$  allows us to scale the pure Cartesian momentum distribution ( $\alpha = 0$ ) to one multiplied with some modifier  $G(\mathbf{p})$  at  $\alpha = 1$  (which is later chosen to be the radial factor  $p$ ).

<sup>8</sup>This was also noted in the appendix of [240] but its implications for the attoclock were not addressed. Energy-dependent angular offsets were also found for long pulses in elliptical polarization in [241].

Let the Cartesian PMD have a maximum at  $\mathbf{p}_0$ . To observe how the position of the maximum changes with  $\alpha$ , we have to solve

$$\frac{\partial}{\partial \mathbf{p}_j} F(\mathbf{p}, \alpha) = 0. \quad (4.40)$$

Writing  $\mathbf{p} = \mathbf{p}_0 + \Delta\mathbf{p}$  and expanding to first order in  $\alpha$  and  $\Delta\mathbf{p}$ , we find

$$\sum_i \left. \frac{\partial^2 F}{\partial \mathbf{p}_j \partial \mathbf{p}_i} \right|_{\mathbf{p}_0} \Delta \mathbf{p}_i + \left. \frac{\partial^2 F}{\partial \mathbf{p}_j \partial \alpha} \right|_{\mathbf{p}_0} \alpha = 0. \quad (4.41)$$

For  $\alpha \rightarrow 1$ , this evaluates to

$$\frac{1}{|\mathcal{M}|^2} \text{Hess}|\mathcal{M}|^2 \Delta\mathbf{p} + \nabla G = 0. \quad (4.42)$$

That is, if the gradient of the modifier  $G$  is parallel to one of the principal axes of the Hessian of  $|\mathcal{M}|^2$  at the maximum, the maximum can only be shifted in this direction. For a radial function  $G(\mathbf{p}) = p$ , this would be the case for a true rotation of the momentum distribution where (starting from the Coulomb-free momentum distribution where one of the principal axes points in the radial direction) the maximum is rotated around the origin and the principal axes of the quadratic approximation in the vicinity of the maximum are rotated by that same angle. In the attoclock, however, we find that this is not the case. The distribution is “over rotated” in the sense that the internal rotation is larger compared to the external rotation (see Fig. 4.8). Since the PMD is extremely flat as a function of angle in the vicinity of the maximum, a small

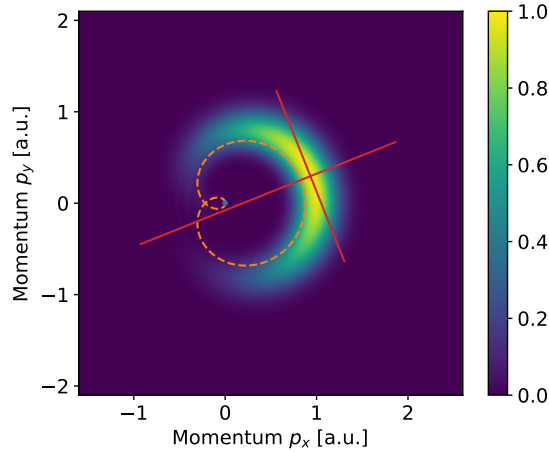


Figure 4.8: Momentum distribution as in Fig. 4.5(b). The red lines mark the principal axes of quadratic expansion of the PMD in the vicinity of the (Cartesian) maximum.

mismatch can induce a large angular shift.

To decide which prescription to use, we consider a classical description of the ionization process where the momentum distribution can be written as [152]

$$|\mathcal{M}(\mathbf{p})|^2 = \int dt \int d\mathbf{v} W(t, \mathbf{v}) \delta(\mathbf{p} - \mathbf{D}(t, \mathbf{v})). \quad (4.43)$$

Here,  $W(t, \mathbf{v})$  is the instantaneous ionization probability per unit time and velocity (for example the PPT rate (2.44)) and the deflection function  $\mathbf{D}(t, \mathbf{v})$  maps the initial conditions to the

final momentum. Assuming a single relevant contribution for every final momentum, we can resolve the  $\delta$ -function to get

$$|\mathcal{M}(\mathbf{p} = \mathbf{D}(t, \nu))|^2 = \frac{W(t, \nu)}{|\det \mathbf{D}'(t, \nu)|}. \quad (4.44)$$

If the most probable ionization time (the maximum of the instantaneous ionization rate) is to be inferred from the maximum of the attoclock PMD, it is evident that the Jacobian must be taken into account, too. In the simple man's model,

$$\mathbf{D}(t, \nu) = -\mathbf{A}(t) + \nu \mathbf{E}_\perp(t)/E(t), \quad (4.45)$$

so the Jacobian can be calculated explicitly and is given by

$$|\det \mathbf{D}'(t, \nu)| = \left| E(t) + \nu \frac{\mathbf{E}(t) \cdot \dot{\mathbf{E}}_\perp(t)}{E(t)^2} \right| = E(t) |1 + \nu k(t)|. \quad (4.46)$$

Here,

$$k(t) = \frac{\dot{\mathbf{A}}(t) \cdot \ddot{\mathbf{A}}_\perp(t)}{|\dot{\mathbf{A}}(t)|^3} \quad (4.47)$$

is identified as the curvature of the vector potential. In circular polarization, there is constant curvature  $|k(t)| = \omega/E_0$ , so the Jacobian is also time independent and we find  $|\det \mathbf{D}'| = \omega p$  (where in 3D the momentum  $\mathbf{p}$  would have to be replaced by the momentum component in the polarization plane). The Jacobian can also be motivated from SFA. Evaluating the saddle-point equation (2.29) for a cw field

$$\begin{aligned} A_x(t) &= -A_0 \cos(\omega t) \\ A_y(t) &= -A_0 \sin(\omega t) \end{aligned} \quad (4.48)$$

in the plane of polarization by writing the saddle-point time as  $t_s = t_r + i t_i$  and separating real and imaginary part, one finds

$$\omega t_r = \angle(p_x, p_y), \quad \cosh(\omega t_i) = \frac{2I_p + p^2 + A_0^2}{2A_0 p}. \quad (4.49)$$

At the saddle point, the second derivative of the action becomes

$$\ddot{S}(\mathbf{p}, t_s) = (\mathbf{p} + \mathbf{A}(t_s)) \cdot \mathbf{E}(t_s) = -i A_0 \omega p \sinh(\omega t_i). \quad (4.50)$$

The bulk of the momentum distribution is located close to the momentum  $p_{\min}$  corresponding to the minimal imaginary part  $t_i$  of the saddle-point  $t_s$ . There,

$$\left. \frac{\partial}{\partial p} \left( \frac{2I_p + p^2 + A_0^2}{2A_0 p} \right) \right|_{p=p_{\min}} = 0 \quad (4.51)$$

which implies

$$p_{\min} = \sqrt{A_0^2 + 2I_p}, \quad \cosh(\omega t_i) = \frac{\sqrt{A_0^2 + 2I_p}}{A_0}, \quad \sinh(\omega t_i) = \frac{\sqrt{2I_p}}{A_0}. \quad (4.52)$$

Inserting this into (4.50), we find

$$\ddot{S}(\mathbf{p}, t_s(\mathbf{p})) = -i \sqrt{2I_p} \omega p + \mathcal{O}((p - p_{\min})^2). \quad (4.53)$$

This implies that the SFA prefactor

$$\sqrt{\frac{-2\pi i}{\dot{S}(\mathbf{p}, t_s)}} \quad (4.54)$$

from the signal in saddle-point approximation (2.30) contains – when it is squared to determine the PMD – the inverse of the classical Jacobian  $\omega p$ .

Both the classical argument as well as the SFA motivate us to use the cylindrical factor  $p$  when determining the maximum of the PMD, as we will do in the following. This procedure is expected to provide the momentum corresponding to the maximum of the instantaneous rate  $W$ . The most accurate prescription would also take the ultrashort pulse envelope into account. Using the actual shape of the vector potential (4.32) including the envelope to calculate the Jacobian (4.46), the maximum is fairly close to the cylindrical one (see the envelope-corrected values in Table 4.3). Good agreement with the cylindrical maximum is also obtained when integrating along lines that are perpendicular to tangent of the instantaneous vector potential instead of integrating in the radial direction.<sup>9</sup>

## 4.7 Intensity scan

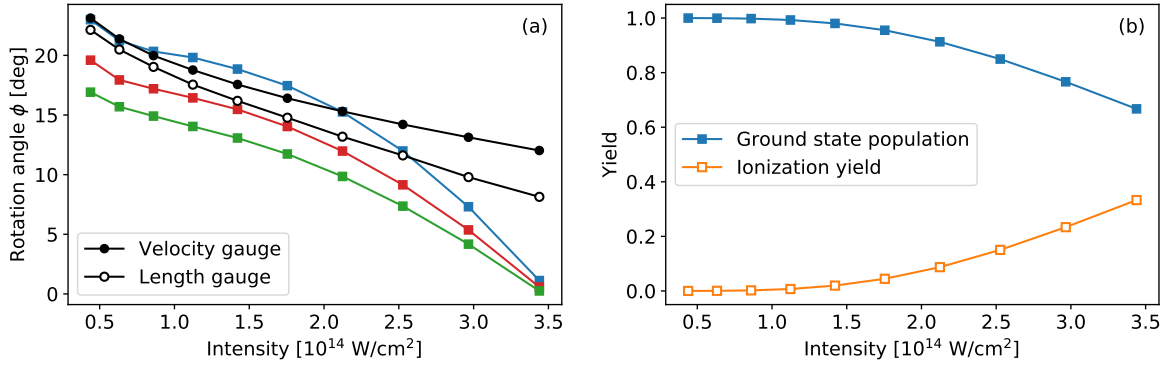


Figure 4.9: (a) Rotation angles of the PMD for various intensities including prefactors 1 (upper blue curve),  $p$  (middle red curve), and  $p^2$  (lower green curve). The angles are compared with rotation angles of time-zero saddle points in velocity gauge (upper black curve) and length gauge (lower black curve). (b) Ground-state population after the end of the pulse and ionization yield. Adapted from Fig. 2 in [210].

Repeating the steps above for various intensities, we find the attoclock angles shown in Fig. 4.9(a). For the angles corresponding to time zero, we have used the fact that the rotation angle of the saddle points at time zero is approximately constant in the region where the momentum distribution is actually concentrated, see Fig. 4.7(b). Therefore, we can assign a single angle that we define for simplicity as the rotation angle of time zero at the radius that corresponds to the maximum of the PMD in cylindrical coordinates.

For low to intermediate intensities, the rotations angles of the PMD are in good agreement with the rotation angles corresponding to time zero. This indicates that the PMD maximum is due to ionization very close to the time of peak field strength. At higher intensities, the rotation

<sup>9</sup>A similar method was used to investigate the longitudinal momentum spread in elliptically polarized laser fields. There, elliptical coordinates were introduced and the PMD was integrated along lines of constant generalized radius [242].

angles are shifted to smaller values because the instantaneous ionization rate maximizes at earlier times due to depletion of the bound state, see also Fig. 4.9(b).<sup>10</sup>

Instead of comparing the angles, we can find the ionization times corresponding to the maxima of the PMD directly. Here, we choose the maxima in cylindrical coordinates and evaluate the integrand in length gauge according to the arguments given above. At fixed momentum  $\mathbf{p}$ , the saddle-point equations (4.3) can be solved for  $t_s$  using Newton's method for a single (complex) variable. Here, we must consider that the exponentials that are required to perform time propagation are precalculated with a given time step  $\Delta t = 0.01$  a.u., leading to a discrete grid of accessible complex times. The Newton iteration leads to times incommensurate with that grid. This could be fixed by changing the time step during the calculation. This requires reevaluating the exponentials, which is computationally expensive. Instead, after each step in the Newton iteration, we continue from the nearest grid point. The iteration stops when the same point is reached twice and the final result is obtained by the last estimate. (The accuracy of this estimate is still much better than the grid spacing). As starting value, we use the imaginary time  $t_i$  at which a saddle point emerges at time zero and estimate the real time using the difference  $\Delta\phi$  between the red curve and the length-gauge curve in Fig. 4.9(a) as  $t_r \approx \Delta\phi/\omega$ . Using these values, convergence can usually be reached in at most three steps.

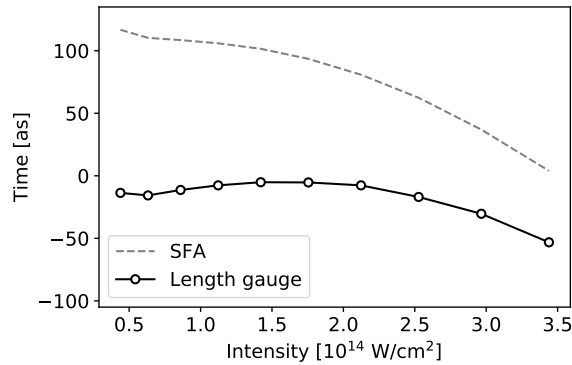


Figure 4.10: Ionization times corresponding to the maxima of the PMD in cylindrical coordinates obtained by finding the stationary points of the Dyson integrand (4.2) in length gauge (black curve) and by solving the SFA saddle-point equation (2.29). Adapted from Fig. 2 in [210].

The result is shown in Fig. 4.10. Compared to the ionization time that the SFA saddle-point equation would assign to the maxima (dashed line in the figure), the ionization times from the Dyson integral are much closer to zero and never positive.<sup>11</sup>

<sup>10</sup>This was also observed in the 3D calculation [78] which we reproduce in Appendix A.1.3. In 3D, however, depletion is less significant compared to 2D. This is because in 3D parabolic coordinates – in which the static tunneling problem can be solved – only a fraction of the full nuclear charge remains in the tunneling coordinate, leading to a larger barrier to tunnel through. A 1D potential that has a weak-field static ionization rate like 3D hydrogen must have (asymptotic) nuclear charge  $Z = 1/2$ . A 2D potential with equivalent static rate requires  $Z = 3/4$ . See Appendix A.5.

<sup>11</sup>Here, a single time of ionization is assigned to a final momentum. Since no trajectory is involved, the observable does not allow us to make a statement about the propagation through the tunneling barrier or the “tunnel exit.” This is different in ARM where the trajectories can be used to derive initial conditions for classical motion [243].

## 4.8 Conclusion

The ability to interpret photoelectron momentum distributions in strong-field ionization in a time-resolved way typically relies on electron trajectories such as classical trajectories, Bohmian trajectories, or quantum orbits. Using the stationary points of the Dyson integral representation of the time-dependent Schrödinger equation, momentum-resolved ionization times can be defined without relying on the concept of an electron trajectory. Although conceptually similar to the stationary points that appear in the quantum-orbit model, they are not equivalent even when the strong-field approximation is applied to the Dyson integral. This is because the stationary points of the full integrand also include the transition matrix element whereas the quantum-orbit model only considers the exponential of the action. Indeed, the relevant saddle point is typically found in imaginary time between the real axis and the “standard” SFA saddle point that is close to the Keldysh time. The relevant saddle point is accompanied by a second irrelevant one closer to the real axis. We derived expressions that provide the positions of the two points in the adiabatic weak-field limit. For large field strengths, the two saddle points merge after which they both become relevant. Using the adiabatic model, we estimated the critical field strength for the merger. Applying the saddle-point approximation to the upper saddle point or the uniform approximation to both saddle points, we found that photoelectron spectra can be calculated accurately.

When the potential after the interaction time in the Dyson integral is taken into account, the saddle points must be determined numerically. Evaluating the stationary-point condition for the attoclock by solving the time-dependent Schrödinger equation in complex time, we obtained the ionization time that corresponds to the maximum of the momentum distribution. Here, two ambiguities must be taken into account. First, the observed attoclock offset angle depends on which volume element is used. Second, the retrieved ionization time depends on the choice of gauge. Arguing that the volume element in cylindrical coordinates should be used and that the Dyson integrand should be evaluated in length gauge, we found that the most probable ionization time is close to the time of peak field strength, supporting previous results that obtained zero ionization time delay [78, 102].

We circumvent the ambiguity in the angle in the next chapter when introducing an attoclock using bicircular fields. There, the Jacobian is constant in the vicinity of the maximum and the initial conditions of the ionization step are directly mapped to the final momentum. We will also apply the trajectory-free retrieval method and evaluate parts of the TDSE momentum distribution in saddle-point approximation. In the future, it would be interesting to apply the definition and retrieval procedure to other field shapes, such as linear polarization where it could be possible to retrieve ionization times of rescattered electrons. The definition could also be generalized to harmonics to find ionization times resolved by harmonic order instead of photoelectron momentum, or to frustrated tunnel ionization [244] to resolve the ionization time of electrons that end up populating Rydberg states.



## Chapter 5

# Attoclock with bicircular fields

Ionization time in linear polarization can be measured with streaking schemes while in circular polarization the attoclock is typically employed. Both techniques provide a certain notion of ionization time that cannot be compared directly because the results are obtained for different field shapes. In this chapter, we demonstrate that the concept of the attoclock can be transferred to the linear regime using counter-rotating bicircular laser fields. Some results of this chapter are published in [245].

### 5.1 Introduction

While the attoclock allows us to measure the time of ionization, it can more generally be seen as a tool to study strong-field ionization in an interference-free and recollision-free environment. The attoclock was used to estimate the importance of multi-electron effects in the ionization step [77, 78, 80], and to investigate the lateral [246, 247], the transverse [248], and the longitudinal [242, 249–252] momentum spread in tunnel ionization. Obtaining an accurate picture of the ionization step is important because it is the first step in the three-step process that leads to rescattering, harmonic generation and non-sequential double ionization. In particular, semi-classical models of strong-field ionization rely on its accurate description [95, 151]. In the adiabatic regime of small Keldysh parameter  $\gamma \ll 1$ , the ionization process becomes quasistatic and independent of the field shape. For the Coulomb potential, or generally in the weak-field limit, the Schrödinger equation can then be separated in parabolic coordinates which leads to the TIPIS model of initial conditions for trajectory-based models [77, 149] or the weak-field asymptotic theory of static ionization rates [253, 254]. For arbitrary field strength, the ionizing system can be described by Siegert states, which are eigenstates of the nonhermitian Hamiltonian describing the atom in a constant electric field with outgoing boundary conditions [255–257]. The real part of the complex-energy eigenvalue  $\varepsilon = \varepsilon_r - i\Gamma/2$  of the Siegert state describes the Stark-shifted energy of the bound state  $\varepsilon_r$  while the imaginary part gives the static ionization rate  $\Gamma$ .

The independence of the ionization step on the field shape in the adiabatic regime implies that the use of circularly polarized fields, which are inherent to the attoclock, is not a limitation. In the nonadiabatic regime, however, significant differences between circular and linear polarization occur already during the ionization step. In linear polarization, the quantum-orbit model predicts a symmetric distribution of the initial velocity of the electron perpendicular and

a nonzero velocity parallel to the instantaneous field direction (See Appendix A.2). The parallel velocity is responsible for the fact that quantum mechanically the  $2U_p$  cutoff is avoided [137]. Soft recollisions under the barrier lead to further enhancement of the signal in the classically forbidden region [258]. On the contrary, in circular polarization the quantum-orbit model predicts zero parallel velocity but an asymmetric distribution of initial perpendicular velocity. This can be viewed as nonadiabatic energy absorption under the tunneling barrier [127, 128] and it can be observed in the PMD as the mean photoelectron energy being higher than the ponderomotive energy [259]. In addition, there is a nonadiabatic asymmetry in ionization rates between co- and counter-rotating orbitals [260, 261].

Ionization time as well as properties of the electron trajectories in linear polarization can be probed using streaking techniques (see Chapter 3 and references therein). However, the part of the PMD that is due to ionization times close to peak field strength is centered around zero momentum and strongly influenced by Coulomb effects [123, 124, 262] while contributions from different ionization times lead to intracycle interference [40, 41]. This makes it hard to observe the tunneling-step directly, e.g. to answer the question whether the time of peak field strength corresponds to most probable ionization time in linear polarization.

In this chapter, we show how the ionization step in approximately linear polarization can be probed with an attoclock technique that employs counter-rotating bicircular fields. First devised by Eichmann et al. [116], bicircular fields consisting of a fundamental infrared field and its second harmonic have become an important tool in strong-field physics. At suitable field-strength ratio of the two colors, the electron can revisit the parent ion which leads to the observation of rescattering [263–268], non-sequential double ionization [269–271], and high-harmonic generation [120, 121]. High-order above-threshold ionization in the bicircular field allows for the retrieval of scattering cross sections in a larger angular range compared to linear polarization [272]. For HHG, conservation of angular momentum dictates that harmonics of order  $3n \pm 1$  are generated which are circularly polarized with helicity  $\pm 1$ . In the time domain, an approximately linearly polarized attosecond pulse emerges during each third of a cycle of the driving field [116].

In contrast to these recollision-based phenomena that require an approximately equal field strength of both circularly polarized colors, we consider the special case of the bicircular field where the field strength ratio of fundamental to second harmonic is exactly 2 : 1. We title the resulting field shape a “quasilinear field” because at this ratio, the bicircular electric field approximates linear polarization near its peaks three times per optical cycle. At the same time, the shape of the vector potential has the attoclock property that time is mapped directly onto the momentum distribution. The relevant quantity, however, is not an offset angle as in the conventional attoclock, but a shift in the direction perpendicular to its maximum. We obtain PMDs for a model helium atom by solving the time-dependent Schrödinger equation and we investigate the attoclock shift with respect to the attosecond time structure of the ionization process.

The chapter is organized as follows. In Section 5.2, we consider the case of equal field-strength ratio to make a connection to the case that is mostly considered in the literature. Then we move to a ratio of 2 : 1. After explaining the main idea behind the quasilinear field and providing the computational details in Section 5.3, first results and the calibration of the clock are provided. In Section 5.4, we use the trajectory-free method developed in Chapter 4 to investigate the attoclock shift and compare our results with circular polarization. To interpret

the results, we evaluate parts of the PMD by applying the saddle-point approximation to the Dyson integral in Section 5.5. In the following sections, we apply established methods to the bicircular attoclock that have previously been used to interpret momentum distributions in the conventional attoclock such as classical backpropagation (Section 5.6), analytical R-matrix theory (Section 5.7), and a related method based on applying the Eikonal approximation to the Dyson integral (Section 5.8). Section 5.9 concludes the chapter.

## 5.2 Strong-field ionization in bicircular laser fields

The vector potential of the bicircular field can be written as

$$\mathbf{A}(t) = -\frac{E_0/\omega}{\sqrt{1+\epsilon^2}} \left[ \begin{pmatrix} \cos(\omega t) \\ \sin(\omega t) \end{pmatrix} + \frac{\epsilon}{2} \begin{pmatrix} \pm \cos(2\omega t) \\ \sin(2\omega t) \end{pmatrix} \right], \quad (5.1)$$

where a positive sign describes a co-rotating bicircular field and a negative sign a counter-rotating one. The derived electric field  $\mathbf{E}(t) = -\dot{\mathbf{A}}(t)$  is given by

$$\mathbf{E}(t) = \frac{E_0}{\sqrt{1+\epsilon^2}} \left[ \begin{pmatrix} -\sin(\omega t) \\ \cos(\omega t) \end{pmatrix} + \epsilon \begin{pmatrix} \mp \sin(2\omega t) \\ \cos(2\omega t) \end{pmatrix} \right], \quad (5.2)$$

so the parameter  $\epsilon$  gives the field-strength ratio between fundamental and second harmonic. When calculating the time-averaged intensity  $I = c\epsilon_0/T \int_0^T dt \mathbf{E}(t)^2$  the mixed terms average out such that the intensity is the sum of the intensities of the two fields. The prefactor is defined such that the intensity becomes independent of the field-strength ratio, i.e.  $I = c\epsilon_0 E_0^2$ .

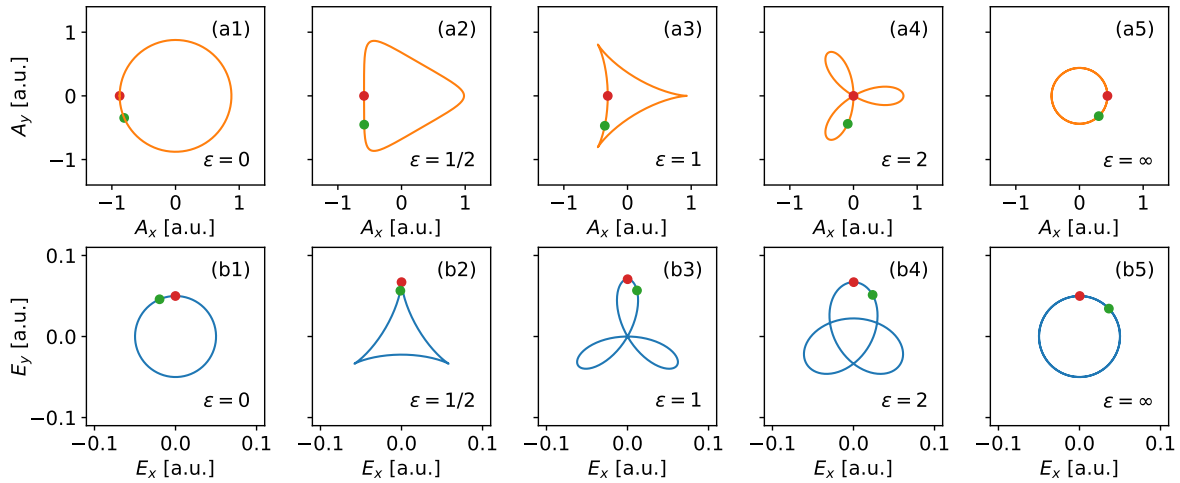


Figure 5.1: Counter-rotating bicircular fields for various field-strength ratios at 800 nm wavelength and  $E_0 = 0.05$  a.u. (intensity  $1.75 \times 10^{14}$  W/cm<sup>2</sup>). (a) Vector potential. (b) Electric field. (1) Only fundamental field. (2) Ratio 2 : 1 of fundamental to second harmonic. (3) Equal field strength. (4) Ratio 1 : 2 of fundamental to second harmonic. (5) Only second harmonic field. The red dot marks  $t = 0$ , the green dot  $t = 172$  as.

The field shape and the vector potential for various ratios of fundamental to second harmonic are shown in Fig. 5.1. For  $\epsilon \rightarrow 0$ , a circularly polarized field of frequency  $\omega$  is retrieved and for  $\epsilon \rightarrow \infty$  a circularly polarized field of frequency  $2\omega$ . In most applications, the field-strength ratio is chosen close to one (Fig. 5.1(3)) because then the recollision-based phenomena can occur.

We solve the 3D TDSE for precisely this case on a Cartesian grid of size  $300 \times 300 \times 300$  a.u. and 1024 points in each dimension with time step  $\Delta t = 0.02$  a.u. and a propagation time of 2000 a.u. The electric field (5.2) with  $\epsilon = 1$ ,  $\omega = 0.05695$  a.u. and  $E_0 = 0.05$  a.u. is multiplied with a trapezoidal envelope of two ascending, six constant and two descending cycles. We consider both the Coulomb potential  $V(r) = -1/r$  as well as a short-range potential  $V(r) = -\alpha/r e^{-r/r_0}$  with  $\alpha \approx 1.908$  and  $r_0 = 1$  a.u. (similar to [78]) that reproduces the correct  $I_p$  of the hydrogen atom. To avoid the singularity, both potentials are converted to pseudopotentials at a radius of 1 a.u. according to the procedure described in Appendix A.1.3. The PMD is measured by projecting outgoing parts of the wave function onto Volkov states via an absorber that covers a distance of 50 a.u. to the boundary of the simulation volume.

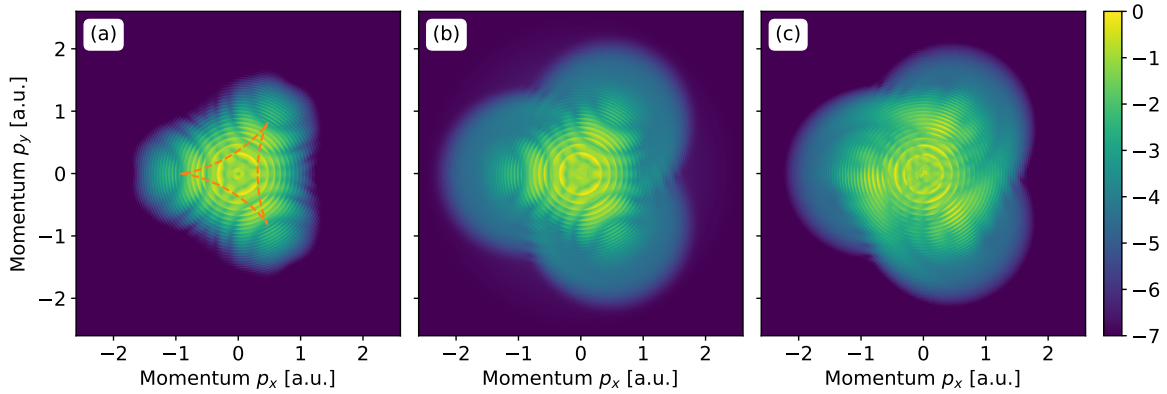


Figure 5.2: Projection of the 3D photoelectron momentum distribution (log-10 scale) for strong-field ionization of atomic hydrogen in a counter-rotating bicircular laser field. (a) KFR amplitude according to (2.23) with matrix element (4.7) at  $\nu = 0$  (short-range potential). (b) TDSE for a short-range potential. (c) TDSE for a long-range potential. All distributions are normalized separately to maximum signal 1.

Results are shown in Fig. 5.2. Already in standard SFA in panel (a), the PMD exhibits strong intracycle interference. Going from the SFA to the TDSE for a short range potential in (b), the direct signal from panel (a) is accompanied by a significant amount of rescattering.<sup>1</sup> In the TDSE for the hydrogen atom in panel (c), there is additional distortion due to the long-range potential.

For high-order ATI and HHG, the bicircular field is often viewed as being made of three overlapping sections of approximately linear polarization in one cycle, each producing one rescattering sphere in the PMD as well as one approximately linearly polarized attosecond pulse. For the maxima of the PMD due to direct electrons, however, this picture does not hold. This is because at the time of peak field strength the tunneling barrier is rotating. In linear polarization, the orientation of the barrier would be constant during each half cycle because the direction in which the field points does not change.

### 5.3 The quasilinear field

A field shape where the electric-field direction remains approximately constant can be created as follows. We consider a bicircular field of field-strength ratio 2 : 1 of fundamental to second

<sup>1</sup>See [264, 265] for a detailed analysis of rescattering in bicircular fields using a saddle-point analysis of the improved SFA.

harmonic (Fig. 5.1(2)), described by the vector potential

$$\mathbf{A}(t) = -\frac{2}{\sqrt{5}} \frac{E_0}{\omega} \left[ \begin{pmatrix} \cos(\omega t) \\ \sin(\omega t) \end{pmatrix} + \frac{1}{4} \begin{pmatrix} -\cos(2\omega t) \\ \sin(2\omega t) \end{pmatrix} \right]. \quad (5.3)$$

At this ratio, the electric field  $\mathbf{E}(t) = -\dot{\mathbf{A}}(t)$  exhibits three sharp peaks per optical cycle of the fundamental field. In the vicinity of the peaks, the field is approximately linearly polarized. Indeed, expanding at  $t = 0$  we find

$$\mathbf{E}(t) = \frac{3E_0}{\sqrt{5}} \left[ \begin{pmatrix} 0 \\ 1 - \frac{1}{2}(\sqrt{2}\omega)^2 t^2 \end{pmatrix} \right] + \mathcal{O}(t^3) \quad (5.4)$$

which corresponds to linear polarization with effective field strength

$$E_{\text{peak}} = \frac{3E_0}{\sqrt{5}} \quad (5.5)$$

and effective frequency

$$\omega_{\text{eff}} = \sqrt{2}\omega \quad (5.6)$$

Here, we choose  $\omega_{\text{eff}} = 0.05695$  a.u. such that the effective frequency corresponds to 800 nm. This means that the true wavelength of the fundamental field is with approximately 1131 nm somewhat larger. We then consider strong-field ionization from the ground state of the soft-core potential

$$V(\mathbf{r}) = \frac{-1}{\sqrt{\mathbf{r}^2 + \alpha}}, \quad (5.7)$$

where in two dimensions  $\alpha \approx 0.0684$  a.u. approximately reproduces the ionization potential  $I_p \approx 0.904$  a.u. of the helium atom.

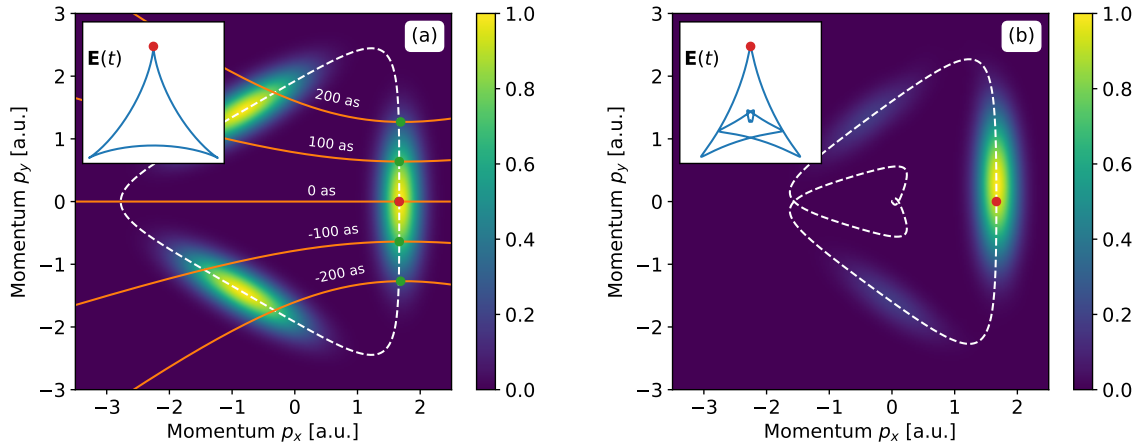


Figure 5.3: 2D Momentum distributions for strong-field ionization of a helium atom in a bicircular field of field-strength ratio 2 : 1 at 1131 nm and field strength  $E_0 = 0.10$  (intensity  $7 \times 10^{14}$  W/cm<sup>2</sup>). (a) Strong-field approximation for a cw field. (b) Time-dependent Schrödinger equation for a short pulse. Adapted from Fig. 1 in [245].

A momentum distribution calculated by numerical integration of the KFR amplitude (2.23) for the field strength  $E_0 = 0.10$  a.u. is shown in Fig. 5.3(a) together with the negative vector potential  $-\mathbf{A}(t)$  and the electric field  $\mathbf{E}(t)$  in the inset. In contrast to the PMD calculated for equal field strengths (Fig. 5.2), there is no intracycle interference in this case. Instead, the

branches are well separated because the vector potential is much larger at the time of peak field strength. Both the lower frequency of the fundamental field ( $\omega \rightarrow \omega/\sqrt{2}$ ) as well as the optimized field strength ratio (1 : 1  $\rightarrow$  2 : 1) help to achieve this. Additionally, considering helium instead of hydrogen allows us to go to larger field strengths.

With the maxima due to direct electrons clearly visible, our aim is to interpret the PMD as an attoclock. For this purpose, the flow of time through the PMD must be determined. In SFA, it is given by the saddle-point equation (2.29). This equation is usually solved for the ionization time  $t_s = t_r + i t_i$  given a momentum  $\mathbf{p}$ . Here, it is useful to consider the inverse<sup>2</sup>

$$\mathbf{p} = -\text{Re}\mathbf{A}(t_s) \pm \text{Im}\mathbf{A}_\perp(t_s) \sqrt{1 - \frac{2I_p}{(\text{Im}\mathbf{A}(t_s))^2}}. \quad (5.8)$$

Here,  $\text{Im}\mathbf{A}_\perp$  is perpendicular to  $\text{Im}\mathbf{A}$  and has the same length. Inserting a fixed value of  $t_r$  we find all momenta that correspond to this given ionization time. The equation gives two branches of solutions which are joined when the square root vanishes at minimal imaginary part  $t_i$  of the ionization time. A few of these lines are also shown in Fig. 5.3(a). Note that because of the forward-backward symmetry of the vector potential, the flow of time must be an even function of time so it is constant to first order in the vicinity of either one of the peaks. We can obtain an expression for this speed of the clock by evaluating (5.8) at  $t_r = 0$  and minimal imaginary part  $t_i$  such that the square root vanishes. The expression then gives

$$\frac{dp_y}{dt_r} = \frac{2E_0}{\sqrt{5}} \left( \cosh(\omega t_i) + \frac{1}{2} \cosh(2\omega t_i) \right) \approx E_{\text{peak}} \cosh(\omega_{\text{eff}} t_i). \quad (5.9)$$

The condition of vanishing square root, on the other hand, reads

$$\sqrt{2I_p} = \frac{2E_0}{\sqrt{5}\omega} \left( \sinh(\omega t_i) + \frac{1}{4} \sinh(2\omega t_i) \right) \approx \frac{E_{\text{peak}}}{\omega_{\text{eff}}} \sinh(\omega_{\text{eff}} t_i). \quad (5.10)$$

Combining these two results, we find

$$\frac{dp_y}{dt_r} \approx E_{\text{peak}} \sqrt{1 + \gamma_{\text{eff}}^2}, \quad \gamma_{\text{eff}} = \frac{\sqrt{2I_p} \omega_{\text{eff}}}{E_{\text{peak}}}. \quad (5.11)$$

Here,  $\gamma_{\text{eff}}$  is the effective Keldysh parameter of the corresponding linearly polarized field. Finally, the absolute value of the momentum is  $p_x^{\text{max}} \approx E_{\text{peak}}/(2\omega)$ , so we obtain for the relative shift in  $p_y$  direction approximately

$$\frac{1}{p_x^{\text{max}}} \frac{dp_y}{dt_r} \approx 2\omega \sqrt{1 + \gamma_{\text{eff}}^2}. \quad (5.12)$$

This can be compared with the conventional attoclock in circular polarization where the flow of time through the momentum distribution is independent of the Keldysh parameter and given simply by  $d\phi/dt = \omega$ , where  $\phi = \angle(p_x, p_y)$ . The factor involving the Keldysh parameter in the bicircular field is due to non-adiabatic initial velocities parallel to the instantaneous field direction which SFA predicts for linear, but not for circular polarization [273]. The additional factor of two is due to the different field geometry.

Fig. 5.3(b) shows the momentum distribution obtained by solving the TDSE for the same parameters as in Fig. 5.3(a). Here, we used the split-operator method on a grid of size

<sup>2</sup>See Appendix A.2 where the expression is derived.

$300 \times 300$  a.u. using 2048 bins in each dimension and multiplied the vector potential (5.3) by an envelope  $f(t) = \cos(\omega t/6)^4$  (3-cycle pulse) to avoid ATI rings in the PMD and obtain a clear maximum. The time step is 0.004 a.u. and we propagate until the final time  $T = 750$  a.u. The maximum of the PMD is clearly shifted towards positive momenta along the  $p_y$  direction.

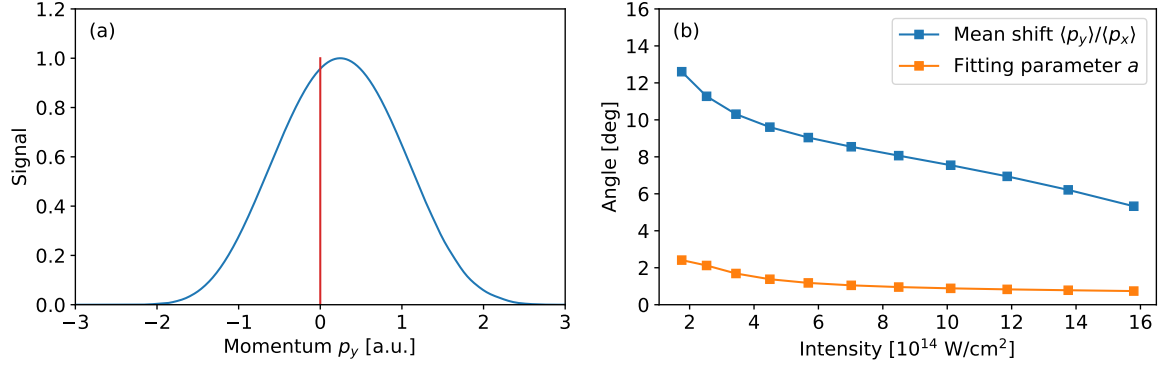


Figure 5.4: (a) Projection of the PMD in Fig. 5.3(b) onto the  $p_y$  axis, normalized to maximum signal 1. (b) Shift and rotation angle of the bulk of the PMD.

This can also be seen when projecting the relevant branch of the PMD onto the  $p_y$  axis, see Fig. 5.4(a). The change in the PMD from the SFA to the TDSE is really a shift, not a rotation as would be the case for the circular attoclock. To verify this, we calculate a linear regression  $p_x = -a p_y + b$  through the main part of the PMD and find  $a \approx 0.018$ . This can be compared to the shift of the mean value  $\langle p_y \rangle / \langle p_x \rangle \approx 0.150$  which is much larger. Converting the two quantities to angle and repeating the TDSE calculation over a wide range of intensities, the result shown in Fig. 5.4(b) is obtained. There, it is evident that the shift of the mean always exceeds the internal rotation by far. This could allow for a simple calibration of the relative phase of the two-color field (which effectively rotates the whole distribution) in an experiment. Another benefit of the quasilinear field is the very good agreement of the peak of the distribution in  $p_x$  direction with the classically expected value  $E_{\text{peak}}/(2\omega)$  which provides a way for intensity calibration.

This is shown in Fig. 5.5(b). For comparison, the peak radial momentum for the circular attoclock is shown in Fig. 5.5(a). There, we have used a two-cycle pulse

$$\mathbf{A}(t) = -\frac{E_0}{\omega} \cos\left(\frac{\omega t}{4}\right)^4 \begin{pmatrix} \cos(\omega t) \\ \sin(\omega t) \end{pmatrix} \quad (5.13)$$

with  $\omega = 0.05695$  a.u. corresponding to 800 nm wavelength but otherwise the same parameters as in the bicircular field. For circular polarization, the maximum is typically found at larger radii compared to the simple man's estimate  $p = E_0/\omega$ . This is a known nonadiabatic effect [259, 260]. To lowest order in the Keldysh parameter, saddle-point SFA predicts an offset from the simple man's prediction of  $\Delta p = \omega/E_0 \cdot I_p/3$  (see Eq. (A.37) in Appendix A.2.1) which agrees reasonably well with the numerical result.

When the initial state carries angular momentum, another offset from the simple man's prediction was found for circular polarization in [260]. To observe this offset, we repeat above calculations for neon and increase the (effective) wavelength to 1600 nm to move more into the adiabatic regime. Here, the Tong-Lin potential (A.14) is used where we have replaced the radius  $r$  by  $\sqrt{r^2 + \alpha}$  and tuned  $\alpha \approx 0.135$  a.u. such that the 2p states of the 2D potential

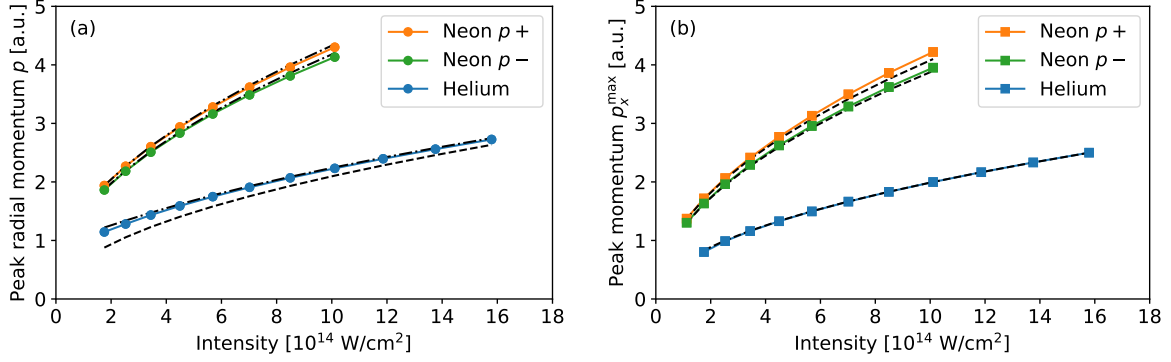


Figure 5.5: (a) Radial momentum at the maximum of the PMD (including prefactor  $p$ ) in the circular attoclock. (b) Momentum  $p_x$  at the maximum of the PMD in the bicircular attoclock. In both panels, the blue curve shows the 2D TDSE result for helium and the black dashed curve shows the classical (adiabatic) estimate ( $E_0/\omega$  for the circularly polarized field and  $E_{\text{peak}}/(2\omega)$  for the bicircular field). In panel (a), the black dot-dashed curve adds the first nonadiabatic correction  $\omega I_p/(3E_0)$  to the classical estimate. The orange and the green curve show the 2D TDSE result for neon at 1600 nm (effective) wavelength and initial states carrying angular momentum  $m = \pm 1$ . In panel (b), the black dashed curves add the adiabatic correction  $mE_{\text{peak}}/(2I_p)$  due to the angular momentum to the classical estimate. In panel (a), the black dot-dashed curves include the adiabatic correction  $mE_0/(2I_p)$  as well as the nonadiabatic correction  $\omega I_p/(3E_0)$ .

reproduce the ionization potential  $I_p \approx 0.793$  a.u. of neon. Interestingly, this offset is also visible in the bicircular case, although the field has no sense of rotation at the time of peak field strength. Indeed, saddle-point SFA predicts that in the adiabatic limit half the angular momentum of the initial state is found as an initial velocity offset at the tunnel exit.

$$I_p/E_{\text{peak}} \cdot \Delta p = m/2 \quad (5.14)$$

(see Appendix A.2.3). Again, we find that this prediction agrees reasonably well with the TDSE result.<sup>3</sup>

## 5.4 Attoclock analysis

Similar to the attoclock analysis for the circularly polarized field in the previous Chapter 4, we wish to interpret the quasilinear field (5.3) as an attoclock and investigate how the time of peak field strength is related to the most probable ionization time. For the circularly polarized field, we found that due to geometrical factors the maximum of the ionization rate does not necessarily correspond to the maximum of the momentum distribution (see Section 4.6). In a classical picture of the ionization process, the ratio between the two is given by the Jacobian (4.46) of the deflection function that connects the initial conditions with the final photoelectron momentum. For the quasilinear field, taking the derivative of the Jacobian at initial velocity

<sup>3</sup>In [260], the difference in position of the maxima was considered a nonadiabatic effect. There, circular polarization was used and momentum was measured in units of  $A_0 = E_0/\omega$ . In these units, the offset becomes  $\Delta p/A_0 = \gamma mE_0/(2I_p)^{3/2}$  when expressed via the Keldysh parameter or  $(\Delta p/A_0 = m/(2K))$  when expressed via the multiphoton parameter). In the adiabatic limit  $\gamma \rightarrow 0$ , only the relative offset goes to zero while an absolute offset is always produced at the ionization step. Our result is also in conflict with [261] where it was stated that in the adiabatic limit, the information about the initial direction of the electron's rotation is lost.



$v = 0$  (perpendicular to the instantaneous field direction), we find

$$\frac{\partial}{\partial t} |\det \mathbf{D}'(t, v)| \Big|_{v=0} = E'(t), \quad \frac{\partial}{\partial v} |\det \mathbf{D}'(t, v)| \Big|_{v=0} = E(t)k(t). \quad (5.15)$$

The time derivative always vanishes at the time of peak field strength. The derivative with respect to the velocity vanishes when the curvature of the vector potential is zero. At the time of peak field strength, this is exactly the case for a counter-rotating bicircular field when the field-strength ratio is chosen 2 : 1. Thus, the Jacobian is constant to first order in the vicinity of the peak of the PMD and cannot influence its position. This motivates us to observe the maximum of the Cartesian PMD directly without further modifications by geometrical factors.

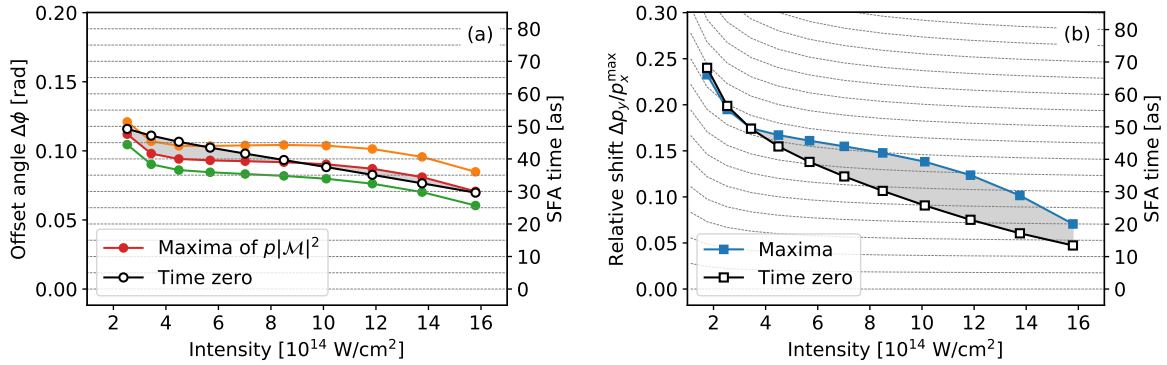


Figure 5.6: (a) Rotation angles  $\Delta\phi$  of the maxima of the PMD in the circular attoclock including prefactors 1 (orange curve),  $p$  (red curve) and  $p^2$  (green curve). (b) Relative shifts  $\Delta p_y/p_x^{\max}$  of the maxima of the PMD in the bicircular attoclock. In both panels, the black lines give the angles or shifts of time zero according to the saddle-point condition for the Dyson integrand (4.3). The SFA scales on the second axis give the time that is associated with a given angle or relative shift according to the SFA saddle-point equation (2.29). Adapted from Fig. 2 in [245].

Fig. 5.6(b) shows the relative shifts  $\Delta p_y/p_x^{\max}$  at time zero for the quasilinear field (5.3) for various intensities while Fig. 5.6(a) shows the corresponding angles  $\Delta\phi$  for the circular attoclock pulse (5.13). Since there is no ambiguity in defining the offset angle for the quasilinear field, there is only one curve for the shift of the PMD maxima in panel (b). In both panels, the gray lines in the background provide the time that one would associate with a given relative shift or angle according to the SFA saddle-point equation (2.29). For the circular attoclock, the SFA flow of time  $d\phi/dt = \omega$  is a constant over all intensities leading to equidistant lines. This is not the case for the bicircular attoclock where the speed of the clock (5.12) depends on the intensity via the Keldysh parameter  $\gamma_{\text{eff}}$ . Qualitatively, the curves in Fig. 5.6(a, b) behave in a similar way with an approximately constant time value at intermediate intensities and a turn to earlier times at higher intensities. As before (see Chapter 4), this is expected due to depletion, see also Fig. 5.7.

To compare the influence of depletion on the PMD we, can write a simple model where the total instantaneous ionization rate  $W(t)$  is written as

$$W(t) = -\dot{P}(t) = \Gamma(t)P(t). \quad (5.16)$$

Here,  $P(t)$  is the population at time  $t$  and  $\Gamma(t)$  is the rate in absence of depletion. The maximum is found where

$$0 = \dot{W}(t) = -\ddot{P}(t) = \dot{\Gamma}(t)P(t) + \Gamma(t)\dot{P}(t) \stackrel{(5.16)}{=} \dot{\Gamma}(t)P(t) - \Gamma(t)^2P(t) \Leftrightarrow \dot{\Gamma}(t) = \Gamma(t)^2 \quad (5.17)$$

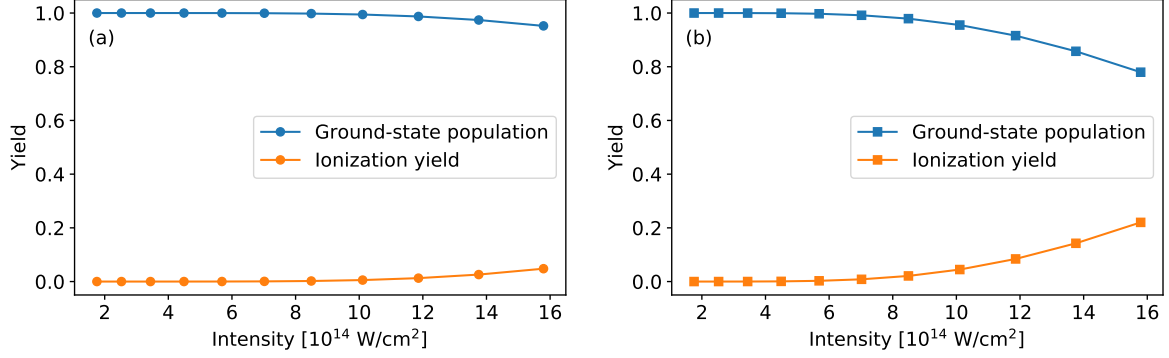


Figure 5.7: Ground-state population after the end of the pulse (blue curve) and ionization yield (orange curve). (a) Circular attoclock. (b) Bicircular attoclock.

Suppose the maximum in the absence of depletion is at  $t_0$ , i.e.  $\dot{\Gamma}(t_0) = 0$ , then we can solve (5.17) approximately via

$$\dot{\Gamma}(t_0 + \Delta t) - \Gamma(t_0 + \Delta t)^2 = \ddot{\Gamma}(t_0)\Delta t - \Gamma(t_0)^2 + \mathcal{O}(\Delta t^2), \quad (5.18)$$

so there is a shift to earlier times given by

$$\Delta t \approx \frac{\Gamma(t_0)^2}{\ddot{\Gamma}(t_0)} = -\Gamma(t_0) \sigma^2 \quad (5.19)$$

Here,  $\sigma^2 = -\Gamma(t_0)/\ddot{\Gamma}(t_0)$  measures the width of the ionization burst. That is, depletion has a negligible effect on an attoclock measurement when (i) the instantaneous ionization rate  $\Gamma(t_0)$  is small; (ii) the width of contributing times  $\sigma$  is small, i.e. the field has a sharp maximum. At this point, the circular and bicircular attoclock behave very differently. At a given intensity, the peak field strength is stronger in the bicircular attoclock by a factor of  $3/\sqrt{5} \approx 1.342$  leading to a higher instantaneous rate. The width is more complicated to compare because in the circular attoclock it is determined by the field envelope. Ideally, if the circular attoclock is to be used to investigate ionization dynamics in circular polarization, the ellipticity should be as small as possible. On the contrary, this increases  $\sigma$  such that depletion effects become strong. In the bicircular attoclock, the shape of the electric field around the maximum is an inherent property of the bicircular field. At the same peak field strength and same (effective) frequency, the bicircular field decreases faster around the maximum compared to elliptical polarization for any ellipticity larger than zero. In this sense, depletion is expected to affect the bicircular attoclock less.

To investigate how the observed shifts in the PMDs relate to the ionization time, we use the trajectory-free method developed in Chapter 4. Varying the momentum in the  $p_y$  direction at fixed  $p_x^{\max}$  and solving the saddle-point equation (4.3) for every such momentum, we obtain the time-to-momentum mapping required to interpret the attoclock momentum distribution.<sup>4</sup>

For the central intensity ( $E_0 = 0.1$  a.u.), this mapping is shown in Fig. 5.8(a). We observe that the slope of the time-momentum curve is in good agreement with the quantum-orbit model which was used to calibrate the clock in Eq. (5.12) and in significant disagreement

<sup>4</sup>In the following, we propagate only until the final time  $T = 300$  a.u. Since the main branch of the PMD originates from times around  $t = 0$  and the photoelectron energies are rather large, the final time is sufficient for those photoelectrons to reach the absorbing boundary of the simulation volume.

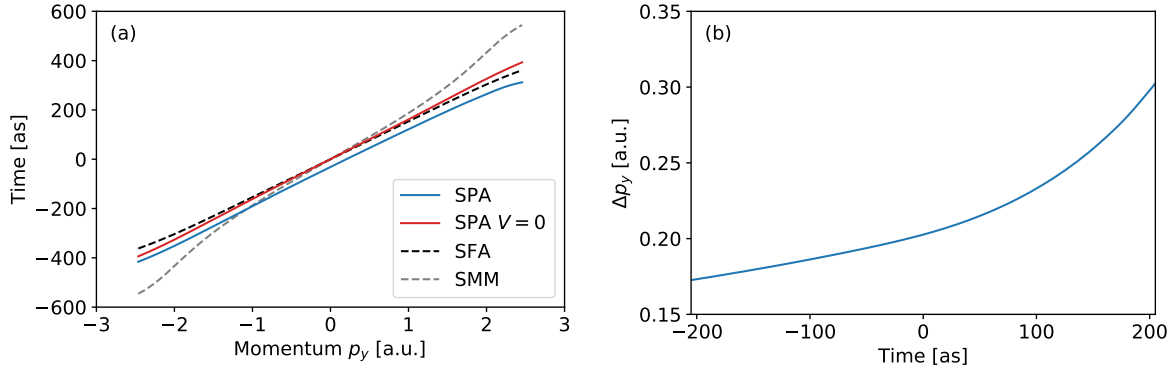


Figure 5.8: (a) Time-to-momentum mapping on a slice through the maximum of the PMD (see Fig. 5.3) along the  $p_x$  direction at  $E_0 = 0.1$ . The blue solid curve gives the real part of the stationary points of the Dyson integrand according to Eq. (4.3). The red solid curve gives the corresponding times when the potential is neglected in the time evolution after the interaction time. The black dashed curve is obtained as the solution of the SFA saddle-point equation (2.29) and the gray dashed curve as the solution of the same equation with  $I_p \rightarrow 0$  (simple man's model SMM). (b) Difference of the momenta in the  $p_y$  direction assigned to a given ionization time between the full evaluation of the saddle-point equation (blue curve in panel (a)) and the potential-free case (red curve in panel (a)).

with the simple man's model, reflecting how the mapping is changed due to the nonvanishing parallel exit velocities. This was already visible in the ionization-time retrieval for truly linear polarization in Chapter 3. (Interestingly, the time-to-momentum mapping derived from (4.3) in the potential-free case is not *exactly* equal to the one derived from the quantum-orbit model. This is because the former also incorporates the SFA matrix element in the saddle-point equation). For a given ionization time, there is a momentum shift  $\Delta p_y$  towards higher momenta compared to the potential-free case, see also Fig. 5.8(b). This shift gets larger for later ionization times which is plausible because the effect of the Coulomb potential on the outgoing photoelectron is smaller when the peak of the electric field is yet to come.

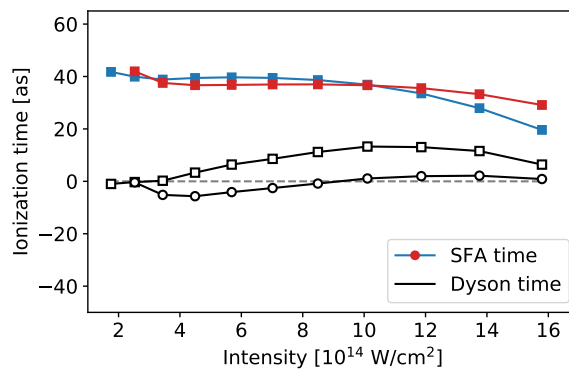


Figure 5.9: Ionization time in the bicircular attoclock (squares) and in the circular attoclock (circles). The black curves give the trajectory-free ionization time according to (4.3) where for the momentum we have used the maximum of the PMD in Cartesian coordinates (prefactor 1) in the bicircular attoclock and in cylindrical coordinates (prefactor  $p$ ) in the circular attoclock. The colored curves give the Coulomb-free ionization time according to the SFA saddle-point equation (2.29). Adapted from Fig. 3 in [245].

In Fig. 5.6(b), the momentum shift corresponding to time zero is compared to the attoclock shift of the momentum distribution for various intensities. Similarly, varying the angle at

constant radial momentum we find the offset angle that correspond to time zero in the circular attoclock. This is shown in Fig. 5.6(a). Alternatively, we solve the saddle-point equation (4.3) with  $\mathbf{p}$  at the maximum to find the dominant ionization time directly. This is shown in Fig. 5.9. As expected, the retrieved times resemble closely the difference between the curves of maximum signal and the curves of time zero on the SFA time scale in Fig. 5.6. We find that for small intensities the ionization time for the maxima is close to zero. For higher intensities, the quasilinear case shows a delay of more than 10 attoseconds that is not present in the circular case.

## 5.5 Saddle-point approximation in the Dyson integral

To what extend stationary points in the Dyson integral can be interpreted as ionization times depends on how well the ionization amplitude can be described with knowledge of the integrand in the vicinity of the stationary points, i.e. it depends on the applicability of the saddle-point approximation. While in Section (4.2) we found that the saddle-point approximation can give good results when the strong-field approximation is employed, the same question has not been answered when the potential is taken into account.

Similar to the previous section, we vary the momentum along the  $p_y$  direction to obtain the time-momentum relation, but go one step further and evaluate the Dyson integrand (4.2) and its first and second derivative along the way. This allows us to calculate the contribution of the respective stationary point to the photoelectron momentum distribution in saddle-point approximation using (4.17).

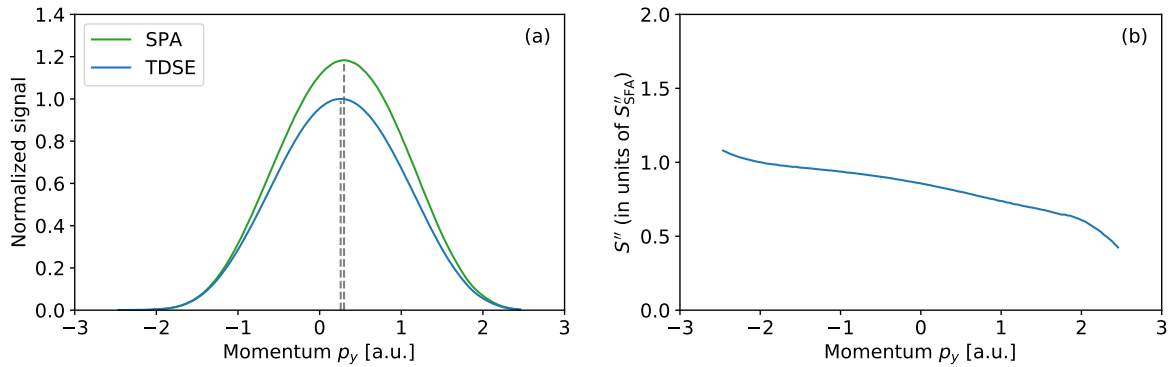


Figure 5.10: Saddle-point approximation of the Dyson integral in the bicircular attoclock at  $E_0 = 0.1$  a.u. (a) Blue curve, slice through the photoelectron momentum distribution from Fig. 5.3(b) in  $p_y$  direction through the maximum, normalized to maximum signal 1. Green curve, PMD evaluated on the same line by applying the saddle-point approximation according to (4.17), multiplied with the same normalization constant. The maxima of the two curves are highlighted with gray dashed lines. (b) Value of the second derivative  $\ddot{S}(\mathbf{p}, t_s)$  in units of the SFA value  $\ddot{S}_{SFA} = \sqrt{2I_p} E_{\text{peak}} \sqrt{1 + \gamma_{\text{eff}}^2}$  for linear polarization at peak field strength based on the action (2.24). Panel (a) is adapted from Fig. 1 in [245].

The result for  $E_0 = 0.1$  a.u. is shown in Fig. 5.10(a) in comparison with a slice through the maximum of the PMD taken directly from the solution of the TDSE (see Fig. 5.3(b)). We observe reasonable agreement in the vicinity of the maximum and very good agreement for negative  $p_y$  momenta, i.e. those momenta that correspond to ionization times before the time of peak field strength. Interestingly, the position of the maximum of the distribution obtained

in saddle-point approximation shows an even larger momentum shift compared to the one obtained directly from the TDSE. This can be attributed to the prefactor in Eq. (4.17) that gets larger for later ionization times (see Fig. 5.10(b)). Indeed, when the prefactor is neglected in the saddle-point approximation, the position of the maximum agrees with the momentum shift from time zero.

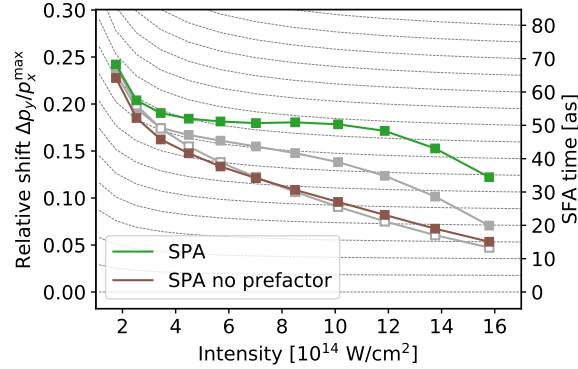


Figure 5.11: Attoclock shift of the momentum distribution in saddle-point approximation (4.17) (green curve) and in saddle-point approximation neglecting the prefactor (brown curve). For reference, the curves from Fig. 5.6 are reprinted as gray lines in the background.

This is shown in Fig. 5.11 where we have calculated the attoclock shift of the momentum distribution in saddle-point approximation for many intensities, both with and without the prefactor. Going to smaller intensities where no ionization-time delay was found, the position of the maximum is not changed by the prefactor and agrees reasonably well with the shifted maximum of the PMD.

To get a better understanding of the applicability of the saddle-point approximation to the full Dyson integral (4.1), a closer investigation of the structure of the integrand  $\mathcal{D}(\mathbf{p}, t)$  is required. Mapping the complete integrand at fixed  $\mathbf{p}$  in the complex time plane by direct numerical evaluation is not feasible because one solution of the TDSE is required to evaluate the integrand for one complex time. Fortunately, we can decrease the computational effort significantly by using complex analysis.

For a holomorphic function  $f(z)$ , the function values on a given region  $U$  of the complex plane and all derivatives are determined by its values on the boundary  $\partial U$  and can be calculated<sup>5</sup> using Cauchy's integral formula

$$f^{(n)}(z) = \frac{n!}{2\pi i} \oint_{\partial U} dw \frac{f(w)}{(w-z)^{n+1}}. \quad (5.20)$$

Alternatively, we can use the fact that with  $z = x + iy$  and  $f = u + iv$ ,  $u$  and  $v$  are harmonic functions, i.e. they satisfy Laplace's equation  $\Delta u = \Delta v = 0$ . Finding the values of  $f$  on the inside of  $U$  is therefore equivalent to solving the Dirichlet-type boundary-value problem for  $u$  and  $v$  given their values on  $\partial U$ .

We assume  $\mathcal{D}(\mathbf{p}, t)$  to be holomorphic in  $t$  for a given momentum  $\mathbf{p}$ , at least in a region of the complex time plane, and evaluate it at  $E_0 = 0.1$  a.u. in a rectangle that extends from  $-30$  a.u. to  $30$  a.u. in real time and  $0$  a.u. to  $8$  a.u. in complex time. We traverse the boundary of the rectangle in steps of  $0.2$  a.u. while solving the TDSE to obtain  $\mathcal{D}(\mathbf{p}, t)$  for  $t$  on the boundary,

<sup>5</sup>Assuming the boundary  $\partial U$  consists of piecewise smooth curves [274].

but for all  $\mathbf{p}$  at once. If  $\mathcal{D}(\mathbf{p}, t)$  is indeed holomorphic, its integral around the boundary of the rectangle must vanish. In other words, the integral  $\mathcal{J}$  along the section on the real line must be equal to  $\mathcal{J}'$ , the sum of the three integrals with imaginary time component. Indeed, evaluating  $\mathcal{J}$  and  $\mathcal{J}'$  at the maximum of the momentum distribution ( $\mathbf{p} = \mathbf{p}_{\max}$ ) and defining  $\Delta\mathcal{J} = \mathcal{J} - \mathcal{J}'$  we find  $|\Delta\mathcal{J}/\mathcal{J}| = 7.60 \times 10^{-5}$  using the trapezoidal rule ( $1.60 \times 10^{-5}$  using Simpson's rule), which is reasonably close to zero. We thus proceed with evaluating the Cauchy integral to find the values of  $\mathcal{D}(\mathbf{p}, t)$  on the inside of the rectangle. Additionally, we solve Laplace's equation for the real and imaginary part on a grid commensurate with the boundary points by discretizing the Laplace operator with three-point finite differences and using a simple relaxation algorithm.

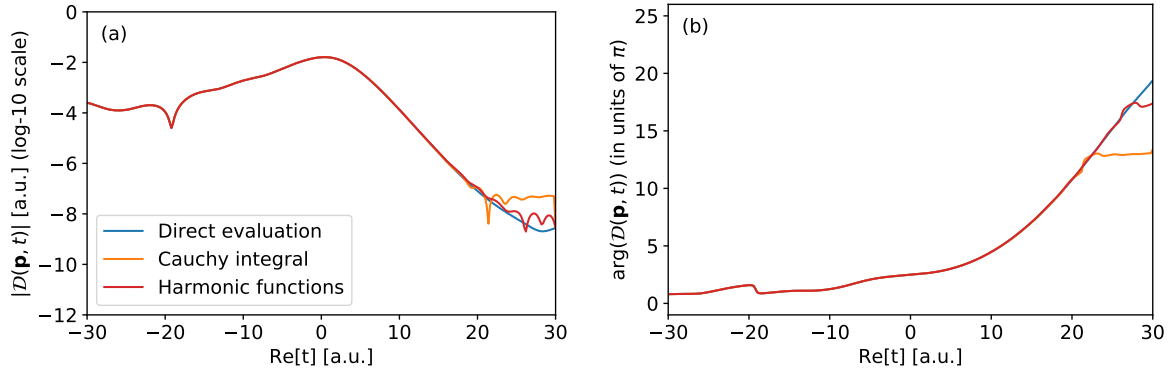


Figure 5.12: Dyson integrand  $\mathcal{D}(\mathbf{p}_{\max}, t)$  at  $E_0 = 0.10$  a.u. on a slice through the complex-time plane at  $\text{Im}(t) = 4$  a.u. (a) Absolute value (in a.u., log-10 scale). (b) Phase (unwrapped and shifted by an arbitrary value). In both panels, the blue curve gives the values obtained by direct numerical wave-function propagation, the orange curve those obtained by evaluating Cauchy's integral (5.20), and the red curve those obtained by solving the boundary-value problem for Laplace's equation.

Fig. 5.12 shows the values of  $\mathcal{D}(\mathbf{p}_{\max}, t)$  obtained in this way on a slice at  $\text{Im}(t) = 4$  a.u. through the rectangle. This is compared with evaluating  $\mathcal{D}(\mathbf{p}_{\max}, t)$  directly by solving the TDSE numerically in the complex plane on the same slice. Here, we find very good agreement (with the exception of very late times where the integrand is so small that it is negligible for the integral anyway).

Fig. 5.13 shows the absolute value, phase and logarithmic derivative of  $\mathcal{D}(\mathbf{p}_{\max}, t)$  on the inside of the rectangle as calculated by solving Laplace's equation. The logarithmic derivative in panel (c) reveals the position of the main stationary point  $S_1$  in good agreement with the previous calculation relying on a direct evaluation of the integrand (see Fig. 5.9). From the stationary point, we follow the contour of steepest descent (white line). From panel (a), it is evident that towards positive  $t_r$  the integrand is decreasing rapidly, as is required for a successful application of the saddle-point approximation. Towards negative  $t_r$ , however, the steepest descent contour ends in a zero  $Z_1$  of the integrand (a pole of the logarithmic derivative). From this zero, the integration path can be continued via another stationary point  $S_2$  to end up in yet another zero  $Z_2$ , that is connected via a third stationary point  $S_3$  to a zero  $Z_3$  that marks the electric field minimum before the main peak of the field.

For comparison, the structure of the Dyson integrand in SFA is shown in Fig. 5.14. There, the signal shows forward-backward symmetry in time and features only one relevant stationary point as in Section 4.2.<sup>6</sup>

<sup>6</sup>The difference to the previous calculation, apart from the species and the field shape, is that in Section 4.2, the

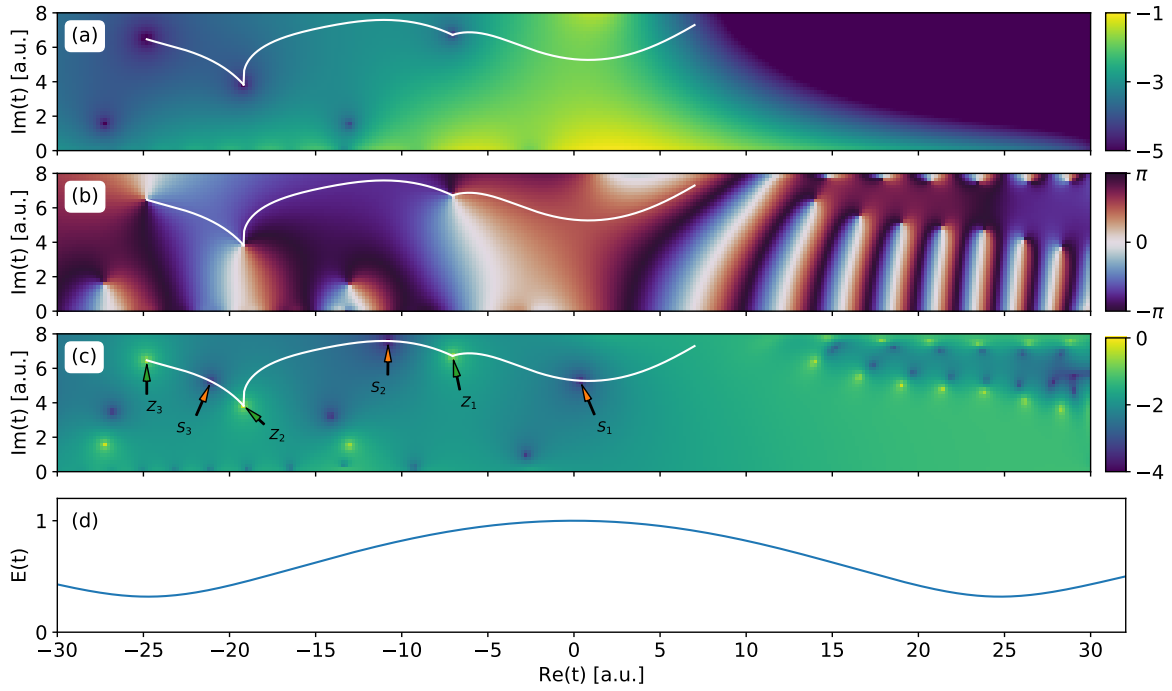


Figure 5.13: Complete mapping of the Dyson integrand  $\mathcal{D}(\mathbf{p}_{\max}, t)$  at  $E_0 = 0.10$  a.u. in a region of the complex time plane, calculated by solving the boundary-value problem for the Laplace equation in the real and imaginary part of  $\mathcal{D}$ . (a) Absolute value  $|\mathcal{D}|$  of the integrand (in a.u., log-10 scale). (b) Phase  $\arg(\mathcal{D})$  of the integrand (arb. shifted). (c) Absolute value of the logarithmic derivative  $|\partial_t \mathcal{D}/\mathcal{D}|$  (in a.u., log-10 scale). (d) Magnitude of the electric field (normalized to maximum value 1). In panels (a), (b), and (c), the white line moves through stationary points in the direction of steepest descent, i.e. at constant phase. These stationary points are marked as  $S_1$ ,  $S_2$ , and  $S_3$  in panel (c). Segments of the contour end in zeros marked as  $Z_1$ ,  $Z_2$ , and  $Z_3$ . The zeros in the upper right corner are artifacts from the numerical solution of the boundary-value problem.

Going back to the situation where the potential is taken into account, parameterizing the path by the real time  $t_r$  and writing the imaginary time on the path as a function  $t_i(t_r)$ , the contribution of the path to the Dyson integral becomes

$$-i \int dt_r (1 + it'_i(t_r)) \mathcal{D}(\mathbf{p}, t_r + it_i(t_r)). \quad (5.21)$$

The integrand (including the line element) along the three branches of the path is shown in Fig. 5.15(a).

The dominant contribution is picked up in the main branch that corresponds to the previously-found stationary point  $S_1$ . However, the two earlier segments also add to the final value of the integral, but with a different phase which is shown in Fig. 5.15(b).

In Fig. 5.16, we calculate the PMD on a slice through the maximum as in Fig. 5.10, but now going beyond the saddle-point approximation, integrating the Dyson integrand in complex time and considering all three branches (red curve) or considering only the last segment (orange curve).<sup>7</sup> When considering only the last segment, we find very good agreement with the signal obtained in saddle-point approximation, implying that the disagreement with the TDSE

expression for the matrix element was approximated by taking only the long-range behavior of the wave function into account. This is not the case here.

<sup>7</sup>Since the integral is path independent, we have evaluated it numerically along a straight line that starts in a zero  $Z_1$  or  $Z_3$  and ends in the upper right corner of the rectangle where the integrand is vanishingly small.

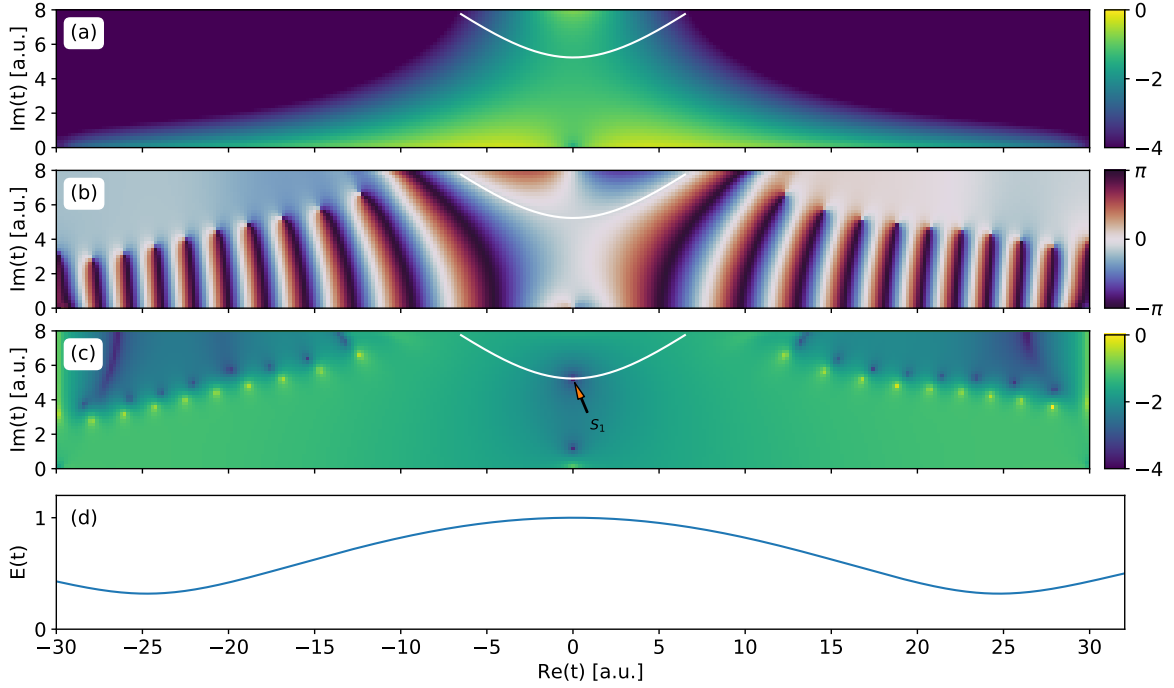


Figure 5.14: Mapping of the Dyson integrand as in Fig. 5.13 when employing the strong-field approximation, i.e. neglecting the potential  $V$  in time-propagation after the interaction time. Since there is no attoclock shift of the maximum in this case, the momentum at which the integrand is evaluated is chosen as  $p_y = 0$  while  $p_x$  is the same as in Fig. 5.13.

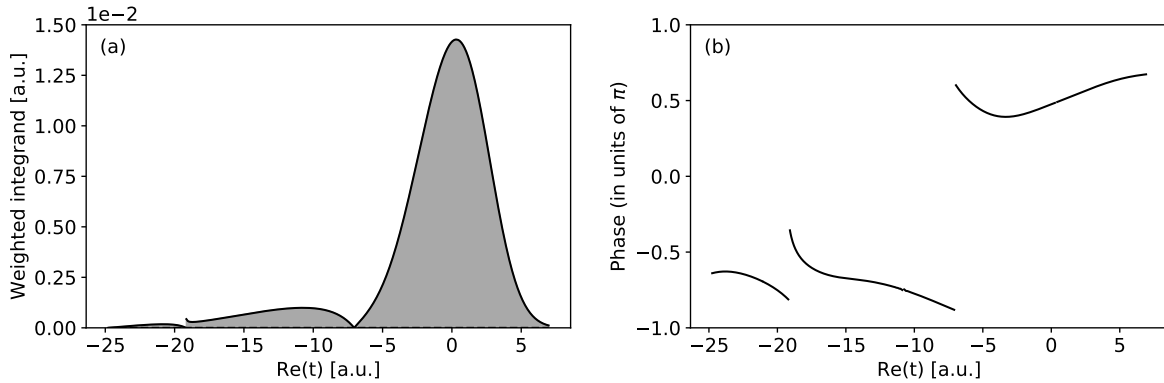


Figure 5.15: Absolute value (a) and phase (b) of the Dyson integrand (5.21) at  $\mathbf{p} = \mathbf{p}_{\max}$  and  $E_0 = 0.10$  a.u. on the steepest descent contour (white line in Fig. 5.13).

is not due to a failure of the SPA to describe the integrand in the vicinity of the saddle-point. Instead, the disagreement can be attributed to neglecting the earlier contributions from the main cycle of the field. Taking them into account leads to almost perfect agreement with the TDSE result. The earlier contributions reflect a fundamental asymmetry present in the Dyson integral when the potential is taken into account. An interaction with the electric field at earlier times does not necessarily lead to immediate ionization, but it can “prepare” later ionization and thus contribute to some momentum, that would otherwise be attributed only to a later time. This is different from the strong-field approximation where an interaction with the field always leads to ionization.

Going one step further, it is clear that when the potential is taken into account, even previ-



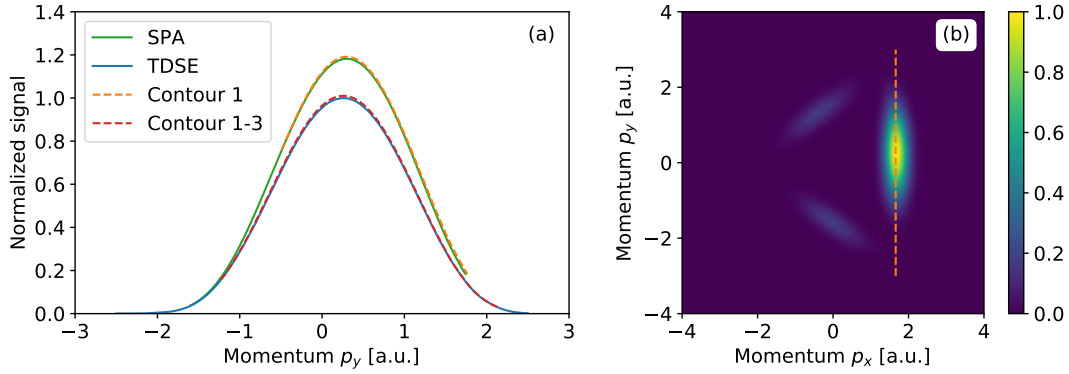


Figure 5.16: (a) Various approximations of the PMD at  $E_0 = 0.1$  a.u. Blue curve, slice through the TDSE photoelectron momentum distribution in  $p_y$  direction through the maximum, normalized to maximum signal 1. Green curve, PMD evaluated on the same line by applying the saddle-point approximation according to (4.17) as in Fig. 5.10, but with the integrand evaluated using Cauchy's formula. Orange curve, numerical evaluation of the integral of the last segment of the steepest-descent contour (white line in Fig. 5.13). Red curve, numerical evaluation of all three segments. (b) Momentum distribution as in Fig. 5.3(a). The orange dashed line indicates the slice along which the PMD is evaluated in panel (a).

ous cycles of the electric field cannot be neglected if the photoelectron momentum distribution is to be reproduced including its phase, because the Stark shift in previous cycles leads to a deviation of the phase of the bound state from the field-free approximation. Also, if depletion is important, contributions of previous cycles must cancel out contributions from the main cycle so the total amplitude can decrease accordingly. In our case, the ionization yield is rather small (about 0.84 percent) so the absolute value of the PMD can be reproduced well by considering only the main cycle of the field.

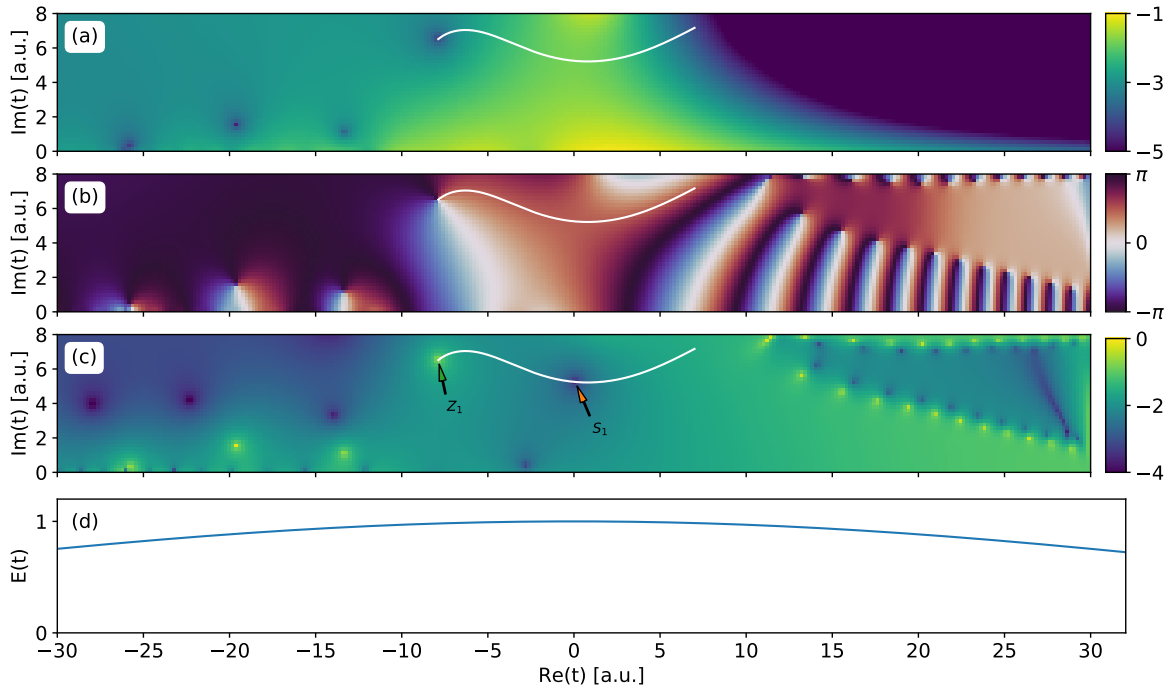


Figure 5.17: Mapping of the Dyson integrand as in Fig. 5.13 but for the circularly polarized field (5.13) at the same peak field strength and the maximum of the momentum distribution.

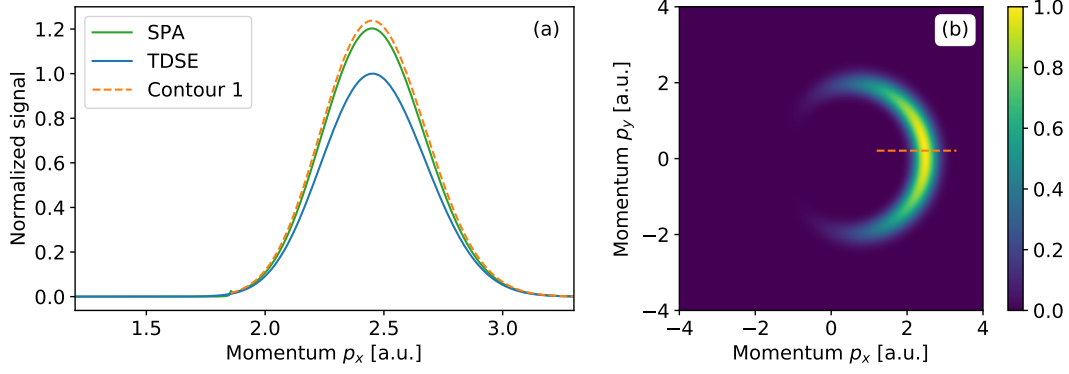


Figure 5.18: (a) Approximations on a slice in  $p_x$  direction through the maximum of the PMD in circular polarization. Blue curve, slice through the TDSE photoelectron momentum distribution in  $p_y$  direction through the maximum, normalized to maximum signal 1. Green curve, PMD evaluated on the same line by applying the saddle-point approximation according to (4.17). Orange curve, numerical evaluation of the integral on the steepest-descent contour (white line in Fig. 5.17). (b) PMD for the same peak field strength as in the bicircular case. The orange line indicates the slice along which the PMD is evaluated in panel (a).

Fig. 5.17 shows the integrand for circular polarization where we have chosen the same peak field strength as in the bicircular case. Around the main stationary point, the structure is not qualitatively different to the quasilinear case with the steepest descent contour ending in a zero of the integrand. Attempting to approximate the PMD using the saddle-point method, we also find a similar behavior. The contribution to the integral due to the main stationary point can be well approximated with the saddle-point method, but considering solely this contribution leads to a slight overestimation of the signal.

## 5.6 Classical backpropagation

For the conventional attoclock, much of the discussion about how to interpret the momentum distribution is rooted in the fact that a variety of different methods are used to obtain the time-to-momentum mapping. While in the previous section we have used the concept of the Dyson integral representation, in the next two sections we are going to apply methods to the quasilinear field that are already established for the conventional attoclock.

One of these methods is the classical backpropagation. [102–104]. Classical backpropagation starts from the ionized wave packet  $\psi(x, y)$  after the end of the laser pulse. The wave function defines a local momentum by its phase gradient

$$\mathbf{v}(x, y) = \nabla \arg \psi(x, y) = \text{Im} \left( \frac{\nabla \psi(x, y)}{\psi(x, y)} \right). \quad (5.22)$$

Assuming the wave packet is located sufficiently far from the ion such that the potential can be approximated by a Coulomb potential, the local velocity can be mapped to final momentum  $(p_x, p_y)$  via Kepler's formula [95, 149]

$$(p_x, p_y) = \mathbf{D}_F(x, y) = p \frac{p(\mathbf{L} \times \mathbf{a}) - \mathbf{a}}{1 + p^2 L^2}, \quad \frac{p^2}{2} = \frac{v^2}{2} - \frac{1}{r}. \quad (5.23)$$

Here,  $\mathbf{L} = \mathbf{r} \times \mathbf{v}$  and  $\mathbf{a} = \mathbf{v} \times \mathbf{L} - \mathbf{r}/r$  is the Runge-Lenz vector. For fixed  $\psi$ , we call  $\mathbf{D}_F(x, y)$  the forward deflection function. A backwards deflection function  $(t, v) = \mathbf{D}_B(x, y)$  leading to

the space of initial condition is defined by propagating classical trajectories starting at position  $(x, y)$  with velocity  $\mathbf{v}(x, y)$  backwards in time in the presence of the potential and the laser field until a tunneling criterion is met. As in previous works [102, 103], we use the velocity criterion that stops backpropagation at the ionization time  $t$  when there is a zero of the velocity in instantaneous field direction.<sup>8</sup> The initial velocity  $\mathbf{v}$  is then taken as the remaining component perpendicular to the instantaneous field direction.

Knowledge of the backwards deflection function allows us to define the instantaneous ionization rate

$$W(t, \mathbf{v}) = \frac{|\psi(x, y)|^2}{|\det \mathbf{D}'_{\mathbf{B}}(x, y)|} \quad (5.24)$$

while the forward deflection function can be used to calculate the momentum distribution

$$|\mathcal{M}(p_x, p_y)|^2 = \frac{|\psi(x, y)|^2}{|\det \mathbf{D}'_{\mathbf{F}}(x, y)|} \quad (5.25)$$

Eliminating the wave function  $|\psi(x, y)|^2$ , we find the familiar expression (4.44) where now we have access to the full Jacobian which can be calculated as

$$|\det \mathbf{D}'(t, \mathbf{v})| = |(\mathbf{D}_{\mathbf{F}} \circ \mathbf{D}_{\mathbf{B}}^{-1})'(t, \mathbf{v})| = \frac{|\mathbf{D}'_{\mathbf{F}}(x, y)|}{|\mathbf{D}'_{\mathbf{B}}(x, y)|} \quad (5.26)$$

We solve the 2D TDSE with the split-operator method on a Cartesian grid of size  $600 \times 600$  a.u. and 4096 points in each dimension and time step 0.004 a.u. To avoid oscillations in the phase of the electron wave packet that impede a clear definition of the local momentum  $\mathbf{v}$  (especially at low intensities), the initial state has to be extremely stable under time evolution. Therefore, we do not use the exact ground state of the (grid) Hamiltonian but instead an eigenstate of the time-evolution operator at finite time step as explained in Appendix A.1.2. For a practical calculation, the wave packet does not really have to be propagated to the end of the laser pulse. Instead, starting from position  $(x, y)$  and local momentum  $\mathbf{v}(x, y)$  one can solve Newton's equations of motion forward in time in the presence of the laser field until the pulse is over before going to the Kepler orbit. For the bicircular attoclock pulse, we choose the final time  $T = 78.016$  a.u. (before the end of the pulse but after the main ionization burst located at time zero) while for the circular attoclock pulse we choose  $T = 110.332$  a.u. (after the end of the pulse).

Results for the intermediate intensity ( $E_0 = 0.10$  a.u.) for the circular attoclock setup are shown in Fig. 5.19. Knowledge of both mappings  $\mathbf{D}_{\mathbf{F}}$  from position to momentum and  $\mathbf{D}_{\mathbf{B}}$  from position to initial conditions allows us to relate a momentum  $(p_x, p_y)$  with a given set of initial conditions  $(t, \mathbf{v})$  and vice versa. This is shown using contour lines in Fig. 5.19. The contour lines in the space of initial conditions (a) show fixed radial momentum and emission angle of the photoelectron while the contour lines in the momentum distribution (c) show fixed ionization time and initial velocity. The effect of the Jacobian (5.26) can be seen as a change in the area formed by the contour lines (where in (a) a fixed size would indicate a Jacobian  $|\det \mathbf{D}'| \propto p$  since the contour lines map to polar coordinates).

The corresponding result for the bicircular attoclock is shown in Fig. 5.20. The scaling of the  $t$  and  $\mathbf{v}$  axes in (a) is chosen exactly as  $1/E_{\text{peak}} \approx 7.45$  a.u. such that in the simple man's model and in the vicinity of the maximum the contour lines would be squares of equal size. There,

<sup>8</sup>See also [104] where other possible criteria have been explored.

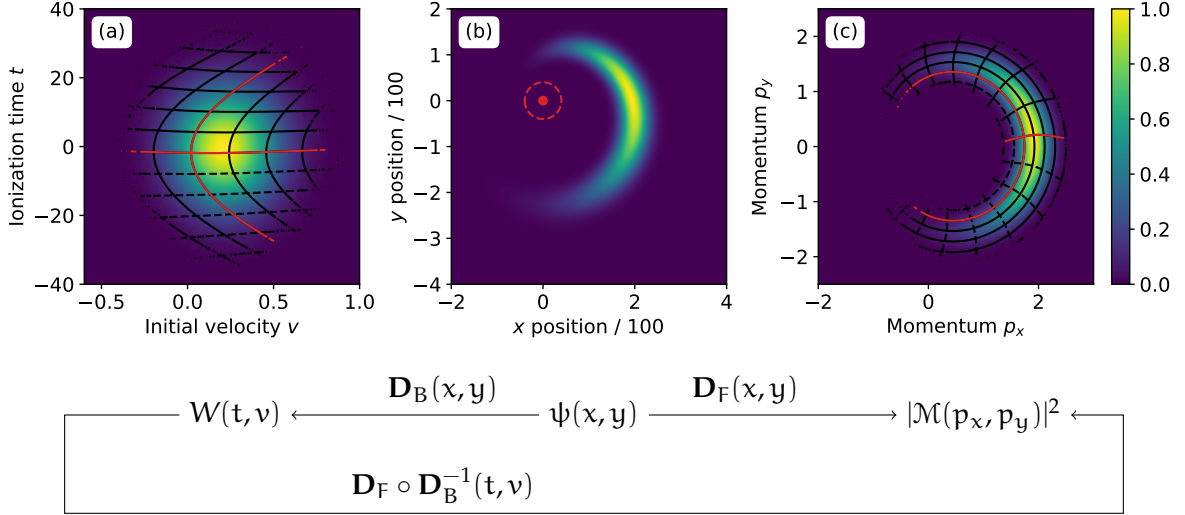


Figure 5.19: Classical backpropagation of an electron wave packet in the circular attoclock at  $E_0 = 0.1$  a.u. (a) Distribution of backpropagated trajectories in the space of initial conditions. (b) Electron wave packet at the end of the laser pulse. (c) Photoelectron momentum distribution calculated via forward propagation of the EWP in (b). All distributions are normalized to maximum signal 1. In (b) a mask has been used to remove the contribution from the bound state and isolate the wave packet. The horizontal contour lines in (a) indicate a fixed angle in the PMD with a spacing of  $20^\circ$  and the red line located at zero angle. The vertical contour lines indicate fixed radial momentum in (c) with spacing 0.2 a.u. and the red line at  $E_0/\omega \approx 1.76$  a.u. Radial contour lines in (c) show constant initial velocity with spacing 0.2 a.u. and the red line located at zero. Angular contour lines show constant time of ionization with a spacing of 5 a.u. and the red line located at zero. Dashed lines indicate negative values.

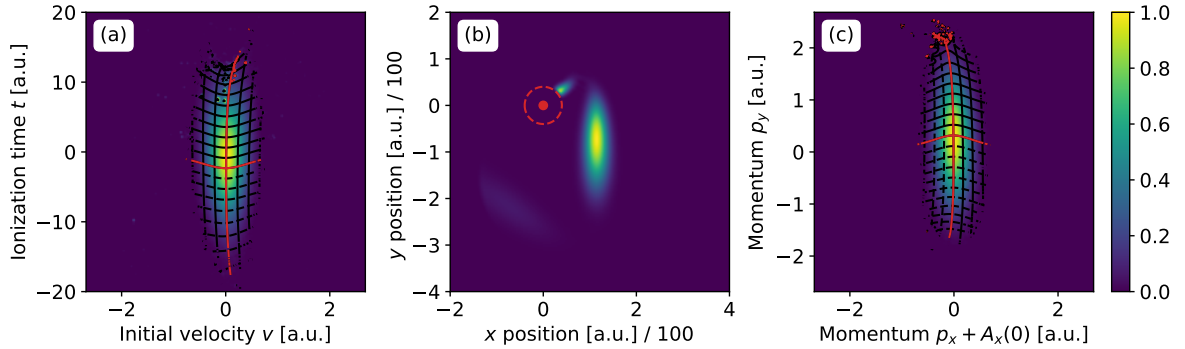


Figure 5.20: Classical backpropagation of an electron wave packet in the bicircular attoclock at  $E_0 = 0.1$  a.u. (a) Distribution of initial conditions. (b) Electron wave packet during the pulse. (c) Photoelectron momentum distribution. All distributions are normalized to maximum signal 1. In (b) a mask has been used to remove the contribution from the bound state and isolate the wave packet. Horizontal contour lines in (a) show a fixed value of the final  $p_y$  momentum with spacing 0.2 a.u. the red line at zero momentum. Vertical contour lines show fixed  $p_x$  momentum with spacing 0.2 a.u. and the red line at  $-A_x(0) \approx 1.67$  a.u. Vertical contour lines in (c) show fixed initial velocity with spacing 0.2 a.u. and the red line at zero velocity. Horizontal contour lines show constant time of ionization with spacing  $0.2/E_{\text{peak}} \approx 1.49$  a.u. and the red line at time zero.

the speed of the clock in the vicinity of the maximum is assumed to be  $dp_y/dt = E_{\text{peak}} \approx 0.134$  a.u. and initial velocity maps directly to final momentum,  $dp_x/dv = 1$  a.u. In (c), the contour lines are chosen by the same argument such that in the simple man's model they would form squares of equal size around the maximum. Using classical backpropagation to

evaluate the Jacobian at the maximum of the PMD we find

$$\begin{pmatrix} \frac{\partial p_x}{\partial t} & \frac{\partial p_x}{\partial v} \\ \frac{\partial p_y}{\partial t} & \frac{\partial p_y}{\partial v} \end{pmatrix} \approx \begin{pmatrix} -0.001 \text{ a.u.} & 0.896 \text{ a.u.} \\ 0.136 \text{ a.u.} & -0.007 \text{ a.u.} \end{pmatrix}. \quad (5.27)$$

The small values on the diagonal imply that the two coordinates are well separated. The fact that  $\partial p_x / \partial v < 1$  a.u. means that there is some focusing in velocity coordinate in the sense that the momentum distribution gets narrower compared to the distribution of initial conditions. In the time coordinate we find good agreement with the value from the simple man's model rather than the non-adiabatic SFA expression (5.11) which gives  $dp_y/dt \approx E_{\text{peak}} \sqrt{1 + \gamma_{\text{eff}}^2} \approx 0.154$  a.u. for the effective Keldysh parameter  $\gamma_{\text{eff}} \approx 0.571$  has to be taken into account. This is not surprising. Just like the simple man's model, classical backpropagation relies on vanishing tunnel-exit velocities in the instantaneous field direction whereas SFA includes such velocities. Writing this velocity as  $v_y(t) = p_y(t) + A_y(t)$ , we find from (5.11) that

$$v_y(0) = 0, \quad \frac{dv_y}{dt} \approx E_{\text{peak}} \left( \sqrt{1 + \gamma_{\text{eff}}^2} - 1 \right), \quad (5.28)$$

so in the the ascending quarter cycle the velocity is parallel to the acceleration of the photoelectron whereas in the descending quarter cycle the velocity is antiparallel to the acceleration. In the first case (lower part of the PMD) a backpropagating electron will reach zero velocity after it reaches the SFA velocity, leading to an earlier ionization time for a given momentum. In the second case (upper part of the PMD) the electron will reach zero velocity before turning around and reaching the SFA velocity, leading to a later ionization time. Thus there is a larger time range required to produce the entire PMD in classical backpropagation compared to SFA. This could be responsible for some of the artifacts in Fig. 5.20. In circular polarization on the other hand, the SFA predicts vanishing initial velocities in the instantaneous field direction and it was found that the distribution of initial conditions from backpropagation agrees very well with the SFA [103, 104]. The incompatibility of SFA initial conditions with the assumption of vanishing initial velocity when using backpropagation for (quasi) linear polarization could be mitigated by choosing a different tunnel-exit criterion. Some progress towards such a "non-adiabatic velocity criterion" was already made in [104]. However, we stick to the commonly used zero-velocity criterion here.

Fig. 5.21 shows the relative shifts and offset angles of the maxima obtained by forward propagation of the electron wave packet which are found to be in very good agreement with earlier results from the TDSE (shown in the background). In addition to this, classical backpropagation allows us to find the maximum of the instantaneous ionization rate  $W(t, v)$  and use the deflection function  $\mathbf{D}(t, v)$  to find the corresponding momenta and their angles/shifts. This is also shown in Fig. 5.21. In the circular attoclock, the angles corresponding to maximum (differential) ionization rate are always smaller compared to the Cartesian angles (and also smaller than the cylindrical ones). In the bicircular attoclock, we find that there is good agreement at low intensities whereas at higher intensities the shift corresponding to maximum rate is somewhat smaller.

To define the time of ionization, classical backpropagation gives us several possibilities. We can (i) find the initial conditions  $(t, v)$  that lead to the maximum of the momentum distribution,

$$(t_{\text{ion}}, v_{\text{ion}}) = \mathbf{D}^{-1} \left( \arg \max_{(p_x, p_y)} |\mathcal{M}(p_x, p_y)|^2 \right); \quad (5.29)$$

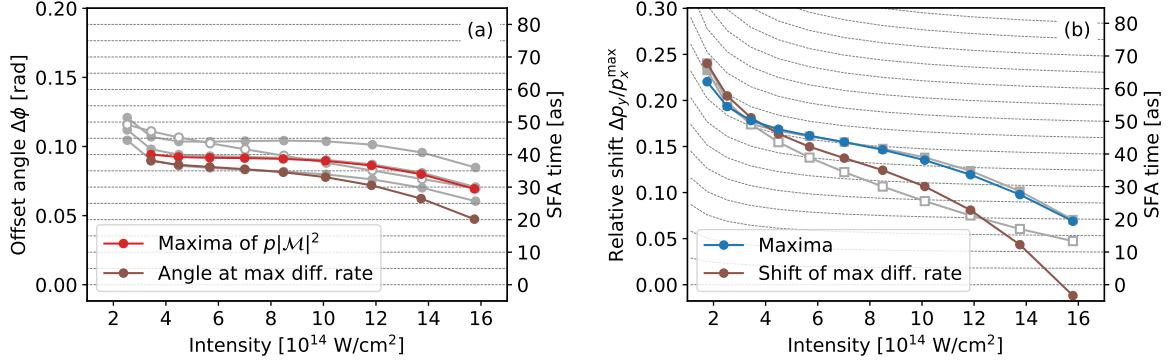


Figure 5.21: (a) Rotation angles of the maxima of the PMD in the circular attoclock obtained by forward propagation of an electron wave packet (red curve) and rotation angles of the momenta  $\mathbf{D}(t, \mathbf{v})$  that correspond to the maxima of the instantaneous double-differential ionization rate  $W(t, \mathbf{v})$  (brown curve). (b) Relative shifts in the bicircular attoclock obtained by forward propagation (blue curve) and relative shifts corresponding to the maximum of the instantaneous ionization rate (brown curve). In both panels, the curves from Fig. 5.6 are reprinted in gray.

(ii) find the maximum of the double-differential distribution  $W(t, \mathbf{v})$ ,

$$(t_{\text{ion}}, \mathbf{v}_{\text{ion}}) = \arg \max_{(t, \mathbf{v})} W(t, \mathbf{v}); \quad (5.30)$$

(iii) integrate over the initial velocity to find the most probable ionization time,

$$t_{\text{ion}} = \arg \max_t \int d\mathbf{v} W(t, \mathbf{v}). \quad (5.31)$$

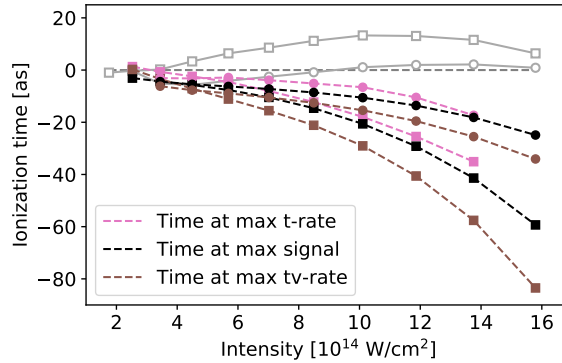


Figure 5.22: Ionization time from classical backpropagation. Squares show results for the bicircular attoclock and circles show results for the circular attoclock. Results are colored in black when obtained according to definition (5.29), brown when obtained according to definition (5.30) and purple when definition (5.31) is used. Curves from Fig. 5.9 are shown in gray in the background. Adapted from Fig. 3 in [245].

The results for all three possibilities are shown in Fig. 5.22. Independently of what definition is used, we find that the ionization time is generally zero for small intensities and negative for high intensities. Generally, the maximum of the double-differential rate gives the most negative values, the maximum of the integrated distribution the least negative and the time corresponding to the maximum of the PMD something in between. However, ionization times in the bicircular attoclock are always more negative compared to the circular attoclock when the same definition is used for both.

Apart from using the bicircular attoclock to mimic linear polarization, which is an experimentally feasible scheme, a half-cycle pulse could also be used, at least theoretically, to investigate ionization dynamics in linear polarization. This was done for a half-cycle in one dimension in [275]. There, the PMD was thought of being composed of classical trajectories that start at a predefined tunnel exit with vanishing velocity. Then, the instantaneous ionization rate  $W(t)$  was obtained such that the distribution of the final momenta of these classical trajectories matches the PMD. This is actually similar to classical backpropagation but not equivalent. By imposing an additional constraint (the tunnel exit position) it is possible to reproduce the PMD but not the intermediate (position-space) wave packet on the way to the detector. Classical backpropagation drops the constraint on the tunnel-exit position and is able to reproduce also the intermediate wave packet. The results are still similar. Negative ionization times were also found in [275] and we have verified that comparably large negative ionization times are obtained for a half-cycle pulse in 1D when classical backpropagation is used instead.

## 5.7 Analytical R-matrix theory

Another theoretical method that can be used to obtain a time-to-momentum mapping is analytical R-matrix theory (introduced in Section 2.5). It was applied to the (conventional) attoclock setup in [78, 94, 240] and lead to the conclusion that the maximum of the PMD corresponds well to the time of peak field strength.

Although ARM theory uses trajectories that are not influenced themselves by the atomic potential, the attoclock rotation of the momentum distribution is present in the theory. This is the case even if the unperturbed SFA saddle-point  $t_s$  from (2.29) is used to evaluate the action (2.42). It can be understood intuitively in terms of complex-step differentiation [276]. For a function  $f$  that is real on the real axis, its derivative can be estimated accurately using

$$\text{Im}f(x + ih) = f'(x) h + \mathcal{O}(h^3). \quad (5.32)$$

When the standard integration path from  $t_s$  down to the real axis  $t_r = \text{Re } t_s$  and then to the final time  $T$  is chosen, the Coulomb correction (2.43) in the ARM action (2.42) can be split in an under-the-barrier and beyond-the-barrier contribution,<sup>9</sup>

$$S_{C1}(\mathbf{p}, t_s) = \int_{t_s - i\kappa^{-2}}^{t_r} dt' V(\mathbf{r}_L(t'; \mathbf{p}, t_s)), \quad S_{C2}(\mathbf{p}, t_s) = \int_{t_r}^T dt' V(\mathbf{r}_L(t'; \mathbf{p}, t_s)). \quad (5.33)$$

In the second part, we split the outgoing electron trajectory into its real and (constant) imaginary part,

$$\text{Im } S_{C2}(\mathbf{p}, t_s) = \int_{t_r}^T dt' \text{Im } V(\text{Re } \mathbf{r}_L(t'; \mathbf{p}, t_s) + i \text{Im } \mathbf{r}_L(t_r; \mathbf{p}, t_s)). \quad (5.34)$$

Note that the imaginary part of the electron trajectory satisfies

$$\begin{aligned} \text{Im } \mathbf{r}_L(t_r; \mathbf{p}, t_s) &= \text{Im} \int_{t_s}^{t_r} dt (\mathbf{p} + \mathbf{A}(t)) \\ &= \nabla_{\mathbf{p}} \text{Im} \left\{ -I_p t_s + \frac{1}{2} \int_{t_s}^T dt (\mathbf{p} + \mathbf{A}(t))^2 \right\} = \nabla_{\mathbf{p}} \text{Im } S_{\text{SFA}}(\mathbf{p}, t_s). \end{aligned} \quad (5.35)$$

<sup>9</sup>It is not always possible to evaluate the Coulomb correction along this path because sometimes there is an intersection with a branch cut [148, 258]. For the attoclock in the vicinity of the maximum, however, this is usually not the case.

Here, we could replace  $t_r$  by  $T$  in the upper limit of the integral because all contributions to the integral between  $t_r$  and  $T$  are real. In the vicinity of a maximum of the PMD, the gradient is small. Using complex-step differentiation, we can now relate the potential being evaluated on a *complex* trajectory to a force evaluated on a *real* trajectory:

$$\begin{aligned} & \int_{t_r}^T dt' \operatorname{Im} V(\operatorname{Re} \mathbf{r}_L(t'; \mathbf{p}, t_s) + i \operatorname{Im} \mathbf{r}_L(t_r; \mathbf{p}, t_s)) \\ & \approx \nabla_{\mathbf{p}} \operatorname{Im} S_{\text{SFA}}(\mathbf{p}, t_s) \cdot \underbrace{\int_{t_r}^T dt' \nabla V(\operatorname{Re} \mathbf{r}_L(t'; \mathbf{p}, t_s))}_{-\Delta \mathbf{p}}. \end{aligned} \quad (5.36)$$

Here, the integral encodes the accumulated classical force  $\Delta \mathbf{p}$  acting on the electron on the outgoing trajectory. Now the complete action can be written as

$$\begin{aligned} \operatorname{Im} S_{\text{ARM}}(\mathbf{p}, t_s) & \approx \operatorname{Im} S_{\text{SFA}}(\mathbf{p}, t_s) - \Delta \mathbf{p} \cdot \nabla_{\mathbf{p}} \operatorname{Im} S_{\text{SFA}}(\mathbf{p}, t_s) + \operatorname{Im} S_{\text{C1}}(\mathbf{p}, t_s) \\ & \approx \operatorname{Im} S_{\text{SFA}}(\mathbf{p} - \Delta \mathbf{p}, t_s) + \operatorname{Im} S_{\text{C1}}(\mathbf{p}, t_s) \end{aligned} \quad (5.37)$$

and taking the under-the-barrier contribution aside, the beyond-the-barrier contribution of the Coulomb-correction leads to a shift of the maximum of the PMD by  $\Delta \mathbf{p}$ . Since for the attoclock the under-the-barrier contribution is forward-backward symmetric in time, it does not by itself lead to an attoclock offset angle (although it influences the observed angle when the beyond-the-barrier contribution is taken into account). It follows that when the potential is zero (sufficiently small) already when the under-the-barrier motion is completed, the attoclock offset angle is zero. This is usually the case for a short-range potential where zero offset is nicely confirmed by the TDSE [78, 226, 277].

To define the ionization time at the maximum of the PMD, note that the modification of the action (2.42) by the Coulomb correction suggests a modification of the saddle point time  $t_s$ . This was used by Torlina et al. [78, 147] to define the ionization time for a given momentum  $\mathbf{p}$  within ARM theory as a stationary point of the boundary-matched action,

$$\left. \frac{\partial}{\partial t} S_{\text{SFA}}(\mathbf{p}, t) \right|_{t=t_s} + \left. \frac{\partial}{\partial t} S_{\text{C}}(\mathbf{p}, t) \right|_{t=t_s} = 0. \quad (5.38)$$

Arguing that the Coulomb correction is small, they used this equation to derive a first-order correction to the SFA saddle point as  $t_s = t_s^{(0)} + \Delta t_{\text{C}}$  with

$$\Delta t_{\text{C}} = - \frac{\partial_t S_{\text{C}}(\mathbf{p}, t_s^{(0)})}{\partial_t^2 S_{\text{SFA}}(\mathbf{p}, t_s^{(0)})}. \quad (5.39)$$

This expression was then used to find the time-to-momentum mapping for the attoclock. In this section, we apply ARM theory to the bicircular attoclock. Potential, pulse shape, envelope and parameters are chosen exactly as for the TDSE calculations in Section 5.3.

First, we obtain the momentum distribution (2.41) within ARM theory and its maximum for every intensity.<sup>10</sup> The relative shift of this maximum in  $p_y$  direction is shown in Fig. 5.23(b).

<sup>10</sup>The PMD has been evaluated in the way presented by Pisanty [148], i.e. including the prefactor  $\propto 1/\sqrt{\dot{S}(\mathbf{p}, t_s)}$  and using the unperturbed saddle-point  $t_s^{(0)}$  in the action (2.42), noting that a first-order correction to the saddle point can change the result only to second order. This is slightly different from the version used by Torlina et al. in [78, 147] where the first-order corrected saddle point (5.39) was used to evaluate the action but the prefactor was neglected. There, it was argued that the prefactor has no angular dependence and cannot influence angle-resolved spectra. However, already from Section 4.5 we know that multiplying the PMD with radial factors does influence the angle at which the maximum is found.



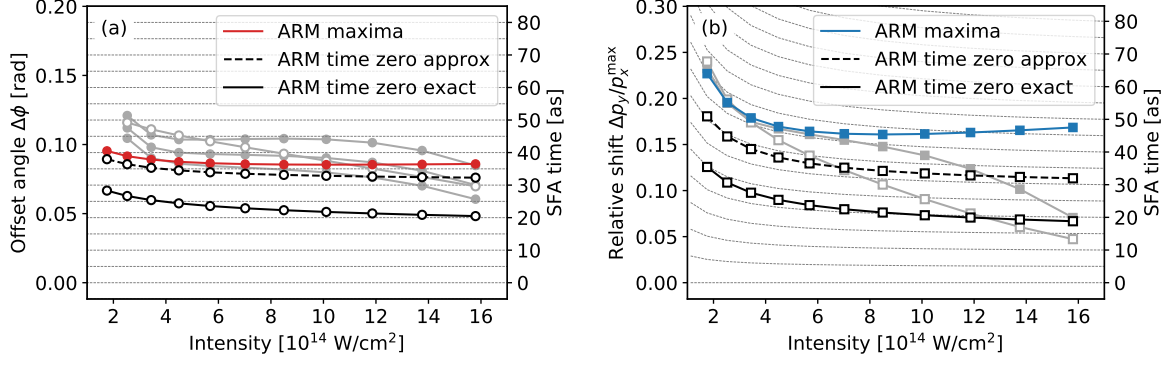


Figure 5.23: (a) Rotation angles of the PMD maxima (including prefactor  $p$ ) in the circular attoclock from ARM theory (red curve) and rotation angles of the momenta that correspond to time zero (black curves). (b) Relative shifts in the bicircular attoclock from ARM theory (blue curve) and relative shifts that correspond to time zero (black curves). In both panels, the dashed black line gives the first-order approximation (5.39) and the solid black line gives the exact solution of the saddle-point equation (5.38). The curves from Fig. 5.6, showing the TDSE result, are reprinted in gray.

For comparison, Fig. 5.23(a) shows the corresponding offset angle in the circular attoclock (5.13). Second, we find the relative shift (or the rotation angle in the circular attoclock) that according to (5.38) is attributed to time zero. More precisely, for the bicircular attoclock, we choose the classically expected value  $p_x = E_{\text{peak}}/(2\omega)$  and search  $p_y$  such that  $\text{Re } t_s = 0$ . For the circular attoclock, the radial momentum  $p$  is chosen as the maximum of the PMD obtained for a cw field from saddle-point SFA neglecting the prefactor [260] and the angle is tuned such that  $\text{Re } t_s = 0$ . We evaluate both the first-order correction to the SFA saddle-point time (5.39) as well as the full solution according to the definition (5.38). We find that the relative shift derived from the full solution is actually significantly smaller compared to both the PMD maximum and the shift derived from the first-order correction to the SFA saddle-point. This is also the case for the rotation angle in the circular attoclock.

To understand the origin of this discrepancy, one has to go back to the expression for the ionization amplitude (2.35) from which ARM theory is derived. Inserting the eikonal-Volkov propagator (2.36) and collecting all terms in the exponential, the action can be written as (5.50) where  $\mathbf{r}(\phi) = a(\cos(\phi), \sin(\phi))$  is restricted to points on the boundary that separates the inner and the outer region at radius  $a$  in the tunneling barrier [93]. With the action parameterized by  $t$  and  $\phi$ , we solve the saddle-point equations

$$\left. \frac{\partial}{\partial t} S(\mathbf{p}, t, \mathbf{r}(\phi_a)) \right|_{t=t_a} = 0, \quad \left. \frac{\partial}{\partial \phi} S(\mathbf{p}, t_a, \mathbf{r}(\phi)) \right|_{\phi=\phi_a} = 0 \quad (5.40)$$

numerically for different matching radii  $a$  and obtain the momenta  $\mathbf{p}$  for which  $\text{Re } t_a = 0$ .

For the circular attoclock, the rotation angle that corresponds to time zero is shown in Fig. 5.24(a). The angle shows a strong dependence on the matching radius  $a$  such that no physical angle can be defined. However, introducing a perturbation parameter  $\alpha$  and replacing  $V \rightarrow \alpha V$  in (2.39), we can construct a first-order approximation

$$t_a^{(1)} = t_a^{(0)} + 1 \cdot \left. \frac{\partial t_a(\alpha)}{\partial \alpha} \right|_{\alpha=0} \quad (5.41)$$

which is shown to be independent of the matching radius in Fig. 5.24(b) and allows for the definition of a physical rotation angle. This result is not entirely surprising since the Eikonal-

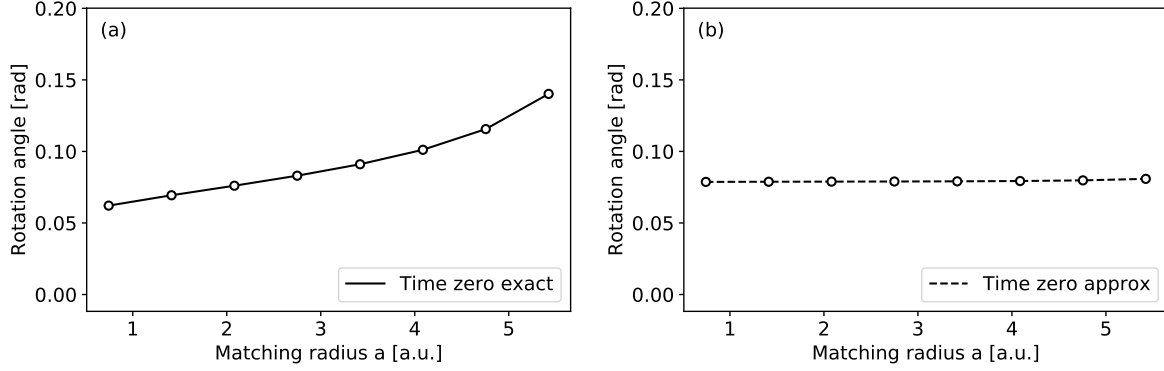


Figure 5.24: Boundary-dependence of the angle that corresponds to time zero in the circular attoclock at  $E_0 = 0.10$  a.u. (a) Exact solution of (5.40) with the action (2.39). (b) First-order approximation according to (5.41).

Volkov Ansatz takes the potential into account only approximately via a linear term in the action.

Going back to the action (2.42) from which the saddle points were obtained originally, we note that the lower limit in the Coulomb integral  $t_s - i\kappa^{-2}$  is obtained only after matching the Coulomb phase in the action to the asymptotic tail of the bound-state wave function. Since the boundary-matching effectively introduces a choice of the matching radius  $a_0 = 1/\kappa$  (see Appendix A.4.2), an exact solution of the saddle-point equation produces a value at the lower end of the curve in Fig. 5.24(a) which is too small. Thus one can say that when solving the saddle-point equation (5.38), it is not true that a first-order solution can be used because the influence of the potential is small. Rather, the consistent first-order solution must be used because it is the only way to extract a meaningful quantity from the boundary-matched action. Still, the strong dependence of the rotation angle in Fig. 5.24(a) raises the question about how good the assumption of ARM theory about the linear correction to the action being sufficient in the tunneling region really is. Moreover, we note that even the first-order solution in Fig. 5.23 gives angles and shifts that are smaller than the angles and shifts of the PMD maxima.

It is possible to derive a quadratic correction to the action. We start from the semiclassical propagator (2.48) which gives an action

$$S_{\text{SC}}(\mathbf{p}, T; \mathbf{r}, t) = \dot{\mathbf{r}}_N(t) \cdot \mathbf{r} + \int_t^T dt' \left\{ \frac{1}{2} \dot{\mathbf{r}}_N(t')^2 + V(\mathbf{r}_N(t')) - \mathbf{r}_N(t') \cdot \nabla V(\mathbf{r}_N(t')) \right\} \quad (5.42)$$

evaluated along the Newtonian trajectory

$$\ddot{\mathbf{r}}_N(t') = -\nabla V(\mathbf{r}_N(t')) - \mathbf{E}(t'), \quad \mathbf{r}_N(t) = \mathbf{r}, \quad \dot{\mathbf{r}}_N(T) = \mathbf{p} \quad (5.43)$$

with initial position  $\mathbf{r}$  and final momentum  $\mathbf{p}$ . Integrating once and assuming the pulse is over at time  $T$  such that  $\mathbf{A}(T) = 0$ , the electron velocity becomes

$$\dot{\mathbf{r}}_N(t') = \mathbf{p} + \mathbf{A}(t') + \int_{t'}^T dt'' \nabla V(\mathbf{r}_N(t'')). \quad (5.44)$$

Using this expression, the action can be rewritten as (see Appendix A.4.4)

$$S_{\text{SC}}(\mathbf{p}, T; \mathbf{r}, t) = (\mathbf{p} + \mathbf{A}(t)) \cdot \mathbf{r} + \int_t^T dt' \frac{1}{2} (\mathbf{p} + \mathbf{A}(t'))^2 + \int_t^T dt' V(\mathbf{r}_N(t')) - \frac{1}{2} \int_t^T dt' \left( \int_{t'}^T dt'' \nabla V(\mathbf{r}_N(t'')) \right)^2. \quad (5.45)$$

We want to include only terms up to quadratic order in the potential  $V$ . Since the last term in the action is already squared, we can replace the full trajectory  $\mathbf{r}_N(t')$  with the Coulomb-free trajectory

$$\mathbf{r}_0(t') = \mathbf{r} + \int_t^{t'} dt'' (\mathbf{p} + \mathbf{A}(t'')). \quad (5.46)$$

For the linear term, we have to take the first-order correction of the trajectory due to the potential into account. Writing

$$\mathbf{r}_N(t') = \mathbf{r}_0(t') + \int_t^{t'} dt'' \int_{t''}^T dt''' \nabla V(\mathbf{r}_N(t''')) \quad (5.47)$$

we find up to quadratic order

$$\begin{aligned} \int_t^T dt' V(\mathbf{r}_N(t')) &= \int_t^T dt' V(\mathbf{r}_0(t')) \\ &+ \int_t^T dt' \nabla V(\mathbf{r}_0(t')) \cdot \int_t^{t'} dt'' \int_{t''}^T dt''' \nabla V(\mathbf{r}_0(t''')). \end{aligned} \quad (5.48)$$

Using partial integration, this can be expressed as

$$\begin{aligned} \int_t^T dt' V(\mathbf{r}_N(t')) &= \int_t^T dt' V(\mathbf{r}_0(t')) \\ &+ \int_t^T dt' \left( \int_{t'}^T dt'' \nabla V(\mathbf{r}_0(t'')) \right)^2 \\ &- \int_{t'}^T dt'' \nabla V(\mathbf{r}_0(t'')) \cdot \int_t^{t'} dt'' \int_{t''}^T dt''' \nabla V(\mathbf{r}_0(t''')) \Big|_t^T. \end{aligned} \quad (5.49)$$

The boundary term vanishes while the term in the second line adds to the last term in (5.45). Thus, the action including quadratic terms in  $V$  becomes

$$\begin{aligned} S_{SC}(\mathbf{p}, T; \mathbf{r}, t) &= (\mathbf{p} + \mathbf{A}(t)) \cdot \mathbf{r} + \int_t^T dt' \frac{1}{2} (\mathbf{p} + \mathbf{A}(t'))^2 \\ &+ \int_t^T dt' V(\mathbf{r}_0(t')) + \frac{1}{2} \int_t^T dt' \left( \int_{t'}^T dt'' \nabla V(\mathbf{r}_0(t'')) \right)^2. \end{aligned} \quad (5.50)$$

When the phase evolution of the bound state is also incorporated into the action, the result is equivalent to the action used in ARM theory (2.39), the only difference being a new quadratic term that can be evaluated along the Coulomb-free electron trajectory.

Including this term in the action and solving the saddle-point equation (5.40), we find that the attoclock rotation angle corresponding to time zero still depends on the matching radius, see Fig. 5.25(a). However, constructing a second-order estimate,

$$t_a^{(2)} = t_a^{(0)} + 1 \cdot \left. \frac{\partial t_a(\alpha)}{\partial \alpha} \right|_{\alpha=0} + 1^2 \cdot \frac{1}{2} \left. \frac{\partial^2 t_a(\alpha)}{\partial \alpha^2} \right|_{\alpha=0}, \quad (5.51)$$

we find independence of the boundary and a well-defined rotation angle that is larger than the first-order estimate (5.51) that takes the potential into account only via the linear term, see Fig. 5.25(b).

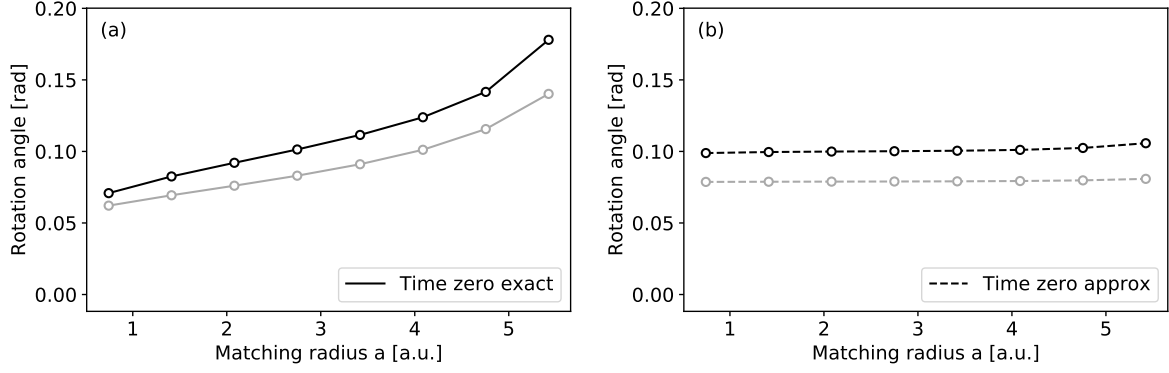


Figure 5.25: Boundary-dependence of the angle that corresponds to time zero in the circular attoclock at  $E_0 = 0.10$  a.u. (a) Exact solution of (5.40) with the action (5.50) that includes the potential in a linear and a quadratic term. The gray line is reprinted from Fig. 5.24(a) and gives the exact solution to the same equation but with the action (2.39) that includes the potential only via the linear term. (b) Second-order approximation according to (5.51). The gray line is reprinted from Fig. 5.24(b) and gives the first-order approximation according to (5.41).

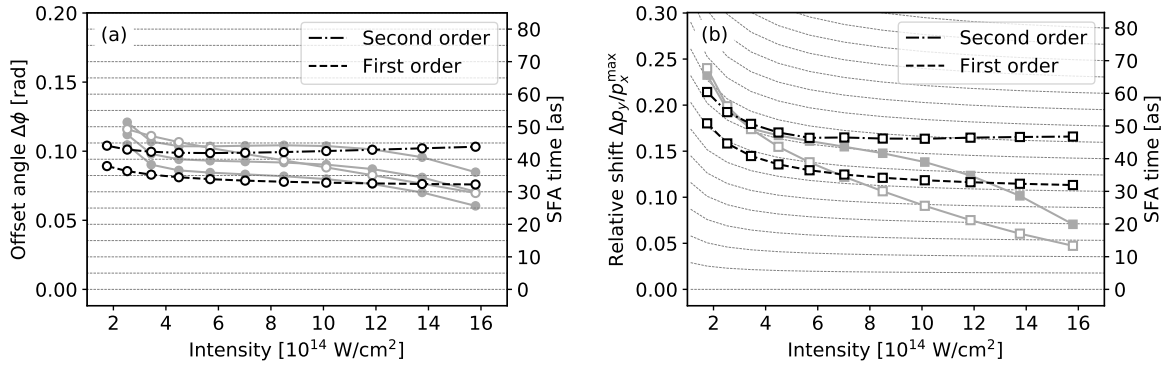


Figure 5.26: (a) Rotation angles of the momenta that correspond to time zero in the circular attoclock. (b) Relative shifts in the bicircular attoclock. In both panels, the dashed line gives the first-order estimate (5.41) using the linear term in the action while the dot-dashed line shows the second-order estimate (5.51) employing also the quadratic term in the action. The curves from Fig. 5.6 are reprinted in gray.

The boundary-independent first- and second-order estimates are shown in Fig. 5.26 for all intensities. We find that the first-order version consistently reproduces the saddle points calculated previously using the boundary-matched action (Fig. 5.23), while the second-order estimate gives larger angles and shifts that give somewhat better agreement with the angles and shifts obtained directly from the TDSE.

## 5.8 Eikonal approximation in the Dyson integral

Instead of applying the eikonal-Volkov approximation to the ARM expression for the ionization amplitude (2.35), it is also possible to apply it directly to the Dyson expression (4.1) as was demonstrated by Klaiber for a half-cycle pulse and a 1D model atom [278].

Approximating the bound-state wave function by its (2D) asymptote  $\psi_0(\mathbf{r}) \propto r^{\nu-1/2} e^{-\kappa r}$  with  $\nu = Z/\kappa$ , the ionization amplitude (in length gauge) becomes

$$\mathbf{M}(\mathbf{p}) \propto -i \int_0^T dt \int d^2r e^{-iS(\mathbf{p},t,r)} (\mathbf{E}(t) \cdot \mathbf{r}) r^{\nu-1/2} e^{-\kappa r}. \quad (5.52)$$

Here, the action  $S$  is the same as in Eq. (2.39), containing the kinetic part from standard SFA, the phase evolution of the bound state, and the Coulomb correction as in ARM theory. Here, the quadratic term from (5.50) that we derived from the semiclassical propagator (2.48) can also be included.<sup>11</sup> The entire integrand is then written as an exponential

$$\mathbf{M}(\mathbf{p}) \propto -i \int_0^T dt \int d^2\mathbf{r} e^{-iS_{\text{tot}}(\mathbf{p}, t, \mathbf{r})} \quad (5.53)$$

with

$$S_{\text{tot}}(\mathbf{p}, t, \mathbf{r}) = S(\mathbf{p}, t, \mathbf{r}) + i \log(\mathbf{E}(t) \cdot \mathbf{r}) + i(\nu - 1/2) \log r - i\kappa r. \quad (5.54)$$

The ionization time can now be defined as stationary point of the total action via

$$\left. \frac{\partial}{\partial t} S_{\text{tot}}(\mathbf{p}, t, \mathbf{r}_s) \right|_{t=t_s} = 0, \quad \nabla_{\mathbf{r}} S_{\text{tot}}(\mathbf{p}, t_s, \mathbf{r})|_{\mathbf{r}=\mathbf{r}_s} = 0. \quad (5.55)$$

Compared to ARM theory, this is much closer to our trajectory-free definition (4.3) in the sense that not only the action, but also the non-exponential part is considered in the saddle-point equation. The main difference to our exact calculation, apart from using the eikonal-Volkov approximation and the asymptotic expression for the bound state, is that an additional saddle-point approximation in the spatial integral is employed.

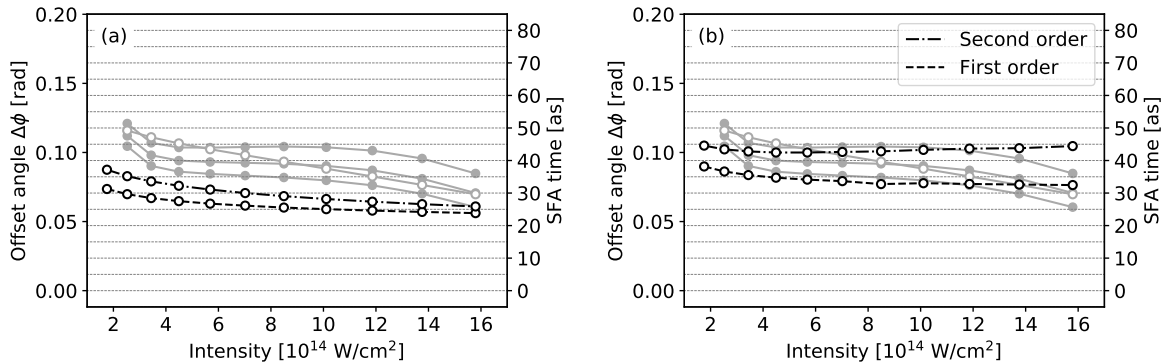


Figure 5.27: Rotations angles of momenta corresponding to time zero in the circular attoclock according to (5.55). (a) Exact solution. (b) Approximate solution. In both panels, the dashed line corresponds to angles obtained from the action (2.39) including terms linear in  $V$  while for the dot-dashed line also the quadratic term (5.50) has been included.

Again, we solve the saddle-point equations numerically to find the angles that correspond to  $\text{Re } t_s = 0$ . For the circular attoclock, the result is shown in Fig. 5.27(a) for an exact solution of (5.55) and in Fig. 5.27(b) using a first or second-order expansion around the potential-free saddle point. Our ability to evaluate an exact solution stems from the fact that instead of choosing a boundary as in ARM theory and fixing the distance to the core, the additional saddle point equation for the position coordinate selects an initial position  $\mathbf{r}_s$  within the tunneling barrier automatically, eliminating the ambiguity due to arbitrary choice of the matching radius. The

<sup>11</sup>The quadratic term was also found in the 1D study [278] using the eikonal approximation. There, another term was found that includes the Laplacian of the potential. This term was called a “quantum term” because it is of order  $\hbar^0$  whereas the quadratic correction also found from the semiclassical propagator is of order  $1/\hbar$ . For the Coulomb potential in 3D, the quantum term does not contribute since  $\Delta(1/r) = -\delta(r)/r^2$ . In 2D, the term would contribute but we neglect it in the present study.

imaginary part of the corresponding saddle-point time  $t_s$  is somewhere between the Keldysh time and the real axis, reflecting the reduced distance the electron has to travel in imaginary time to reach the tunnel exit position compared to boundary-matched ARM theory where it starts at the origin.

We find that the exact solution in Fig. 5.27(a) is still too small by some extent, while the approximate solutions in Fig. 5.27(b) are almost indistinguishable from the ARM results in Fig. 5.26. Both show some disagreement with the trajectory-free ionization times. Thus, we conclude that the difference is probably not due to a fundamentally different saddle-point equation, but rather due to the approximations made in the integral. Already in Section 5.4 we have seen that the structure of stationary points in the complex plane is significantly altered by the fact that there can be bound-state dynamics after the interaction operator has acted on the bound state. This is neglected when the eikonal-Volkov approximation is used.

## 5.9 Conclusion

In this chapter, an in-depth analysis of photoelectron momentum distributions from strong-field ionization with two types of fields has been provided, a circular laser field and a bicircular laser field of field-strength ratio 2 : 1 of fundamental to second harmonic (quasilinear field). The bicircular field approximates linear polarization close to the time of peak field strength while the shape of the vector potential resembles an attoclock. Absence of intracycle interference, rescattering, and geometrical effects lead to a very easy to analyze signal that allows us to study the region of the momentum distribution that corresponds to ionization close to the time of peak field strength. The momentum distribution shows an attoclock shift from which we retrieved the most probable ionization time using the trajectory-free method based on the Dyson integral presented in Chapter 4. We found that in the quasilinear field the ionization time can show a small ionization-time delay of approximately 10 attoseconds with respect to the time of peak field strength that is not present in circular polarization.

The ionization time retrieved from the Dyson integral is similar, but not equivalent to the one obtained using analytical R-matrix theory. There, ionization time is also defined as a stationary point of an integral representation of the ionization amplitude, but the ansatz is fundamentally different. While the integration variable in the Dyson integral marks the interaction time with the electric field, the integration variable in ARM theory marks the time of transition through a boundary. Despite this conceptual difference, the retrieved ionization times behave very similarly when the eikonal-Volkov approximation is used instead of a full numerical evaluation. This is still true when a quadratic correction to the action based on a semiclassical propagator is employed. The differences emerge when going beyond these approximations. By evaluating the Dyson integrand in the complex plane numerically, we showed that around a given ionization time there is a fundamental asymmetry between earlier and later times due to bound-state dynamics that is not present when the eikonal-Volkov approximation is used. We believe that this is connected to the fact that the structure of stationary points is altered. In this context, we note that a weakness of the Dyson expression in terms of physical interpretation is the field-free time evolution of the bound state before the interaction time. When this does not adequately reflect the true time evolution, it must be compensated by the time evolution after the interaction time, as the result of the Dyson integral is exact.

It could be possible to derive a better splitting between free time evolution and interaction in the Dyson expression that takes the phase-evolution and depletion of the bound state into account. The stationary points of that expression could lead to an even better definition of trajectory-free ionization time. Alternatively, it could be possible to evaluate the stationary points of the R-matrix Ansatz (2.35) fully numerically. This would involve a full solution of the TDSE in the inner region and circumvent the problem of approximating the true time evolution by field-free time evolution. However, two challenges would have to be overcome. First, the wave function in the inner region must be evaluated numerically in complex time. This involves propagation in the direction of positive imaginary time which is inherently unstable. Second, the propagator from the R-matrix surface to the final momentum must be evaluated. It is not obvious how to achieve this efficiently in complex time when the potential is taken into account nonperturbatively. Additionally – although it is clear that the ionization amplitude is independent of the boundary radius – it would have to be checked that the ionization times are, too.<sup>12</sup>

## 5.10 Outlook

Coming back to tailored fields in general, we note that the counter-rotating bicircular field of field-strength ratio 2 : 1 is not all that they have to offer for the attoclock idea. For example, a tricircular  $\omega - 2\omega + 4\omega$  field [279] can be used to approximate a linearly polarized field even better than the bicircular  $\omega - 2\omega$  field considered in this chapter. Indeed, the electric field (shown in Fig. 5.28(b)) derived from the vector potential (Fig. 5.28(a))

$$\mathbf{A}(t) = -\frac{16}{\sqrt{357}} \frac{E_0}{\omega} \left[ \begin{pmatrix} \cos(\omega t) \\ \sin(\omega t) \end{pmatrix} + \frac{5}{16} \begin{pmatrix} -\cos(2\omega t) \\ \sin(2\omega t) \end{pmatrix} + \frac{1}{64} \begin{pmatrix} \cos(4\omega t) \\ \sin(4\omega t) \end{pmatrix} \right] \quad (5.56)$$

satisfies<sup>13</sup>  $\mathbf{E}(t) = E_{\text{peak}} \cos(\omega_{\text{eff}} t) \mathbf{e}_y + \mathcal{O}(t^4)$  with peak field strength  $E_{\text{peak}} = 9\sqrt{3/119} E_0 \approx 1.429 E_0$  and effective frequency is  $\omega_{\text{eff}} = 2\sqrt{2/3} \omega \approx 1.633 \omega$ .

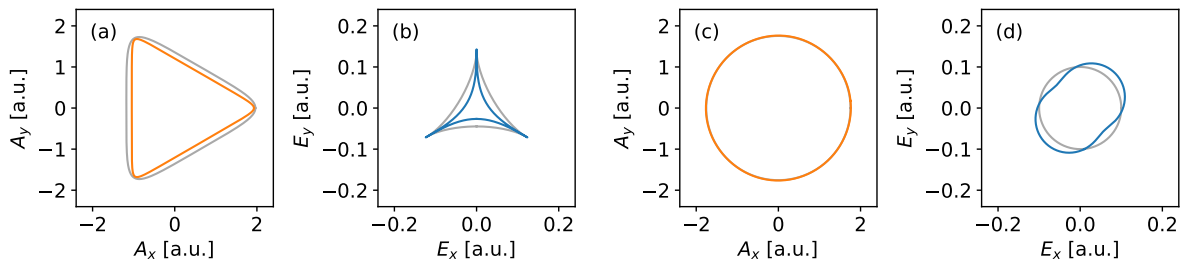


Figure 5.28: (a) Vector potential of the “tricircular attoclock” (5.56) at  $E_0 = 0.1$  a.u. and 800 nm wavelength (orange curve). The gray line shows the “bicircular attoclock” (5.3) at the same intensity and the same wavelength. (b) Electric field strength. The blue curve shows the tricircular field and the gray curve shows the bicircular field. (c) Vector potential (5.57) for the “variable-speed attoclock” at  $E_0 = 0.1$  a.u., 800 nm wavelength and  $\epsilon = 0.05$ . The gray line shows the vector potential for  $\epsilon = 0$ . (d) Electric field strength. The blue curve shows the tailored field and the gray curve shows the circular field.

<sup>12</sup>That is to say, the real part of the saddle-point time. The imaginary part should depend on the boundary radius because the electron must traverse real distance with imaginary velocity.

<sup>13</sup>Around the time of peak field strength, this is one order better than the bicircular field (5.4).

Another possibility is the “variable-speed attoclock.” It is possible to devise a field shape where the vector potential lies on a circle but it is traversed with variable angular speed. The vector potential

$$\mathbf{A}(t) = -\frac{E_0}{\omega} \left[ \begin{pmatrix} \cos(\omega t) \\ \sin(\omega t) \end{pmatrix} + \epsilon \begin{pmatrix} \sin(\omega t) \\ \cos(\omega t) \end{pmatrix} + \epsilon \begin{pmatrix} -\sin(3\omega t) \\ \cos(3\omega t) \end{pmatrix} \right] \quad (5.57)$$

satisfies  $A(t) = E_0/\omega + \mathcal{O}(\epsilon^2)$  and  $\angle(A_x(t), A_y(t)) = \pi + \omega t + 2\epsilon \cos(2\omega t) + \mathcal{O}(\epsilon^3)$ . Because of the variable speed, the field strength  $E(t) = E_0 - 4\epsilon E_0 \sin(2\omega t) + \mathcal{O}(\epsilon^2)$  is time dependent. First calculations using ARM theory seem to indicate that in this field the ambiguity in the attoclock offset angle is mitigated. A similar situation can be created noting that close to the field maximum, generally a pulse envelope leads to a vector potential that is curved stronger than a circle while a nonzero ellipticity leads to a vector potential that is curved less. At the right value of the ellipticity, the effect of the pulse envelope can be compensated. For example, for a two-cycle  $\sin^4$  envelope, the vector potential

$$\mathbf{A}(t) = -\frac{E_0}{\omega} \cos\left(\frac{\omega t}{4}\right)^4 \begin{pmatrix} \cos(\omega t) \\ \sin(\omega t)\sqrt{5}/2 \end{pmatrix} \quad (5.58)$$

satisfies  $A(t) = E_0/\omega + \mathcal{O}(t^4)$ , i.e. it lies on a circle in the vicinity of the maximum at  $t = 0$ . More realistically, the envelope is applied to the electric field. For a two-cycle  $\cos^2$  pulse, the electric field

$$\mathbf{E}(t) = E_0 \cos\left(\frac{\omega t}{4}\right)^2 \begin{pmatrix} \cos(\omega t) \\ \sin(\omega t)\sqrt{3}/2 \end{pmatrix} \quad (5.59)$$

leads to  $A(0) = 2\sqrt{3}/3 E_0/\omega \approx 1.15 E_0/\omega$  and  $A(t) = A(0) + \mathcal{O}(t^4)$ .



## Chapter 6

# Streaking with tailored fields

After transferring the concept of the attoclock to linear polarization, in this chapter we apply streaking to the quasilinear field provided by the bicircular attoclock. This allows us to improve upon the ionization time retrieval in several ways and unify the two previously distinct notions of ionization time provided by the attoclock for circular polarization and streaking for linear polarization. Most results from this chapter are published in [280].

### 6.1 Introduction

Ionization-time measurements in strong-field ionization have previously relied either on streaking (see Chapter 3) or on the attoclock (see Chapter 4). It is important to understand how these two different notions of ionization time are related.

A direct comparison is problematic because the attoclock measures ionization time in circular polarization while streaking can only be applied to linear polarization where it has strong limitations such as the inability to resolve low-energy electrons (because of strong Coulomb effects), high-energy electrons (because there is overlap with the onset of the backscattering plateau) or photoelectrons originating in the rising slope of the electric field (because they are hidden under the Coulomb-focused long trajectories). This is true for both the two-color scheme presented by Henkel and Lein [114] and extend upon in Chapter 3 as well as in the parallel two-color scheme presented by Porat et al. [115]. Similarly, in the HHG-based scheme [112, 113], electrons launched during the rising slope of the field cannot recombine and consequently cannot be resolved.

Part of the problem has been solved in Chapter 5, where we have implemented an attoclock using bicircular fields and transferred the attoclock concept to (quasi) linear polarization. In this Chapter, we apply streaking to the quasilinear field provided by the bicircular attoclock which allows us to compare the two approaches directly. Here, we consider both the orthogonal scheme as described in Chapter 4 as well as the parallel scheme from Porat et al. [115].

The fact that the quasilinear field points in an approximately constant direction near the time of ionization leads to another advantage that is absent from the circular attoclock. It enables us to probe orientation-dependent properties of anisotropic systems such as molecules without mixing contributions from different angles between molecular axis and polarization axis. Here, we apply the quasilinear field to an asymmetric potential resembling the polar helium hydride molecular ion to measure the time of ionization for both possible orientations.

The chapter is organized as follows. While a derivation of the time-to-phase mapping in orthogonal streaking was provided already in Chapter 3, the corresponding mapping for the parallel scheme has yet to be derived. Thus, in Section 6.2 we consider the parallel scheme in the framework of the strong-field approximation. Section 6.3 then gives the details of applying both the orthogonal and the parallel scheme to the quasilinear field. In Section 6.4, we provide the results for a model helium atom while in Section 6.6 we extend the retrieval scheme to a helium hydride model. Section 6.7 concludes the chapter.

## 6.2 The parallel two-color scheme

In the parallel two-color scheme as described in the work of Porat [115] and the original work on phase-of-the-phase spectroscopy [170], a weak second-harmonic probe field is applied in addition to a strong fundamental where the relative phase between the two can be controlled. Measuring the modulation of the PMD as a function of the two-color phase, momentum-resolved ionization times can be retrieved. Limiting ourselves to the signal along the direction of the two fields, we can write in one dimension

$$A_{\omega}(t) = -\frac{E_0}{\omega} \sin(\omega t) \quad (6.1)$$

for the fundamental and

$$A_{2\omega}(t, \phi) = -\frac{\epsilon E_0}{2\omega} \sin(2\omega t + \phi) \quad (6.2)$$

for the second harmonic. The total vector potential is

$$A(t, \phi) = A_{\omega}(t) + A_{2\omega}(t, \phi) \quad (6.3)$$

and the derived electric field

$$E(t) = E_{\omega}(t) + E_{2\omega}(t, \phi). \quad (6.4)$$

The presence of the  $2\omega$ -field modulates the signal as a function of the relative phase  $\phi$ . Our goal is to relate the optimal relative phase  $\phi$  that maximizes the signal at a given momentum  $p$  to the time of ionization  $t$ . Here, two effects have to be taken into account. (i) The  $2\omega$  electric field changes the field strength at ionization time, influencing the observed yield directly; (ii) The  $2\omega$  vector potential changes the mapping from observed photoelectron momentum to ionization time, also influencing the yield because the change in ionization time leads to a change of the field strength of the fundamental field.

In the simple man's model, we consider a momentum  $p$  which originates from ionization at time  $t_0$ . The presence of the probe field leads to a momentum shift

$$\Delta p = -A_{2\omega}(t_0, \phi) \quad (6.5)$$

such that at  $p$  we now observe photoelectrons that would have final momentum  $p - \Delta p = p + A_{2\omega}(t_0, \phi)$  in the absence of the  $2\omega$  field. These photoelectrons originate from a different ionization time  $t_0 - \Delta t$ . Since the time-momentum mapping without  $2\omega$  field reads  $p = -A_{\omega}(t_0)$ , we have

$$\Delta t = \Delta p / E_{\omega}(t_0) = -A_{2\omega}(t_0, \phi) / E_{\omega}(t_0). \quad (6.6)$$

The electric field at this ionization time is  $E_\omega(t_0) + \Delta E_\omega$ , where

$$\Delta E_\omega = -\dot{E}_\omega(t_0)\Delta t = A_{2\omega}(t_0, \phi) \dot{E}_\omega(t_0)/E_\omega(t_0). \quad (6.7)$$

Thus, the total electric field leading to momentum  $p$  in the presence of the  $2\omega$  field is

$$E_\omega(t_0) + E_{2\omega}(t_0, \phi) + \Delta E_\omega = E_\omega(t_0) + E_{2\omega}(t_0, \phi) + A_{2\omega}(t_0, \phi) \dot{E}_\omega(t_0)/E_\omega(t_0). \quad (6.8)$$

We assume that the signal is maximized when the total electric field is maximal. Therefore, for a maximum in the delay scan to occur, the derivative with respect to the relative phase must vanish,

$$\frac{\dot{E}_\omega(t_0)}{E_\omega(t_0)} \frac{\partial A_{2\omega}(t_0, \phi)}{\partial \phi} \Big|_{\phi=\phi_0} + \frac{\partial E_{2\omega}(t_0, \phi)}{\partial \phi} \Big|_{\phi=\phi_0} = 0. \quad (6.9)$$

Inserting expressions (6.1) and (6.2) for the  $\omega$  and  $2\omega$  fields, we find

$$-2 \cos(\omega t_0) \sin(\phi_0 + 2\omega t_0) + \cos(\phi_0 + 2\omega t_0) \sin(\omega t_0) = 0. \quad (6.10)$$

Expanding  $t_0$  in a power series in  $\phi_0$ , this can be solved via

$$-2\omega t_0 = \frac{4}{3}\phi_0 + \frac{4}{81}\phi_0^3 + \mathcal{O}(\phi_0^5). \quad (6.11)$$

This equation allows us to relate the measurable quantity  $\phi_0$  to the time of ionization  $t_0$ . Since the third-order term is already small, it is sufficient to use the linear expression. Thus, we find that the simple relation (3.3),  $-2\omega t_0 = \phi_0$ , from orthogonal streaking has to be modified by a correction factor of  $4/3$  when the parallel scheme is used instead.

The same result can be obtained using the strong-field approximation. As usual, we can assume that, since the perturbation is small, the modification of the signal due to the second-harmonic field can be expressed as a modification of the action (2.24)

$$\Delta S(\phi, t_s) = \int_{t_s}^T dt (p + A_\omega(t)) A_{2\omega}(t, \phi). \quad (6.12)$$

Here,  $t_s = t_r + i t_i$  is the unperturbed saddle point (2.29) which satisfies

$$\frac{1}{2}(p + A_\omega(t_s))^2 + I_p = 0 \quad \Leftrightarrow \quad p = -\text{Re } A_\omega(t_s), \quad \text{Im } A_\omega(t_s) = \sqrt{2I_p}. \quad (6.13)$$

The signal at a given momentum is maximized when

$$\frac{\partial}{\partial \phi} \text{Im } \Delta S(\phi, t_s) \Big|_{\phi=\phi_0} = 0. \quad (6.14)$$

Inserting the expression (6.1) and (6.2) for the  $\omega$  and  $2\omega$  fields and replacing  $p$  according to (6.13), the maximum condition becomes

$$\frac{A_0^2 \epsilon}{6\omega} \sinh(\omega t_i)^3 (-2 \cos(\omega t_r) \sin(\phi_0 + 2\omega t_r) + \cos(\phi_0 + 2\omega t_r) \sin(\omega t_r)) = 0. \quad (6.15)$$

The term that depends on the imaginary time  $t_i$  factorizes, making the maximum condition independent of the ionization potential and exactly equivalent to the classical expression (6.10) when the time  $t$  is replaced by the real part  $t_r$  of the complex ionization time  $t_s$ . This agreement is quite remarkable because the central assumption about vanishing initial velocity parallel to

the instantaneous field direction which is used in the simple man's model is in the case of nonadiabatic tunnel ionization not compatible with the quantum-orbit model.

Since in truly linear polarization the PMD is strongly affected by Coulomb effects, a pure SFA description as given above is typically inadequate to model the effect of the probe field.<sup>1</sup> However, in the quasilinear field (5.3) which we are going to use in the following, Coulomb effects are much less important.

### 6.3 Computational details

We solve the two-dimensional time-dependent Schrödinger equation (2.11) on a grid of size  $400 \times 400$  a.u. using 2048 points in each dimension with time step 0.006 a.u. and propagate up to  $T = 752$  a.u. The atomic potential  $V(r)$  is chosen as before (5.7) to model a helium atom in two dimensions. The vector potential is defined as

$$\mathbf{A}(t) = f(t)(\mathbf{A}_{\omega_{\text{eff}}}(t) + A_{2\omega_{\text{eff}}}(t, \phi) \mathbf{e}_s). \quad (6.16)$$

Here,  $\mathbf{A}_{\omega_{\text{eff}}}(t)$  is the bicircular field (5.3) with  $\omega_{\text{eff}} = \sqrt{2} \omega$  used in chapter 5. To implement both orthogonal streaking as well as the parallel scheme, the probe field

$$A_{2\omega_{\text{eff}}}(t, \phi) = -\frac{\epsilon}{2} \frac{3E_0}{\sqrt{5} \omega_{\text{eff}}} \sin(2\omega_{\text{eff}}t + \phi) \quad (6.17)$$

is added. Here,  $\epsilon = 0.02$ ,  $\omega_{\text{eff}} = 0.05695$  a.u. (800 nm) and the envelope  $f(t) = \cos(\omega t/6)^4$  (3-cycle pulse) is the same as was used in Chapter 5. The direction of the probe field  $\mathbf{e}_s$  is chosen as  $\mathbf{e}_s = \mathbf{e}_x$  in the case of orthogonal streaking and  $\mathbf{e}_s = \mathbf{e}_y$  in for the parallel scheme. In both cases, we vary the relative phase  $\phi$  between 0 and  $2\pi$  in 32 steps.

### 6.4 Results

For both the orthogonal and the parallel scheme, we want to retrieve the ionization time from the modulation of the signal as a function of the relative phase. For the derivation of the the phase-to-time mappings (3.14) and (6.11) for the two schemes, the signal in the direction of the fundamental component was considered. When the quasilinear field is used instead, a slight modification is required.

The quasilinear field mimics linear polarization, but the vector potential in the vicinity of the maximum at  $t = 0$  is shifted away from zero. This would suggest to use the shifted  $p_x = -A_x(0)$  axis to perform the ionization time retrieval. In practice, this is problematic because the bicircular field breaks the exact symmetry that is present in truly linear polarization. Instead, to implement orthogonal streaking, we obtain a reference curve by finding the maximum of the  $p_x$ -dependent signal for every  $p_y$ . The probe field then moves the maximum away from the reference ("streaking") and we track for every  $p_y$  the distance between the streaked maximum to the reference in  $p_x$  direction.

The result is shown in Fig. 6.1(a). There, the black solid line indicates the optimal phase in the sense that the maximum lies on the reference. To implement the PTC scheme, we project the main branch of the PMD onto the  $p_y$  axis and observe for every  $p_y$  the modulation of the

<sup>1</sup>In the experiment [115] the CCSFA was used to relate the measured optimal phase to ionization time.

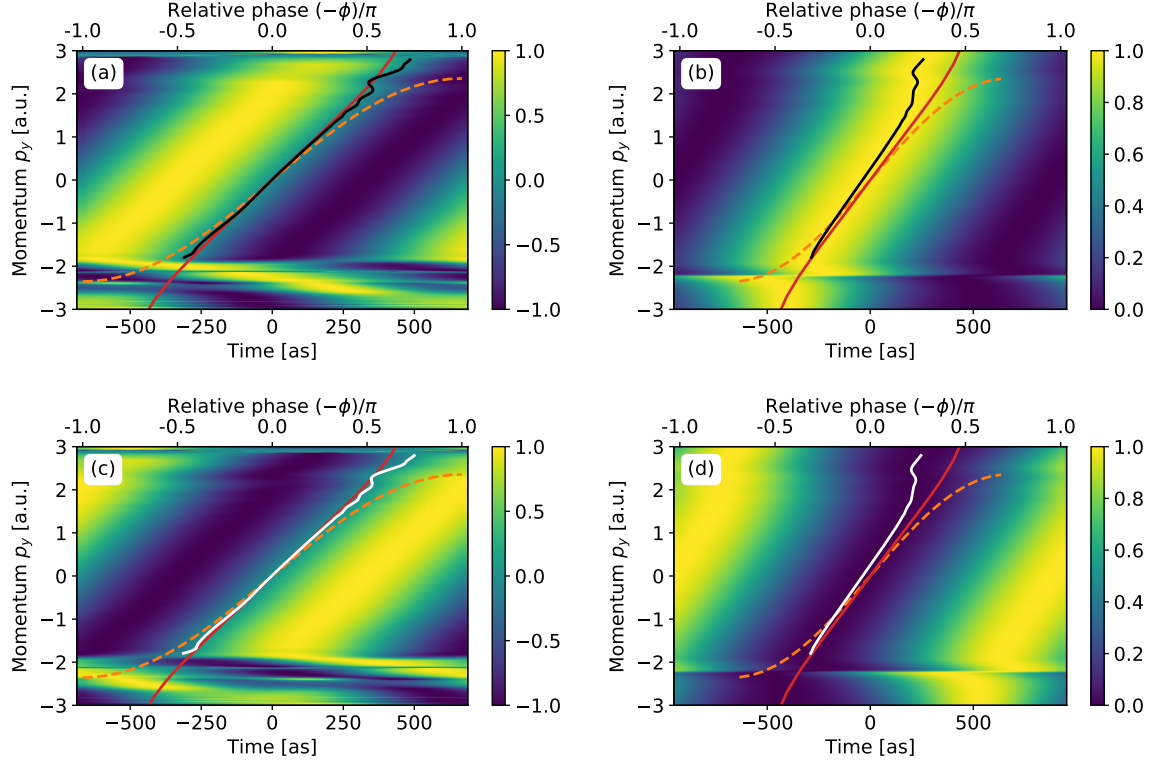


Figure 6.1: (a) Orthogonal streaking. The image shows the difference in  $p_x$  position of the streaked maximum to the reference as a function of the relative phase  $\phi$ , normalized for every  $p_y$  separately to maximum absolute value 1. The black solid line gives for every  $p_y$  the optimal phase  $\phi_0$  for which the position of the maximum coincides with the reference. Time is converted to phase via Eq. (3.14). (b) Parallel two-color scheme. The image shows the modulation of the signal as a function of the relative phase  $\phi$ , normalized for every momentum  $p_y$  separately to vary between 0 and 1. Relative phase is converted to time according to Eq. (6.11). (c, d) Same as (a, b) but with the relative phase shifted by  $\pi$  and using minimization instead of maximization in case of the PTC scan. In all four panels, the red solid line shows the momentum-dependent ionization time for linear polarization according to the quantum-orbit model; the orange dashed line shows the ionization time according to the simple man's model. Here, the result for linear polarization (see Chapter 3) with effective frequency and field strength was used to map the  $p_y$  momentum to ionization time. Panels (a) and (b) are adapted from Fig. 3 in [280].

signal as a function of the relative phase. The result is shown in Fig. 6.1(b). There, the black solid line shows the optimal phase where the signal is maximized. Converting phase to time<sup>2</sup> via Eq. (6.11) we find that the momentum-resolved ionization time is shifted with respect to the prediction by the quantum-orbit model (red solid curve). At  $t = 0$  we find  $p_y = 0.255$  a.u. in very good agreement with the attoclock shift of the momentum distribution ( $\Delta p_y = 0.245$  a.u.). In orthogonal streaking, however, this attoclock shift is not visible. Converting phase to time via Eq. (3.14), we find almost perfect agreement with the ionization time predicted by the quantum orbit model ( $p_y = 0.015$  a.u. for  $t = 0$ ).

Fig. 6.1(c) shows the result from the OTC delay scan when the phase of the streaking field

<sup>2</sup>Taking also the pulse envelope into account, we find from the classical maximum condition (6.9) an additional factor of  $27/26$  which we apply here. Deriving the envelope correction from SFA, the time-to-phase conversion (6.11) becomes dependent on the ionization potential  $I_p$ . This was not the case for the cw fields where in (6.15) the term involving the imaginary part  $t_i$  of the complex ionization time  $t_s$  separated. However, for small Keldysh parameter  $\gamma \rightarrow 0$  the numerical value of the classical correction is retrieved. For the case considered here, the nonadiabatic correction to the pulse-envelope correction is small and will be neglected.

is shifted by  $\pi$ . While  $\pi$  periodicity was present on the on-axis signal in the OTC scan for truly linear polarization (see Chapter 3), this is not necessarily the case for the quasilinear field.<sup>3</sup> In the parallel scheme, shifting the phase of the streaking field by  $\pi$  leads to attenuation instead of amplification of the ionization yield. Thus, in Fig. 6.1(d) we find for every  $p_y$  the optimal phase that leads to a *minimum* in the delay scan.

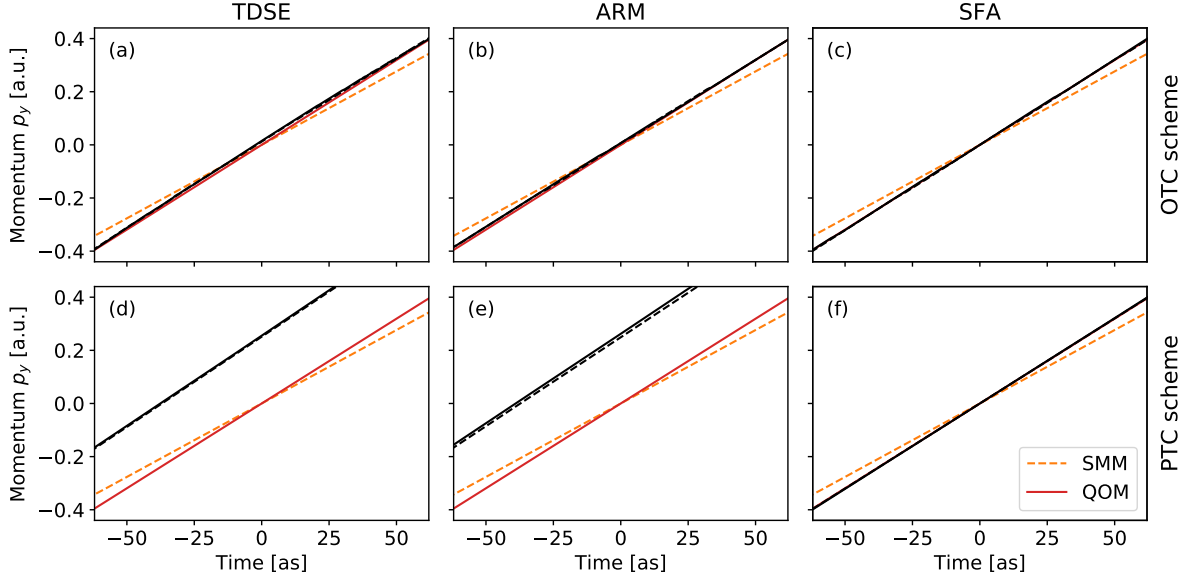


Figure 6.2: Delay scan around time zero in comparison with different models. The upper row (a-c) shows orthogonal streaking; the lower row (d-f) shows the parallel scheme. The first column (a,d) shows the TDSE result as in Fig. 6.1. The second and third columns show the corresponding results when the modulation of the signal is calculated in ARM theory (b,e) or SFA (c,f). The black solid lines show the ionization time obtained by converting the optimal relative phase. The dashed lines show the corresponding result when the relative phase of the streaking field is shifted by  $\pi$  and minimization instead of maximization is used in case of the parallel scheme. In all panels, the predicted ionization time in the quantum-orbit model and simple man's model for linear polarization are marked as red solid and orange dashed lines, respectively.

Fig. 6.2(a,d) shows the two types of optimization curves together in a region around zero momentum shift for orthogonal streaking (a) and the parallel scheme (d) where in both cases good agreement between the two variants is found. Fig. 6.2(b,e) and (c,f) show the retrieved ionization time when the momentum distribution is calculated using ARM theory or saddle-point SFA (in both cases we have included a prefactor  $\propto \dot{S}^{-1/2}$  in the amplitude). As expected, the numerically retrieved ionization time in SFA follows consistently the real part of the SFA saddle-point time. Small deviations to this behavior are expected due to: (i) a small difference between the ionization time in quasilinear polarization compared to truly linear polarization; (ii) contributing higher-order terms in the conversion rule (6.11); (iii) higher-order effects in the relative field strength of the streaking field that have not been considered in the derivation; (iv) mixing of momenta corresponding to different ionization times due to the projection; (v) the nonadiabatic terms in the envelope correction factor; (vi) The SFA prefactor. Going beyond SFA and taking the Coulomb potential into account perturbatively using ARM

<sup>3</sup>In 3D, defining a reference could be avoided altogether by applying the probe field in the  $z$  direction. In this case, the signal would be  $\pi$  periodic in the  $p_x, p_y$  plane where ionization times could be retrieved for every momentum. This scheme could also be applied to the conventional attoclock. Experimental implementation would be challenging for it effectively requires a three-dimensional field shape.

theory, the behavior observed in the TDSE calculations is well reproduced.

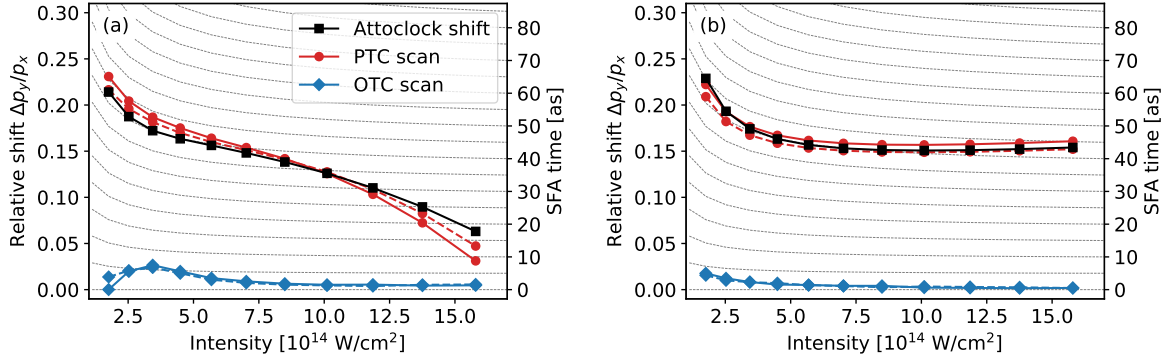


Figure 6.3: Momentum shift of time zero in comparison with the attoclock shift of the momentum distribution in TDSE (a) or ARM (b). In both panels, the black solid curve gives the attoclock shift of the momentum distribution. The red solid curve shows the retrieved ionization time from the parallel scheme while the blue solid curve gives the ionization time retrieved from orthogonal streaking. The dashed curve give the corresponding result when the phase of the streaking field is shifted by  $\pi$  and minimization instead of maximization is used in case of the PTC scan. Panel (a) is adapted from Fig. 4 in [280].

Fig. 6.3 shows the momentum shift of time zero obtained from the orthogonal and the parallel scheme for many intensities in comparison with the attoclock shift of the momentum distribution using the TDSE (a) or ARM (b). We find that the agreement between the parallel scheme and the attoclock shift persists at all intensities with small deviations at higher intensities where depletion is important. Orthogonal streaking, on the other side, always gives values close to zero.

To explain this, note that the quasilinear field has a well-defined direction during the ionization process. Effects that could change the position of the maximum of the PMD, such as an initial velocity of the photoelectron or the Coulomb force of the parent ion acting on the outgoing electron point in the direction of the instantaneous electric field. That is, they can shift the distribution only on its integral, i.e. the negative vector potential. So do depletion and a possible ionization-time delay. In case of orthogonal streaking, the combined vector potential must be considered which at  $\phi = 0$  crosses the reference vector potential ( $\epsilon = 0$ ) at  $p_y = 0$ . Independent of whether the distribution is shifted along the streaked vector potential, the point at which the maximum lies on the reference is still  $p_y = 0$  which is thus assigned to  $t = 0$ . This effect can be seen clearly from the streaked PMD in Fig. 6.4 (where we have increased the relative field strength in the probe field to  $\epsilon = 0.1$  for better visibility).

More formally, the invisibility of the attoclock shift in the OTC scheme can be understood in an Coulomb-corrected simple man's model where attoclock shift is due to the force of the potential on the outgoing electron and acts in the instantaneous field direction which defines the tunneling direction. When a field in both the  $x$  and  $y$  component is present, the ratio of the Coulomb-shifts  $\Delta p_x$  and  $\Delta p_y$  in the two components is equal to the field strength-ratio

$$\frac{\Delta p_x}{\Delta p_y} = \frac{E_x(t_0, \phi)}{E_y(t_0)}. \quad (6.18)$$

For the two-color scheme in the absence of the potential shift, we write  $p_y = -A_y(t_0)$ . The Coulomb potential leads to a momentum change  $\Delta p_y$  such that the same  $p_y$  now originates

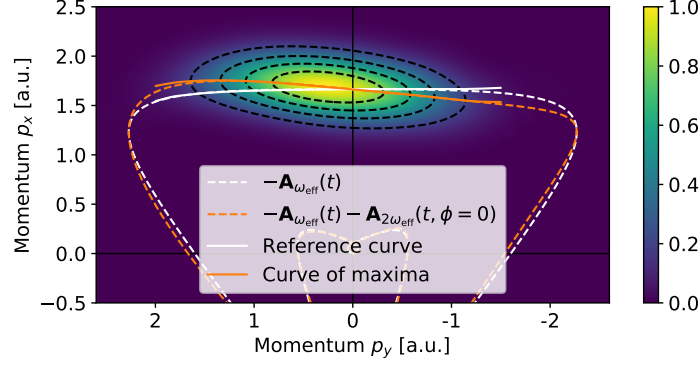


Figure 6.4: Photoelectron momentum distribution from the solution of the 2D TDSE (normalized to maximum signal 1). In addition to the bicircular field (6.16), the probe field (6.17) with  $\phi = 0$  and  $\epsilon = 0.1$  has been applied in the  $x$  direction (“orthogonal streaking”). The black dashed lines show contours of constant signal  $s$  in steps of  $\Delta s = 0.2$ . The white dashed line shows the negative vector potential without probe field and the orange dashed line shows the negative vector potential in the presence of the probe field. The reference curve (maxima of the PMD without probe field) is shown as a white solid curve while the curve of maxima in the presence of the probe field is shown as a solid orange curve.

from a different ionization time  $t_0 + \Delta t$ , i.e.

$$p_y = -A_y(t_0 + \Delta t) + \Delta p_y = -A_y(t_0) + \underbrace{E_y(t_0)\Delta t + \Delta p_y}_{=0} \quad (6.19)$$

from which we conclude

$$\Delta t = -\frac{\Delta p_y}{E_y(t_0)}. \quad (6.20)$$

In the  $2\omega$  component, suppose the relative phase is tuned such that in the absence of the Coulomb potential no deflection occurs,  $0 = p_x = -A_x(t_0, \phi_0)$ . Incorporating a possible Coulomb shift  $\Delta p_x$  in the direction of the streaking field, we have instead

$$\begin{aligned} p'_x &= -A_x(t_0 + \Delta t, \phi_0) + \Delta p_x \\ &= \underbrace{-A_x(t_0, \phi_0)}_{=0} + E_x(t_0, \phi_0)\Delta t + \Delta p_x \stackrel{(6.20)}{=} \Delta p_y \left( \frac{\Delta p_x}{\Delta p_y} - \frac{E_x(t_0, \phi_0)}{E_y(t_0)} \right) \stackrel{(6.18)}{=} 0. \end{aligned} \quad (6.21)$$

Thus, the optimal phase that leads to no deflection of the photoelectron in the absence of the Coulomb potential for some  $p_y$  is still the optimal phase for the same  $p_y$  momentum when the potential is taken into account. To fix this, the Coulomb potential would have to be taken into account already in the derivation of the phase-to-time mapping, introducing similar ambiguities as the conventional ionization-time retrieval based on the attoclock.

In the parallel scheme, the agreement of the attoclock shift with the momentum corresponding to time zero can be related to the observation made by Ivanov et al. that in order to maximize the additional yield due to a weak perturbing field  $\delta E$  that is applied to a strong field  $E$ , the delay between the two fields must be chosen such that the perturbation amplifies the peak of the strong field. [281]. Formally, the yield is a nonlinear functional of the electric field,  $P[E]$ , defining a functional derivative via

$$P[E + \delta E] - P[E] = \int_0^T dt \frac{\delta P[E]}{\delta E(t)} \delta E(t) + \mathcal{O}(\delta E^2). \quad (6.22)$$



It was shown numerically that for a short pulse peaking at  $t = 0$ , the maximum of the functional derivative

$$\frac{\delta P[E]}{\delta E(t)} \quad (6.23)$$

is also found at  $t \approx 0$ . In our case we can understand the  $2\omega_{\text{eff}}$ -field as a small perturbation in that sense and write

$$P[E_{\omega_{\text{eff}}} + E_{2\omega_{\text{eff}}}] - P[E_{\omega_{\text{eff}}}] = \int_0^T dt \frac{\delta P[E_{\omega_{\text{eff}}}]}{\delta E(t)} E_{2\omega_{\text{eff}}}(t, \phi) + \mathcal{O}(\epsilon^2). \quad (6.24)$$

The  $2\omega_{\text{eff}}$  field thus probes the functional derivative at  $t \approx -\phi/(2\omega_{\text{eff}})$ .

In Fig. 6.5(a) the modulation of the yield at  $E_0 = 0.1$  a.u. in the main branch of the PMD as a function of  $\phi$  is shown. In Fig. 6.5(b) we obtain the optimal phase that maximizes the yield and

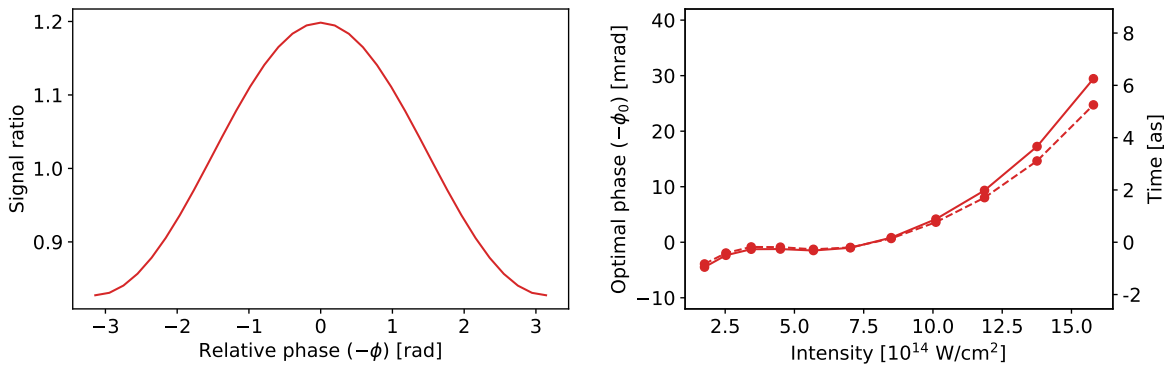


Figure 6.5: Phase dependence of the overall yield. (a) Modulation of the signal ratio for the main branch of the quasilinear field at  $E_0 = 0.10$  a.u. as a function of the relative phase  $\phi$ . (b) Optimal phase at which a maximum (solid line) or minimum (dashed line, here the phase must be shifted by  $\pi$ ) of the signal ratio is obtained. Phase is converted to time according to  $2\omega_{\text{eff}}t + \phi = 0$ .

find – in agreement with Ivanov’s results – that the phase is very close to zero for intensities where depletion is negligible. Our main result Fig. 6.3(a) can be seen as a momentum-resolved version of this. Not only the overall yield is maximized by amplifying the fundamental field at its peak, but also the signal at the maximum of the PMD, which is thus assigned to the time of peak field strength.<sup>4</sup>

## 6.5 Experimentally realistic parameters

Finally, we want to consider two additional points which are important for the experimental implementation. First, the possibility to achieve converged results even when using a larger field strength in the probe field, and second, using a different frequency in the probe field. For the parallel scheme, let  $f(p_y, \phi, \epsilon)$  denote the signal in the presence of the probe field projected onto the  $p_y$  axis. We can write

$$f(p_y, \phi, \epsilon) = f(p_y, \phi, 0) + \epsilon \left. \frac{\partial}{\partial \epsilon} f(p_y, \phi, \epsilon) \right|_{\epsilon=0} + \mathcal{O}(\epsilon^2). \quad (6.25)$$

<sup>4</sup>In this context, we note that it would be interesting to try and generalize Ivanov’s idea by evaluating the functional derivative not only for the overall yield, but also for the photoelectron momentum distribution.

Since  $f(p_y, \phi, 0)$  does not depend on  $\phi$ , the maximum condition  $\partial_\phi f(p_y, \phi, \epsilon) = 0$  in the parallel scheme for  $\epsilon \rightarrow 0$  evaluates to a condition on the derivative,

$$\left. \frac{\partial}{\partial \phi} \frac{\partial}{\partial \epsilon} f(p_y, \phi, \epsilon) \right|_{\epsilon=0} = 0. \quad (6.26)$$

For orthogonal streaking, let  $g(p_y, \phi, \epsilon) = p_x^{\max} - p_x^{\text{ref}}$  denote  $p_y$ -dependent distance between the maximum position  $p_x^{\max}$  in the presence of the streaking field and the reference position  $p_x^{\text{ref}}$  without streaking field. Writing

$$g(p_y, \phi, \epsilon) = \epsilon \left. \frac{\partial}{\partial \epsilon} g(p_y, \phi, \epsilon) \right|_{\epsilon=0} + \mathcal{O}(\epsilon)^2, \quad (6.27)$$

the streaking condition  $g(p_y, \phi, \epsilon) = 0$  for  $\epsilon \rightarrow 0$  evaluates to

$$\left. \frac{\partial}{\partial \epsilon} g(p_y, \phi, \epsilon) \right|_{\epsilon=0} = 0. \quad (6.28)$$

Thus, an accurate retrieval of the ionization time requires an accurate evaluation of the derivatives  $\partial_\epsilon f$  and  $\partial_\epsilon g$ . Instead of just using a small value of  $\epsilon$  as above, we can use higher  $\epsilon$  together with a more accurate formula to evaluate the derivative. This requires the evaluation at negative  $\epsilon$ , which is equivalent to shifting the relative phase  $\phi$  to  $\phi + \pi$  as above.

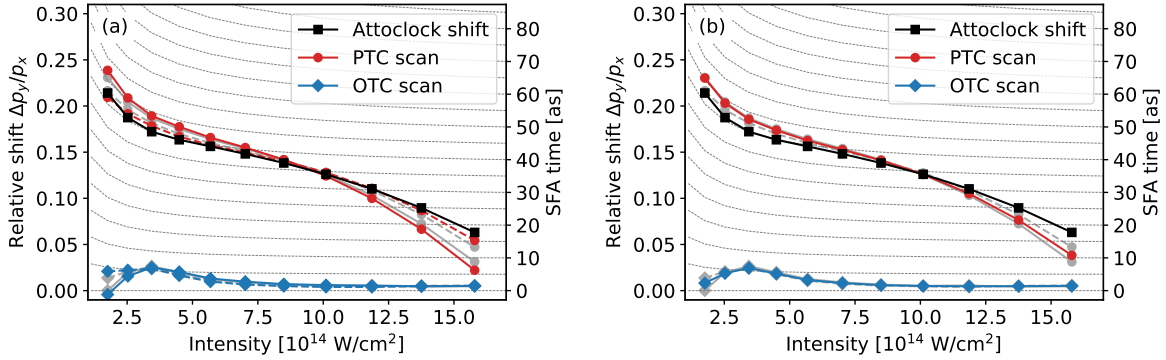


Figure 6.6: Momentum shift of time zero in comparison with the attoclock shift of the momentum distribution for larger field-strength of the streaking field. (a) As in Fig. 6.3(a) but for  $\epsilon = 0.04$ . (b) Time zero shifts obtained by evaluating the derivatives (6.26) and (6.28) using a calculation for  $\epsilon = 0.04$  and the three-point formula for the derivative. The curves from Fig. 6.3(a) for  $\epsilon = 0.02$  are reprinted gray in the background. Panel (a) is adapted from Fig. 4 in [280].

Fig. 6.6(a) shows the time-zero shifts as in Fig. 6.3(a) but at  $\epsilon = 0.04$  instead of  $\epsilon = 0.02$ . Here, some disagreement with the previous result is found. Using the calculations at  $\epsilon = 0.04$  and the three-point formula to evaluate the derivatives, the result shown in Fig. 6.6(b) is found and it agrees nicely with the average of the two  $\epsilon = 0.02$  curves.

As for the second point, the frequency  $2\omega_{\text{eff}}$  was chosen such that direct comparison with previous results for linear polarization is possible. When solving the TDSE, we have the freedom of choosing the vector potential as we wish, but in a realistic experiment the current choice of frequency is problematic for two reasons. First, the ratio of the required frequency to the fundamental frequency used in the laboratory  $2\omega_{\text{eff}}/\omega = 2\sqrt{2}$  is not easily accessible. Second, the fact that the ratio is not even a rational number implies that the field is not periodic. For

Frequency	Effective frequency ratio $\alpha$	First order	Third order
$2\omega$	1.41421	2.00000	0.66667
$2\omega_{\text{eff}}$	2.00000	1.33333	0.04938
$3\omega$	2.12132	1.28571	0.03499

Table 6.1: Correction factors for the parallel scheme according to (6.32).

us, this was not a problem because of the ultrashort pulse envelope, but in an experiment with a long pulse, periodicity is required.

In principle, one could use the same approach as in the ionizing field also in the probe field. Superimposing linearly polarized  $2\omega$  and  $4\omega$  fields, we can write

$$A_{2\omega_{\text{eff}}}(t) = -\frac{\epsilon}{2} \frac{2E_0}{\sqrt{5}\omega} \left( \sin(2\omega t + \phi) + \frac{1}{4} \sin(4\omega t + 2\phi) \right). \quad (6.29)$$

Close to the maximum ( $\phi = -2\omega t$ ) this can be expanded as

$$E_{2\omega_{\text{eff}}}(t, \phi_{\text{eff}}) = \epsilon E_{\text{peak}} \left( 1 - \frac{1}{2} (2\omega_{\text{eff}} t + \phi_{\text{eff}})^2 + \mathcal{O}((2\omega_{\text{eff}} t + \phi_{\text{eff}})^4) \right) \quad (6.30)$$

where we have introduced the effective phase shift  $\phi_{\text{eff}} = \sqrt{2} \phi$ . Then the 4/3 rule can be used as is when an additional conversion factor  $\sqrt{2}$  is taken into account to convert the relative phase  $\phi$  of the streaking field to the effective relative phase  $\phi_{\text{eff}}$  needed to perform the ionization time retrieval. On the other hand, there is no particular reason to use  $2\omega_{\text{eff}}$  other than comparability with linear streaking schemes and a linearly polarized field with frequency  $2\omega$  or  $3\omega$  could be used instead. The former corresponds to an effective frequency multiplier of  $2\omega/\omega_{\text{eff}} = \sqrt{2}$ . The latter corresponds to  $3\omega/\omega_{\text{eff}} = 3/\sqrt{2}$ . Repeating the calculations from Section 6.2 for these relative frequencies  $\alpha$  (with  $\alpha = \sqrt{2}$  or  $\alpha = 3/\sqrt{2}$ ), we find the general result

$$-\alpha \cos(\omega t_0) \sin(\phi_0 + \alpha \omega t_0) + \cos(\phi_0 + \alpha \omega t_0) \sin(\omega t_0) = 0 \quad (6.31)$$

which can be solved approximately via

$$-\alpha \omega t_0 = \frac{\alpha^2}{\alpha^2 - 1} \phi_0 + \frac{\alpha^2}{3(\alpha^2 - 1)^3} \phi_0^3 + \mathcal{O}(\phi_0^5). \quad (6.32)$$

Some values of the phase-to-time conversion factors are listed in Table 6.1. The  $3\omega$  case is particularly appealing because it is very close to using  $2\omega_{\text{eff}}$  which is reflected in a similar conversion factor and also a low contribution of higher order terms.  $2\omega$  could be used in principle but the conversion factor is quite high which leads to lower absolute accuracy in the retrieved ionization time. Additionally, the nonlinear terms contribute significantly. This is because the  $2\omega$  case is closer to the limiting case  $\sqrt{2}\omega = \omega_{\text{eff}}$  for which the maximum of the streaking field is exactly as sharp as the maximum of the bicircular field and the ionization time retrieval becomes impossible. This is reflected in a divergence of the coefficients in the expansion (6.32).

Fig. 6.7 shows the time-to-momentum mapping at  $E_0 = 0.10$  a.u. for the orthogonal and the parallel scheme, obtained by solving the TDSE for various frequencies in the probe field and using the conversion factors (6.32) for the parallel scheme. We find good agreement between the variants.

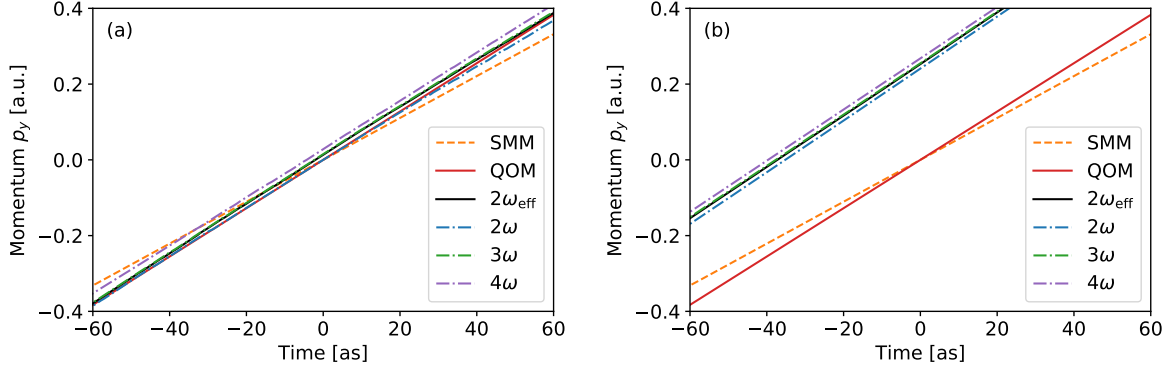


Figure 6.7: Time-to-momentum mapping around time zero as in Figs. 6.2(a,d). (a) Orthogonal streaking. (b) Parallel scheme. Both panels show the average of the two variants (one with the phase shifted by  $\pi$ ).

## 6.6 Orientation dependence in molecules

Since one branch of the momentum distribution in the quasilinear field originates from a region where the electric field points along an approximately constant direction, we can use it to study orientation dependent properties in strong-field ionization of molecules.<sup>5</sup> We consider the  $\text{HeH}^+$  model from Chapter 3 with potential (3.17) aligned along the  $y$  direction and probe both possible orientations where ionization can occur either via the helium or the hydrogen side. We set  $E_0 = 0.18$  a.u. and consider several effective wavelengths  $\lambda_{\text{eff}} = \lambda/\sqrt{2}$ .

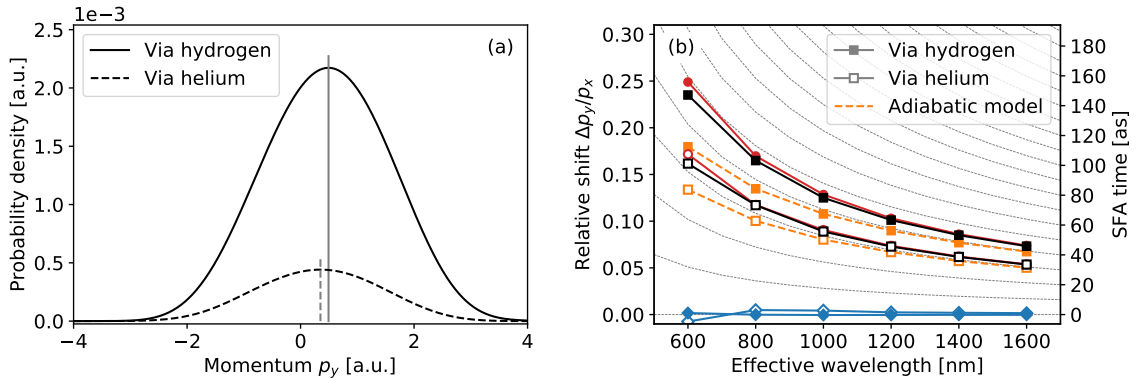


Figure 6.8: (a) Projection of the main branch of the PMD onto the  $p_y$  axis at  $\lambda_{\text{eff}} = 800$  nm. Solid curve, molecular ion oriented such that ionization occurs at the hydrogen side. Dashed curve, ionization at the helium side. The gray vertical lines indicate the position of the PMD maximum. (b) Attoclock shift of the momentum distribution and streaking of the  $\text{HeH}^+$  model at  $E_0 = 0.18$  a.u. and various wavelengths. Black curves, attoclock shift of the momentum distribution. Red curves, parallel scheme. Blue curves, orthogonal streaking. Orange dashed lines, adiabatic model as explained in the text. The open symbols show the case where the molecular ion is oriented such that ionization takes place via the helium side. The filled symbols correspond to ionization via the hydrogen side. For results obtained by the orthogonal or the parallel scheme, we have taken the average of the two possible ways (one with the phase shifted by  $\pi$ ). Panel (b) is adapted from Fig. 4 in [280].

Solving the 2D TDSE with the same parameters as above, we find significant differences in the momentum distributions. Fig. 6.8(a) shows the projections of the PMDs onto the  $p_y$  axis at  $\lambda_{\text{eff}} = 800$  nm. There, it is evident that both the ionization yield as well as the attoclock shift

<sup>5</sup>Molecular attoclock setups with conventional attoclock pulses were also considered in [282–284]. In [285], the attoclock offset angle was shown to be different in the forward and backward direction for a chiral molecule.

depend on the orientation. At  $\lambda_{\text{eff}} = 800$  nm, the yield in the main lobe of the three-lobe PMD is  $1.24 \times 10^{-3}$  when ionizing via the helium side and  $6.27 \times 10^{-3}$  when ionizing via the hydrogen side. Converting the different attoclock shifts to a time difference according to (5.12),

$$\Delta t = \frac{\Delta p_y}{p_x^{\text{max}} 2\omega \sqrt{1 + \gamma_{\text{eff}}^2}}, \quad (6.33)$$

we find an apparent ionization-time delay of 13.13 as when ionizing via the helium side compared to the hydrogen side. Fig. 6.8(b) shows the attoclock shift of the momentum distribution in the quasilinear field for both orientations and several wavelengths. This shift is generally larger when ionization occurs via the hydrogen side with an approximately constant apparent delay of more than 10 attoseconds. Next, we evaluate both two-color schemes as above with  $\epsilon = 0.02$  to find the shift that corresponds to  $t = 0$ , the peak of the pulse. As before, orthogonal streaking always gives values close to zero. When the parallel scheme is employed, the time-zero momentum shift again agrees with the attoclock shift of the momentum distribution. This is true for both orientations, suggesting that the apparent delay does not correspond to a real delay in ionization time.

In fact, the difference in the attoclock shift can be understood in a simple classical model without assuming a delay in ionization time, but considering that the tunnel-exit position depends on the orientation via an orientation-dependent ionization potential. To obtain  $I_p(E)$ , we solve the 2D TDSE in a small box of size  $200 \times 200$  a.u. and 1024 points in each dimension with time step  $\Delta t = 0.02$  a.u. in a slowly varying electric field  $E(t) = \alpha t$  while absorbing outgoing parts of the wave function via an absorber that covers a distance of 25 a.u. from the boundary of the simulation volume. From the time dependent calculation, we extract the field-dependent ionization potential as

$$I_p(E, \alpha) = \text{Re} \left( \frac{\langle \psi(t) | -i\partial_t | \psi(t) \rangle}{\langle \psi(t) | \psi(t) \rangle} \right) \Big|_{t=E/\alpha}. \quad (6.34)$$

Assuming

$$I_p(E, \alpha) = I_p(E) + \alpha \frac{\partial}{\partial \alpha} I_p(E, \alpha) \Big|_{\alpha=0} + \mathcal{O}(\alpha^2) \quad (6.35)$$

and running the calculation for two different slopes  $\alpha$  and  $2\alpha$ , we can eliminate the linear term and extrapolate to the quasistatic case  $\alpha \rightarrow 0$  via

$$I_p(E) \approx 2I_p(E, \alpha) - I_p(E, 2\alpha). \quad (6.36)$$

For  $\alpha = 1.25 \times 10^{-3}$  a.u. we find (in atomic units)  $I_p(E) \approx 1.657 \pm 0.403E + 0.633E^2$  where the “+” case denotes ionization via the helium side and the “−” case denotes ionization via the hydrogen side. We use the field-dependent ionization potential to find the tunnel-exit position  $y_0$  according to the TIPIS model,<sup>6</sup>

$$y_0 = \frac{I_p(E) + \sqrt{I_p(E)^2 - 4\beta(E)E}}{2E}, \quad \beta(E) = Z - \frac{\sqrt{2I_p(E)}}{4} \quad (6.37)$$

with  $Z = 2$ .

<sup>6</sup>See Section 2.6. In this case, the 2D version [104] must be used. There, the separation constant  $\beta$  is different from the 3D expression (2.46). Note also that the TIPIS model requires the potential to be approximately  $-Z/r$  in the tunneling region. For the potential under consideration (3.17), this is the case because the origin has been chosen symmetrically between the two centers.

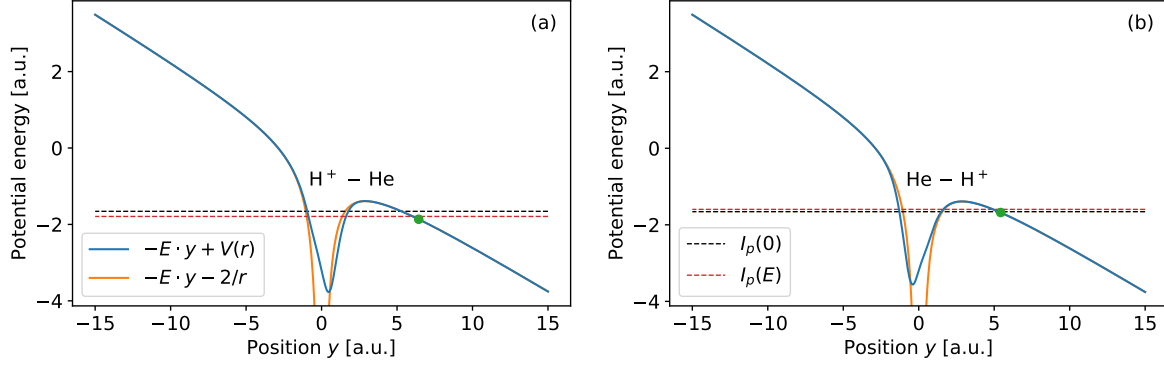


Figure 6.9: Molecular potential (3.17) in the presence of a strong field  $E \approx 0.24$  a.u. (a) Molecular ion oriented such that ionization takes place via the helium side. (b) Reverse orientation where ionization occurs via the hydrogen side. In both panels, the blue curve is the complete potential, the orange curve assumes a  $-2/r$  potential for the molecule, the black dashed line shows the field-free ionization potential and the red dashed line shows the shifted ionization potential. The green dots show the tunnel-exit position according to the TIPIS model (6.37).

This is illustrated in Fig. 6.9. Different tunnel-exit positions lead to different attoclock shifts. To calculate them approximately, we solve Newton's equations of motion in a static field,

$$\ddot{y}(t) = -Z/y^2 + E, \quad y(0) = y_0, \quad \dot{y}(0) = 0. \quad (6.38)$$

The attoclock shift is then determined as  $\Delta p = p(t) - p_0(t)$  for large  $t$  where  $p(t)$  is the time dependent momentum from the solution of Newton's equation and  $p_0(t) = Et$  is the time dependent momentum in the same setting with  $Z = 0$ . It is shown for both orientations as orange dashed line in Fig. 6.8 and good agreement with the TDSE results is found in the long-wavelength limit where the static approximation is expected to work best.

## 6.7 Conclusion

In this chapter, streaking with a weak probe field was applied to the quasilinear field (introduced in Chapter 5) to determine the time of ionization for various momenta in the photoelectron momentum distribution. The ionization time is inferred from the optimal relative phase between the driving field and the probe via a simple linear relation with a constant factor that depends on whether the probe field is orthogonal or parallel to the driving field. Compared to applying the schemes to linear polarization, the bicircular field offers several advantages. The absence of intracycle interference and strong Coulomb effects allows us to reach attosecond precision in the delay scan, resolve the region around the maximum of the momentum distribution, and compare the attoclock shift of the momentum distribution with the momentum that is assigned to the time of peak field strength by the two-color scheme. Using solutions of the TDSE as well as ARM theory, we found that orthogonal streaking (as introduced in Chapter 3) measures ionization time as if the Coulomb potential were not present and the time of peak field strength is assigned to the maximum of the Coulomb-free momentum distribution. Switching to parallel polarization, the time of peak field strength is instead assigned to the Coulomb-shifted maximum of the momentum distribution. Physically, the conflicting results can be understood in that the orthogonal scheme relies for its phase-to-time mapping on the propagation step in the probe field which itself can be altered by Coulomb effects. The parallel

scheme, on the other hand, relies on modifying the signal already at the ionization step. Here, the agreement between the Coulomb-shifted maximum of the momentum distribution and the time of peak field strength persists even in case of an asymmetric molecule, although the attoclock shift depends on the orientation. This orientation dependence can be understood as a modification of the tunnel-exit position due to an orientation-dependent ionization potential.

The physical explanation for orthogonal streaking not being able to reveal Coulomb effects assumed a sufficiently adiabatic situation. Although we found no significant differences for the frequencies considered here, it might be fruitful to consider much higher frequencies in the probe field and investigate whether the delay scan becomes sensitive to the attoclock shift. Taking Coulomb effects into account in orthogonal streaking by modifying the phase-to-time mapping would have to rely on similar assumptions made for trajectory-based models for the attoclock. Instead, the scheme could be used to calibrate the relative phase between the bicircular field and the probe.

The absence of the attoclock shift in the orthogonal scheme could explain why in the HHG-based ionization-time retrieval that uses OTC fields, the retrieved ionization times agreed so well with the Coulomb-free SFA ionization times [113]. This is the case although a Coulomb-correction to both the ionization and the return time – similar to the attoclock shift – is also present in HHG.<sup>7</sup> It would be interesting to revisit the parallel scheme in HHG [111, 176] and investigate whether – similar to photoelectrons – the Coulomb correction can be resolved there. Coming back to the parallel scheme with photoelectrons, the attoclock shifts for both orientations of the asymmetric molecule could be compared with the momenta that correspond to the peak of the pulse according to the stationary points of the Dyson integral.

Finally, we note that a force on the outgoing electron trajectory perpendicular to the driving field can be implemented not only externally by a probe field, Such a force is present naturally due to the magnetic component of the laser field [287]. It leads to a momentum transfer in light-propagation direction which can be observed experimentally or be seen in TDSE calculations when going beyond the electric dipole approximation [288, 289]. The point of minimal momentum transfer defines a momentum that can be used as reference for the attoclock [290]. However, similar to the OTC scheme, this momentum corresponds rather to the maximum of the Coulomb-free momentum distribution instead of the Coulomb-shifted maximum [280].

---

<sup>7</sup>Using ARM theory, Torlina et al. derived a first-order correction to the saddle-point times for ionization and recombination [286]. In a simple classical model it can be shown that in the adiabatic limit the correction to the return time vanishes while the correction to the ionization time (for fixed harmonic order) depends only the ionization potential  $I_p$  and is given by  $\Delta t = -\pi/(2I_p)^{3/2}$  which evaluates to approximately  $-31.3$  as for helium. This is similar to the attoclock formula (4.20) which states that the Coulomb force on the outgoing electron shifts the mapping from angle to time in the attoclock by the same value.





## Chapter 7

# Summary and conclusion

Strong-field physics allows us to access attosecond time scales and angstrom spatial scales via different mechanisms. In strong-field ionization, variations of the electric field strength modulate the ionization probability on the subcycle time scale. Recollision phenomena that lead to the generation of high harmonics and rescattered photoelectrons are sensitive to the attosecond dynamics in atoms and molecules and the electron trajectory during excursion.

In this thesis, we explored the time structure of the strong-field ionization process, which is the first step in the three-step process that leads to rescattering and high-harmonic generation. Our main observable was the photoelectron momentum distribution. This choice allowed us to investigate field shapes where the ionization step can be observed directly without having to take complications due to the recollision step into account. In this scope, we explored three main concepts and their applications for attosecond time-retrieval: two-color schemes, bicircular laser fields, and the Dyson integral representation of the ionization amplitude.

The Dyson integral provides via its stationary points a mapping from the final photoelectron momentum to the time of ionization. This mapping does not require the notion of an electron trajectory which makes it independent of assumptions about Newtonian motion. Considering strong-field ionization in a circularly polarized laser field (“attoclock”) and searching for the stationary points by numerical wave-function propagation in complex time, we found that the maximum of the photoelectron momentum distribution corresponds well to the time of peak field strength.

Bicircular fields can be used to create a different kind of attoclock where close to the time of peak field strength the laser field is approximately linearly polarized (“quasilinear field”). Applying the trajectory-free method to this field, we found a delay of about 10 attoseconds between the most probable ionization time and the time of peak field strength. While ultimately the origin of the albeit small delay remains unresolved, we have made progress in understanding the time structure of the Dyson integral by calculating its integrand in a large region of the complex plane. Here, we found that for an accurate description of the ionization amplitude, times much earlier than the expected ionization time cannot be neglected.

In contrast to the purely theoretical definition of ionization time in the Dyson integral, two-color schemes provide a time-to-momentum mapping that is derived from an experimentally observable quantity – the momentum distribution changing with the two-color phase. We applied two-color schemes to both a linearly polarized driver and to the bicircular field. The latter allowed us to obtain a signal without intracycle interference or rescattering and to resolve the region of the momentum distribution originating from around the time of peak field strength.

We found that the measured ionization time is compatible with the idea that ionization is most probable at the time of peak field strength when the probe field is parallel to the driving field, and that ionization time is measured as if the Coulomb potential were not present when the probe field is orthogonal to the driving field. Both statements remain true for an asymmetric molecule even though the momentum distribution shows an orientation dependence.

Our results lead to a better understanding of the time structure of strong-field ionization and to what extent it is possible to assign a single ionization time to a final momentum. The methods that we developed can be used to investigate how such times depend on the applied field, and how different methods to measure these times relate to each other.

The concepts and methods introduced in this thesis have many applications and potential for future work. First of all, the quasilinear field should be investigated further. Most of the research on the circular attoclock could be easily transferred to the quasilinear field, such as the definition of ionization time that measures the probability flow through the tunnel exit [228]. The bicircular field is also the perfect testing ground for investigating the emergence of longitudinal velocity components during nonadiabatic tunnel ionization. In this regard, classical backpropagation could be used together with the recently introduced nonadiabatic velocity criterion [104] that takes a possible initial longitudinal velocity of the photoelectron into account. Another interesting concept is the lateral width of the momentum distribution [246, 247]. There, the idea is that not only the ionization probability maximizes close to the time of peak field strength, but also the width of the distribution of initial transverse velocities. Thus, the lateral width is an alternative attoclock observable that could be investigated for the bicircular field. A very important application of the bicircular field is the study of molecules. For an arbitrarily aligned molecule subject to an elliptically polarized pulse, attosecond time retrieval with attoclock methods is difficult because the variation in the ionization rate due to the field competes with the variation in the rate due to the molecular structure [284]. This effect should be mitigated in the bicircular field because the direction of the field remains constant. Thus, we believe that the quasilinear field could become a powerful tool to analyze orientation-dependent properties of strong-field ionization of molecules.

As for the trajectory-free method, several solutions of the TDSE are usually required to find the ionization time for a single momentum. An efficient propagation scheme together with GPU support allowed us to perform the large number of calculations required to find ionization times for many momenta, but not for the entire momentum distribution. Using Cauchy's formula, the integrand can be evaluated much easier. This could make generating a time-to-momentum mapping for the entire momentum distribution feasible. By integrating the signal over slices of equal time, the ionization rate and its maximum could be obtained. This procedure would avoid the problem of geometrical factors that must be taken into account when the maximum of the momentum distribution is used to infer the most probable ionization time. Being able to calculate the Dyson integrand in extended regions of the complex plane could also help solving the problem that momentum distributions calculated from the TDSE have limited value in terms of interpretability compared to using trajectory-based models of strong-field ionization. For example, interfering contributions in the momentum distribution such as intracycle interference structures that originate from ionization at different times could be disentangled by calculating them independently of each other. Most generally, since the application of the Dyson integral is not limited to strong-field physics, its stationary points could be used to interpret other phenomena in a time resolved way.

# Appendix A

## Methods

### A.1 Time-dependent Schrödinger equation

#### A.1.1 Calculating the momentum distribution

To obtain the photoelectron momentum distribution, we introduce a complex absorbing potential  $iV_C$  that separates the wave function into an inner and outer part,  $|\psi(t)\rangle = |\psi_1(t)\rangle + |\psi_2(t)\rangle$  such that we can write two Schrödinger equations

$$i\partial_t |\psi_1(t)\rangle = H(t)|\psi_1(t)\rangle - iV_C |\psi_1(t)\rangle \quad (\text{A.1})$$

for the inner part and

$$i\partial_t |\psi_2(t)\rangle = H(t)|\psi_2(t)\rangle + iV_C |\psi_1(t)\rangle \quad (\text{A.2})$$

for the outer part, respectively [14]. Here, the complex potential absorbs parts of the inner wave function  $|\psi_1(t)\rangle$  which in turn acts as a source term for  $|\psi_2(t)\rangle$ . This splitting is exact in the sense that the sum of the two equations cancels the absorbing potential and the full Schrödinger equation for  $|\psi(t)\rangle$  is retrieved. If the absorbing potential is located far away from the nucleus and provides for efficient absorption and negligible reflection, the potential  $V$  in the time evolution for  $|\psi_2(t)\rangle$  can be neglected. Then an explicit solution for  $|\psi_2(t)\rangle$  can be given as

$$|\psi_2(t)\rangle \approx -i \int_0^t dt' U_V(t, t') iV_C |\psi_1(t')\rangle. \quad (\text{A.3})$$

Taking the Fourier transform at time  $T$  and using the Volkov states (2.19), we obtain

$$\begin{aligned} \mathcal{M}(\mathbf{p}) &= \langle \psi_{\mathbf{p}}^{(-)} | \psi(T) \rangle \\ &\approx \langle \mathbf{p} | \psi_2(T) \rangle = -i \int_0^T dt e^{-\frac{i}{2} \int_t^T dt' (\mathbf{p} + \mathbf{A}(t'))^2} J(\mathbf{p}, t). \end{aligned} \quad (\text{A.4})$$

Here, the source term in length gauge is

$$J(\mathbf{p}, t) = \frac{1}{(2\pi)^{3/2}} \int d^3r e^{-i(\mathbf{p} + \mathbf{A}(t)) \cdot \mathbf{r}} iV_C \psi_1(\mathbf{r}, t) \quad (\text{A.5})$$

and in velocity gauge the canonical momentum has to be used. This method, already used in [14, 291], is similar to the time-dependent surface-flux amplitude [292] where the source term is given by

$$J(\mathbf{p}, t) = \frac{1}{(2\pi)^{3/2}} \int d\sigma e^{-i(\mathbf{p} + \mathbf{A}(t)) \cdot \mathbf{r}} \cdot \left( \frac{\mathbf{p} + \mathbf{A}(t) + \hat{\mathbf{p}}}{2} \right) \psi(\mathbf{r}, t). \quad (\text{A.6})$$

Here, the integral over  $\mathbf{r}$  is evaluated on a surface encompassing the simulation volume. While these methods allows us to omit a fully numerical calculation of the outer wave function  $|\psi_2(t)\rangle$ , the inner part  $|\psi_1(t)\rangle$  usually has to be solved fully numerically. To this end, we employ the split-operator method [201]. There, the full time-evolution operator for a short time period in velocity gauge is approximated as

$$U(t + \Delta t, t) = e^{-i\Delta t/2 V} e^{-i\Delta t/2 (\mathbf{p} + \mathbf{A}(t + \Delta t/2))^2} e^{-i\Delta t/2 V} + \mathcal{O}(\Delta t^3). \quad (\text{A.7})$$

The wave function is usually represented on an up to three-dimensional Cartesian grid where the fast Fourier transformation<sup>1</sup> can be used to switch between position and momentum-space representation. There, the diagonal terms in the splitting scheme can easily be applied. Since calculating exponentials numerically is expensive, the kinetic-energy part is split again into

$$e^{-i\Delta t/2 (\mathbf{p} + \mathbf{A}(t + \Delta t/2))^2} = \prod_{i=1}^D e^{-i\Delta t/2 (p_i + A_i(t + \Delta t/2))^2}. \quad (\text{A.8})$$

In  $D$  dimensions on a grid with  $N$  bins in each dimension, this reduces the number of exponentials that have to be calculated from  $N^D$  to  $ND$ . In each (or every few) time steps, the source term (A.5) is evaluated, also using the FFT, and accumulated according to (A.4).

Aside from the number of bins, the grid on which the TDSE is solved numerically is characterized by a length  $L$  which represents the size of the simulation volume in position space. The use of the FFT to evaluate the source term (A.5) then imposes conditions on the grid on which the momentum distribution is represented. Let  $\Delta x = L/N$  denote the grid spacing in position space. Then the momentum space resolution is  $\Delta k = 2\pi/L$  and  $k_{\max} = \pi/\Delta x$  is the maximal momentum that can be represented on the grid. Part of the problem in calculating accurate photoelectron momentum distributions is that the physical scales imposed by the problem and the relations given by the FFT may not always be compatible. The size of the atom imposes a minimal grid spacing  $\Delta x \ll 1/\kappa$  (where  $\kappa = \sqrt{2I_p}$ ) but the momentum distribution is most accurately represented if the maximal grid momentum is of the same order as the expected photoelectron momentum,  $k_{\max} \approx 3F_0/\omega$ . Using the relation between  $\Delta x$  and  $k_{\max}$ , this implies  $F_0 \gg \kappa\omega$ . Depending on the species and pulse parameters, this condition may or may not be fulfilled. To mitigate the problem, we usually switch to a larger spacing when evaluating the source term (A.5). In the 3D case, we can additionally calculate high-resolution slices of the momentum distribution. For example, setting  $p_z = 0$ , the source term in velocity gauge can be written as

$$J(\mathbf{p}, t) = \frac{1}{(2\pi)^{2/2}} \int d^2\mathbf{r} e^{-i\mathbf{p}\cdot\mathbf{r}} \left( \frac{1}{(2\pi)^{1/2}} \int dz iV_C \psi_1(\mathbf{r}, t) \right). \quad (\text{A.9})$$

That is, the wave function can be first reduced to 2D by integrating out the  $z$  coordinate before it is Fourier transformed. Because the 2D Fourier transform is much faster and memory conserving it can be done on larger grid (using zero padding) which allows us to increase the resolution significantly.

<sup>1</sup>For the 3D calculations, we use the FFTW library which is parallelized on single nodes via OpenMP and on multiple nodes via MPI. In 2D, we use MATLAB's implementation of CUDA FFT on Nvidia GPUs.

### A.1.2 Obtaining the bound state

The ground state or a low-lying excited state in a potential  $V$  is frequently calculated using imaginary time propagation. There, the short-time propagator  $e^{-\Delta t H_0}$  (imaginary time step  $-\Delta t$ ) is repeatedly applied. For a random initial state

$$|\psi\rangle = \sum_{\mathbf{n}} c_{\mathbf{n}} |\mathbf{n}\rangle, \quad H_0 |\mathbf{n}\rangle = E_{\mathbf{n}} |\mathbf{n}\rangle \quad (\text{A.10})$$

this leads to an exponential suppression of all contributions depending on the energy eigenvalue,

$$e^{-t H_0} |\psi\rangle = \sum_{\mathbf{n}} c_{\mathbf{n}} e^{-t E_{\mathbf{n}}} |\mathbf{n}\rangle. \quad (\text{A.11})$$

After renormalizing the state, all contributions with energy larger than the ground-state energy are reduced in every step and the series converges to the ground state of  $H_0$ . For a practical calculation, the short-time propagator must be approximated which induces an error. When using the split-operator scheme, one can show (using the Baker-Campbell-Hausdorff formula) that this error corresponds to actually propagating the state according to a different Hamiltonian

$$H_{\text{eff}}(\Delta t) = T + V + \frac{1}{24} [V + 2T, [V, T]] \Delta t^2 + \mathcal{O}(\Delta t^4). \quad (\text{A.12})$$

Since the error term contains the time step, the effective Hamiltonian is different for a real time step  $\Delta t$  and an imaginary time step  $-\Delta t$ , i.e. the eigenstate is found for a different system compared to which it is propagated for later. To minimize the effect of the error term, one could use smaller and smaller time steps for the imaginary time propagation. Instead, we use the *power method*. This can be thought of as approximating the short-time propagator as

$$e^{-\Delta t H_0} \approx (\mathbb{I} - \Delta t H_0) \quad (\text{A.13})$$

which seems like a crude approximation but gives the exact eigenstates of  $H_0$  (unless  $\Delta t$  is too large in which case it will diverge).

When a high stability of the initial state is required, we find the ground state of the real time evolution operator directly. To this end, note that the spectrum of  $e^{-i\Delta t H_0}$  lies on the unit circle in the complex plane as shown in Fig. A.1. By applying the power method to the operator  $e^{-i\Delta t H_0} + i\mathbb{I}$ , the iteration via repeated application of the operator will converge to the ground state because as it has the largest eigenvalue (by absolute value). When approximating the short-time propagator using the split-operator method, the iteration converges to a state that is not exactly the ground state of  $H_0$  but instead of  $H_{\text{eff}}$ . As opposed to the ground state of  $H_0$ , this state is exactly conserved in subsequent real-time propagation for finite step size  $\Delta t$ .

When the real-time evolution starts in the presence of an absorbing potential, some parts of the initial state are also absorbed. This leads to a background in the PMD that decreases the dynamic range that can be accessed in the simulation. To mitigate this problem – for example when both direct and rescattered electrons up to the cutoff are to be resolved – we let the numerically obtained ground state relax in the presence of the absorber until the absorption per unit time falls below some threshold.

### A.1.3 Choice of the potential

For any single-active-electron calculation, an effective potential has to be devised. Ideally, this potential takes the atomic nucleus (or the nuclei in case of a molecule) into account, as well as

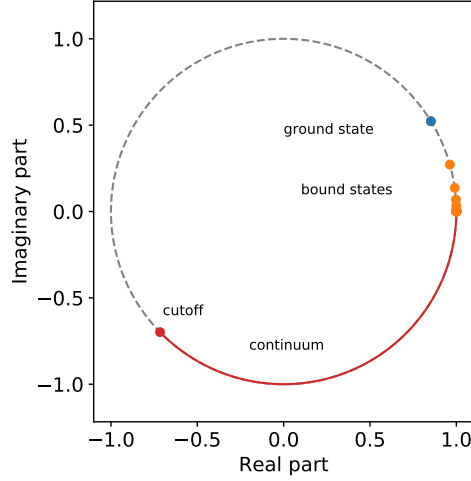


Figure A.1: Sketch of a typical spectrum of the short-time propagator. The position of the ground state depends on the time step while the continuum cutoff depends on the time step and the grid spacing.

	$\alpha_0$	$\alpha_1$	$\alpha_2$	$\alpha_3$	$\alpha_4$	$\alpha_5$	$\alpha_6$	$I_p$
H	1.0	0.000	0.000	0.000	0.000	0.000	0.000	0.500
Yu	0.0	1.908	1.000	0.000	0.000	0.000	0.000	0.500
He	1.0	1.231	0.662	-1.325	1.236	-0.231	0.480	0.904
Ne	1.0	8.069	2.148	-3.570	1.986	0.931	0.602	0.793
Ar	1.0	16.039	2.007	-25.543	4.525	0.961	0.443	0.580
Xe	1.0	51.356	2.112	-99.927	3.737	1.644	0.431	0.445
Ne <sup>+</sup>	2.0	8.043	2.715	0.506	0.982	-0.043	0.401	1.505
Ar <sup>+</sup>	2.0	14.989	2.217	-23.606	4.585	1.011	0.551	1.016

Table A.1: Parameters for the Tong-Lin potential (A.14) taken from [75].

the effect of the other electrons in a multi-electron system in an approximate way. A popular choice is the potential

$$V(r) = -\frac{\alpha_0 + \alpha_1 e^{-\alpha_2 r} + \alpha_3 r e^{-\alpha_4 r} + \alpha_5 e^{-\alpha_6 r}}{r} \quad (\text{A.14})$$

derived by Tong and Lin [293] using density-functional theory. Parameters for many atoms can be found in [75] which we reprint in Table A.1 for convenience. The first parameter  $\alpha_0$  always gives the asymptotic charge of the ion and  $\alpha_0 + \alpha_1 + \alpha_5 = Z$  adds up to the nuclear charge.

When the TDSE (2.11) is solved with the split-operator FFT method, it is best to avoid the the  $r \rightarrow 0$  singularity. This can be achieved by converting the potential into a pseudo potential according to the procedure described by Troullier and Martins in [294]. The basic idea is to calculate the bound-state wave function

$$\psi(r, \theta, \phi) = R_l^{\text{AE}}(r) Y_{lm}(\theta, \phi) \quad (\text{A.15})$$

and introduce a cutoff radius  $r_{cl}$  below which the radial wave function is replaced with

$$R_l^{\text{PP}}(r) = \begin{cases} R_l^{\text{AE}}(r), & r > r_{cl} \\ r^l \exp(p(r)), & r \leq r_{cl} \end{cases} \quad (\text{A.16})$$

	$r_{cl}$	$c_2$	$c_4$	$c_6$	$c_8$	$c_{10}$	$c_{12}$
H	1.0	$-1.115 \cdot 10^{+0}$	$-2.486 \cdot 10^{-1}$	$1.957 \cdot 10^{+0}$	$-2.419 \cdot 10^{+0}$	$1.309 \cdot 10^{+0}$	$-2.717 \cdot 10^{-1}$
Yu	1.0	$-1.910 \cdot 10^{+0}$	$-7.295 \cdot 10^{-1}$	$4.237 \cdot 10^{+0}$	$-5.122 \cdot 10^{+0}$	$2.752 \cdot 10^{+0}$	$-5.694 \cdot 10^{-1}$
He	1.5	$-1.227 \cdot 10^{+0}$	$-3.013 \cdot 10^{-1}$	$6.555 \cdot 10^{-1}$	$-3.498 \cdot 10^{-1}$	$8.376 \cdot 10^{-2}$	$-7.736 \cdot 10^{-3}$
Ne	1.5	$-2.129 \cdot 10^{+0}$	$-6.473 \cdot 10^{-1}$	$1.336 \cdot 10^{+0}$	$-7.055 \cdot 10^{-1}$	$1.676 \cdot 10^{-1}$	$-1.537 \cdot 10^{-2}$
Ar	1.5	$-5.270 \cdot 10^{-1}$	$-3.967 \cdot 10^{-2}$	$-5.400 \cdot 10^{-2}$	$5.302 \cdot 10^{-2}$	$-1.520 \cdot 10^{-2}$	$1.503 \cdot 10^{-3}$
Xe	2.0	$1.423 \cdot 10^{-1}$	$-2.893 \cdot 10^{-3}$	$-6.711 \cdot 10^{-2}$	$2.238 \cdot 10^{-2}$	$-2.970 \cdot 10^{-3}$	$1.467 \cdot 10^{-4}$
Ne <sup>+</sup>	1.5	$-2.157 \cdot 10^{+0}$	$-6.648 \cdot 10^{-1}$	$1.334 \cdot 10^{+0}$	$-7.026 \cdot 10^{-1}$	$1.668 \cdot 10^{-1}$	$-1.530 \cdot 10^{-2}$
Ar <sup>+</sup>	1.5	$-5.237 \cdot 10^{-1}$	$-3.918 \cdot 10^{-2}$	$-6.085 \cdot 10^{-2}$	$5.632 \cdot 10^{-2}$	$-1.592 \cdot 10^{-2}$	$1.566 \cdot 10^{-3}$

Table A.2: Parameters for the wave function (A.16) from which the pseudo potential (A.19) can be generated.

Here,  $p$  is a polynomial

$$p(r) = c_0 + c_2 r^2 + c_4 r^4 + c_6 r^6 + c_8 r^8 + c_{10} r^{10} + c_{12} r^{12} \quad (\text{A.17})$$

and the seven coefficients are determined by the condition that (i) the transition between the two wave functions at  $r_{cl}$  is continuous up to the fourth derivative; (ii) the curvature of the pseudo potential at the origin is zero; (iii) the norm of the wave function is conserved. To calculate the radial wave function  $R_l^{\text{AE}}(r)$ , we solve the radial Schrödinger equation

$$-\frac{1}{2} \frac{d}{dr} (r R_l^{\text{AE}}(r)) + \left( \frac{l(l+1)}{2r^2} + V(r) \right) (r R_l^{\text{AE}}(r)) = \mathcal{E} (r R_l^{\text{AE}}(r)) \quad (\text{A.18})$$

using an adaptive step size backwards differentiation method and match the solution at  $r < 10^{-4}$  a.u. to the asymptotic solution  $r^l (l - rZ + 1)$  while at  $r > 10$  a.u. we match to the large  $r$  asymptotic solution  $r^{Z/\kappa-1} e^{-\kappa r}$ .

In Table A.2 we approximate some coefficients from which pseudo wave functions for the Tong-Lin potential (A.14) can be built.<sup>2</sup> From the pseudo wave function, the pseudo potential is generated by inserting the pseudo wave function in the radial Schrödinger equation (A.18) and solving for the potential, giving

$$V_l^{\text{PP}}(r) = \begin{cases} V(r), & r > r_{cl} \\ \mathcal{E}_l + \frac{l+1}{r} p'(r) + \frac{p''(r) + (p'(r))^2}{2}, & r \leq r_{cl} \end{cases}. \quad (\text{A.19})$$

Inserting the energy of the bound state  $\mathcal{E}_l$  enforces the correct asymptotic behavior of the resulting potential.

The Tong-Lin potential for helium, its pseudo potential, the ground-state wave function and the pseudo wave function are shown in Fig. A.2. The asymptotically correct behavior of the pseudo wave function ensures that all properties of the ionization process in length-gauge saddle-point SFA are reproduced. Additionally, the correct asymptotic behavior of the pseudo potential ensures that weak field static ionization rates [253, 254] are reproduced.

Also in the regime of nonadiabatic tunnel ionization, good results can be obtained. Fig. A.3 shows the attoclock offset angle (a) and ionization yield (b) for strong-field ionization of hydrogen in attoclock configuration (the pulse (4.32) is chosen as in Chapter 4). Here, we have

<sup>2</sup>The cutoff radius is always chosen greater than the outermost node of the radial wave function. Thus, the pseudo wave function does not have nodes. If the bound state of the original potential is an s state, the corresponding bound state of the pseudo potential is a 1s state. Similarly, considering a p state of the original potential, the corresponding bound state of the pseudopotential is a 2p state.

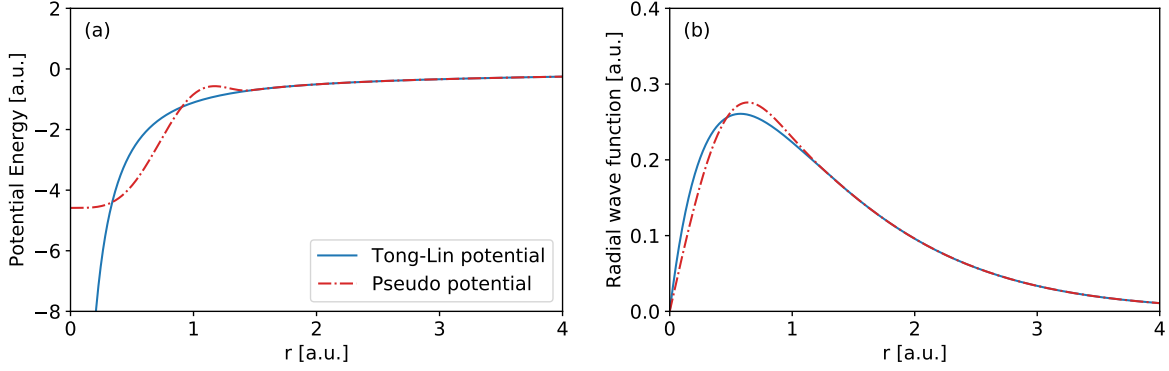


Figure A.2: (a) Tong-Lin potential (A.14) for helium and its ( $l = 0$ ) pseudo potential (A.19) for cutoff radius  $r_{cl} = 1.5$  a.u. (b) Ground-state radial wave function  $rR(r)$  for the Tong-Lin Potential and pseudo wave function.

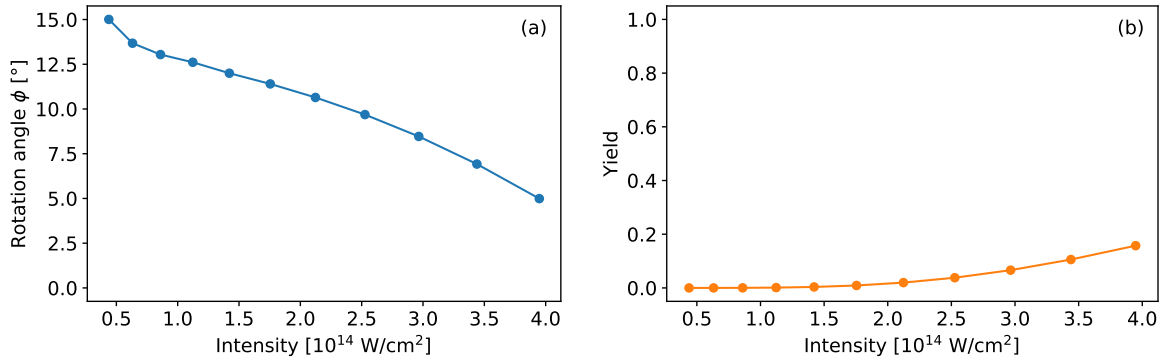


Figure A.3: Attoclock offset angles (a) and ionization yield (b) for 3D hydrogen in attoclock configuration. In (a), the PMD has been multiplied by  $p^2$  as in [78] before the angles have been obtained using the maxima of the PMD.

solved the 3D TDSE with the pseudo potential (A.19) on a grid of size  $256 \times 256 \times 256$  a.u. and 768 points in each dimension over a time of 1000 a.u. with time step 0.02 a.u. As usual, the PMD is obtained by projecting outgoing parts of the wave function onto Volkov states. Both the offset angles as well as the yield are in excellent agreement with the values provided in [78] where the TDSE has been solved for the same pulse parameters but with the full Coulomb potential.

While direct ionization can be well described using the pseudo potential, rescattering of the electron on the parent ion causes difficulties. Fig. A.4 shows differential cross sections calculated using positive-energy solutions of the radial Schrödinger equation (A.18) and the method described in the appendix of [295] for both the Tong-Lin and the pseudo potential. Good results are obtained for hydrogen and helium, but significant disagreement is found for neon and argon.

To improve the agreement, one would have to use a different potential for each angular momentum  $l$ . While this is easily implemented in a solver that relies on a decomposition of the time-dependent wave function into spherical harmonics, it is not straightforward to achieve in Cartesian coordinates. The next best thing we can do is to distinguish even and odd parity and use an  $l = 0$  potential for even parity and  $l = 1$  for the odd-parity component. For neon, using the 2s and 2p states at cutoff radius  $r_{cl} = 1.5$  a.u., good agreement with the original differential cross section is obtained. In argon, however, no significant improvement is found (here, the 3s



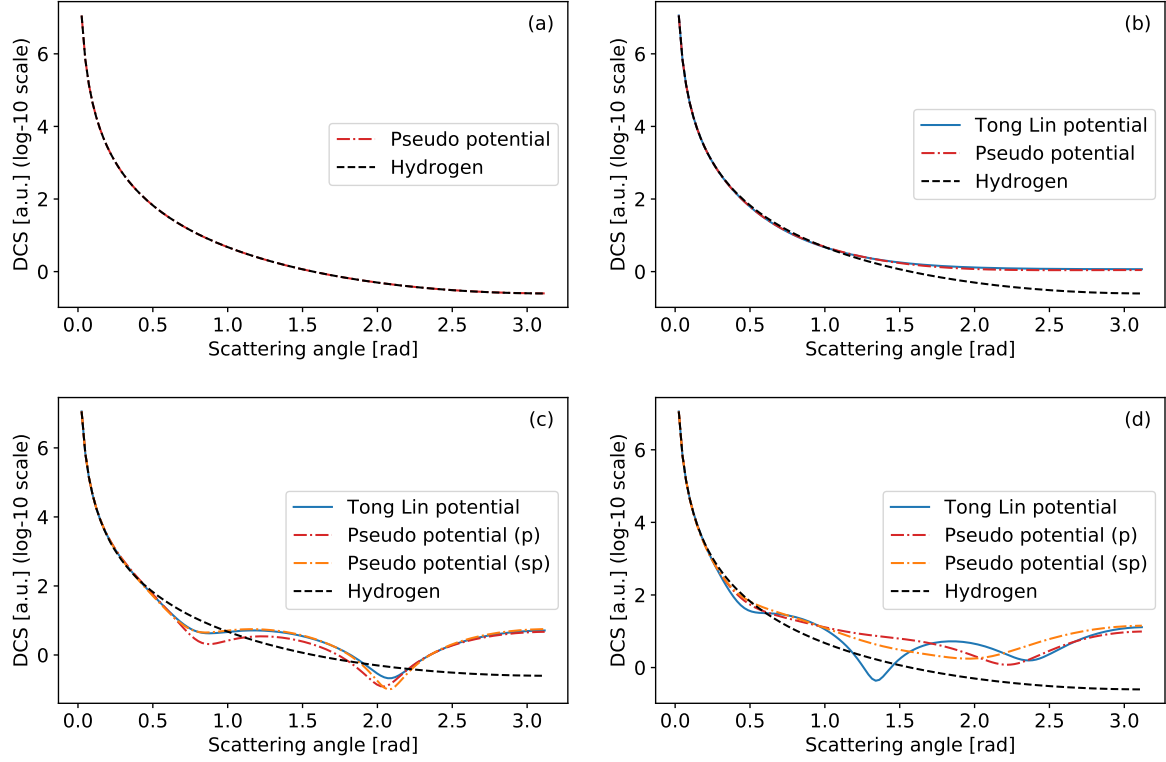


Figure A.4: Differential scattering cross sections at 1 a.u. momentum for various species. (a) Hydrogen. (b) Helium. (c) Neon. (d) Argon. In all panels, the black dashed line gives the Rutherford cross section. The cross section for the Tong-Lin potential (A.14) and the given species is shown as blue solid line. When the pseudo potential (A.19) is used instead, the cross section marked as a red dashed line is found instead. The orange dashed line give the cross section when different potentials are used depending on angular momentum.

and  $3p$  states at cutoff radius  $r_{cl} = 1.5$  a.u were used).

#### A.1.4 Choice of the absorbing potential

The absorbing potential is chosen as a  $n$ th-order polynomial (usually  $n = 4$ )

$$V_C(r) = \begin{cases} 0 & r < r_0 \\ \alpha(r - r_0)^n & r \geq r_0 \end{cases}. \quad (\text{A.20})$$

To determine a suitable value for  $\alpha$ , we go to a simplified 1D setting and write a wave function in the absorber region at momentum  $p$  using the eikonal approximation as

$$\psi(r) = \psi(r_0) \exp\left(ip(r - r_0) - \frac{1}{p} \int_{r_0}^r dr' V_C(r')\right) \quad (\text{A.21})$$

such that the transmission coefficient becomes

$$\epsilon = \frac{|\psi(r_0 + \Delta r)|^2}{|\psi(r_0)|^2} = \exp\left(-\frac{2\alpha(\Delta r)^{n+1}}{p(n+1)}\right). \quad (\text{A.22})$$

This allows us to choose some desired transmission error at the relevant energy scale of the problem (specified by  $p$ ) to determine the strength of the absorbing potential as

$$\alpha = \frac{(n+1)p}{2(\Delta r)^{n+1}} (-\log \epsilon). \quad (\text{A.23})$$

Usually  $10^{-15} \leq \epsilon \leq 10^{-10}$  and  $p$  is chosen somewhat above the cutoff momentum in a given calculation. Then the absorber is made wide enough such that reflections become manageable.

## A.2 Strong-field approximation

### A.2.1 Adiabatic expansion of the saddle-point equation

To solve the SFA saddle-point equations (2.29), one can employ a Taylor-expansion of the vector potential around a given real part  $t_r$  of the ionization time [296],

$$\mathbf{A}(t) = \mathbf{A}(t_r) - \sum_{n=1}^{\infty} \frac{\mathbf{E}^{(n-1)}(t_r)}{n!} (it_i)^n. \quad (\text{A.24})$$

Here,  $\mathbf{E}^{(n)}(t_r)$  denotes the  $n$ th derivative of the electric field. Denoting by  $\mathbf{v}_0 = \mathbf{p} + \mathbf{A}(t_r)$  the tunnel-exit velocity of the photoelectron, the saddle-point equation becomes

$$\left( \mathbf{v}_0 - \sum_{n=1}^{\infty} \frac{\mathbf{E}^{(n-1)}}{n!} (it_i)^n \right)^2 + 2I_p = 0. \quad (\text{A.25})$$

Here, we have omitted the argument  $t_r$  for simplicity. The strong-field ionization problem typically involves two different time scales provided by the Keldysh time  $\sqrt{2I_p}/E_0$  (where  $E_0$  is a characteristic field strength of the problem) and the frequency  $\omega$  of the applied laser field. Their dimensionless combination is the Keldysh parameter  $\gamma$ . We choose to measure real time in terms of the frequency,  $t_r = \hat{t}_r/\omega$ , and imaginary time in multiples of the Keldysh time,  $t_i = \sqrt{2I_p}/E_0 \hat{t}_i$ . Then, a dimensionless electric field can be written as  $\mathbf{E}^{(n)} = E_0 \omega^n \hat{\mathbf{E}}^{(n)}$ . Also introducing a dimensionless velocity  $\mathbf{v}_0 = \sqrt{2I_p} \hat{\mathbf{v}}_0$  and inserting these definitions into (A.25), the saddle-point equation becomes<sup>3</sup>

$$\left( \hat{\mathbf{v}}_0 - \sum_{n=1}^{\infty} \frac{\gamma^{n-1} \hat{\mathbf{E}}^{(n-1)}}{n!} (i\hat{t}_i)^n \right)^2 + 1 = 0. \quad (\text{A.26})$$

Including terms up to first order in  $\gamma$ ,

$$\left( \hat{\mathbf{v}}_0 - i\hat{t}_i \hat{\mathbf{E}} + \frac{1}{2} \gamma \hat{t}_i^2 \hat{\mathbf{E}}' \right)^2 + 1 = 0. \quad (\text{A.27})$$

Defining the auxiliary velocity

$$\hat{\mathbf{w}}_0 = \hat{\mathbf{v}}_0 + \frac{1}{2} \gamma \hat{t}_i^2 \hat{\mathbf{E}}' \quad (\text{A.28})$$

and separating real and imaginary part, we find

$$\hat{\mathbf{w}}_0 \cdot \hat{\mathbf{E}} = 0 \quad (\text{A.29})$$

and

$$\hat{\mathbf{w}}_0^2 - \hat{t}_i^2 \hat{\mathbf{E}}^2 + 1 = 0. \quad (\text{A.30})$$

---

<sup>3</sup>Note that the Keldysh parameter appears in different order compared to the imaginary time. Therefore, an expansion to fixed order in imaginary time, as performed for example in [297], is not equivalent to an expansion to fixed order in the Keldysh parameter. In particular, in the adiabatic limit, the Keldysh parameter goes to zero but the imaginary time does not have to.

This suggests the general procedure to choose any auxiliary velocity  $\hat{\mathbf{w}}_0$  that satisfies (A.29), then solving (A.30) for the imaginary time and find the true initial velocity  $\hat{\mathbf{v}}_0$  from (A.28). At  $\gamma \rightarrow 0$  the difference between the two velocities vanishes and the conditions

$$\mathbf{v}_0 \cdot \mathbf{E} = 0, \quad t_i^2 = \frac{2I_p + \mathbf{v}_0^2}{E^2} \quad (\text{A.31})$$

are retrieved. This is the foundation of the zero-transverse-velocity assumption in SCTS and related models (see Section 2.6).

The effect of the first-order correction (A.28) is essentially a modification of the initial velocity in the direction of  $\mathbf{E}'$ . In linear polarization ( $\mathbf{E} \parallel \mathbf{E}'$ ), this leads to an initial velocity of the photoelectron in tunneling direction [95, 98, 204]. In circular polarization (where  $\mathbf{E} \perp \mathbf{E}'$ ), it leads to a modification of the velocity perpendicular to the tunneling direction.

### A.2.2 Adiabatic limit of the action

Using the same expansion as above, the imaginary part of the action (2.24) that determines the ionization rate, can be evaluated in the adiabatic limit. We define a scaled (imaginary part of the) action

$$\text{Im } \hat{S} = \left( \frac{(2I_p)^{3/2}}{E_0} \right)^{-1} \text{Im } S. \quad (\text{A.32})$$

Then we can write

$$\begin{aligned} 2\text{Im } \hat{S} &= -\hat{t}_i + \text{Im} \int_0^{\hat{t}_i} (-id\hat{t}) \left( \hat{\mathbf{v}}_0 - i\hat{t}\hat{\mathbf{E}} + \frac{1}{2}\gamma\hat{t}^2\hat{\mathbf{E}}' + \mathcal{O}(\gamma^2) \right)^2 \\ &= -\hat{t}_i - \int_0^{\hat{t}_i} d\hat{t} \left( \hat{\mathbf{v}}_0^2 - \hat{t}^2\hat{\mathbf{E}}^2 + \gamma\hat{t}^2\hat{\mathbf{E}}' \cdot \hat{\mathbf{v}}_0 + \mathcal{O}(\gamma^2) \right) \\ &= -\hat{t}_i(1 + \hat{\mathbf{v}}_0^2) + \frac{1}{3}\hat{t}_i^3\hat{\mathbf{E}}^2 - \frac{1}{3}\gamma\hat{t}_i^3\hat{\mathbf{E}}' \cdot \hat{\mathbf{v}}_0 + \mathcal{O}(\gamma^2). \end{aligned} \quad (\text{A.33})$$

Inserting the lowest-order solution for the saddle point,

$$2\text{Im } \hat{S} = -\frac{2(1 + \hat{\mathbf{v}}_0^2)^{3/2}}{3\hat{\mathbf{E}}} - \gamma \frac{(1 + \hat{\mathbf{v}}_0^2)^{3/2}}{3\hat{\mathbf{E}}^3} \hat{\mathbf{E}}' \cdot \hat{\mathbf{v}}_0 + \mathcal{O}(\gamma^2). \quad (\text{A.34})$$

For  $\gamma \rightarrow 0$ , the exponent of the ADK rate (2.44) is retrieved. The first-order correction leads to an offset of the maximum position in the photoelectron momentum distribution. It can be found by maximizing (A.34) subject to the constraint  $\hat{\mathbf{v}}_0 \cdot \hat{\mathbf{E}} = 0$  and is given by

$$\Delta\hat{\mathbf{v}}_0 = -\frac{\gamma}{6\hat{\mathbf{E}}^2} \left( \hat{\mathbf{E}}' - \frac{\hat{\mathbf{E}}' \cdot \hat{\mathbf{E}}}{\hat{\mathbf{E}}^2} \hat{\mathbf{E}} \right). \quad (\text{A.35})$$

The term in parentheses is the component of  $\hat{\mathbf{E}}'$  perpendicular to the electric field  $\hat{\mathbf{E}}$ . In linear polarization, the first-order correction vanishes because  $\hat{\mathbf{E}} \parallel \hat{\mathbf{E}}'$ . In circular polarization, on the other hand,  $\hat{\mathbf{E}} \perp \hat{\mathbf{E}}'$  and the correction has observable consequences. To evaluate it, we go back to atomic units. There, the velocity offset becomes

$$\Delta\mathbf{v}_0 = -\frac{I_p}{3E^2} \left( \hat{\mathbf{E}} - \frac{\hat{\mathbf{E}} \cdot \mathbf{E}}{E^2} \mathbf{E} \right). \quad (\text{A.36})$$

For circular polarization  $\mathbf{A}(t) = -E_0/\omega (\cos(\omega t), \sin(\omega t))$ , the correction evaluates to [260, 298–300]

$$|\Delta \mathbf{v}_0| = \frac{\omega I_p}{3E_0} \quad (\text{A.37})$$

and it points in the direction of the negative vector potential. Therefore, it leads to a higher mean photoelectron energy compared to the adiabatic case [301].

### A.2.3 Angular momentum states

Consider an initial state carrying angular momentum  $(l, m)$  with asymptotic behavior

$$\psi_0(\mathbf{r}) \rightarrow A r^{\nu-1} e^{-\kappa r} Y_{lm}(\hat{\mathbf{r}}), \quad \nu = Z/\kappa. \quad (\text{A.38})$$

In saddle-point approximation where the SFA matrix element (2.25) is evaluated close to the pole, it will include a term  $e^{im\phi}$  [143] where  $\phi$  is the tunneling angle which (for a field in the  $xy$  plane) is given by

$$\tan \phi = \frac{p_y + A_y(t_s)}{p_x + A_x(t_s)}. \quad (\text{A.39})$$

Since  $\phi$  is complex, the absolute value  $|e^{im\phi}|^2 = e^{-m 2\text{Im} \phi}$  is different from one. This leads to a modification of the signal depending on the magnetic quantum number  $m$  of the initial state [260, 302]. Here, both the yield as well as the expected photoelectron energy are modified. In the adiabatic limit  $\gamma \rightarrow 0$ , the tunneling angle simplifies to

$$\tan \phi = \frac{v_y - it_i E_y}{v_x - it_i E_x} \quad (\text{A.40})$$

where  $v_x = p_x + A_x$  and  $v_y = p_y + A_y$ . Here, all fields are evaluated at the real part  $t_r$  of the saddle-point time  $t_s$ . The imaginary part of the tunneling angle is given by

$$2\text{Im} \phi = \log \sqrt{\frac{(v_x - it_i E_y)^2 + (v_y + it_i E_x)^2}{(v_x + it_i E_y)^2 + (v_y - it_i E_x)^2}} = \frac{2 \mathbf{v} \cdot \mathbf{E}_\perp}{\sqrt{2I_p} E} + \mathcal{O}(v^3) \quad (\text{A.41})$$

where  $\mathbf{E}_\perp = (-E_y, E_x, 0)$ . Thus, the signal (restricting ourselves to the exponential part) is determined by

$$2\text{Im} S - m 2\text{Im} \phi = -\frac{2(2I_p)^{3/2}}{3E} - \frac{\sqrt{2I_p} v^2}{E} - \frac{2m \mathbf{v} \cdot \mathbf{E}_\perp}{\sqrt{2I_p} E} + \mathcal{O}(v^3) \quad (\text{A.42})$$

and the maximum is found at

$$\mathbf{v}_0 \approx -\frac{m \mathbf{E}_\perp}{2I_p}. \quad (\text{A.43})$$

Noting that  $\mathbf{r}_0 = -I_p \mathbf{E}/E^2$  can be thought of the position of the tunnel exit, this can be put in the suggestive form

$$\mathbf{L}_{\text{exit}} = \mathbf{r}_0 \times \mathbf{v}_0 = \left( -\frac{I_p \mathbf{E}}{E^2} \right) \times \left( -\frac{m \mathbf{E}_\perp}{2I_p} \right) = \frac{m}{2} \mathbf{e}_z, \quad (\text{A.44})$$

indicating that half the angular momentum of the initial state “survives” the static tunneling process.

### A.2.4 Explicit solution of the saddle-point equation

Consider the saddle-point equation (2.29)

$$\frac{1}{2}(\mathbf{p} + \mathbf{A}(t_s))^2 + I_p = 0 \quad (\text{A.45})$$

with the vector potential  $\mathbf{A}$  evaluated at the saddle-point time  $t_s$ . Decomposing  $\mathbf{A}(t_s)$  into real and imaginary part, this can be written as

$$\begin{aligned} (\mathbf{p} + \text{Re } \mathbf{A}(t_s))^2 &= (\text{Im } \mathbf{A}(t_s))^2 - 2I_p, \\ (\mathbf{p} + \text{Re } \mathbf{A}(t_s)) \cdot \text{Im } \mathbf{A} &= 0. \end{aligned} \quad (\text{A.46})$$

The first equation implies that the real part of initial velocity at the complex ionization time  $\mathbf{p} + \text{Re } \mathbf{A}(t_s)$  lies on a circle of radius  $\sqrt{(\text{Im } \mathbf{A}(t_s))^2 - 2I_p}$ . The second equation implies that it also lies on a line perpendicular to  $\text{Im } \mathbf{A}(t_s)$ . The solution of both the real and imaginary part of the saddle-point equation is given by the two intersections, so the final momentum is given by

$$\mathbf{p} = -\text{Re } \mathbf{A}(t_s) \pm \frac{\text{Im } \mathbf{A}_\perp(t_s)}{|\text{Im } \mathbf{A}(t_s)|} \sqrt{(\text{Im } \mathbf{A}(t_s))^2 - 2I_p}. \quad (\text{A.47})$$

Here,  $\text{Im } \mathbf{A}_\perp$  is perpendicular to  $\text{Im } \mathbf{A}$  and has the same length. For a given  $\text{Re } t_s$  the imaginary part  $\text{Im } t_s$  must be large enough for the square root to be real. The expression can be seen as a generalization of the simple man's expression

$$\mathbf{p} = -\mathbf{A}(t_r) \pm \frac{\mathbf{E}_\perp(t_r)}{|\mathbf{E}(t_r)|} v \quad (\text{A.48})$$

which is retrieved from (A.47) in the adiabatic limit where we can replace  $\mathbf{A}(t_s) = \mathbf{A}(t_r) - it_i \mathbf{E}(t_r)$  and  $t_i = \sqrt{2I_p + v^2}/E(t_r)$ . Here,  $v$  is the initial velocity perpendicular to the instantaneous field direction.

## A.3 Stationary points of the full Dyson integrand

To analyze the structure of the saddle points, it is useful to measure the imaginary time in units of the Keldysh time,  $\hat{t}_i = t_i/t_K$ , and set  $\alpha = E_0/(2I_p^{\text{eff}})^{3/2}$ . With these definitions, the saddle-point condition (4.13) becomes

$$\hat{f}(\hat{t}_i) = 2\alpha(1 - \hat{t}_i^2) - \hat{t}_i(1 - \hat{t}_i^2)^2 + 4\hat{t}_i^2\alpha(v + 2) = 0. \quad (\text{A.49})$$

For  $\alpha \rightarrow 0$ , the two solutions approach  $\hat{t}_i^{(0)} \rightarrow 0$  and  $\hat{t}_i^{(1)} \rightarrow 1$ . To find an approximate solution in the weak field case, we write  $\hat{t}_i^{(0)}$  as a power series in  $\alpha$  and  $\hat{t}_i^{(1)}$  as a power series in  $\sqrt{\alpha}$ . Inserting the series expansions into (A.49) and solving order by order for the coefficients, we find

$$\hat{t}_i^{(0)} = 2\alpha + \mathcal{O}(\alpha^3), \quad \hat{t}_i^{(1)} = 1 - \sqrt{\alpha(v + 2)} - \alpha/2 + \mathcal{O}(\alpha^{3/2}) \quad (\text{A.50})$$

from which (4.14) is obtained by reinserting  $\hat{t}_i$  and  $\alpha$  in terms of their definition.

To find the critical field strength where the two solutions merge, we have to solve  $\hat{f}(\hat{t}_i) = 0$  and  $\hat{f}'(\hat{t}_i) = 0$  for  $\alpha^{\text{crit}}$  and  $\hat{t}_i^{\text{crit}}$ , given  $v$ . The solutions define two functions  $g$  and  $h$  such that

$$\alpha^{\text{crit}} = g(v), \quad \hat{t}_i^{\text{crit}} = h(v). \quad (\text{A.51})$$

Although their explicit form is quite cumbersome, they can be represented accurately by their (1, 1) Padé approximants at  $\nu = 0$  given by

$$g(\nu) = \frac{4(10 + \nu)}{27(15 + 4\nu)}, \quad h(\nu) = \frac{75 + 8\nu}{225 + 54\nu}. \quad (\text{A.52})$$

The result (4.15) in the main text can be obtained by reinserting the definitions of  $\alpha$  and  $\hat{t}_i$  into (A.51).

## A.4 Analytical R-matrix theory

### A.4.1 Correction after the end of the laser pulse

For a long-range potential  $V(r) \simeq -Z/r$ , the ARM correction to the action (2.43) after the end of the laser pulse must also be considered. It can be evaluated in closed form [146] and one finds

$$\int_T^\infty dt' V(\mathbf{r}_L(t'; \mathbf{p}, t_s)) = \int_T^\infty dt \frac{-Z}{\sqrt{(\mathbf{r} + \mathbf{p}(t - T))^2}} = \frac{Z}{p} \log(\mathbf{r} \cdot \mathbf{p} + r p). \quad (\text{A.53})$$

Here,  $\mathbf{r} = \mathbf{r}_L(T; \mathbf{p}, t_s)$  is the position of the photoelectron at time  $T$ . The integral is actually divergent but the divergent part is always real and depends only on the final momentum and not on the position. It therefore does not affect the observable spectrum and can be omitted. It is the same expression also found in the asymptotic expression for the Coulomb scattering state [135]

$$\psi_{\mathbf{p}}^{(-)}(\mathbf{r}) \simeq e^{i\mathbf{p} \cdot \mathbf{r}} e^{iZ/p \log(\mathbf{r} \cdot \mathbf{p} + r p)} \quad \text{as} \quad r + \mathbf{r} \cdot \mathbf{p}/p \rightarrow \infty. \quad (\text{A.54})$$

### A.4.2 Boundary matching for soft-core potentials

The lower limit  $t_\kappa = t_s - i a_0/\kappa$  in the integral (2.43) must be chosen to fit the under-the-barrier contribution of the Coulomb correction of the action to the asymptotic tail of the bound-state wave function [93], i.e.

$$(\kappa a)^{Z/\kappa} = \exp\left(-\frac{1}{\kappa} \int_{a_0}^a dz \frac{-Z}{\sqrt{z^2 + \alpha}}\right). \quad (\text{A.55})$$

The integral can be evaluated to

$$\int_{a_0}^a dz \frac{1}{\sqrt{z^2 + \alpha}} = \log\left(\frac{a + \sqrt{a^2 + \alpha}}{a_0 + \sqrt{a_0^2 + \alpha}}\right) \quad (\text{A.56})$$

such that condition (A.55) becomes

$$(\kappa a)^{Z/\kappa} = \exp\left(\frac{Z}{\kappa} \log\left(\frac{a + \sqrt{a^2 + \alpha}}{a_0 + \sqrt{a_0^2 + \alpha}}\right)\right). \quad (\text{A.57})$$

In the asymptotic region  $\sqrt{a^2 + \alpha} \simeq a$ , so  $a$  cancels and we find

$$\kappa = \frac{2}{a_0 + \sqrt{a_0^2 + \alpha}} \quad \Rightarrow \quad a_0 = \frac{1}{\kappa} - \frac{\alpha\kappa}{4}. \quad (\text{A.58})$$

Then the lower limit becomes

$$t_\kappa = t_s - i\kappa^{-2} + i\alpha/4. \quad (\text{A.59})$$

For  $\alpha = 0$ , the familiar result for the Coulomb potential is retrieved.

### A.4.3 Momentum shift in the attoclock

In the adiabatic limit  $\gamma \rightarrow 0$ , the momentum shift

$$\Delta \mathbf{p} = - \int_{t_r}^T dt' \nabla V(\text{Re } \mathbf{r}_L(t'; \mathbf{p}, t_s)) \quad (\text{A.60})$$

from (5.36) can be evaluated exactly.<sup>4</sup> Using the expansion (A.24) for  $\gamma \rightarrow 0$  and  $\mathbf{v}_0 = 0$ , the position of the photoelectron at  $t_r$  is

$$\text{Re } \mathbf{r}_L(t_r; \mathbf{p}, t_s) = \text{Re} \int_{t_s}^{t_r} dt (\mathbf{p} + \mathbf{A}(t)) = \text{Re} \int_{t_s}^{t_r} dt \mathbf{A}(t) = - \frac{I_p \mathbf{E}(t_r)}{E(t_r)^2}. \quad (\text{A.61})$$

Here, we have used the fact that  $t_i = \sqrt{2I_p}/E(t_r)$  according to (A.31). After the tunnel exit, the photoelectron is accelerated with constant acceleration such that for  $t > t_r$ ,

$$\text{Re } \mathbf{r}_L(t; \mathbf{p}, t_s) = - \frac{I_p \mathbf{E}(t_r)}{E(t_r)^2} - \frac{1}{2} \mathbf{E}(t_r)(t - t_r)^2. \quad (\text{A.62})$$

Inserting this into (A.60) and assuming a Coulomb-potential for  $V = -1/r$  after the tunnel exit, the integral can be evaluated analytically. The result is

$$\Delta \mathbf{p} = \frac{\pi \mathbf{E}(t_r)}{(2I_p)^{3/2}}. \quad (\text{A.63})$$

For the bicircular attoclock,  $\mathbf{E} \parallel \mathbf{e}_y$  while the  $p_x$  position of the maximum is given by  $p_x^{\text{max}} \approx E_{\text{peak}}/(2\omega)$ . Thus, the relative shift becomes

$$\frac{\Delta p_y}{p_x^{\text{max}}} \approx \frac{2\pi\omega}{(2I_p)^{3/2}}. \quad (\text{A.64})$$

For the circular attoclock, the maximum is located at radial momentum  $p_r \approx E_0/\omega$  and one finds [234, 235]

$$\Delta \phi \approx \frac{\pi\omega}{(2I_p)^{3/2}}. \quad (\text{A.65})$$

### A.4.4 Semiclassical action

We consider the action

$$S_{\text{SC}}(\mathbf{p}, T; \mathbf{r}, t) = \dot{\mathbf{r}}_N(t) \cdot \mathbf{r} + \int_t^T dt' \left\{ \frac{1}{2} \dot{\mathbf{r}}_N(t')^2 + V(\mathbf{r}_N(t')) - \mathbf{r}_N(t') \cdot \nabla V(\mathbf{r}_N(t')) \right\} \quad (\text{A.66})$$

from the semiclassical propagator (2.48). Here,  $\mathbf{r}_N(t')$  describes a Newtonian trajectory

$$\ddot{\mathbf{r}}_N(t') = -\nabla V(\mathbf{r}_N(t')) - \mathbf{E}(t'), \quad \mathbf{r}_N(t) = \mathbf{r}, \quad \dot{\mathbf{r}}_N(T) = \mathbf{p} \quad (\text{A.67})$$

that starts at initial position  $\mathbf{r}$  at time  $t$  and ends with final momentum  $\mathbf{p}$  at time  $T$ . Inserting the electron velocity

$$\dot{\mathbf{r}}_N(t') = \mathbf{p} + \mathbf{A}(t') + \int_{t'}^T dt'' \nabla V(\mathbf{r}_N(t'')), \quad (\text{A.68})$$

<sup>4</sup>The Keldysh parameter  $\gamma$  was originally thought of describing the time associated with tunneling compared to the period of the field. By studying the dependence of  $\Delta \mathbf{p}$  on the upper limit  $T$  in (A.60), one can show that  $\gamma$  also describes the time in which a given percentage of the attoclock shift is acquired, relative to the period of the field. In the adiabatic limit  $\gamma \rightarrow 0$ , the attoclock shift is acquired in a time much shorter than the field period such that the direction of the field can be assumed to be constant.

The kinetic part of the action (A.66) evaluates to

$$\begin{aligned}
& \dot{\mathbf{r}}_N(t) \cdot \mathbf{r} + \int_t^T dt' \frac{1}{2} \dot{\mathbf{r}}_N(t')^2 \\
&= (\mathbf{p} + \mathbf{A}(t)) \cdot \mathbf{r} + \int_t^T dt' \frac{1}{2} (\mathbf{p} + \mathbf{A}(t'))^2 \\
&+ \mathbf{r} \cdot \int_t^T dt' \nabla V(\mathbf{r}_N(t')) + \int_t^T dt' (\mathbf{p} + \mathbf{A}(t')) \cdot \int_{t'}^T dt'' \nabla V(\mathbf{r}_N(t'')) \\
&+ \frac{1}{2} \int_t^T dt' \left( \int_{t'}^T dt'' \nabla V(\mathbf{r}_N(t'')) \right)^2.
\end{aligned} \tag{A.69}$$

In the last part of the action(A.66), we can use partial integration to get

$$\begin{aligned}
& - \int_t^T dt' \mathbf{r}_N(t') \cdot \nabla V(\mathbf{r}_N(t')) \\
&= \mathbf{r}_N(t') \cdot \int_{t'}^T dt'' \nabla V(\mathbf{r}_N(t'')) \Big|_t^T - \int_t^T dt' \dot{\mathbf{r}}_N(t') \cdot \int_{t'}^T dt'' \nabla V(\mathbf{r}_N(t'')).
\end{aligned} \tag{A.70}$$

Here, the first term is equal to

$$\mathbf{r}_N(t') \cdot \int_{t'}^T dt'' \nabla V(\mathbf{r}_N(t'')) \Big|_t^T = -\mathbf{r} \cdot \int_t^T dt' \nabla V(\mathbf{r}_N(t')) \tag{A.71}$$

while the second term can be written as

$$\begin{aligned}
& - \int_t^T dt' \dot{\mathbf{r}}_N(t') \cdot \int_{t'}^T dt'' \nabla V(\mathbf{r}_N(t'')) \\
&= - \int_t^T dt' (\mathbf{p} + \mathbf{A}(t')) \cdot \int_{t'}^T dt'' \nabla V(\mathbf{r}_N(t'')) - \int_t^T dt' \left( \int_{t'}^T dt'' \nabla V(\mathbf{r}_N(t'')) \right)^2.
\end{aligned} \tag{A.72}$$

The two contributions (A.71) and (A.72) cancel exactly the second line on the r.h.s. of Eq. (A.69) while adding to the term in the last line, but with a different sign. Leaving the Coulomb-phase term in (A.66) untouched, the semiclassical action becomes

$$\begin{aligned}
S_{SC}(\mathbf{p}, T; \mathbf{r}, t) &= (\mathbf{p} + \mathbf{A}(t)) \cdot \mathbf{r} + \int_t^T dt' \frac{1}{2} (\mathbf{p} + \mathbf{A}(t'))^2 \\
&- \frac{1}{2} \int_t^T dt' \left( \int_{t'}^T dt'' \nabla V(\mathbf{r}_N(t'')) \right)^2 + \int_t^T dt' V(\mathbf{r}_N(t))
\end{aligned} \tag{A.73}$$

which is equal to (5.45) in the main text.

## A.5 Static ionization rates

For a bound state in  $D = 1, 2, 3$  dimensions with asymptotic behavior

$$\psi_0(r) \rightarrow \frac{B}{\sqrt{2\pi}} r^\alpha e^{-\kappa r}, \quad \alpha = \frac{Z}{\kappa} - \frac{D-1}{2}, \tag{A.74}$$



the weak-field static ionization rate is given by<sup>5</sup>

$$\Gamma_D(B, Z) = |B|^2 \left(\frac{\kappa}{2\pi}\right)^{(3-D)/2} \left(\frac{2\kappa^2}{E}\right)^{2Z/\kappa - (D-1)/2} e^{-2\kappa^3/(3E)}. \quad (\text{A.75})$$

Although the exponential part is the same in all dimensions, the prefactor and thus the rate depends on the dimension. The choice of dimension can be compensated for by altering  $Z$ . For a 1D potential with asymptotic nuclear charge  $Z_1$  to have the same field-strength scaling of the rate as a 3D potential with charge  $Z_3$ , we require that the exponent in the prefactor be the same, i.e.

$$\frac{2Z_3}{\kappa} - 1 = \frac{2Z_1}{\kappa} \Rightarrow Z_1 = Z_3 - \frac{\kappa}{2}. \quad (\text{A.76})$$

For a 2D potential, the condition reads

$$\frac{2Z_3}{\kappa} - 1 = \frac{2Z_2}{\kappa} - \frac{1}{2} \Rightarrow Z_2 = Z_3 - \frac{\kappa}{4}. \quad (\text{A.77})$$

In particular, for a 1D model potential to have the same field-strength scaling of the rate as hydrogen, the asymptotic nuclear charge must be  $Z_1 = 1/2$ . For a 2D model potential, the asymptotic nuclear charge must be  $Z_2 = 3/4$ .

A similar result was obtained using a completely different approach in [306, 307]. There, a 1D effective potential for hydrogen was created as follows. From the ground-state wave function  $\psi_0(r) = e^{-r}/\sqrt{\pi}$ , the density  $e^{-2r}/\pi$  is obtained. Projecting this density onto the  $z$  axis, the one-dimensional density  $(|z|+1/2)e^{-2|z|}$  is found from which a one-dimensional wave function  $\psi_0(z) = \sqrt{|z|+1/2}e^{-|z|}$  is generated. Then, by inversion of the 1D time-independent Schrödinger equation, a potential is found. It is given by

$$V_1(z) = -\frac{3+4|z|}{2(1+2|z|)^2} \quad (\text{A.78})$$

and, in accordance with the argument above, has asymptotic nuclear charge  $1/2$ .

This agreement is quite general. Generating a density from the asymptotic expression (A.74) in 3D and projecting it onto the  $z$  axis, we find for large  $|z|$

$$\rho_1(z) \simeq \int_0^\infty d\rho \rho \left( B_3 \left( \sqrt{\rho^2 + z^2} \right)^{Z_3/\kappa - 1} e^{-\kappa\sqrt{\rho^2 + z^2}} \right)^2 \simeq \left( \frac{B_3 e^{-\kappa|z|} |z|^{Z_3/\kappa - 1/2}}{\sqrt{2\kappa}} \right)^2. \quad (\text{A.79})$$

This asymptotic behavior matches the 1D asymptote (A.74) when  $Z_1 = Z_3 - \kappa/2$  as above. For the prefactor, we find

$$\frac{B_3}{\sqrt{2\kappa}} = \frac{B_1}{\sqrt{2\pi}} \Rightarrow B_1 = \sqrt{\frac{\pi}{\kappa}} B_3. \quad (\text{A.80})$$

Inserting the prefactor  $B_1$  and the corrected charge  $Z_1$  into the expression for the rate (A.75), we find  $\Gamma_1(B_1, Z_1) = \Gamma_3(B_3, Z_3)/2$ , i.e. the field-strength scaling of the rate turns out correct, but

---

<sup>5</sup>For the ground state of hydrogen ( $D = 3$ ,  $Z = 1$ ,  $\kappa = 1$ ,  $B = \sqrt{2}$ ) the expression was already given by Landau and Lifshitz [303]. For a short-range potential ( $Z = 0$ ), the exact same expression can be obtained from the strong-field approximation in saddle-point approximation in the adiabatic limit. The general 3D expression was derived in [3, 5, 304]. In general, the derivation makes use of a separation of the Schrödinger equation in parabolic coordinates where the asymptotic tail of the wave function in the tunneling region is matched to a WKB solution, see [253]. For the 1D and 2D case, the derivation of the 3D case can be repeated almost unchanged. The 1D expression is also provided in [305].

the rate is underestimated by a constant factor of 2. Similarly, for a 2D model potential we find

$$\rho_2(\rho) \simeq \int_{-\infty}^{\infty} dz \left( \frac{B_3}{\sqrt{2\pi}} \left( \sqrt{\rho^2 + z^2} \right)^{Z_3/\kappa - 1} e^{-\kappa \sqrt{\rho^2 + z^2}} \right)^2 \simeq \left( \frac{B_3 e^{-\kappa \rho} \rho^{Z_3/\kappa - 3/4}}{\sqrt{2}(\pi\kappa)^{1/4}} \right)^2. \quad (\text{A.81})$$

This asymptotic behavior matches the 2D asymptote (A.74) when  $Z_2 = Z_3 - \kappa/4$  as above. For the prefactor, we find

$$\frac{B_3}{\sqrt{2}(\pi\kappa)^{1/4}} = \frac{B_2}{\sqrt{2\pi}} \Rightarrow B_2 = \left( \frac{\pi}{\kappa} \right)^{1/4} B_3. \quad (\text{A.82})$$

Inserting the prefactor  $B_2$  and the corrected charge  $Z_2$  into the expression for the rate (A.75), we find  $\Gamma_2(B_2, Z_2) = \Gamma_3(B_3, Z_3)/\sqrt{2}$ , i.e. in a 2D density-based potential, the rate is underestimated by a constant factor of  $\sqrt{2}$ .

To fix the error in the rates, as well as extend the 3D/2D or 3D/1D correspondence beyond the weak-field case, a *current-density* based potential could be used instead. Solving the time-independent Schrödinger equation in three dimensions in a static external electric field, we obtain the ionizing Siegert state  $\psi_3$  with complex energy according to the procedure described in [308]. From the Siegert state, a density  $n_3 = |\psi_3|^2$  as well as a current density  $\mathbf{j}_3 = \text{Im} \bar{\psi}_3 \nabla \psi_3$  is found and projected onto the symmetry axis to obtain quantities  $n_1$  and  $j_1$ . Then, a 1D (ionizing) wave function  $\psi_1$  can be written as [309]

$$\psi_1(z) = \sqrt{n_1(z)} \exp \left( i \int_0^z dz' \frac{j_1(z')}{n_1(z')} \right). \quad (\text{A.83})$$

Inverting the 1D time-independent Schrödinger equation using this state and the same complex energy value as for the 3D Siegert state, a (real) potential  $V_1$  is obtained.

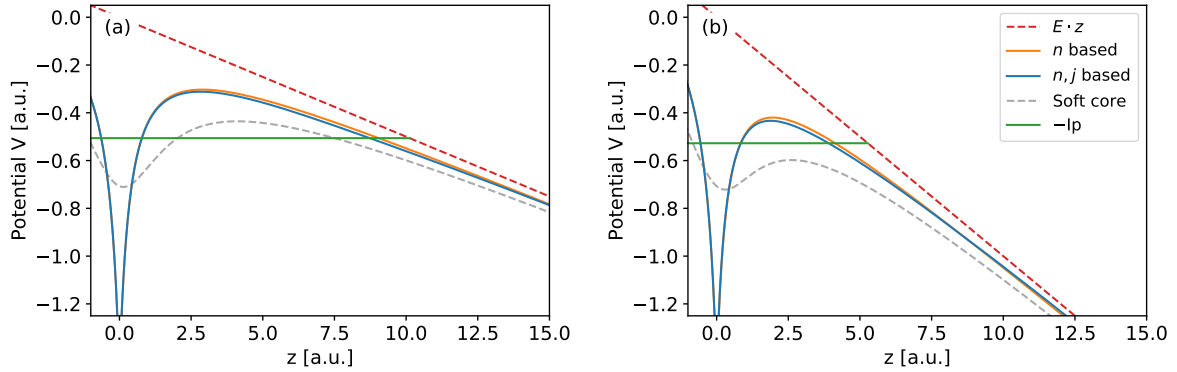


Figure A.5: Current-density based potentials. (a) Field strength  $E = -0.05$  a.u. (b) Field strength  $E = -0.10$  a.u. In both panels, the orange line shows  $V_1(z) + E \cdot z$  where  $V_1$  is the density-based potential (A.78). The blue line gives the current-density based potential for the given field strength. The green line indicates the Stark-shifted ionization potential (real part of the complex energy eigenvalue). The gray dashed line shows the frequently used soft-core potential  $-1/\sqrt{z^2 + 2} + E \cdot z$  for reference.

This is shown in Fig. A.5. As expected, the current-density based potential is smaller compared to the density-based potential in the tunneling region, reflecting its ability to provide a larger ionization rate. To make use of the potential in a time dependent calculation, a viable approach could be to calculate it for various field strengths and then make an adiabatic approximation where the potential at time  $t$  is given by the current-density based potential

of field strength  $E(t)$ . Although the current-density based potential corresponds to  $Z = 1/2$  when the field is turned off, it can be expected to give meaningful results for observables such as Coulomb momentum shifts. The potential is derived from the exact 3D Siegert state so for a static field it must describe the Coulomb attraction properly. This suggests that the asymptotic (large  $z$ ) behavior of the current-density based potential (in the presence of a field  $E < 0$ ) is  $-0.5/z + E \cdot z$  only in the barrier region, but beyond the barrier it changes to  $-1/r + E \cdot z + c(E)$  with a field-dependent offset  $c(E)$ . The purely density-based potential, on the other hand, always corresponds to  $Z = 1/2$  and cannot be expected to take Coulomb effects beyond the barrier into account properly.



# Bibliography

- [1] P. Agostini, F. Fabre, G. Mainfray, G. Petite, and N. K. Rahman, "Free-Free Transitions Following Six-Photon Ionization of Xenon Atoms," [Physical Review Letters](#) **42**, 1127 (1979).
- [2] W. Becker, F. Grasbon, R. Kopold, D. B. Milošević, G. G. Paulus, and H. Walther, "Above-Threshold Ionization: From Classical Features to Quantum Effects," [Advances In Atomic, Molecular, and Optical Physics](#) **48**, 35 (2002).
- [3] A. M. Perelomov, V. S. Popov, and M. V. Terent'ev, "Ionization of Atoms in an Alternating Electric Field," *Sov. Phys. JETP* **23**, 924 (1966).
- [4] A. M. Perelomov, V. S. Popov, and M. V. Terent'ev, "Ionization of Atoms in an Alternating Electric Field: II," *Sov. Phys. JETP* **24**, 207 (1967).
- [5] M. V. Ammosov, N. B. Delone, and V. P. Krainov, "Tunnel ionization of complex atoms and of atomic ions in an alternating electromagnetic field," *Sov. Phys. JETP* **64**, 1191 (1986).
- [6] P. Eckle, M. Smolarski, P. Schlup, J. Biegert, A. Staudte, M. Schöffler, H. G. Muller, R. Dörner, and U. Keller, "Attosecond angular streaking," [Nature Physics](#) **4**, 565 (2008).
- [7] P. Eckle, A. N. Pfeiffer, C. Cirelli, A. Staudte, R. Dörner, H. G. Muller, M. Büttiker, and U. Keller, "Attosecond Ionization and Tunneling Delay Time Measurements in Helium," [Science](#) **322**, 1525 (2008).
- [8] G. G. Paulus, W. Nicklich, H. Xu, P. Lambropoulos, and H. Walther, "Plateau in above threshold ionization spectra," [Physical Review Letters](#) **72**, 2851 (1994).
- [9] T. Zuo, A. D. Bandrauk, and P. B. Corkum, "Laser-induced electron diffraction: A new tool for probing ultrafast molecular dynamics," [Chemical Physics Letters](#) **259**, 313 (1996).
- [10] M. Lein, J. P. Marangos, and P. L. Knight, "Electron diffraction in above-threshold ionization of molecules," [Physical Review A](#) **66**, 051404 (2002).
- [11] A. McPherson, G. Gibson, H. Jara, U. Johann, T. S. Luk, I. A. McIntyre, K. Boyer, and C. K. Rhodes, "Studies of multiphoton production of vacuum-ultraviolet radiation in the rare gases," [Journal of the Optical Society of America B](#) **4**, 595 (1987).
- [12] M. Ferray, A. L'Huillier, X. F. Li, L. A. Lompre, G. Mainfray, and C. Manus, "Multiple-harmonic conversion of 1064 nm radiation in rare gases," [Journal of Physics B](#) **21**, L31 (1988).

- [13] D. N. Fittinghoff, P. R. Bolton, B. Chang, and K. C. Kulander, "Observation of nonsequential double ionization of helium with optical tunneling," *Physical Review Letters* **69**, 2642 (1992).
- [14] M. Lein, E. K. U. Gross, and V. Engel, "Intense-Field Double Ionization of Helium: Identifying the Mechanism," *Physical Review Letters* **85**, 4707 (2000).
- [15] T. Morishita, A.-T. Le, Z. Chen, and C. D. Lin, "Accurate Retrieval of Structural Information from Laser-Induced Photoelectron and High-Order Harmonic Spectra by Few-Cycle Laser Pulses," *Physical Review Letters* **100**, 013903 (2008).
- [16] D. Ray, B. Ulrich, I. Bocharova, C. Maharjan, P. Ranitovic, B. Gramkow, M. Magrakvelidze, S. De, I. V. Litvinyuk, A. T. Le, T. Morishita, C. D. Lin, G. G. Paulus, and C. L. Cocke, "Large-Angle Electron Diffraction Structure in Laser-Induced Rescattering from Rare Gases," *Physical Review Letters* **100**, 143002 (2008).
- [17] M. Okunishi, T. Morishita, G. Prümper, K. Shimada, C. D. Lin, S. Watanabe, and K. Ueda, "Experimental Retrieval of Target Structure Information from Laser-Induced Rescattered Photoelectron Momentum Distributions," *Physical Review Letters* **100**, 143001 (2008).
- [18] M. Meckel, D. Comtois, D. Zeidler, A. Staudte, D. Pavičić, H. C. Bandulet, H. Pépin, J. C. Kieffer, R. Dörner, D. M. Villeneuve, and P. B. Corkum, "Laser-Induced Electron Tunneling and Diffraction," *Science* **320**, 1478 (2008).
- [19] C. I. Bлага, J. Xu, A. D. DiChiara, E. Sistrunk, K. Zhang, P. Agostini, T. A. Miller, L. F. DiMauro, and C. D. Lin, "Imaging ultrafast molecular dynamics with laser-induced electron diffraction," *Nature* **483**, 194 (2012).
- [20] M. Lein, "Molecular imaging using recolliding electrons," *Journal of Physics B* **40**, R135 (2007).
- [21] H. J. Wörner, H. Niikura, J. B. Bertrand, P. B. Corkum, and D. M. Villeneuve, "Observation of Electronic Structure Minima in High-Harmonic Generation," *Physical Review Letters* **102**, 103901 (2009).
- [22] J. Itatani, J. Levesque, D. Zeidler, H. Niikura, H. Pépin, J. C. Kieffer, P. B. Corkum, and D. M. Villeneuve, "Tomographic imaging of molecular orbitals," *Nature* **432**, 867 (2004).
- [23] S. Haessler, J. Caillat, W. Boutu, C. Giovanetti-Teixeira, T. Ruchon, T. Auguste, Z. Diveki, P. Breger, A. Maquet, B. Carré, R. Taïeb, and P. Salières, "Attosecond imaging of molecular electronic wavepackets," *Nature Physics* **6**, 200 (2010).
- [24] C. Vozzi, M. Negro, F. Calegari, G. Sansone, M. Nisoli, S. De Silvestri, and S. Stagira, "Generalized molecular orbital tomography," *Nature Physics* **7**, 822 (2011).
- [25] M. Lein, "Attosecond Probing of Vibrational Dynamics with High-Harmonic Generation," *Physical Review Letters* **94**, 053004 (2005).
- [26] S. Baker, J. S. Robinson, C. A. Haworth, H. Teng, R. A. Smith, C. C. Chirilă, M. Lein, J. W. G. Tisch, and J. P. Marangos, "Probing Proton Dynamics in Molecules on an Attosecond Time Scale," *Science* **312**, 424 (2006).

- [27] P. M. Paul, E. S. Toma, P. Breger, G. Mullot, F. Augé, P. Balcou, H. G. Muller, and P. Agostini, "Observation of a Train of Attosecond Pulses from High Harmonic Generation," *Science* **292**, 1689 (2001).
- [28] I. P. Christov, M. M. Murnane, and H. C. Kapteyn, "High-Harmonic Generation of Attosecond Pulses in the "Single-Cycle" Regime," *Physical Review Letters* **78**, 1251 (1997).
- [29] M. Hentschel, R. Kienberger, C. Spielmann, G. A. Reider, N. Milosevic, T. Brabec, P. Corkum, U. Heinzmann, M. Drescher, and F. Krausz, "Attosecond metrology," *Nature* **414**, 509 (2001).
- [30] R. Kienberger, E. Goulielmakis, M. Uiberacker, A. Baltuska, V. Yakovlev, F. Bammer, A. Scrinzi, T. Westerwalbesloh, U. Kleineberg, U. Heinzmann, M. Drescher, and F. Krausz, "Atomic transient recorder," *Nature* **427**, 817 (2004).
- [31] P. B. Corkum, N. H. Burnett, and M. Y. Ivanov, "Subfemtosecond pulses," *Optics Letters* **19**, 1870 (1994).
- [32] G. Sansone, E. Benedetti, F. Calegari, C. Vozzi, L. Avaldi, R. Flammini, L. Poletto, P. Villoresi, C. Altucci, R. Velotta, S. Stagira, S. D. Silvestri, and M. Nisoli, "Isolated Single-Cycle Attosecond Pulses," *Science* **314**, 443 (2006).
- [33] M. Chini, K. Zhao, and Z. Chang, "The generation, characterization and applications of broadband isolated attosecond pulses," *Nature Photonics* **8**, 178 (2014).
- [34] T. Gaumnitz, A. Jain, Y. Pertot, M. Huppert, I. Jordan, F. Ardana-Lamas, and H. J. Wörner, "Streaking of 43-attosecond soft-X-ray pulses generated by a passively CEP-stable mid-infrared driver," *Optics Express* **25**, 27506 (2017).
- [35] E. Goulielmakis, Z.-H. Loh, A. Wirth, R. Santra, N. Rohringer, V. S. Yakovlev, S. Zherebtsov, T. Pfeifer, A. M. Azzeer, M. F. Kling, S. R. Leone, and F. Krausz, "Real-time observation of valence electron motion," *Nature* **466**, 739 (2010).
- [36] H. Wang, M. Chini, S. Chen, C.-H. Zhang, F. He, Y. Cheng, Y. Wu, U. Thumm, and Z. Chang, "Attosecond Time-Resolved Autoionization of Argon," *Physical Review Letters* **105**, 143002 (2010).
- [37] M. Chini, B. Zhao, H. Wang, Y. Cheng, S. X. Hu, and Z. Chang, "Subcycle ac Stark Shift of Helium Excited States Probed with Isolated Attosecond Pulses," *Physical Review Letters* **109**, 073601 (2012).
- [38] M. Schultze, M. Fieß, N. Karpowicz, J. Gagnon, M. Korbman, M. Hofstetter, S. Neppl, A. L. Cavalieri, Y. Komninos, T. Mercouris, C. A. Nicolaides, R. Pazourek, S. Nagele, J. Feist, J. Burgdörfer, A. M. Azzeer, R. Ernstorfer, R. Kienberger, U. Kleineberg, E. Goulielmakis, F. Krausz, and V. S. Yakovlev, "Delay in Photoemission," *Science* **328**, 1658 (2010).
- [39] K. Klünder, J. M. Dahlström, M. Gisselbrecht, T. Fordell, M. Swoboda, D. Guénot, P. Johnsson, J. Caillat, J. Mauritsson, A. Maquet, R. Taïeb, and A. L'Huillier, "Probing Single-Photon Ionization on the Attosecond Time Scale," *Physical Review Letters* **106**, 143002 (2011).

- [40] F. Lindner, M. G. Schätzel, H. Walther, A. Baltuška, E. Goulielmakis, F. Krausz, D. B. Milošević, D. Bauer, W. Becker, and G. G. Paulus, "Attosecond Double-Slit Experiment," *Physical Review Letters* **95**, 040401 (2005).
- [41] D. G. Arbó, E. Persson, and J. Burgdörfer, "Time double-slit interferences in strong-field tunneling ionization," *Physical Review A* **74**, 063407 (2006).
- [42] D. G. Arbó, K. L. Ishikawa, K. Schiessl, E. Persson, and J. Burgdörfer, "Intracycle and intercycle interferences in above-threshold ionization: The time grating," *Physical Review A* **81**, 021403 (2010).
- [43] D. B. Milošević, "Possibility of introducing spin into attoscience with spin-polarized electrons produced by a bichromatic circularly polarized laser field," *Physical Review A* **93**, 051402 (2016).
- [44] K. Liu and I. Barth, "Nonadiabatic tunnel ionization of current-carrying orbitals of pre-aligned linear molecules in strong circularly polarized laser fields," *Physical Review A* **94**, 043402 (2016).
- [45] B. Ritchie, "Theory of the angular distribution of photoelectrons ejected from optically active molecules and molecular negative ions," *Physical Review A* **13**, 1411 (1976).
- [46] N. A. Cherepkov, "Circular dichroism of molecules in the continuous absorption region," *Chemical Physics Letters* **87**, 344 (1982).
- [47] S. Ghimire, A. D. DiChiara, E. Sistrunk, P. Agostini, L. F. DiMauro, and D. A. Reis, "Observation of high-order harmonic generation in a bulk crystal," *Nature Physics* **7**, 138 (2011).
- [48] O. Schubert, M. Hohenleutner, F. Langer, B. Urbanek, C. Lange, U. Huttner, D. Golde, T. Meier, M. Kira, S. W. Koch, and R. Huber, "Sub-cycle control of terahertz high-harmonic generation by dynamical Bloch oscillations," *Nature Photonics* **8**, 119 (2014).
- [49] M. Hohenleutner, F. Langer, O. Schubert, M. Knorr, U. Huttner, S. W. Koch, M. Kira, and R. Huber, "Real-time observation of interfering crystal electrons in high-harmonic generation," *Nature* **523**, 572 (2015).
- [50] T. T. Luu, M. Garg, S. Y. Kruchinin, A. Moulet, M. T. Hassan, and E. Goulielmakis, "Extreme ultraviolet high-harmonic spectroscopy of solids," *Nature* **521**, 498 (2015).
- [51] D. Golde, T. Meier, and S. W. Koch, "High harmonics generated in semiconductor nanostructures by the coupled dynamics of optical inter- and intraband excitations," *Physical Review B* **77**, 075330 (2008).
- [52] G. Vampa, C. R. McDonald, G. Orlando, D. D. Klug, P. B. Corkum, and T. Brabec, "Theoretical Analysis of High-Harmonic Generation in Solids," *Physical Review Letters* **113**, 073901 (2014).
- [53] G. Vampa, T. J. Hammond, N. Thiré, B. E. Schmidt, F. Légaré, C. R. McDonald, T. Brabec, and P. B. Corkum, "Linking high harmonics from gases and solids," *Nature* **522**, 462 (2015).



- [54] M. Wu, S. Ghimire, D. A. Reis, K. J. Schafer, and M. B. Gaarde, "High-harmonic generation from Bloch electrons in solids," *Physical Review A* **91**, 043839 (2015).
- [55] N. Tancogne-Dejean, O. D. Mücke, F. X. Kärtner, and A. Rubio, "Impact of the Electronic Band Structure in High-Harmonic Generation Spectra of Solids," *Physical Review Letters* **118**, 087403 (2017).
- [56] K. K. Hansen, D. Bauer, and L. B. Madsen, "Finite-system effects on high-order harmonic generation: From atoms to solids," *Physical Review A* **97**, 043424 (2018).
- [57] P. Hommelhoff, C. Kealhofer, and M. A. Kasevich, "Ultrafast Electron Pulses from a Tungsten Tip Triggered by Low-Power Femtosecond Laser Pulses," *Physical Review Letters* **97**, 247402 (2006).
- [58] R. Bormann, M. Gulde, A. Weismann, S. V. Yalunin, and C. Ropers, "Tip-Enhanced Strong-Field Photoemission," *Physical Review Letters* **105**, 147601 (2010).
- [59] M. Schenk, M. Krüger, and P. Hommelhoff, "Strong-Field Above-Threshold Photoemission from Sharp Metal Tips," *Physical Review Letters* **105**, 257601 (2010).
- [60] M. Krüger, M. Schenk, and P. Hommelhoff, "Attosecond control of electrons emitted from a nanoscale metal tip," *Nature* **475**, 78 (2011).
- [61] G. Herink, D. R. Solli, M. Gulde, and C. Ropers, "Field-driven photoemission from nanostructures quenches the quiver motion," *Nature* **483**, 190 (2012).
- [62] H. Yanagisawa, S. Schnepf, C. Hafner, M. Hengsberger, D. E. Kim, M. F. Kling, A. Landsman, L. Gallmann, and J. Osterwalder, "Delayed electron emission in strong-field driven tunnelling from a metallic nanotip in the multi-electron regime," *Scientific Reports* **6**, 35877 (2016).
- [63] A. T. J. B. Eppink and D. H. Parker, "Velocity map imaging of ions and electrons using electrostatic lenses: Application in photoelectron and photofragment ion imaging of molecular oxygen," *Review of Scientific Instruments* **68**, 3477 (1997).
- [64] M. Wollenhaupt, M. Krug, J. Köhler, T. Bayer, C. Sarpe-Tudoran, and T. Baumert, "Three-dimensional tomographic reconstruction of ultrashort free electron wave packets," *Applied Physics B* **95**, 647 (2009).
- [65] C. Smeenk, L. Arissian, A. Staudte, D. M. Villeneuve, and P. B. Corkum, "Momentum space tomographic imaging of photoelectrons," *Journal of Physics B* **42**, 185402 (2009).
- [66] C. Bordas, F. Paulig, H. Helm, and D. L. Huestis, "Photoelectron imaging spectrometry: Principle and inversion method," *Review of Scientific Instruments* **67**, 2257 (1996).
- [67] M. J. J. Vrakking, "An iterative procedure for the inversion of two-dimensional ion/photoelectron imaging experiments," *Review of Scientific Instruments* **72**, 4084 (2001).

- [68] O. Jagutzki, A. Cerezo, A. Czasch, R. Dorner, M. Hattas, V. Mergel, U. Spillmann, K. Ullmann-Pfleger, T. Weber, H. Schmidt-Böcking, and G. D. W. Smith, "Multiple hit readout of a microchannel plate detector with a three-layer delay-line anode," *IEEE Transactions on Nuclear Science* **49**, 2477 (2002).
- [69] J. Ullrich, R. Moshhammer, A. Dorn, R. Dörner, L. P. H. Schmidt, and H. Schmidt-Böcking, "Recoil-ion and electron momentum spectroscopy: Reaction-microscopes," *Reports on Progress in Physics* **66**, 1463 (2003).
- [70] J. Itatani, F. Quéré, G. L. Yudin, M. Y. Ivanov, F. Krausz, and P. B. Corkum, "Attosecond Streak Camera," *Physical Review Letters* **88**, 173903 (2002).
- [71] P. B. Corkum, N. H. Burnett, and F. Brunel, "Above-threshold ionization in the long-wavelength limit," *Physical Review Letters* **62**, 1259 (1989).
- [72] J. L. Krause, K. J. Schafer, and K. C. Kulander, "High-order harmonic generation from atoms and ions in the high intensity regime," *Physical Review Letters* **68**, 3535 (1992).
- [73] P. B. Corkum, "Plasma perspective on strong field multiphoton ionization," *Physical Review Letters* **71**, 1994 (1993).
- [74] G. G. Paulus, W. Becker, W. Nicklich, and H. Walther, "Rescattering effects in above-threshold ionization: A classical model," *Journal of Physics B* **27**, L703 (1994).
- [75] Q. Zhang, P. Lan, and P. Lu, "Empirical formula for over-barrier strong-field ionization," *Physical Review A* **90**, 043410 (2014).
- [76] H. G. Muller, "Numerical simulation of high-order above-threshold-ionization enhancement in argon," *Physical Review A* **60**, 1341 (1999).
- [77] A. N. Pfeiffer, C. Cirelli, M. Smolarski, D. Dimitrovski, M. Abu-samha, L. B. Madsen, and U. Keller, "Attoclock reveals natural coordinates of the laser-induced tunnelling current flow in atoms," *Nature Physics* **8**, 76 (2012).
- [78] L. Torlina, F. Morales, J. Kaushal, I. Ivanov, A. Kheifets, A. Zielinski, A. Scrinzi, H. G. Muller, S. Sukiasyan, M. Ivanov, and O. Smirnova, "Interpreting attoclock measurements of tunnelling times," *Nature Physics* **11**, 503 (2015).
- [79] A. Emmanouilidou, A. Chen, C. Hofmann, U. Keller, and A. S. Landsman, "The effect of electron-electron correlation on the attoclock experiment," *Journal of Physics B* **48**, 245602 (2015).
- [80] V. P. Majety and A. Scrinzi, "Absence of electron correlation effects in the Helium attoclock setting," *Journal of Modern Optics* **64**, 1026 (2017).
- [81] A. Zielinski, V. P. Majety, and A. Scrinzi, "Double photoelectron momentum spectra of helium at infrared wavelength," *Physical Review A* **93**, 023406 (2016).
- [82] F. Wilken and D. Bauer, "Adiabatic Approximation of the Correlation Function in the Density-Functional Treatment of Ionization Processes," *Physical Review Letters* **97**, 203001 (2006).

- [83] F. Wilken and D. Bauer, "Momentum distributions in time-dependent density-functional theory: Product-phase approximation for nonsequential double ionization in strong laser fields," *Physical Review A* **76**, 023409 (2007).
- [84] D. Hochstuhl and M. Bonitz, "Time-dependent restricted-active-space configuration-interaction method for the photoionization of many-electron atoms," *Physical Review A* **86**, 053424 (2012).
- [85] S. Bauch, L. K. Sørensen, and L. B. Madsen, "Time-dependent generalized-active-space configuration-interaction approach to photoionization dynamics of atoms and molecules," *Physical Review A* **90**, 062508 (2014).
- [86] V. P. Majety, A. Zielinski, and A. Scrinzi, "Photoionization of few electron systems: A hybrid coupled channels approach," *New Journal of Physics* **17**, 063002 (2015).
- [87] L. V. Keldysh, "Ionization in the Field of a Strong Electromagnetic Wave," *Sov. Phys. JETP* **20**, 1307 (1965).
- [88] F. H. M. Faisal, "Collision of electrons with laser photons in a background potential," *Journal of Physics B* **6**, L312 (1973).
- [89] H. R. Reiss, "Effect of an intense electromagnetic field on a weakly bound system," *Physical Review A* **22**, 1786 (1980).
- [90] M. Lewenstein, P. Balcou, M. Y. Ivanov, A. L'Huillier, and P. B. Corkum, "Theory of high-harmonic generation by low-frequency laser fields," *Physical Review A* **49**, 2117 (1994).
- [91] P. Salières, B. Carré, L. L. Déroff, F. Grasbon, G. G. Paulus, H. Walther, R. Kopold, W. Becker, D. B. Milošević, A. Sanpera, and M. Lewenstein, "Feynman's Path-Integral Approach for Intense-Laser-Atom Interactions," *Science* **292**, 902 (2001).
- [92] D. B. Milošević, G. G. Paulus, D. Bauer, and W. Becker, "Above-threshold ionization by few-cycle pulses," *Journal of Physics B* **39**, R203 (2006).
- [93] L. Torlina and O. Smirnova, "Time-dependent analytical R-matrix approach for strong-field dynamics. I. one-electron systems," *Physical Review A* **86**, 043408 (2012).
- [94] J. Kaushal and O. Smirnova, "Nonadiabatic Coulomb effects in strong-field ionization in circularly polarized laser fields," *Physical Review A* **88**, 013421 (2013).
- [95] N. I. Shvetsov-Shilovski, M. Lein, L. B. Madsen, E. Räsänen, C. Lemell, J. Burgdörfer, D. G. Arbó, and K. Tórkési, "Semiclassical two-step model for strong-field ionization," *Physical Review A* **94**, 013415 (2016).
- [96] S. V. Popruzhenko, G. G. Paulus, and D. Bauer, "Coulomb-corrected quantum trajectories in strong-field ionization," *Physical Review A* **77**, 053409 (2008).
- [97] S. V. Popruzhenko and D. Bauer, "Strong field approximation for systems with Coulomb interaction," *Journal of Modern Optics* **55**, 2573 (2008).

- [98] T.-M. Yan, S. V. Popruzhenko, M. J. J. Vrakking, and D. Bauer, "Low-Energy Structures in Strong Field Ionization Revealed by Quantum Orbits," *Physical Review Letters* **105**, 253002 (2010).
- [99] T.-M. Yan and D. Bauer, "Sub-barrier Coulomb effects on the interference pattern in tunneling-ionization photoelectron spectra," *Physical Review A* **86**, 053403 (2012).
- [100] T.-M. Yan, S. V. Popruzhenko, and D. Bauer, "Trajectory-Based Coulomb-Corrected Strong Field Approximation," in *Progress in Ultrafast Intense Laser Science*, Springer Series in Chemical Physics (Springer, Berlin, Heidelberg, 2013).
- [101] X.-Y. Lai, C. Poli, H. Schomerus, and C. F. d. M. Faria, "Influence of the Coulomb potential on above-threshold ionization: A quantum-orbit analysis beyond the strong-field approximation," *Physical Review A* **92**, 043407 (2015).
- [102] H. Ni, U. Saalman, and J.-M. Rost, "Tunneling Ionization Time Resolved by Backpropagation," *Physical Review Letters* **117**, 023002 (2016).
- [103] H. Ni, U. Saalman, and J.-M. Rost, "Tunneling exit characteristics from classical back-propagation of an ionized electron wave packet," *Physical Review A* **97**, 013426 (2018).
- [104] H. Ni, N. Eicke, C. Ruiz, J. Cai, F. Oppermann, N. I. Shvetsov-Shilovski, and L.-W. Pi, "Tunneling criteria and a nonadiabatic term for strong-field ionization," *Physical Review A* **98**, 013411 (2018).
- [105] N. B. Baranova, A. N. Chudinov, A. A. Shulginov, and B. Y. Zel'dovich, "Polarization dependence of the phase of interference between single- and two-photon ionization," *Optics Letters* **16**, 1346 (1991).
- [106] Y.-Y. Yin, C. Chen, D. S. Elliott, and A. V. Smith, "Asymmetric photoelectron angular distributions from interfering photoionization processes," *Physical Review Letters* **69**, 2353 (1992).
- [107] M. Shapiro, J. W. Hepburn, and P. Brumer, "Simplified laser control of unimolecular reactions: Simultaneous ( $\omega_1, \omega_3$ ) excitation," *Chemical Physics Letters* **149**, 451 (1988).
- [108] M. Richter, M. Kunitski, M. Schöffler, T. Jahnke, L. P. H. Schmidt, M. Li, Y. Liu, and R. Dörner, "Streaking Temporal Double-Slit Interference by an Orthogonal Two-Color Laser Field," *Physical Review Letters* **114**, 143001 (2015).
- [109] M. Richter, M. Kunitski, M. Schöffler, T. Jahnke, L. P. H. Schmidt, and R. Dörner, "Ionization in orthogonal two-color laser fields: Origin and phase dependences of trajectory-resolved Coulomb effects," *Physical Review A* **94**, 033416 (2016).
- [110] L. Brugnera, D. J. Hoffmann, T. Siegel, F. Frank, A. Zair, J. W. G. Tisch, and J. P. Marangos, "Trajectory Selection in High Harmonic Generation by Controlling the Phase between Orthogonal Two-Color Fields," *Physical Review Letters* **107**, 153902 (2011).
- [111] N. Dudovich, O. Smirnova, J. Levesque, Y. Mairesse, M. Y. Ivanov, D. M. Villeneuve, and P. B. Corkum, "Measuring and controlling the birth of attosecond XUV pulses," *Nature Physics* **2**, 781 (2006).

- [112] D. Shafir, H. Soifer, B. D. Bruner, M. Dagan, Y. Mairesse, S. Patchkovskii, M. Y. Ivanov, O. Smirnova, and N. Dudovich, "Resolving the time when an electron exits a tunnelling barrier," *Nature* **485**, 343 (2012).
- [113] J. Zhao and M. Lein, "Determination of Ionization and Tunneling Times in High-Order Harmonic Generation," *Physical Review Letters* **111**, 043901 (2013).
- [114] J. Henkel and M. Lein, "Analysis of electron trajectories with two-color strong-field ionization," *Physical Review A* **92**, 013422 (2015).
- [115] G. Porat, G. Alon, S. Rozen, O. Pedatzur, M. Krüger, D. Azoury, A. Natan, G. Orenstein, B. D. Bruner, M. J. J. Vrakking, and N. Dudovich, "Attosecond time-resolved photoelectron holography," *Nature Communications* **9**, 2805 (2018).
- [116] H. Eichmann, A. Egbert, S. Nolte, C. Momma, B. Wellegehausen, W. Becker, S. Long, and J. K. McIver, "Polarization-dependent high-order two-color mixing," *Physical Review A* **51**, R3414 (1995).
- [117] S. Long, W. Becker, and J. K. McIver, "Model calculations of polarization-dependent two-color high-harmonic generation," *Physical Review A* **52**, 2262 (1995).
- [118] D. B. Milošević and W. Becker, "Attosecond pulse trains with unusual nonlinear polarization," *Physical Review A* **62**, 011403(R) (2000).
- [119] D. B. Milošević and W. Sandner, "Extreme-ultraviolet harmonic generation near 13 nm with a two-color elliptically polarized laser field," *Optics Letters* **25**, 1532 (2000).
- [120] A. Fleischer, O. Kfir, T. Diskin, P. Sidorenko, and O. Cohen, "Spin angular momentum and tunable polarization in high-harmonic generation," *Nature Photonics* **8**, 543 (2014).
- [121] O. Kfir, P. Grychtol, E. Turgut, R. Knut, D. Zusin, D. Popmintchev, T. Popmintchev, H. Nembach, J. M. Shaw, A. Fleischer, H. Kapteyn, M. Murnane, and O. Cohen, "Generation of bright phase-matched circularly-polarized extreme ultraviolet high harmonics," *Nature Photonics* **9**, 99 (2015).
- [122] T. Brabec, M. Y. Ivanov, and P. B. Corkum, "Coulomb focusing in intense field atomic processes," *Physical Review A* **54**, R2551 (1996).
- [123] A. Rudenko, K. Zrost, T. Ergler, A. B. Voitkiv, B. Najjari, V. L. B. de Jesus, B. Feuerstein, C. D. Schröter, R. Moshhammer, and J. Ullrich, "Coulomb singularity in the transverse momentum distribution for strong-field single ionization," *Journal of Physics B* **38**, L191 (2005).
- [124] D. Comtois, D. Zeidler, H. Pépin, J. C. Kieffer, D. M. Villeneuve, and P. B. Corkum, "Observation of Coulomb focusing in tunnelling ionization of noble gases," *Journal of Physics B* **38**, 1923 (2005).
- [125] Y. Huismans, A. Rouzée, A. Gijsbertsen, J. H. Jungmann, A. S. Smolkowska, P. S. W. M. Logman, F. Lépine, C. Cauchy, S. Zamith, T. Marchenko, J. M. Bakker, G. Berden, B. Redlich, A. F. G. van der Meer, H. G. Muller, W. Vermin, K. J. Schafer, M. Spanner,

- M. Y. Ivanov, O. Smirnova, D. Bauer, S. V. Popruzhenko, and M. J. J. Vrakking, "Time-Resolved Holography with Photoelectrons," *Science* **331**, 61 (2011).
- [126] X.-B. Bian, Y. Huismans, O. Smirnova, K.-J. Yuan, M. J. J. Vrakking, and A. D. Bandrauk, "Subcycle interference dynamics of time-resolved photoelectron holography with mid-infrared laser pulses," *Physical Review A* **84**, 043420 (2011).
- [127] M. Klaiber, K. Z. Hatsagortsyan, and C. H. Keitel, "Tunneling Dynamics in Multiphoton Ionization and Attoclock Calibration," *Physical Review Letters* **114**, 083001 (2015).
- [128] M. Klaiber and J. S. Briggs, "Crossover from tunneling to multiphoton ionization of atoms," *Physical Review A* **94**, 053405 (2016).
- [129] D. Bauer, "Two-dimensional, two-electron model atom in a laser pulse: Exact treatment, single-active-electron analysis, time-dependent density-functional theory, classical calculations, and nonsequential ionization," *Physical Review A* **56**, 3028 (1997).
- [130] C. Yu and L. B. Madsen, "Above-threshold ionization of helium in the long-wavelength regime: Examining the single-active-electron approximation and the two-electron strong-field approximation," *Physical Review A* **95**, 063407 (2017).
- [131] P. Lan, M. Ruhmann, L. He, C. Zhai, F. Wang, X. Zhu, Q. Zhang, Y. Zhou, M. Li, M. Lein, and P. Lu, "Attosecond Probing of Nuclear Dynamics with Trajectory-Resolved High-Harmonic Spectroscopy," *Physical Review Letters* **119**, 033201 (2017).
- [132] P. Wustelt, F. Oppermann, L. Yue, M. Möller, T. Stöhlker, M. Lein, S. Gräfe, G. G. Paulus, and A. M. Sayler, "Heteronuclear Limit of Strong-Field Ionization: Fragmentation of  $\text{HeH}^+$  by Intense Ultrashort Laser Pulses," *Physical Review Letters* **121**, 073203 (2018).
- [133] S. Brennecke and M. Lein, "High-order above-threshold ionization beyond the electric dipole approximation: Dependence on the atomic and molecular structure," *Physical Review A* **98**, 063414 (2018).
- [134] S. Brennecke and M. Lein, "High-order above-threshold ionization beyond the electric dipole approximation," *Journal of Physics B* **51**, 094005 (2018).
- [135] J. R. Taylor, *Scattering Theory: The Quantum Theory on Nonrelativistic Collisions*, 1st ed. (John Wiley, New York, 1972).
- [136] D. M. Wolkow, "Über eine Klasse von Lösungen der Diracschen Gleichung," *Zeitschrift für Physik* **94**, 250 (1935).
- [137] S. V. Popruzhenko, "Keldysh theory of strong field ionization: History, applications, difficulties and perspectives," *Journal of Physics B* **47**, 204001 (2014).
- [138] D. Bauer, D. B. Milošević, and W. Becker, "Strong-field approximation for intense-laser-atom processes: The choice of gauge," *Physical Review A* **72**, 023415 (2005).
- [139] A. Lohr, M. Kleber, R. Kopold, and W. Becker, "Above-threshold ionization in the tunneling regime," *Physical Review A* **55**, R4003 (1997).

- [140] I. A. Ivanov, C. H. Nam, and K. T. Kim, "Strong-field approximation and its modifications as evolution equations," *Physical Review A* **99**, 013417 (2019).
- [141] A. Galstyan, O. Chuluunbaatar, A. Hamido, Y. V. Popov, F. Mota-Furtado, P. F. O'Mahony, N. Janssens, F. Catoire, and B. Piraux, "Reformulation of the strong-field approximation for light-matter interactions," *Physical Review A* **93**, 023422 (2016).
- [142] N. L. Manakov and L. P. Rapport, "Particle with low binding energy in a circularly polarized field," *Sov. Phys. JETP* **42**, 430 (1975).
- [143] G. F. Gribakin and M. Y. Kuchiev, "Multiphoton detachment of electrons from negative ions," *Physical Review A* **55**, 3760 (1997).
- [144] I. Petersen, *Photoelectron Momentum Distributions from Recollision-Free Strong-Field Ionization of Atoms and Molecules* (Verlag Dr. Hut, Munich, 2014).
- [145] O. Smirnova, M. Spanner, and M. Ivanov, "Coulomb and polarization effects in sub-cycle dynamics of strong-field ionization," *Journal of Physics B* **39**, S307 (2006).
- [146] O. Smirnova, M. Spanner, and M. Ivanov, "Analytical solutions for strong field-driven atomic and molecular one- and two-electron continua and applications to strong-field problems," *Physical Review A* **77**, 033407 (2008).
- [147] L. Torlina, F. Morales, H. G. Muller, and O. Smirnova, "Ab initio verification of the analytical R-matrix theory for strong field ionization," *Journal of Physics B* **47**, 204021 (2014).
- [148] E. Pisanty and M. Ivanov, "Slalom in complex time: Emergence of low-energy structures in tunnel ionization via complex-time contours," *Physical Review A* **93**, 043408 (2016).
- [149] N. I. Shvetsov-Shilovski, D. Dimitrovski, and L. B. Madsen, "Ionization in elliptically polarized pulses: Multielectron polarization effects and asymmetry of photoelectron momentum distributions," *Physical Review A* **85**, 023428 (2012).
- [150] F. Grossmann, *Theoretical Femtosecond Physics*, Springer Series on Atomic, Optical, and Plasma Physics (Springer Berlin Heidelberg, Berlin, Heidelberg, 2008).
- [151] M. Li, J.-W. Geng, H. Liu, Y. Deng, C. Wu, L.-Y. Peng, Q. Gong, and Y. Liu, "Classical-Quantum Correspondence for Above-Threshold Ionization," *Physical Review Letters* **112**, 113002 (2014).
- [152] A. Kästner, U. Saalman, and J. M. Rost, "Electron-Energy Bunching in Laser-Driven Soft Recollisions," *Physical Review Letters* **108**, 033201 (2012).
- [153] S. Brennecke, N. Eicke, and M. Lein, "Gouy's Phase Anomaly in Electron Waves Produced by Strong-Field Ionization," *Physical Review Letters* **124**, 153202 (2020).
- [154] N. Eicke and M. Lein, "Extracting trajectory information from two-color strong-field ionization," *Journal of Modern Optics* **64**, 981 (2017).
- [155] C. I. Blaga, F. Catoire, P. Colosimo, G. G. Paulus, H. G. Muller, P. Agostini, and L. F. DiMauro, "Strong-field photoionization revisited," *Nature Physics* **5**, 335 (2009).

- [156] W. Quan, Z. Lin, M. Wu, H. Kang, H. Liu, X. Liu, J. Chen, J. Liu, X. T. He, S. G. Chen, H. Xiong, L. Guo, H. Xu, Y. Fu, Y. Cheng, and Z. Z. Xu, "Classical Aspects in Above-Threshold Ionization with a Midinfrared Strong Laser Field," *Physical Review Letters* **103**, 093001 (2009).
- [157] A. Kästner, U. Saalmann, and J. M. Rost, "Energy bunching in soft recollisions revealed with long-wavelength few-cycle pulses," *Journal of Physics B* **45**, 074011 (2012).
- [158] K. Zhang, Y. H. Lai, E. Diesen, B. E. Schmidt, C. I. Blaga, J. Xu, T. T. Gorman, F. Légaré, U. Saalmann, P. Agostini, J. M. Rost, and L. F. DiMauro, "Universal pulse dependence of the low-energy structure in strong-field ionization," *Physical Review A* **93**, 021403 (2016).
- [159] C. Y. Wu, Y. D. Yang, Y. Q. Liu, Q. H. Gong, M. Wu, X. Liu, X. L. Hao, W. D. Li, X. T. He, and J. Chen, "Characteristic Spectrum of Very Low-Energy Photoelectron from Above-Threshold Ionization in the Tunneling Regime," *Physical Review Letters* **109**, 043001 (2012).
- [160] J. Dura, N. Camus, A. Thai, A. Britz, M. Hemmer, M. Baudisch, A. Senftleben, C. D. Schröter, J. Ullrich, R. Moshhammer, and J. Biegert, "Ionization with low-frequency fields in the tunneling regime," *Scientific Reports* **3**, 2675 (2013).
- [161] E. Diesen, U. Saalmann, M. Richter, M. Kunitski, R. Dörner, and J. M. Rost, "Dynamical Characteristics of Rydberg Electrons Released by a Weak Electric Field," *Physical Review Letters* **116**, 143006 (2016).
- [162] H. G. Muller, P. H. Bucksbaum, D. W. Schumacher, and A. Zavriyev, "Above-threshold ionisation with a two-colour laser field," *Journal of Physics B* **23**, 2761 (1990).
- [163] K. J. Schafer and K. C. Kulander, "Phase-dependent effects in multiphoton ionization induced by a laser field and its second harmonic," *Physical Review A* **45**, 8026 (1992).
- [164] M. D. Perry and J. K. Crane, "High-order harmonic emission from mixed fields," *Physical Review A* **48**, R4051 (1993).
- [165] D. W. Schumacher, F. Weihe, H. G. Muller, and P. H. Bucksbaum, "Phase Dependence of Intense Field Ionization: A Study Using Two Colors," *Physical Review Letters* **73**, 1344 (1994).
- [166] S. Watanabe, K. Kondo, Y. Nabekawa, A. Sagisaka, and Y. Kobayashi, "Two-Color Phase Control in Tunneling Ionization and Harmonic Generation by a Strong Laser Field and Its Third Harmonic," *Physical Review Letters* **73**, 2692 (1994).
- [167] G. G. Paulus, F. Grasbon, H. Walther, P. Villoresi, M. Nisoli, S. Stagira, E. Priori, and S. D. Silvestri, "Absolute-phase phenomena in photoionization with few-cycle laser pulses," *Nature* **414**, 182 (2001).
- [168] A. Baltuška, T. Udem, M. Uiberacker, M. Hentschel, E. Goulielmakis, C. Gohle, R. Holzwarth, V. S. Yakovlev, A. Scrinzi, T. W. Hänsch, and F. Krausz, "Attosecond control of electronic processes by intense light fields," *Nature* **421**, 611 (2003).



- [169] G. G. Paulus, F. Lindner, H. Walther, A. Baltuška, E. Goulielmakis, M. Lezius, and F. Krausz, "Measurement of the Phase of Few-Cycle Laser Pulses," [Physical Review Letters](#) **91**, 253004 (2003).
- [170] S. Skruszewicz, J. Tiggesbäumker, K.-H. Meiwes-Broer, M. Arbeiter, T. Fennel, and D. Bauer, "Two-Color Strong-Field Photoelectron Spectroscopy and the Phase of the Phase," [Physical Review Letters](#) **115**, 043001 (2015).
- [171] M. A. Almajid, M. Zabel, S. Skruszewicz, J. Tiggesbäumker, and D. Bauer, "Two-color phase-of-the-phase spectroscopy in the multiphoton regime," [Journal of Physics B](#) **50**, 194001 (2017).
- [172] D. Würzler, N. Eicke, M. Möller, D. Seipt, A. M. Sayler, S. Fritzsche, M. Lein, and G. G. Paulus, "Velocity map imaging of scattering dynamics in orthogonal two-color fields," [Journal of Physics B](#) **51**, 015001 (2018).
- [173] J. Tan, Y. Li, Y. Zhou, M. He, Y. Chen, M. Li, and P. Lu, "Identifying the contributions of multiple-returning recollision orbits in strong-field above-threshold ionization," [Optical and Quantum Electronics](#) **50**, 57 (2018).
- [174] V. A. Tulsy, M. A. Almajid, and D. Bauer, "Two-color phase-of-the-phase spectroscopy with circularly polarized laser pulses," [Physical Review A](#) **98**, 053433 (2018).
- [175] V. A. Tulsy, B. Krebs, J. Tiggesbäumker, and D. Bauer, "Revealing laser-coherent electron features using phase-of-the-phase spectroscopy," [Journal of Physics B](#) **53**, 074001 (2020).
- [176] O. Pedatzur, G. Orenstein, V. Serbinenko, H. Soifer, B. D. Bruner, A. J. Uzan, D. S. Brambila, A. G. Harvey, L. Torlina, F. Morales, O. Smirnova, and N. Dudovich, "Attosecond tunnelling interferometry," [Nature Physics](#) **11**, 815 (2015).
- [177] J. M. Dahlström, A. L'Huillier, and J. Mauritsson, "Quantum mechanical approach to probing the birth of attosecond pulses using a two-colour field," [Journal of Physics B](#) **44**, 095602 (2011).
- [178] J. Tan, Y. Zhou, M. He, Y. Chen, Q. Ke, J. Liang, X. Zhu, M. Li, and P. Lu, "Determination of the Ionization Time Using Attosecond Photoelectron Interferometry," [Physical Review Letters](#) **121**, 253203 (2018).
- [179] J. Tan, Y. Zhou, M. He, Q. Ke, J. Liang, Y. Li, M. Li, and P. Lu, "Time-resolving tunneling ionization via strong-field photoelectron holography," [Physical Review A](#) **99**, 033402 (2019).
- [180] M. Li, H. Xie, W. Cao, S. Luo, J. Tan, Y. Feng, B. Du, W. Zhang, Y. Li, Q. Zhang, P. Lan, Y. Zhou, and P. Lu, "Photoelectron Holographic Interferometry to Probe the Longitudinal Momentum Offset at the Tunnel Exit," [Physical Review Letters](#) **122**, 183202 (2019).
- [181] M. Kübel, Z. Dube, A. Y. Naumov, M. Spanner, G. G. Paulus, M. F. Kling, D. M. Villeneuve, P. B. Corkum, and A. Staudte, "Streak Camera for Strong-Field Ionization," [Physical Review Letters](#) **119**, 183201 (2017).

- [182] L. J. Zipp, A. Natan, and P. H. Bucksbaum, "Probing electron delays in above-threshold ionization," *Optica* **1**, 361 (2014).
- [183] M. Kitzler and M. Lezius, "Spatial Control of Recollision Wave Packets with Attosecond Precision," *Physical Review Letters* **95**, 253001 (2005).
- [184] M. He, Y. Li, Y. Zhou, M. Li, and P. Lu, "Temporal and spatial manipulation of the recolliding wave packet in strong-field photoelectron holography," *Physical Review A* **93**, 033406 (2016).
- [185] G. G. Paulus, W. Becker, and H. Walther, "Classical rescattering effects in two-color above-threshold ionization," *Physical Review A* **52**, 4043 (1995).
- [186] D. Ray, Z. Chen, S. De, W. Cao, I. V. Litvinyuk, A. T. Le, C. D. Lin, M. F. Kling, and C. L. Cocke, "Momentum spectra of electrons rescattered from rare-gas targets following their extraction by one- and two-color femtosecond laser pulses," *Physical Review A* **83**, 013410 (2011).
- [187] X. Xie, S. Roither, S. Gräfe, D. Kartashov, E. Persson, C. Lemell, Li Zhang, M. S. Schöffler, A. Baltuška, J. Burgdörfer, and M. Kitzler, "Probing the influence of the Coulomb field on atomic ionization by sculpted two-color laser fields," *New Journal of Physics* **15**, 043050 (2013).
- [188] D. G. Arbó, "The effect of the Coulomb potential on subcycle interference of electron wave packets in atomic ionization by two-colour laser pulses," *Journal of Physics B* **47**, 204008 (2014).
- [189] X. Xie, S. Roither, D. Kartashov, E. Persson, D. G. Arbó, L. Zhang, S. Gräfe, M. S. Schöffler, J. Burgdörfer, A. Baltuška, and M. Kitzler, "Attosecond Probe of Valence-Electron Wave Packets by Subcycle Sculpted Laser Fields," *Physical Review Letters* **108**, 193004 (2012).
- [190] D. G. Arbó, S. Nagele, X.-M. Tong, X. Xie, M. Kitzler, and J. Burgdörfer, "Interference of electron wave packets in atomic ionization by subcycle sculpted laser pulses," *Physical Review A* **89**, 043414 (2014).
- [191] L. Zhang, X. Xie, S. Roither, Y. Zhou, P. Lu, D. Kartashov, M. Schöffler, D. Shafir, P. B. Corkum, A. Baltuška, A. Staudte, and M. Kitzler, "Subcycle Control of Electron-Electron Correlation in Double Ionization," *Physical Review Letters* **112**, 193002 (2014).
- [192] X. Xie, "Two-Dimensional Attosecond Electron Wave-Packet Interferometry," *Physical Review Letters* **114**, 173003 (2015).
- [193] J.-W. Geng, W.-H. Xiong, X.-R. Xiao, L.-Y. Peng, and Q. Gong, "Nonadiabatic Electron Dynamics in Orthogonal Two-Color Laser Fields with Comparable Intensities," *Physical Review Letters* **115**, 193001 (2015).
- [194] M. Han, P. Ge, Y. Shao, M.-M. Liu, Y. Deng, C. Wu, Q. Gong, and Y. Liu, "Revealing the Sub-Barrier Phase using a Spatiotemporal Interferometer with Orthogonal Two-Color Laser Fields of Comparable Intensity," *Physical Review Letters* **119**, 073201 (2017).

- [195] T. Zuo and A. D. Bandrauk, "Phase control of molecular ionization:  $H_2^+$  and  $H_3^{2+}$  in intense two-color laser fields," *Physical Review A* **54**, 3254 (1996).
- [196] A. D. Bandrauk and S. Chelkowski, "Asymmetric Electron-Nuclear Dynamics in Two-Color Laser Fields: Laser Phase Directional Control of Photofragments in  $H_2^+$ ," *Physical Review Letters* **84**, 3562 (2000).
- [197] H. Ohmura, N. Saito, and M. Tachiya, "Selective Ionization of Oriented Nonpolar Molecules with Asymmetric Structure by Phase-Controlled Two-Color Laser Fields," *Physical Review Letters* **96**, 173001 (2006).
- [198] K. J. Betsch, D. W. Pinkham, and R. R. Jones, "Directional Emission of Multiply Charged Ions During Dissociative Ionization in Asymmetric Two-Color Laser Fields," *Physical Review Letters* **105**, 223002 (2010).
- [199] H. Ohmura, N. Saito, and T. Morishita, "Quantum control of molecular tunneling ionization in the spatiotemporal domain," *Physical Review A* **83**, 063407 (2011).
- [200] H. Li, D. Ray, S. De, I. Znakovskaya, W. Cao, G. Laurent, Z. Wang, M. F. Kling, A. T. Le, and C. L. Cocke, "Orientation dependence of the ionization of CO and NO in an intense femtosecond two-color laser field," *Physical Review A* **84**, 043429 (2011).
- [201] M. D. Feit, J. A. Fleck, and A. Steiger, "Solution of the Schrödinger equation by a spectral method," *Journal of Computational Physics* **47**, 412 (1982).
- [202] P. A. Korneev, S. V. Popruzhenko, S. P. Goreslavski, T.-M. Yan, D. Bauer, W. Becker, M. Kübel, M. F. Kling, C. Rödel, M. Wünsche, and G. G. Paulus, "Interference Carpets in Above-Threshold Ionization: From the Coulomb-Free to the Coulomb-Dominated Regime," *Physical Review Letters* **108**, 223601 (2012).
- [203] J. Henkel, *Phenomena in Strong-Field Interaction with Atoms and Molecules* (Verlag Dr. Hut, Munich, 2015).
- [204] M. Li, Y. Liu, H. Liu, Q. Ning, L. Fu, J. Liu, Y. Deng, C. Wu, L.-Y. Peng, and Q. Gong, "Subcycle Dynamics of Coulomb Asymmetry in Strong Elliptical Laser Fields," *Physical Review Letters* **111**, 023006 (2013).
- [205] K. E. Banyard and C. C. Baker, "Molecular formation and electron correlation in  $HeH^+$ ," *International Journal of Quantum Chemistry* **4**, 431 (1970).
- [206] R. Güsten, H. Wiesemeyer, D. Neufeld, K. M. Menten, U. U. Graf, K. Jacobs, B. Klein, O. Ricken, C. Risacher, and J. Stutzki, "Astrophysical detection of the helium hydride ion  $HeH^+$ ," *Nature* **568**, 357 (2019).
- [207] B. Zhang and M. Lein, "High-order harmonic generation from diatomic molecules in an orthogonally polarized two-color laser field," *Physical Review A* **100**, 043401 (2019).
- [208] H. Geiseler, N. Ishii, K. Kaneshima, K. Kitano, T. Kanai, and J. Itatani, "High-energy half-cycle cutoffs in high harmonic and rescattered electron spectra using waveform-controlled few-cycle infrared pulses," *Journal of Physics B* **47**, 204011 (2014).

- [209] E. Dehghanian, A. D. Bandrauk, and G. Lagmago Kamta, "Enhanced ionization of the non-symmetric  $\text{HeH}^+$  molecule driven by intense ultrashort laser pulses," *The Journal of Chemical Physics* **139**, 084315 (2013).
- [210] N. Eicke and M. Lein, "Trajectory-free ionization times in strong-field ionization," *Physical Review A* **97**, 031402(R) (2018).
- [211] E. P. Wigner, "Lower Limit for the Energy Derivative of the Scattering Phase Shift," *Physical Review* **98**, 145 (1955).
- [212] L. A. MacColl, "Note on the Transmission and Reflection of Wave Packets by Potential Barriers," *Physical Review* **40**, 621 (1932).
- [213] W. Pauli, *General Principles of Quantum Mechanics* (Springer-Verlag, Berlin, Heidelberg, 1980).
- [214] A. S. Landsman and U. Keller, "Attosecond science and the tunnelling time problem," *Physics Reports* **547**, 1 (2015).
- [215] M. Büttiker and R. Landauer, "Traversal Time for Tunneling," *Physical Review Letters* **49**, 1739 (1982).
- [216] G. Orlando, C. R. McDonald, N. H. Protik, G. Vampa, and T. Brabec, "Tunnelling time, what does it mean?" *Journal of Physics B* **47**, 204002 (2014).
- [217] A. I. Baz, "Lifetime of intermediate states," *Yadern. Fiz.* **Vol: 4** (1966).
- [218] C. P. J. Martiny, M. Abu-samha, and L. B. Madsen, "Counterintuitive angular shifts in the photoelectron momentum distribution for atoms in strong few-cycle circularly polarized laser pulses," *Journal of Physics B* **42**, 161001 (2009).
- [219] A. N. Pfeiffer, C. Cirelli, M. Smolarski, and U. Keller, "Recent attoclock measurements of strong field ionization," *Chemical Physics* **414**, 84 (2013).
- [220] A. S. Landsman, M. Weger, J. Maurer, R. Boge, A. Ludwig, S. Heuser, C. Cirelli, L. Gallmann, and U. Keller, "Ultrafast resolution of tunneling delay time," *Optica* **1**, 343 (2014).
- [221] T. Zimmermann, S. Mishra, B. R. Doran, D. F. Gordon, and A. S. Landsman, "Tunneling Time and Weak Measurement in Strong Field Ionization," *Physical Review Letters* **116**, 233603 (2016).
- [222] R. Boge, C. Cirelli, A. S. Landsman, S. Heuser, A. Ludwig, J. Maurer, M. Weger, L. Gallmann, and U. Keller, "Probing Nonadiabatic Effects in Strong-Field Tunnel Ionization," *Physical Review Letters* **111**, 103003 (2013).
- [223] I. A. Ivanov and A. S. Kheifets, "Strong-field ionization of He by elliptically polarized light in attoclock configuration," *Physical Review A* **89**, 021402 (2014).
- [224] E. Yakaboylu, M. Klaiber, and K. Z. Hatsagortsyan, "Wigner time delay for tunneling ionization via the electron propagator," *Physical Review A* **90**, 012116 (2014).

- [225] N. Camus, E. Yakaboylu, L. Fechner, M. Klaiber, M. Laux, Y. Mi, K. Z. Hatsagortsyan, T. Pfeifer, C. H. Keitel, and R. Moshhammer, "Experimental Evidence for Quantum Tunneling Time," *Physical Review Letters* **119**, 023201 (2017).
- [226] U. S. Sainadh, H. Xu, X. Wang, A. Atia-Tul-Noor, W. C. Wallace, N. Douguet, A. Bray, I. Ivanov, K. Bartschat, A. Kheifets, R. T. Sang, and I. V. Litvinyuk, "Attosecond angular streaking and tunnelling time in atomic hydrogen," *Nature* **568**, 75 (2019).
- [227] J. M. Rost and U. Saalman, "Attoclock and tunnelling time," *Nature Photonics* **13**, 439 (2019).
- [228] N. Teeny, E. Yakaboylu, H. Bauke, and C. H. Keitel, "Ionization Time and Exit Momentum in Strong-Field Tunnel Ionization," *Physical Review Letters* **116**, 063003 (2016).
- [229] N. Teeny, C. H. Keitel, and H. Bauke, "Virtual-detector approach to tunnel ionization and tunneling times," *Physical Review A* **94**, 022104 (2016).
- [230] M. Yuan, P. Xin, T. Chu, and H. Liu, "Exploring tunneling time by instantaneous ionization rate in strong-field ionization," *Optics Express* **25**, 23493 (2017).
- [231] N. Douguet and K. Bartschat, "Dynamics of tunneling ionization using Bohmian mechanics," *Physical Review A* **97**, 013402 (2018).
- [232] M. Hartmann, *Determination of Momentum-Dependent Ionization Times in Strong-Field Ionization* (Master's thesis, Leibniz Universität Hannover, Hanover, 2016).
- [233] C. Figueira de Morisson Faria, H. Schomerus, and W. Becker, "High-order above-threshold ionization: The uniform approximation and the effect of the binding potential," *Physical Review A* **66**, 043413 (2002).
- [234] S. P. Goreslavski, G. G. Paulus, S. V. Popruzhenko, and N. I. Shvetsov-Shilovski, "Coulomb Asymmetry in Above-Threshold Ionization," *Physical Review Letters* **93**, 233002 (2004).
- [235] N. I. Shvetsov-Shilovski, D. Dimitrovski, and L. B. Madsen, "Ionization in elliptically polarized pulses: Multielectron polarization effects and asymmetry of photoelectron momentum distributions," *Physical Review A* **85**, 023428 (2012).
- [236] A. W. Bray, S. Eckart, and A. S. Kheifets, "Keldysh-Rutherford Model for the Attoclock," *Physical Review Letters* **121**, 123201 (2018).
- [237] M. Han, P. Ge, Y. Fang, X. Yu, Z. Guo, X. Ma, Y. Deng, Q. Gong, and Y. Liu, "Unifying Tunneling Pictures of Strong-Field Ionization with an Improved Attoclock," *Physical Review Letters* **123**, 073201 (2019).
- [238] W. Xie, M. Li, S. Luo, M. He, K. Liu, Q. Zhang, Y. Zhou, and P. Lu, "Nonadiabaticity-induced ionization time shift in strong-field tunneling ionization," *Physical Review A* **100**, 023414 (2019).
- [239] W. Romberg, "Vereinfachte Numerische Integration," *Kongelige Norske Videnskabers Selskab* **28**, 30 (1955).

- [240] J. Kaushal, F. Morales, L. Torlina, M. Ivanov, and O. Smirnova, "Spin-orbit Larmor clock for ionization times in one-photon and strong-field regimes," *Journal of Physics B* **48**, 234002 (2015).
- [241] H. Xie, M. Li, S. Luo, Y. Li, Y. Zhou, W. Cao, and P. Lu, "Energy-dependent angular shifts in the photoelectron momentum distribution for atoms in elliptically polarized laser pulses," *Physical Review A* **96**, 063421 (2017).
- [242] A. N. Pfeiffer, C. Cirelli, A. S. Landsman, M. Smolarski, D. Dimitrovski, L. B. Madsen, and U. Keller, "Probing the Longitudinal Momentum Spread of the Electron Wave Packet at the Tunnel Exit," *Physical Review Letters* **109**, 083002 (2012).
- [243] J. Kaushal and O. Smirnova, "Looking inside the tunnelling barrier: II. Co- and counter-rotating electrons at the 'tunnelling exit'," *Journal of Physics B* **51**, 174002 (2018).
- [244] T. Nubbemeyer, K. Gorling, A. Saenz, U. Eichmann, and W. Sandner, "Strong-Field Tunneling without Ionization," *Physical Review Letters* **101**, 233001 (2008).
- [245] N. Eicke and M. Lein, "Attoclock with counter-rotating bicircular laser fields," *Physical Review A* **99**, 031402(R) (2019).
- [246] J. Henkel, M. Lein, V. Engel, and I. Dreissigacker, "Adiabaticity in the lateral electron-momentum distribution after strong-field ionization," *Physical Review A* **85**, 021402 (2012).
- [247] I. Dreissigacker and M. Lein, "Quantitative theory for the lateral momentum distribution after strong-field ionization," *Chemical Physics Attosecond Spectroscopy*, **414**, 69 (2013).
- [248] C. Hofmann, T. Zimmermann, A. Zielinski, and A. S. Landsman, "Non-adiabatic imprints on the electron wave packet in strong field ionization with circular polarization," *New Journal of Physics* **18**, 043011 (2016).
- [249] C. Hofmann, A. S. Landsman, C. Cirelli, A. N. Pfeiffer, and U. Keller, "Comparison of different approaches to the longitudinal momentum spread after tunnel ionization," *Journal of Physics B* **46**, 125601 (2013).
- [250] A. S. Landsman, C. Hofmann, A. N. Pfeiffer, C. Cirelli, and U. Keller, "Unified Approach to Probing Coulomb Effects in Tunnel Ionization for Any Ellipticity of Laser Light," *Physical Review Letters* **111**, 263001 (2013).
- [251] C. Hofmann, A. S. Landsman, A. Zielinski, C. Cirelli, T. Zimmermann, A. Scrinzi, and U. Keller, "Interpreting electron-momentum distributions and nonadiabaticity in strong-field ionization," *Physical Review A* **90**, 043406 (2014).
- [252] X. Sun, M. Li, J. Yu, Y. Deng, Q. Gong, and Y. Liu, "Calibration of the initial longitudinal momentum spread of tunneling ionization," *Physical Review A* **89**, 045402 (2014).
- [253] C. Z. Bisgaard and L. B. Madsen, "Tunneling ionization of atoms," *American Journal of Physics* **72**, 249 (2004).

- [254] O. I. Tolstikhin, T. Morishita, and L. B. Madsen, "Theory of tunneling ionization of molecules: Weak-field asymptotics including dipole effects," *Physical Review A* **84**, 053423 (2011).
- [255] A. J. F. Siegert, "On the Derivation of the Dispersion Formula for Nuclear Reactions," *Physical Review* **56**, 750 (1939).
- [256] P. A. Batishchev, O. I. Tolstikhin, and T. Morishita, "Atomic Siegert states in an electric field: Transverse momentum distribution of the ionized electrons," *Physical Review A* **82**, 023416 (2010).
- [257] O. I. Tolstikhin and T. Morishita, "Adiabatic theory of ionization by intense laser pulses: Finite-range potentials," *Physical Review A* **86**, 043417 (2012).
- [258] T. Keil, S. V. Popruzhenko, and D. Bauer, "Laser-Driven Recollisions under the Coulomb Barrier," *Physical Review Letters* **117**, 243003 (2016).
- [259] S. Eckart, K. Fehre, N. Eicke, A. Hartung, J. Rist, D. Trabert, N. Strenger, A. Pier, L. P. H. Schmidt, T. Jahnke, M. S. Schöffler, M. Lein, M. Kunitski, and R. Dörner, "Direct Experimental Access to the Nonadiabatic Initial Momentum Offset upon Tunnel Ionization," *Physical Review Letters* **121**, 163202 (2018).
- [260] I. Barth and O. Smirnova, "Nonadiabatic tunneling in circularly polarized laser fields: Physical picture and calculations," *Physical Review A* **84**, 063415 (2011).
- [261] S. Eckart, M. Kunitski, M. Richter, A. Hartung, J. Rist, F. Trinter, K. Fehre, N. Schlott, K. Henrichs, L. P. H. Schmidt, T. Jahnke, M. Schöffler, K. Liu, I. Barth, J. Kaushal, F. Morales, M. Ivanov, O. Smirnova, and R. Dörner, "Ultrafast preparation and detection of ring currents in single atoms," *Nature Physics* **14**, 701 (2018).
- [262] D. G. Arbó, S. Yoshida, E. Persson, K. I. Dimitriou, and J. Burgdörfer, "Interference Oscillations in the Angular Distribution of Laser-Ionized Electrons near Ionization Threshold," *Physical Review Letters* **96**, 143003 (2006).
- [263] C. A. Mancuso, D. D. Hickstein, P. Grychtol, R. Knut, O. Kfir, X.-M. Tong, F. Dollar, D. Zusin, M. Gopalakrishnan, C. Gentry, E. Turgut, J. L. Ellis, M.-C. Chen, A. Fleischer, O. Cohen, H. C. Kapteyn, and M. M. Murnane, "Strong-field ionization with two-color circularly polarized laser fields," *Physical Review A* **91**, 031402 (2015).
- [264] E. Hasović, W. Becker, and D. B. Milošević, "Electron rescattering in a bicircular laser field," *Optics Express* **24**, 6413 (2016).
- [265] D. B. Milošević and W. Becker, "Improved strong-field approximation and quantum-orbit theory: Application to ionization by a bicircular laser field," *Physical Review A* **93**, 063418 (2016).
- [266] C. A. Mancuso, D. D. Hickstein, K. M. Dorney, J. L. Ellis, E. Hasović, R. Knut, P. Grychtol, C. Gentry, M. Gopalakrishnan, D. Zusin, F. J. Dollar, X.-M. Tong, D. B. Milošević, W. Becker, H. C. Kapteyn, and M. M. Murnane, "Controlling electron-ion rescattering in two-color circularly polarized femtosecond laser fields," *Physical Review A* **93**, 053406 (2016).

- [267] W. Becker and D. B. Milošević, "Above-threshold ionization in a bicircular field: Quantum orbits unfolding in a plane," *Journal of Physics: Conference Series* **826**, 012008 (2017).
- [268] E. Hasović, W. Becker, and D. B. Milošević, "Electron Rescattering in a Bicircular Laser Field," *Journal of Physics: Conference Series* **826**, 012009 (2017).
- [269] S. Eckart, M. Richter, M. Kunitski, A. Hartung, J. Rist, K. Henrichs, N. Schlott, H. Kang, T. Bauer, H. Sann, L. P. H. Schmidt, M. Schöffler, T. Jahnke, and R. Dörner, "Nonsequential Double Ionization by Counterrotating Circularly Polarized Two-Color Laser Fields," *Physical Review Letters* **117**, 133202 (2016).
- [270] C. A. Mancuso, K. M. Dorney, D. D. Hickstein, J. L. Chaloupka, J. L. Ellis, F. J. Dollar, R. Knut, P. Grychtol, D. Zusin, C. Gentry, M. Gopalakrishnan, H. C. Kapteyn, and M. M. Murnane, "Controlling Nonsequential Double Ionization in Two-Color Circularly Polarized Femtosecond Laser Fields," *Physical Review Letters* **117**, 133201 (2016).
- [271] S. Ben, P.-Y. Guo, X.-F. Pan, T.-T. Xu, K.-L. Song, and X.-S. Liu, "Recollision induced excitation-ionization with counter-rotating two-color circularly polarized laser field," *Chemical Physics Letters* **679**, 38 (2017).
- [272] V.-H. Hoang, V.-H. Le, C. D. Lin, and A.-T. Le, "Retrieval of target structure information from laser-induced photoelectrons by few-cycle bicircular laser fields," *Physical Review A* **95**, 031402 (2017).
- [273] M. Li, J.-W. Geng, M. Han, M.-M. Liu, L.-Y. Peng, Q. Gong, and Y. Liu, "Subcycle nonadiabatic strong-field tunneling ionization," *Physical Review A* **93**, 013402 (2016).
- [274] K. Kodaira, *Complex Analysis*, Cambridge Studies in Advanced Mathematics (Cambridge University Press, Cambridge, 2007).
- [275] M. Lein, "Streaking analysis of strong-field ionisation," *Journal of Modern Optics* **58**, 1188 (2011).
- [276] W. Squire and G. Trapp, "Using Complex Variables to Estimate Derivatives of Real Functions," *SIAM Review* **40**, 110 (1998).
- [277] N. Douguet and K. Bartschat, "Attoclock setup with negative ions: A possibility for experimental validation," *Physical Review A* **99**, 023417 (2019).
- [278] M. Klaiber, J. Daněk, E. Yakaboylu, K. Z. Hatsagortsyan, and C. H. Keitel, "Strong-field ionization via a high-order Coulomb-corrected strong-field approximation," *Physical Review A* **95**, 023403 (2017).
- [279] O. Neufeld and O. Cohen, "Optical Chirality in Nonlinear Optics: Application to High Harmonic Generation," *Physical Review Letters* **120**, 133206 (2018).
- [280] N. Eicke, S. Brennecke, and M. Lein, "Attosecond-Scale Streaking Methods for Strong-Field Ionization by Tailored Fields," *Physical Review Letters* **124**, 043202 (2020).



- [281] I. A. Ivanov, C. Hofmann, L. Ortmann, A. S. Landsman, C. H. Nam, and K. T. Kim, "Instantaneous ionization rate as a functional derivative," *Communications Physics* **1**, 81 (2018).
- [282] V. V. Serov, A. W. Bray, and A. S. Kheifets, "Numerical attoclock on atomic and molecular hydrogen," *Physical Review A* **99**, 063428 (2019).
- [283] W. Quan, V. V. Serov, M. Wei, M. Zhao, Y. Zhou, Y. Wang, X. Lai, A. S. Kheifets, and X. Liu, "Attosecond Molecular Angular Streaking with All-Ionic Fragments Detection," *Physical Review Letters* **123**, 223204 (2019).
- [284] A. Khan, D. Trabert, S. Eckart, M. Kunitski, T. Jahnke, and R. Dörner, "Orientation-dependent dissociative ionization of H<sub>2</sub> in strong elliptic laser fields: Modification of the release time through molecular orientation," *Physical Review A* **101**, 023409 (2020).
- [285] K. Fehre, S. Eckart, M. Kunitski, C. Janke, D. Trabert, J. Rist, M. Weller, A. Hartung, M. Pitzer, L. P. H. Schmidt, T. Jahnke, R. Dörner, and M. S. Schöffler, "Angular streaking in strong field ionization of chiral molecules," *Physical Review Research* **1**, 033045 (2019).
- [286] L. Torlina and O. Smirnova, "Coulomb time delays in high harmonic generation," *New Journal of Physics* **19**, 023012 (2017).
- [287] C. T. L. Smeenk, L. Arissian, B. Zhou, A. Mysyrowicz, D. M. Villeneuve, A. Staudte, and P. B. Corkum, "Partitioning of the Linear Photon Momentum in Multiphoton Ionization," *Physical Review Letters* **106**, 193002 (2011).
- [288] A. Ludwig, J. Maurer, B. W. Mayer, C. R. Phillips, L. Gallmann, and U. Keller, "Breakdown of the Dipole Approximation in Strong-Field Ionization," *Physical Review Letters* **113**, 243001 (2014).
- [289] A. Hartung, S. Eckart, S. Brennecke, J. Rist, D. Trabert, K. Fehre, M. Richter, H. Sann, S. Zeller, K. Henrichs, G. Kastirke, J. Hoehl, A. Kalinin, M. S. Schöffler, T. Jahnke, L. P. H. Schmidt, M. Lein, M. Kunitski, and R. Dörner, "Magnetic fields alter strong-field ionization," *Nature Physics* **15**, 1222 (2019).
- [290] B. Willenberg, J. Maurer, B. W. Mayer, and U. Keller, "Sub-cycle time resolution of multiphoton momentum transfer in strong-field ionization," *Nature Communications* **10**, 5548 (2019).
- [291] X. M. Tong, K. Hino, and N. Toshima, "Phase-dependent atomic ionization in few-cycle intense laser fields," *Physical Review A* **74**, 031405 (2006).
- [292] L. Tao and A. Scrinzi, "Photo-electron momentum spectra from minimal volumes: The time-dependent surface flux method," *New Journal of Physics* **14**, 013021 (2012).
- [293] X. M. Tong and C. D. Lin, "Empirical formula for static field ionization rates of atoms and molecules by lasers in the barrier-suppression regime," *Journal of Physics B* **38**, 2593 (2005).
- [294] N. Troullier and J. L. Martins, "Efficient pseudopotentials for plane-wave calculations," *Physical Review B* **43**, 1993 (1991).

- [295] A. Čerkić, E. Hasović, D. B. Milošević, and W. Becker, “High-order above-threshold ionization beyond the first-order Born approximation,” *Physical Review A* **79**, 033413 (2009).
- [296] V. S. Popov, “Imaginary-time method in quantum mechanics and field theory,” *Physics of Atomic Nuclei* **68**, 686 (2005).
- [297] M. V. Frolov, N. L. Manakov, A. A. Minina, S. V. Popruzhenko, and A. F. Starace, “Adiabatic-limit Coulomb factors for photoelectron and high-order-harmonic spectra,” *Physical Review A* **96**, 023406 (2017).
- [298] V. D. Mur, S. V. Popruzhenko, and V. S. Popov, “Energy and momentum spectra of photoelectrons under conditions of ionization by strong laser radiation (The case of elliptic polarization),” *Journal of Experimental and Theoretical Physics* **92**, 777 (2001).
- [299] M. Ohmi, O. I. Tolstikhin, and T. Morishita, “Analysis of a shift of the maximum of photoelectron momentum distributions generated by intense circularly polarized pulses,” *Physical Review A* **92**, 043402 (2015).
- [300] K. Liu, S. Luo, M. Li, Y. Li, Y. Feng, B. Du, Y. Zhou, P. Lu, and I. Barth, “Detecting and Characterizing the Nonadiabaticity of Laser-Induced Quantum Tunneling,” *Physical Review Letters* **122**, 053202 (2019).
- [301] J.-W. Geng, L. Qin, M. Li, W.-H. Xiong, Y. Liu, Q. Gong, and L.-Y. Peng, “Nonadiabatic tunneling ionization of atoms in elliptically polarized laser fields,” *Journal of Physics B* **47**, 204027 (2014).
- [302] I. Barth and O. Smirnova, “Nonadiabatic tunneling in circularly polarized laser fields. II. Derivation of formulas,” *Physical Review A* **87**, 013433 (2013).
- [303] L. D. Landau and E. M. Lifshitz, *Quantum Mechanics: Non-Relativistic Theory*, 3rd ed. (Butterworth-Heinemann, London, 1991).
- [304] B. M. Smirnov and M. I. Chibisov, “The Breaking Up of Atomic Particles by an Electric Field and by Electron Collisions,” *Sov. Phys. JETP* **22**, 585 (1966).
- [305] M. Labeye, F. Risoud, A. Maquet, J. Caillat, and R. Taïeb, “Tunnel ionization of atoms and molecules: How accurate are the weak-field asymptotic formulas?” *Journal of Physics B* **51**, 094001 (2018).
- [306] S. Majorosi, M. G. Benedict, and A. Czirják, “Improved one-dimensional model potentials for strong-field simulations,” *Physical Review A* **98**, 023401 (2018).
- [307] S. Majorosi, M. G. Benedict, F. Bogár, G. Paragi, and A. Czirják, “Density-based one-dimensional model potentials for strong-field simulations in He,  $H_2^+$ , and  $H_2$ ,” *Physical Review A* **101**, 023405 (2020).
- [308] V. V. Kolosov, “A hydrogen atom in a strong electric field,” *Journal of Physics B* **20**, 2359 (1987).
- [309] M. Lein and S. Kümmel, “Exact Time-Dependent Exchange-Correlation Potentials for Strong-Field Electron Dynamics,” *Physical Review Letters* **94**, 143003 (2005).

# Curriculum vitae

## Personal details

Name	Nicolas Thomas Eicke
Date of birth	April 11, 1989
Place of birth	Hanover, Germany

## Education

08/2015–01/2020	Doctoral studies at Leibniz Universität Hannover
10/2012–07/2015	Studies of physics at Leibniz Universität Hannover Thesis: “Variational Methods for Quantum Lattice Systems” Degree: Master of Science (M.Sc.)
10/2009–09/2012	Studies of physics at Leibniz Universität Hannover Thesis: “Investigation of Tunneling Times Based on the Methods of Absorbing Potentials” Degree: Bachelor of Science (B.Sc.)
08/2002–06/2009	Gymnasium Sarstedt Degree: Allgemeine Hochschulreife
08/2000–06/2002	Orientierungsstufe Sarstedt
08/1996–07/2000	Grundschule Sarstedt



# List of publications

- [N. Eicke](#) and M. Lein, "Extracting trajectory information from two-color strong-field ionization," [Journal of Modern Optics](#) **64**, 981 (2017).
- D. Würzler, [N. Eicke](#), M. Möller, D. Seipt, A. M. Saylor, S. Fritzsche, M. Lein, and G. G. Paulus, "Velocity map imaging of scattering dynamics in orthogonal two-color fields," [Journal of Physics B](#) **51**, 015001 (2018).
- [N. Eicke](#) and M. Lein, "Trajectory-free ionization times in strong-field ionization," [Physical Review A](#) **97**, 031402(R) (2018).
- H. Ni, [N. Eicke](#), C. Ruiz, J. Cai, F. Oppermann, N. I. Shvetsov-Shilovski, and L. W. Pi, "Tunneling criteria and a nonadiabatic term for strong-field ionization," [Physical Review A](#) **98**, 013411 (2018).
- S. Eckart, K. Fehre, [N. Eicke](#), A. Hartung, J. Rist, D. Trabert, N. Strenger, A. Pier, L. P. H. Schmidt, T. Jahnke, M. S. Schöffler, M. Lein, M. Kunitski, and R. Dörner, "Direct Experimental Access to the Nonadiabatic Initial Momentum Offset upon Tunnel Ionization," [Physical Review Letters](#) **121**, 163202 (2018).
- M. Kunitski, [N. Eicke](#), P. Huber, J. Köhler, S. Zeller, J. Voigtsberger, N. Schlott, K. Heinrichs, H. Sann, F. Trinter, L. P. H. Schmidt, A. Kalinin, M. S. Schöffler, T. Jahnke, M. Lein, and R. Dörner, "Double-slit photoelectron interference in strong-field ionization of the neon dimer," [Nature Communications](#) **10**, 1 (2019).
- [N. Eicke](#) and M. Lein, "Attoclock with counter-rotating bicircular laser fields," [Physical Review A](#) **99**, 031402(R) (2019).
- [N. Eicke](#), S. Brennecke, and M. Lein, "Attosecond-Scale Streaking Methods for Strong-Field Ionization by Tailored Fields," [Physical Review Letters](#) **124**, 043202 (2020).
- M. Kircher, F. Trinter, S. Grundmann, I. Vela-Perez, S. Brennecke, [N. Eicke](#), J. Rist, S. Eckart, S. Houamer, O. Chuluunbaatar, Y. V. Popov, I. P. Volobuev, K. Bagschik, M. N. Piancastelli, M. Lein, T. Jahnke, M. S. Schöffler, and R. Dörner, "Kinematically Complete Experimental Study of Compton Scattering at Helium Atoms near the Threshold," [Nature Physics](#) **16**, 756 (2020).
- S. Brennecke, [N. Eicke](#), and M. Lein, "Gouy's Phase Anomaly in Electron Waves Produced by Strong-Field Ionization," [Physical Review Letters](#) **124**, 153202 (2020).